HYDRONIC NETWORKS
CONCEPTS AND CONTROL

Jiří Dostál

Doctoral Thesis

January, 2023

Department of Control Engineering
Faculty of Electrical Engineering
Czech Technical University in Prague
`http://www.control.fel.cvut.cz`

Ph.D. programme:

Electrical Engineering and Information Technology

Branch of study:

Control engineering and robotics

Supervisor:

Dr. Vladimír Havlena
Department of Control Engineering
Faculty of Electrical Engineering
Czech Technical University in Prague
Karlovo Náměstí 13
12135 Prague 2
Czech Republic

To my lovely Tereza and Tobin, Ruby, and the offspring to come

Abstract

Hydronic networks distribute heat from a source to thermal zones with heat demand. Present hydronic networks evolve only fractionally and don't keep up with the ongoing rapid digitization of buildings. Only so much can be done with traditional mechanical feedback, and electronic software-based control solutions are taking place. The cost of energy minimization algorithms is probitive, and centralized solutions suffer from maintenance issues.

This thesis rethinks hydronic network control from field components to the building-wide system level. A 'Hydronics 4.0' concept is formulated to enable economic, self-commissioning, remote self-diagnosing hydronic heat delivery. On top of this, the newly developed temperature-feedback hydronic actuators provide decoupling and power delivery linearization. Energy optimization is formulated in a plug-and-play manner and solved on the edge devices (actuators) via node-to-node communication, thus providing resistance to single-point failures and enhancing the maintenance and reconfiguration capabilities.

Advances in components modelling, simulation tools and network solvers, up to network stability, analysis, distributed building model calibration and the concept of distributed optimal control are presented within the thesis.

Keywords: hydronic heating; pumping one-pipe; heat flow control; optimization; distributed control; Hydronics 4.0

Abstrakt

Otopné (hydronické) sítě slouží k distribuci tepla ze zdroje do teplotních zón. Pokrok u současných otopných sítí zaostává za probíhající rapidní digitalizací budov. Tradiční mechanické řídicí prvky neposkytují nové možnosti a začínají se prosazovat elektronická, softwarová řešení. Nasazení optimalizačních algoritmů je v současnosti investičně náročné a centralizovaná řešení mají vysoké nároky na údržbu.

Tato práce reviduje otopné systémy od komponent polní instrumentace až po systémový pohled na úrovni celé budovy. Navrhovaný koncept 'Hydronics 4.0' přináší snížené investiční náklady na materiál a práci díky zjednodušenému automatickému nasazení a vzdálené diagnostice. Nově navržené hydronické aktuátory s teplotní zpětnou vazbou navíc potlačují vzájemné vazby v síti a linearizují dodávku tepla. Optimalizační úloha úspory energie je formulovaná modulárně a řešena přímo na koncových zařízeních, aktuátorech, díky decentralizované komunikaci. Takto je zvýšena robustnost proti poruchám jednotlivých bodů a umožněno optimalizační úlohy snadno udržovat a překonfigurovávat.

Prezentovány jsou pokroky v modelování komponent, simulačních nástrojích a síťových řešičích, až po analýzy síťového chování, stability, distribuované kalibrace modelu budovy a návrhu distribuovaného optimálního řízení.

Klíčová slova: otopný systém; čerpadlová jednotrubka; řízení tepelného toku; optimalizace; distribuované řízení; Hydronics 4.0

Acknowledgements

Even though I always leaned toward process control, the hydronic systems control domain wasn't in my scope until my supervisor and former manager, *Prof. Vladimír Havlena,* introduced me. What started out as an innocent small project of hydronic balancing has developed into me writing my own grant projects and eventually starting a research group. I deeply admire Vladimír not only for his erudition but also for his general view on life. I have learned so much from himnot only in technical skills but also in supervisory and managerial skills. I cherish the time of being around, either at work or during our occasional formal and informal meetings.

I envisioned the pump actuator quite early after starting my PhD, but to develop and prove the concept financing was necessary. And I was supported by no other than the just emerged University Centre for Energy Efficient Buildings, CTU in Prague (UCEEB) and its director, *Lukáš Ferkl*. Lukáš and UCEEB allowed me to grow ever since in terms of securing finances and team headcount; I'm grateful to this day, thank you.

Over the years, I have had the honour to work with many exceptional team members, former but also colleagues to this day: *Tomáš Bäumelt, Jiří Cvrček, Ondřej Zlevor, Pavel Souček, Jiří Valtr, Jiří Kubeš, Jan Hauser, Jan Předota, David Zelenka, Ondřej Šrámek* and *Lukáš Vele*. Guys, you are the reason we could push the tech so far, and I feel privileged to call you friends!

The same applies to my former work colleagues whose wit always fascinated me. I feel proud to once have been part of the distinguished Process Control group and to have the opportunity to learn from you, *Pavel Trnka, Daniel Pachner*, *Jiří Řehoř.* I also appreciate the cooperation with *Václav Prajzner, Zdeněk Hrabálek* and *Marek Scholler.*

I will never forget our sparkling discussions and laughter while taking the hardship of doctoral study with my fellow doctoral candidates *Pavel Otta, Jaroslav Tabaček* and *Kamil Dolinský*. I'm so proud of what you have achieved so far and I can't wait to hear your stories to come.

I must also thank the co-authors of the impacted publications I collaborated with, namely *Ivo Herman* and, once again, *Tomáš Bäumelt*.

Finally, immense gratitude belongs to my partner, *Tereza,* for her endless patience and support! I will make up for the time I couldn't be with you.

Contents

III. Hydronic networks 61

Appendices 151

List of Figures

List of Tables

List of Algorithms

1. Introduction

Energy consumption of dwellings amounts to 40% of the total energy consumption in the European Union [1, 2], from which the majority of 64.7% is used for space heating. During a building life cycle, around 40% of energy is spent on its construction and 60% during operation [3]. There is only a minority of energy efficient buildings (25% [2]) and thus there is a solid opportunity for energy savings. The European Commission in 2016 extended the Paris Agreement by a commitment to reduce CO_2 emissions by 40% by 2030, where energy efficiency measures in buildings are among the main drivers; buildings produce 36% of greenhouse emissions [1].

Modern heating/cooling systems used in the European sector are hydronic systems (also called Variable Water Volume, VWV), the north-American sector uses air distribution systems (called Variable Air Volume, VAV) and the Asia-Pacific area use mostly refrigerant systems (called Variable Refrigerant Flow, VRF). Per the EU report [4] (Fig. 1.1), heating and cooling (H/C) accounted for 50 % of the EU's final energy demand (FED). Space heating accounts for 53 % of FED for H/C and is the major demand source, followed by process heating (32 % of FED for H/C). Space heating is relevant for all EU countries as opposed to space cooling (2% of FED for H/C), which is only relevant for southern countries. The cooling demand in Europe is, however, rising [4].

Energy-saving renovations are ongoing in the whole of Europe, especially after the energy crisis of 2022. Although varying greatly nationally, the EU-wide regulations are gradually pushing building energy losses through the envelope to passive or near-zero/net-zero standards (national definitions differ [5]). The insulation thickness is, however, increasing throughout the whole of Europe [5].

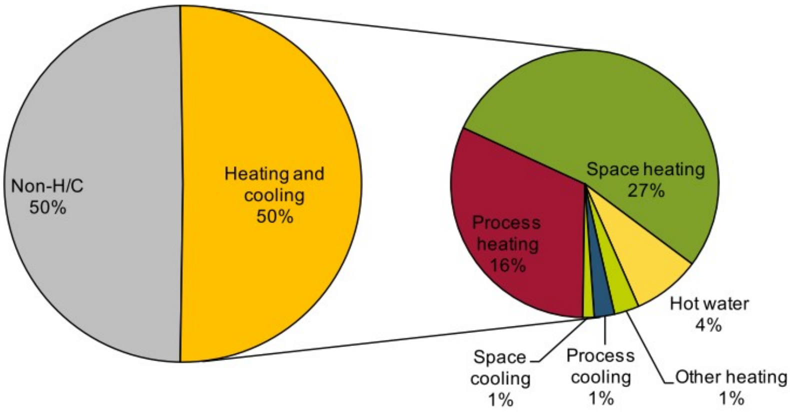

Figure 1.1.: Final energy division of the EU in 2015 [4].

Although a reduction in energy losses through envelope can bring the highest economic gains, it is also necessary to address effectivity of all active technical systems inside the building. From revealing the most obvious issues, such as heating and cooling at the same time to slightly more hidden aspects, such as too early preheating of spaces, moisture accumulation in walls due to too low night setback temperatures, etc. [6]. Apart from direct energy cost, the installation and maintenance cost of systems should also be addressed [7].

Considering further only heating systems, an EU directive [8] recommends newly designed heat generators to be sized for average/typical conditions instead of percentile extremes. Such practice will put higher demands on a heat distribution network as the main heat generator will operate near its maximum ratings for prolonged periods. Efficient and stable control of the heat distribution network is essential to maintain space comfort without switching in any auxiliary heat sources.

The main purpose of a hydronic network is to deliver heat from heat sources to terminal zones. Hydronic networks of the past ran only by gravitational circulation, where correct piping design and realization were necessary to achieve proper circulation/ heat distribution. First circulation pumps were utilized around 1928 (became standard around 1950 [9]) and vastly improved control over the heat distribution process and its versatility. Pressure gained by the fixed-speed pumps allowed to have reasonable flow in almost any heat exchanger in the network. Progressing till the current day, pipes are getting narrower and all circulation pumps are variable speed, but new challenges emerge. Hydraulic networks are often disbalanced causing delays in heat delivery and reduced efficiency of heat sources; on-the-spot solutions to heat delivery issues often come in the form of increasing pump pressure, causing further inefficiencies and noise issues. The commissioning process could be more convenient and faster. Current actuation valves lack remote diagnostic features, failures propagate to tenant comfort levels. Control systems are local, oblivious to the bigger picture, communicating through proprietary protocols and a multitude of gateways, which are gradually becoming impossible to set and maintain after years of service.

Is it possible to build hydronic networks that deliver heat properly and effectively to every zone without the need for a multitude of highly specialized technicians or elaborate simulations? Is there a more efficient and economically favourable alternative? An answer to these questions and possibly others is the objective of this thesis.

1.1. Objectives of the thesis

Ongoing digitization of building components provides only marginal improvements. The cost of system integration and optimal control deployment is prohibitive. Only a radical new concept may overcome the hurdles posed by the hydronic heating of today. It is necessary to rethink-rebuild (bottom to up) hydronic distribution networks (and possibly others) to meet efficiency goals for future buildings.

The thesis objectives are:

- Study hydronic heating in buildings.
- Define an enhancing concept by applying control theory to the building thermal control domain.
- Develop the necessary simulation tools for all involved control and estimation layers.
- Develop and validate the control and estimation algorithms involved in the concept.

1.2. Decentralized building control concept

Commercial buildings are gradually becoming robots we humans built around ourselves. The infrastructures such as HVAC, lighting, access, fire protection, security, phone, IT and others are necessary in order to accommodate human needs indoors. Such systems, overall, consist of thousands of edge devices in a typical commercial building, but also several tens of transcoders and gateways, a handful of communication protocols with their respective master controllers up to one SCADA system, hopefully integrating all of the systems.

A “whole-building” approach, i.e. considering all technical systems together, is envisioned in the roadmap [10] by NREL. There are, however still, barriers to the widespread adoption of the approach nowadays. According to [7] the cost is the main barrier, from which labour expenses take up the majority (for a medium office, HW costs constitute only about 24% of a complete control system). The complexity of the systems leads to specialized labour requirements and associated labour costs. In particular, the more complex the HVAC systems are the more labour cost intensive they are relative to the hardware.

In 2014, I envisioned a hydronic system with a completely decentralized and flat communication architecture, which was eventually shaped into a concept called “Hydronics 4.0” with its associated grant project [11]. The concept stands on the following principles

1. edge-to-edge communication architecture (flat), control and analytics at the edge,
2. daisy-chained power-over-ethernet,
3. zero-commissioning hydronic actuators, remote self-diagnostics,
4. optimized hydronic network topology,
5. distributed model-based optimization algorithm.

The aim is to minimize complexity in communication by using standardized IT infrastructure and avoiding in-between controllers and gateways. Thus, labour is saved, as is the case for power-over-ethernet concept adoption which greatly simplifies wiring. Hydronic actuators with temperature feedback allow robust zero commissioning and remote self-diagnosis of hydronic networks. Incorporating pumping one-pipe hydronic branches may further decrease installation and HW costs. Lastly, capable communicating edge devices can solve optimization tasks in a distributed/decentralized manner, including global resource restrictions.

Fig. 1.2 depicts a multilayer conceptual visualization of a heating system. Floor plan and zoning determine the first layers of interactions - the *zone-to-zone coupling*. Considering commercial buildings, zone comfort is driven by fan coil units (FCU), which may or may not be *coupled through ductwork*. A heating coil of an FCU is controlled by a hydronic actuator (valve, local pump), and there are disturbances caused by *hydronic network coupling*. A hydronic actuator comprises an actuation part (i.e. el. motor) and a sensoric part (e.g. temperature sensors). Electronic peripheries connect to a microcontroller (MCU). The MCU communicates over Ethernet, which always has the star topology, but once the power-over-ethernet (PoE) is daisy-chained (connection in series), it brings about a *PoE network topology coupling*. The MCU contains a local power controller, as well as self-diagnostic routines. Indoor air quality (IAQ) is governed by a distributed/decentralized control and optimization layer, whose *message exchange network* is the last node relation of the whole stack. The nodes - hydronic edge devices - are intertwined, and it is crucial to detangle (=decouple) as many dependencies as possible.

A suggestion from the report for the U.S. Department of Energy [7] from 2022 reads: “A cost-reduction strategy might be to embed controllers at equipment similar to the way edge computing networks operate, which conceptually reduces the number of devices and controllers and the associated labour costs”, which fully aligns with the “Hydronics 4.0” concept outlined.

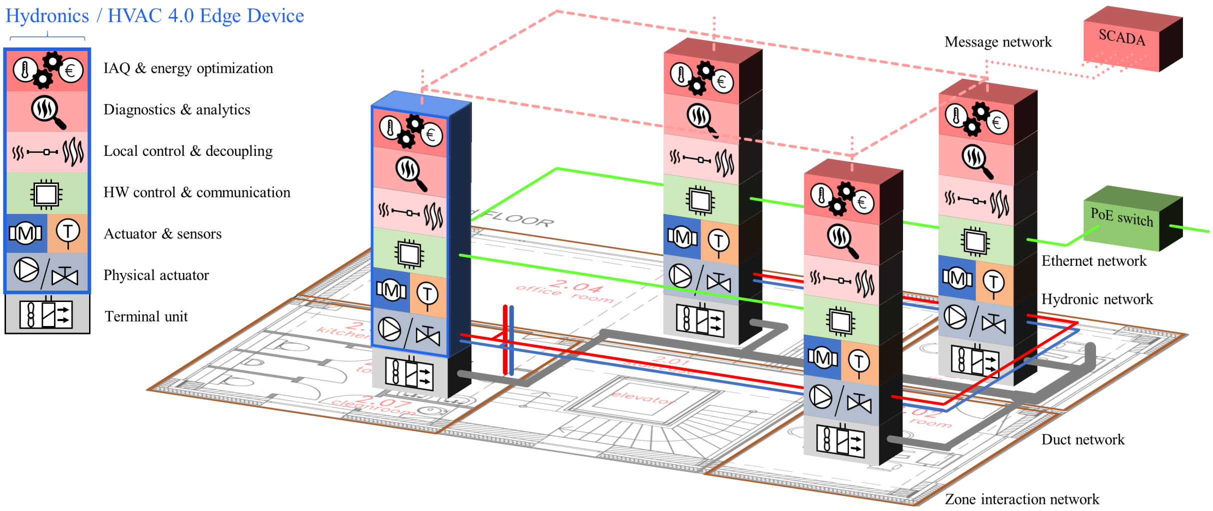

Figure 1.2.: The “Hydronics 4.0” concept. Each edge device (e.g. actuator) consists of multiple HW and algorithmic layers. There are multiple coupling to other edge devices with different topologies.

1.3. Structure of the thesis

The thesis is organized into four parts in the bottom-up fashion according to physical scale:

Part I – Hydronic components Describes important field-level components of hydronic networks; their governing physics, modelling and important variants. Chapter 4 contains an original method to accurately solve heat exchanger thermal equations for prevailing convection conditions.

Part II – Load power control Covers strategies for regulating the heat output of a heat terminal by managing the velocity of a heat transfer liquid. Chapter 6 describes a patented method and device for controlling absolute heat flow without the use of a flowmeter. Real-world validation of the device performance with a testbed description rounds off the part.

Part III – Hydronic networks Describes and analyses traditional hydronic topologies, as well as, less known decentralized pumping hydronic networks. Chapter 9 provides an original stability analysis of distributed controllers in the two-pipe hydronic network and also, so far not published, inlet temperature drop mitigation methods for the pumping one-pipe system. The part is completed by hydronic network control strategies.

Part IV – Building level control Scopes the entire building's thermal control. Chapter 12 provides the methodology of creating a building model in a distributed manner and Chapter 13 outlines decentralized/distributed and centralized (optimal) control strategies.

State-of-the-art sections precede important results distributed throughout the body of the thesis.

Chapters and sections based on original publications are, for convenience, labelled by footnotes in the respective titles.

Part I.

Hydronic components

A hydronic network consist of hydronic components. The components can be of purely hydraulic domain, such as circulators, valves, pipes, etc., or couple the hydraulic domain with a thermal domain such as boilers, chillers, radiators, fan coil units, and so on.

We can categorize the hydraulic components into hydraulic resistances (pipes, valves, hydraulic model of a heat exchanger, etc.) and pressure sources (circulators, elevated tanks, etc.).

A component hydraulic model describes the relation between flow and pressure potential. The flow can be interchangeably defined as either a flow of mass (common notation $\dot{m}$) or a volumetric flow (common notation $\dot{V}$, Q) where the relation between the two is

$$\dot{m} = \rho \dot{V},$$

where ρ stands for liquid density. Both descriptions are equally useful as both can be conserved properties in hydraulic scenarios.

Pressure potential is equal to a differential pressure (common notation Δp) between two positions in a hydraulic circuit. Hydraulic literature also defines the pressure potential in terms of a hydraulic head (common notation H). The hydraulic head is a specific measurement of a liquid pressure, more precisely, a height of a liquid column generating certain liquid pressure difference to the environment surrounding the liquid column

$$\Delta p = H \rho g$$
$$H = \frac{\Delta p}{\rho g},$$

where ρ is the working fluid density and g is the acceleration due to gravity. Hydraulic head is useful in describing centrifugal pumps as their characteristics tent to be independent of the liquid density and provides practical basis for pump specification in liquid elevation scenarios. Hydraulic head is expressed in units of distance (e.g. m or to improve clarity as $\mathrm{m_{w.c.}}$).

2. Hydraulic resistance

A hydraulic resistance is, as in its electrical analogy, a measure of how much of a hydraulic potential is lost over a hydraulic component under given flow

$$\Delta p = f_R\left(Q,R\right),$$

where R represents the hydraulic resistance and f_R is a function to be derived further on. The resistance description is useful in determining pressure/head loss of a hydraulic circuit.

Conversely, as in the electrical analogy, hydraulic conductivity is a measure of how strongly a hydraulic component impedes flow under a given pressure potential

$$Q = f_R^{-1}\left(\Delta p,R\right) = f_K\left(\Delta p,K\right),$$

where K represents the hydraulic conductivity. The exact relation between the hydraulic resistance and conductivity is to be derived further on. The conductivity expression is beneficial in describing flow control valves, for example.

A head loss in general may be of one of the following kind:

- a “major” head loss due to viscous friction of a fluid on a hydraulic component wall, e.g. in pipes etc.,
- a “minor” head loss due to hydrodynamic energy losses in bends, connections, contractions, expansions, etc.,
- a variable hydraulic conductivity, e.g. valve

2.1. Viscous friction resistance

For all flows in this chapter, we will assume that a pipe is filled with the fluid being transported. As opposed to open-channel pipe, where the sole driving force of the flow is gravity, the driving force in a pipe flow is mainly a pressure difference between the ends of a pipe. Flow regimes may be, according to Reynolds, *laminar, transitional* or *turbulent.*

The most important dimensionless parameter for a flow pipe, describing, for example, the flow regime, is the Reynolds number

$$\mathrm{Re} = \frac{\rho v D_h}{\mu},$$

where v $[\mathrm{m}/\mathrm{s}]$ is an average velocity of the flow in a pipe, D_h [m] is a hydraulic diameter of a pipe, ρ $[\mathrm{kg}/\mathrm{m}^3]$ is a fluid density and μ $[\mathrm{kg}/\mathrm{m{\cdot}s}]$ is a dynamic viscosity of the fluid. For a flow in a pipe, the formula also reads as

$$\mathrm{Re} = \frac{Q D_h}{\nu A_c},$$

where Q $[\mathrm{m}^3/\mathrm{s}]$ is a volumetric flow, $\nu = \mu/\rho$ $[\mathrm{m}^2/\mathrm{s}]$ is a kinematic viscosity and A_c $\left[\mathrm{m}^3\right]$ a cross-sectional area of the pipe. For circular pipe, the hydraulic diameter D_h [m] equals to the inside pipe diameter d [m]. The flow in a round pipe is laminar if the Reynolds number is less than approximately 2100 and turbulent if it is greater than approximately 4000 [12, p. 386]. In between, the flow may switch between laminar and turbulent in a random fashion; this region is called transitional.

Without further notice, the flow is for simplicity considered fully developed unless specifically stated otherwise.

The best known representation of the pipe viscous friction is given by Darcy-Weisbach formula [12, eq. 8.34]

$$H = f_D \frac{L}{D_h} \frac{\operatorname{sign}\left(v\right) v^2}{2g},$$

where H_f [m] is a head loss due to friction, L [m] is length of a pipe, D_h [m] is a hydraulic diameter of the pipe, $v = {}^{Q}/_{(\rho \cdot A_c)}$ [${}^{\mathrm{m}}/_{\mathrm{s}}$] is average flow velocity, g [${}^{\mathrm{m}}/_{\mathrm{s}^2}$] is a local gravitation due to gravity and f_D [−] is the Darcy friction factor. For circular pipes, the hydraulic diameter is equal to the actual diameter of the pipe $D_h = D$ and the cross-section area is $A_c = \pi \frac{D^2}{4}$, so the head loss formula becomes

$$H = 8 f_D \frac{L \operatorname{sign}(Q)}{g \pi^2 \rho^2 D^5} Q^2. \tag{2.1}$$

In the laminar region (Re< 2100), the Darcy friction factor depends solely on the Reynolds number [12, eq. 8.19]

$$f_D = \frac{64}{\mathrm{Re}}.$$

In the turbulent region (Re > 4000), the Darcy friction factor is solved iteratively from a Colebrook formula [12, eq. 8.35a]

$$\frac{1}{\sqrt{f_D}} = -2 \ln \left(\frac{1}{3.7} \frac{\epsilon}{D} + \frac{2.51}{\mathrm{Re} \sqrt{f_D}} \right),$$

where an initial solution can be given by a Haaland formula [12, eq. 8.35b]

$$\frac{1}{\sqrt{f_D}} = -1.8 \ln \left(\left(\frac{1}{3.7} \frac{\epsilon}{D} \right)^{1.1} + \frac{6.9}{\mathrm{Re}} \right),$$

which gives the Darcy factor explicitly. Given that the solution to the Haaland formula varies by 2% from that of Colebrook and that the Colebrook formula approximates the friction factor with ±15% accuracy over the whole range, it is probably sufficient to use just the Haaland formula for computationally extensive simulations [13, p. 370].

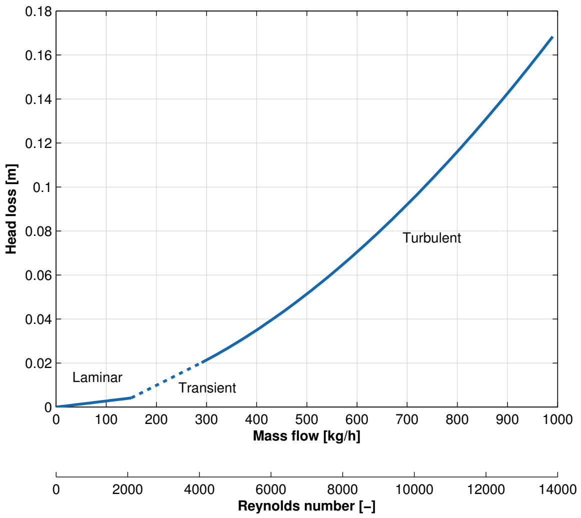

Figure 2.1.: Pipe viscous friction head loss by Darcy-Weisbach formula ($L = 10\mathrm{m}, D = 2.54\mathrm{cm}$).

For smooth pipes, there is a correlation developed by Petukhov [14, eq. 8.21], which gives the friction factor in an explicit form as

$$f_D = (0.79 \ln(\mathrm{Re}_D) - 1.64)^{-2} \quad 3000 \leq \mathrm{Re}_D \leq 5 \cdot 10^6$$

2.2. Hydrodynamic losses

Any hydraulic system has friction and hydrodynamic losses called *minor losses*. These are due to

- pipe entrance or exit,
- bends, elbows, tees or other flow arrangement changes,
- expansion or contraction.

The flow pattern in fittings and bends is rather complex, so the losses are commonly measured experimentally. The head loss is usually given in the following form

$$H = \operatorname{sign}(v)\, k \frac{v^2}{2g} = k \frac{\operatorname{sign}(Q)}{2gA_c^2} Q^2,$$

where $k\,[-]$ is the measured dimensionless loss coefficient [13, eq. 6.78]. The loss coefficient is often not correlated to Reynolds number but rather to the physical shape of the bend or fitting (diameter, angle, etc.).

2.3. Generic hydraulic resistance/conductivity

Friction head loss or similarly hydraulic resistance of complex structures is generally nearly impossible to derive analytically. The friction loss is therefore measured, and the data are correlated to the generic formula

$$\Delta p = RQ^m, \tag{2.2}$$

where Δp [bar] is a pressure loss, R is a hydraulic resistance, $Q\,[\mathrm{m^3/h}]$ is flow, and m is a flow exponent. Analytically, for a straight pipe, the exponent is given by the Darcy-Weisbach formula (2.1) as $m = 2$, the Hazen-Williams formula gives $m = 1.85$ [15]. The exponent can, however, be fitted arbitrarily to measured data if necessary.

A generic hydraulic conductivity is

$$Q = K \sqrt[m]{\Delta p}, \tag{2.3}$$

The hydraulic conductivity unit is $[\mathrm{m^3/(h{\cdot}bar^{0.5})}]$, but for the sake of practicality, a simplified formulation version $[\mathrm{bar} \rightarrow \mathrm{m^3/h}]$ or similarly $\left[\mathrm{m^3/h}\big|_{1\mathrm{bar}}\right]$ is defined and used throughout the thesis.

Unless stated specifically otherwise, the exponent from Darcy-Weisbach formula, $m = 2$, is used throughout the thesis.

Series and parallel connections of hydraulic resistance and conductivities is covered in Sec. A.1.

2.4. Variable hydraulic resistance

A variable hydraulic resistance/conductivity mainly occurs in valves. A valve is governed by

$$Q(x) = K_\mathrm{v}(x) \operatorname{sign}(\Delta p) \sqrt{\Delta p} \tag{2.4}$$

where $Q\,[\mathrm{m^3/h}]$ is the volumetric flow through the valve, Δp [bar] is a differential pressure across the valve, $K_v(x)\left[\mathrm{m^3/h}\big|_{1\mathrm{bar}}\right]$ is a flow factor defining the amount of flow at a certain valve position and pressure $\Delta p = 1\mathrm{bar} = 10^5\mathrm{Pa}$ and $x \in \langle 0,1 \rangle$ is a relative valve opening. A valve size is defined by its saturation flow at 1bar named $K_{vs}\left[\mathrm{m^3/h}\big|_{1\mathrm{bar}}\right]$ and by a flow through the valve when it is fully closed named $K_{v0}\left[{}^{\mathrm{m}^3}\!/\mathrm{H}\big|_{1\mathrm{bar}}\right]$. Formally

$$\begin{aligned} K_{\mathrm{v}}(x) &= \frac{Q}{\sqrt{\Delta p}} \\ K_{\mathrm{vs}} &= \left.\frac{Q}{\sqrt{\Delta p}}\right|_{x=1,\,\Delta p=1\mathrm{bar}}, \\ K_{\mathrm{v0}} &= \left.\frac{Q}{\sqrt{\Delta p}}\right|_{x=0,\,\Delta p=1\mathrm{bar}}. \end{aligned}$$

The shape of the valve characteristics is usually given by a ratio of the latter constants, also called *rangeability* r. Rangeability of 50 is common.

$$r = \left.\frac{Q_{\mathrm{max}}}{Q_{\mathrm{min}}}\right|_{\Delta p=1\mathrm{bar}} = \frac{K_{\mathrm{vs}}}{K_{\mathrm{v0}}}.$$

The equation 2.4 can be rearranged to give pressure difference

$$\Delta p(x) = \mathrm{sign}(Q)\left(\frac{Q}{K_{\mathrm{v}}(x)}\right)^2$$

The hydraulic head loss across the valve is given by the formula

$$H_{\mathrm{v}}(x) = \frac{\Delta p}{\rho g} = \frac{\mathrm{sign}(Q)}{\rho g K_{\mathrm{v}}^2(x)} Q^2,$$

where the H_V [m] is the valve head loss, $Q\,[{}^{\mathrm{m}^3}\!/\mathrm{h}]$ volumetric flow, $\rho\,[{}^{\mathrm{kg}}\!/\mathrm{m}^3]$ fluid density, $g\,[{}^{\mathrm{m}}\!/\mathrm{s}^2]$ gravity acceleration and $K_{\mathrm{v}}(x)\left[{}^{\mathrm{m}^3}\!/\mathrm{h}\big|_{\Delta p=1\mathrm{bar}}\right]$ flow factor at valve opening $x \in \langle 0,1 \rangle$.

The most important part of a valve is its stroke-to-K_{v} characteristics defined by a valve insert. The most common insert types and their respective describing functions are covered in Sec. A.2. An equal-percentage characteristic convenient for controlling heat exchanger power output is described by

$$K_{\mathrm{v}}(x) = K_{\mathrm{vs}} r^{x-1}.$$

3. Pressure source

A hydraulic pressure source can be either a pump or an elevated body of liquid - a tank. A tank provides the pressure proportional to a hydraulic head as $\Delta p = H\rho g$. A hydronic circulator is an elementary component in modern hydronic networks. It is usually a centrifugal pump, a device designed to transfer electrical power into hydraulic power of a fluid through a rotating impeller. The fluid flows from an inlet to the centre of the impeller and out along its blade. The centrifugal force hereby increases the kinetic energy of the fluid, and consequently, the velocity and pressure are increased.

Electrical power P_e [W] is at a pump drive converted into rotational mechanical power P_{shaft} [W]

$$P_{\text{shaft}} = \eta_1 P_{\text{e}},$$

the shaft powers the impeller, thus transferring the mechanical power into hydraulic power P_h [W]

$$P_{\text{h}} = \eta_2 P_{\text{shaft}} = Q\Delta p.$$

The total efficiency of a pump is defined as a ratio of the hydraulic power produced to the electrical power consumed

$$\eta_{\text{tot}} = \eta_1\eta_2 = \frac{P_{\text{h}}}{P_{\text{e}}} = \frac{Q\Delta p}{P_{\text{e}}}.$$

Pressure of the working fluid is in the pump industry commonly measured in the hydraulic head, which relates to pressure as

$$\Delta p = H\rho g,$$

where Δp [Pa] is a pressure difference between two points in hydraulic setting, ρ [$^{\text{kg}}/_{\text{m}^3}$] is a density of the fluid, g [$^{\text{m}}/_{\text{s}^2}$] is gravitational acceleration and H [m] is a height of equivalent fluid column, i.e. hydraulic head. Such a measure is motivated by the natural, historical objective of a pump to elevate fluid.

When impeller rotational velocity changes, so does the kinetic energy given to the fluid and thus also the pressure. It turns out that so-called affinity laws can well predict the variation of the pump performance with speed change.

3.1. Affinity laws

When the angular velocity of the pump shaft is changed, the consequences can be predicted using affinity laws. The laws are derived under the assumption of geometrical similarity of velocity triangles during speed changes. More information about the derivation can be found at [16]. The first law represents the linearity of a flow change with speed

$$Q(n) \quad = \quad Q_{\text{n}}\left(\frac{n}{n_{\text{n}}}\right), \tag{3.1}$$

where Q_{n} is a nominal pump flow at $n = n_{\text{n}}$, n_{n} is nominal speed (usually the full speed or the design point) and n is the actual speed of the pump. The variables are intentionally given without units, as the laws hold for all appropriate units. The second law states that the pump head scales quadratically with speed

$$H(n) = H_{\text{n}}\left(\frac{n}{n_{\text{n}}}\right)^2, \tag{3.2}$$

where H_n is a nominal pump head at $n = n_n$. The third law is derived easily from the first two and describes the variation of pump shaft power with speed

$$P_{shaft}(n) = Q_n H_n \left(\frac{n}{n_n}\right)^3 . \tag{3.3}$$

The latter formula assumes that the efficiency of the pump remains constant. That is rarely true in practice. Modelling the efficiency scale to decrease with speed, (3.3) can be compensated for by decreasing the scaling exponent. More information is be given in Sec. A.3.1.

3.2. Pump characteristics

A pump is well defined by its head-flow characteristics and either efficiency or power consumption characteristics. Small circulation pump characteristics are plotted in Fig. 3.1.

The head-flow characteristics at nominal pump speed can be approximated by a polynomial

$$H(Q)|_{n=n_n} = \sum_{i=0}^{d_H} a_{i,n} Q^i \tag{3.4}$$

and usually a second order approximation ($d_H = 2$) is sufficient, so the pump head variation with the flow at nominal conditions is given by

$$H(Q)|_{n=n_n} = a_{2,n}(Q)^2 + a_{1,n}Q + a_{0,n}.$$

The electric power consumption at nominal conditions can also represented by a polynomial

$$P_e(Q)|_{n=n_n} = \sum_{i=0}^{d_P} b_{i,n} Q^i , \tag{3.5}$$

where the first or second order ($d_P = 1$ or 2) should sufficiently capture the relationship.

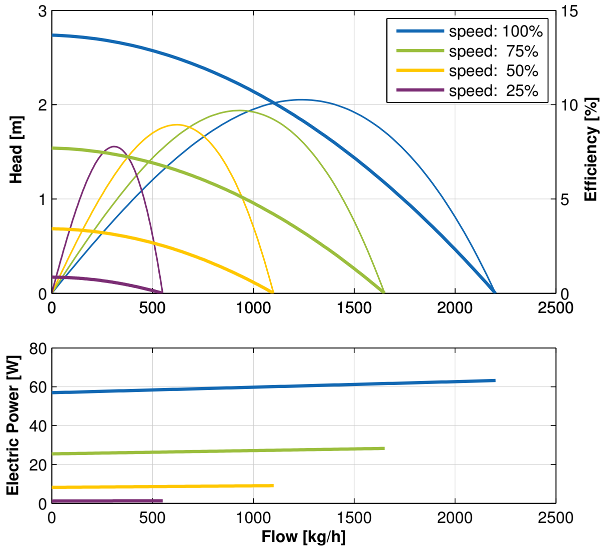

Figure 3.1.: Pump characteristics of a residential circulation pump.

Varying the pump speed by a ratio

$$S = \frac{n}{n_{\mathrm{n}}}$$

results by the affinity laws (3.1), (3.2) in adapted pump head-flow polynomial with coefficients

$$\begin{aligned} a_i(S) &= a_{i,\mathrm{n}} S^{2-i} \\ b_i(S) &= b_{i,\mathrm{n}} S^{(3-\chi-i)}, \end{aligned}$$

where the detailed description may be found in Sec. A.3.1.

Hydraulic power characteristic is described by a polynomial

$$P_{\mathrm{h}}(H,Q,S) = \sum_{i=0}^{d_{\mathrm{H}}+1} c_i(S)\, Q^i,$$

where the coefficients are (see Sec. A.3.2 for derivation)

$$\begin{aligned} & c_i(S) = \tfrac{1}{3{,}6 \cdot 10^3} \rho g \cdot a_{i-1}(S), i = 1 \ldots d_{\mathrm{H}} + 1 \\ & c_0 = 0. \end{aligned}$$

The best efficiency point is found using relations found in Sec. A.3.3. The energy efficiency index of a pump is described in Sec. A.3.4.

3.3. Generic pump model

Pump characteristics may be fully described by a variety of models, however, due to the theory given in Sec. 3.1 a low-order polynomial function in two parameters provides sufficient basis functions to capture real-world pump behaviour. The polynomial model has the following generic form

$$\begin{aligned} H(Q,S) &= \mathrm{pol}_H(Q,S) \\ P_{\mathrm{e}}(Q,S) &= \mathrm{pol}_{P_{\mathrm{e}}}(Q,S). \end{aligned} \tag{3.6}$$

When fitting the model (3.6) to data, it is beneficial to enforce shape constraints to ensure

- for $H(Q,S)$,
  - concave in flow
  - monotonically increasing in speed
  - non-negative
- and for $P_{\mathrm{e}}(Q,S)$,
  - monotonically increasing in flow
  - monotonically increasing in speed
  - non-negative.

Polynomial shape constraints can be translated into linear constraints in parameters [17, 18] instead of being calculated on a grid in the input space. An example of such a characteristic is in Fig. 3.2.

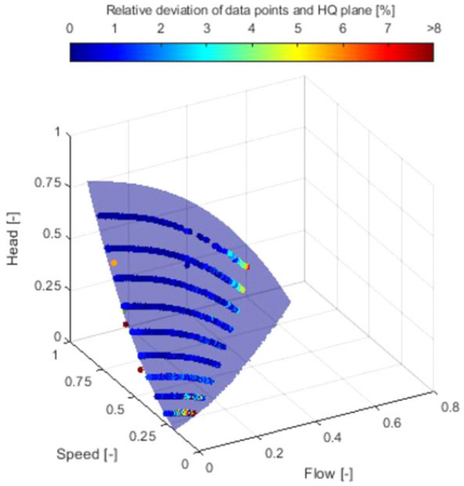

Figure 3.2.: A 2D polynomial model with shape constraints fitted to real pump data.

4. Heat exchanger

A heat exchanger (HX) is a device designed for transferring heat between two working fluids. Most common heat exchanger found in the HVAC industry is the water-to-air heat exchanger with either forced air convection (e.g. fan coil unit) or natural convection (e.g. convectors), the gas-to-water HX (e.g. gas boiler), the water-to-water (e.g. domestic heat transfer station) and the air-to-air (e.g. ventilation recuperation unit) heat exchanger.

Residential hydronic heating systems use as heat sources mainly boilers, either wood, coal, oil or gas-fired and increasingly, in the recent past, also heat pumps. On a smaller scale, purely electric heating is used. Apartment block buildings situated in cities mainly use district heating and superheated-steam-to-water heat exchangers.

Cooling hydronic systems use chillers as the main heat/cold source. The heat transfer fluid, in this case, is commonly ethylene glycol solution or other solutions providing a lower freezing point than water. A 30-70% glycol water solution has a freezing point $-13.7°\mathrm{C}$, but the payoff is a lowered specific heat capacity $3.768\,{}^{\mathrm{kJ}}/_{\mathrm{kg \cdot K}}$ (90% of pure water). A great deal of information about heat sources is provided in [19, chap. 3].

Commercial building HVAC systems use as heat emitters mainly fan coil units or convectors. Residential buildings often use natural-convection radiators or floor radiant heating.

A hydraulic and thermal description of a heat exchanger follows.

4.1. Hydraulic model

From the hydraulic point of view, a heat exchanger is a hydraulic resistance, and as such, it is defined by a generic hydraulic loss formula 2.2.

The hydraulic resistances of boilers/chillers are difficult to obtain from the datasheets. Old solid-fuel-fired heaters had low hydraulic resistance, whereas the new condensation boilers have very high resistance and also commonly incorporate a built-in pump (of unknown specification) to compensate for the head loss and to provide circulation.

Friction loss of natural-convection radiators is low; fan coil units have generally high hydraulic losses; convectors stand in between, but the most hydraulically resistant are underfloor heating installations. See Fig. 6.5 for hydraulic conductivities of numerous randomly sampled heat terminals.

4.2. Thermal model[1]

A heat exchanger system is, from the mathematical point of view, an instance of a general advection-diffusion-reaction equation being a special case of a general continuity equation. The following sections will provide a method for solving an advection-diffusion-reaction equation by the standard finite volume method (Sec. 4.2.2) and by an original mixed-mesh finite volume method (Sec. 4.2.3). Implementation of the latter method for a heat exchanger is provided in Sec. 4.2.5.

---

[1] Based on the original paper: Jiří Dostál and Vladimír Havlena. “Mixed Mesh Finite Volume Method for 1D Hyperbolic Systems with Application to Plug-flow Heat Exchangers”. In: *Mathematics* 9.20 (Oct. 2021), p. 2609. ISSN: 2227-7390. DOI: `10.3390/math9202609`

4.2.1. Problem formulation

Consider a general continuity equation in one spatial dimension

$$\partial_t \boldsymbol{q} + \partial_x \boldsymbol{f} = \boldsymbol{s}, \tag{4.1}$$

where the flux $\boldsymbol{f}(x,t)$ is of the form

$$\boldsymbol{f} = \boldsymbol{V}\boldsymbol{q} + \boldsymbol{D}\nabla\boldsymbol{q}$$

and the variables of interest (states) $\boldsymbol{q}(x,t) : \mathbb{R} \times \mathbb{R} \to \mathbb{R}^n$ are defined on a spatial domain $x \in \Omega$ and time domain $t \in \mathcal{J}$, $\boldsymbol{V}(t)$ is a matrix of time-dependent transport velocities, $\boldsymbol{D}$ is a diffusion coefficient matrix, $\boldsymbol{s}(\boldsymbol{q},x,t) \in \mathbb{R}^n$ is a source/sink term and $\partial_t = \partial/\partial t, \partial_x = \partial/\partial x$ are shorthand notations for partial differential operators with respect to time and space (Euler notation), respectively.

Under the assumption of incompressible fluid, spatially invariant transport velocity and constant diffusion coefficients, we get a common advection-diffusion-reaction equation

$$\partial_t \boldsymbol{q} + \boldsymbol{V}\partial_x \boldsymbol{q} + \boldsymbol{D}\partial_x^2 \boldsymbol{q} = \boldsymbol{s}. \tag{4.2}$$

Focusing further on highly advective systems (with the Péclet number much larger than 10) the diffusion term is marginal, and can be omitted [21]. Consider now the initial boundary value problem (IBVP) for the system (4.3), where $\boldsymbol{q}_0(x)$ is an initial spatial profile at time $t = t_0$ and boundary conditions at $x = 0$ are $\boldsymbol{b}(t)$ (transport velocities are considered non-negative in the positive direction of x),

$$\begin{aligned} \partial_t \boldsymbol{q} + \boldsymbol{V}\partial_x \boldsymbol{q} &= \boldsymbol{s} && \text{(4.3a)} \\ \boldsymbol{q}(x,t_0) &= \boldsymbol{q}_0(x) && \text{(4.3b)} \\ \boldsymbol{q}(0,t) &= \boldsymbol{b}(t). && \text{(4.3c)} \end{aligned}$$

The goal is to obtain a transient solution for the variables $\boldsymbol{q}(x,t)$ on a defined time interval $\mathcal{J} \equiv \langle t_0, T\rangle$. In particular, to obtain a numerical solution that preserves the wave behaviour of the system without introducing numerical diffusion.

4.2.2. Finite volume method

A finite volume method (FVM) is one of the numerical solution techniques used for solving fluid dynamics problems. The core of the method lies in the usage of the divergence theorem on cells of finite volume and then on an approximation of the cell boundary fluxes from cell averages (a cell-centred method is assumed). More specifically, define a grid of N nodes, equidistant for simplicity, with a node-to-node distance $\Delta x = 1/N$. For any $\boldsymbol{h} : \mathbb{R} \times \mathbb{R} \to \mathbb{R}^n$ define a notation of an average value over one grid length,

$$\overline{(\boldsymbol{h})}_x(t) = \frac{1}{\Delta x}\int_{c(x)} \boldsymbol{h}(s,t)\,\mathrm{d}s, \tag{4.4}$$

where the interval $c(x) = \langle x - \Delta x/2, x + \Delta x/2\rangle$. Now, applying the cell average to (4.3) and using the divergence theorem results in a system of ordinary differential equations for all cell-average variables

$$\frac{\mathrm{d}}{\mathrm{d}t}\boldsymbol{q}_i + \frac{\boldsymbol{V}}{\Delta x}\left(\boldsymbol{q}_{i-1/2} - \boldsymbol{q}_{i+1/2}\right) = \boldsymbol{s}_i, \tag{4.5}$$

where $\boldsymbol{q}_i = \overline{(\boldsymbol{q})}_{x_i}$ is a cell average about position $x_i = (i - 1/2)\,\Delta x, i = 1, \ldots, N$, $\boldsymbol{q}_{i\pm 1/2} = \boldsymbol{q}(x_i \pm \Delta x/2, t)$ denote left and right face values, and $\boldsymbol{s}_i = \overline{(\boldsymbol{s})}_{x_i}$ is a cell source term average. The face value approximation depends on the numerical scheme used. In the first-order upwind scheme, for example, are the face values simply $\boldsymbol{q}_{i-1/2} = \boldsymbol{q}_{i-1}, \boldsymbol{q}_{i+1/2} = \boldsymbol{q}_i$. The first-order upwind approximation is monotone (no non-physical oscillations) but introduces a considerable numerical diffusion. Higher-order schemes bring higher accuracy, where the solution is smooth, but by the order barrier theorem [22] cannot be monotone. The remedy is to approximate the face values by low order scheme, where the solution has high gradients and by high order scheme, where the solution is smooth. The switch between schemes is performed according to a slope/flux limiter function and the method coined the term MUSCL [23]. Numerous limiters were introduced over the past five decades, starting by Van Leer [24]. An important class of slope limiters is one forbidding an appearance of any new local extrema - the total variation diminishing class [25]. In the MUSCL scheme, the face values are approximated, component-wise, as

$$\begin{aligned} q_{i-1/2} &= q_{i-1} + \frac{\phi\left(r_{i-1}\right)}{2}\left(q_{i-1} - q_{i-2}\right) \\ q_{i+1/2} &= q_i + \frac{\phi\left(r_i\right)}{2}\left(q_i - q_{i-1}\right), \end{aligned}$$

where the slope limiter function is, for example, the one by Van Leer [24]

$$\phi\left(r\right) = \frac{r + |r|}{1 + |r|}$$

and the smoothness monitor is

$$r_i = \frac{q_i - q_{i-1}}{q_{i+1} - q_i}. \tag{4.6}$$

See [26, 27] for more schemes and slope limiters.

Time evolution of (4.5) is obtained using standard integration techniques such as RK4; special care, however, has to be taken concerning the sampling period. In order to contain the physical domain of dependence in the numerical domain of dependence (or, in other words, avoid interaction with adjacent Riemann problems), the sampling period must satisfy the Courant–Friedrichs–Lewy (CFL) condition [28]

$$\max\left(\left|\mathrm{eig}\left(\boldsymbol{V}\right)\right|\right)\Delta t \leq \Delta x. \tag{4.7}$$

4.2.3. Mixed-mesh finite volume method

The challenge of the numerical approximation of hyperbolic transport equations is to obtain high accuracy of the solution in both discontinuous and smooth regions [29]. Highly advective systems also present a challenge for the finite volume method. The cells are considered coherent (ideally mixed); consequently the flux at one boundary immediately influences fluxes at all the other boundaries. The numerical propagation speed is, therefore, always infinite for FVM. Pure discontinuities, as well, always dissolve into smooth step changes. The finer the grid, the less the phenomenon is observed. An exact solution, advecting discontinuities sharp, is obtained for an infinite number of cells [30].

To overcome this fundamental limitation, we propose a modified approach.

Remark 1. Where coherent cells of finite volumes are used, an exact finite transport speed is only preserved by moving the grid by this velocity.

A Mixed-mesh Finite Volume Method (MMFVM) based on the observation of Remark 1 is presented here. The underlying principle is simple: advect (move) cells of the flowing field and simultaneously solve FVM for both the moving and static cells until the moving grid passes the static grid by one grid length; sample the state and reinitialize all moving cells to their starting positions and assign appropriate cell averages. The idea was first introduced in the preceding conference papers [31, 32] and will be generalized here. We believe a similar approach was used in [33, 34], but a description of the spatially discretized system and its analysis is missing therein.

Definition 1 (Monocharacteristic hyperbolic system)**.** A system of the form (4.1), where the flux Jacobian $\boldsymbol{J} \equiv \partial \boldsymbol{f} / \partial \boldsymbol{q}$ can be decomposed to

$$\boldsymbol{J} = v\boldsymbol{R}\boldsymbol{D}\boldsymbol{R}^{-1}, \boldsymbol{D} = \mathrm{diag}\left(d_1, \ldots, d_n\right), d_i \in \{0,1\}\,\forall i \tag{4.8}$$

with $v(t) \in \mathbb{R}$ being a space-independent velocity and $\boldsymbol{R}$ being a square decomposition matrix is a monocharacteristic hyperbolic system, e.i. the system has a monocharacteristic hyperbolic property.

Remark 2. Since a hyperbolic system has a diagonalizable flux Jacobian with real eigenvalues, a system is monocharacteristic hyperbolic when the Jacobian has just one non-zero eigenvalue, i.e., when a subset of the vector variable $\boldsymbol{q}$ advects with a transport (characteristic) velocity v, and the rest of $\boldsymbol{q}$ is stationary.

Definition 2 (Normal monocharacteristic form)**.** A normal monocharacteristic form is

$$\partial_t \boldsymbol{q} + v \begin{bmatrix} \boldsymbol{I} & \cdot \\ \cdot & \boldsymbol{0} \end{bmatrix} \partial_x \boldsymbol{q} = \boldsymbol{s} \tag{4.9}$$

or equivalently

$$\partial_t \begin{bmatrix} \boldsymbol{q}_\mathrm{a} \\ \boldsymbol{q}_\mathrm{s} \end{bmatrix} + v \begin{bmatrix} \boldsymbol{I} & \cdot \\ \cdot & \boldsymbol{0} \end{bmatrix} \partial_x \begin{bmatrix} \boldsymbol{q}_\mathrm{a} \\ \boldsymbol{q}_\mathrm{s} \end{bmatrix} = \begin{bmatrix} \boldsymbol{s}_\mathrm{a} \\ \boldsymbol{s}_\mathrm{s} \end{bmatrix}, \tag{4.10}$$

where $\boldsymbol{q} = \begin{bmatrix} \boldsymbol{q}_\mathrm{a}^\mathsf{T} & \boldsymbol{q}_\mathrm{s}^\mathsf{T} \end{bmatrix}^\mathsf{T}$, $\boldsymbol{s} = \begin{bmatrix} \boldsymbol{s}_\mathrm{a}^\mathsf{T} & \boldsymbol{s}_\mathrm{s}^\mathsf{T} \end{bmatrix}^\mathsf{T}$ and $\boldsymbol{q}_\mathrm{a}(x,t) : \mathbb{R} \times \mathbb{R} \to \mathbb{R}^{n_\mathrm{a}}$ is a vector of advected states, $\boldsymbol{q}_\mathrm{s}(x,t) : \mathbb{R} \times \mathbb{R} \to \mathbb{R}^{n_\mathrm{s}}$ is a vector of stationary states and $\boldsymbol{s}_\mathrm{a}(\boldsymbol{q},\boldsymbol{u},t) \in \mathbb{R}^{n_\mathrm{a}}$, $\boldsymbol{s}_\mathrm{s}(\boldsymbol{q},\boldsymbol{u},t) \in \mathbb{R}^{n_\mathrm{s}}$ are respective spatially independent sink/source terms. $\boldsymbol{I}, \boldsymbol{0}$ are square unit and zero matrices of appropriate sizes and $(\cdot)$ denote rectangular zero matrices of the corresponding sizes.

Lemma 1. *A system* (4.1) *with a monocharacteristic property* (4.8) *has a normal monocharacteristic form* (4.9)*,* (4.10).

Proof. We will prove the statement by transformation construction. The system (4.1) can be decomposed using the chain rule as

$$\partial_t \boldsymbol{q} + \left.\frac{\partial \boldsymbol{f}}{\partial \boldsymbol{q}}\right|_{x=\mathrm{const.}} \partial_x \boldsymbol{q} = \boldsymbol{s} - \left.\frac{\partial}{\partial x} \boldsymbol{f}\right|_{\boldsymbol{q}=\mathrm{const.}},$$

where $\boldsymbol{J} \equiv {}^{\partial \boldsymbol{f}}/_{\partial \boldsymbol{q}}|_{x=\mathrm{const.}}$ is the flux Jacobian and $\bar{\boldsymbol{s}} \equiv \boldsymbol{s} - {}^{\partial}/_{\partial x}\boldsymbol{f}|_{\boldsymbol{q}=\mathrm{const.}}$ is an equivalent sink/source term. Since the system is monocharacteristic hyperbolic, $\boldsymbol{J}$ can be decomposed to form (4.8). Defining now a permutation matrix $\boldsymbol{P}$ such that

$$\boldsymbol{P}^\mathsf{T} \boldsymbol{D} \boldsymbol{P} = \begin{bmatrix} \boldsymbol{I} & \cdot \\ \cdot & \boldsymbol{0} \end{bmatrix},$$

the Jacobian is

$$\boldsymbol{J} = v \boldsymbol{R} \boldsymbol{P} \begin{bmatrix} \boldsymbol{I} & \cdot \\ \cdot & \boldsymbol{0} \end{bmatrix} (\boldsymbol{R}\boldsymbol{P})^{-1}.$$

So (4.1) can be rewritten as

$$\begin{aligned} \partial_t \boldsymbol{q} + v \boldsymbol{R}\boldsymbol{P} \begin{bmatrix} \boldsymbol{I} & \cdot \\ \cdot & \boldsymbol{0} \end{bmatrix} (\boldsymbol{R}\boldsymbol{P})^{-1} \partial_x \boldsymbol{q} &= \bar{\boldsymbol{s}} \\ (\boldsymbol{R}\boldsymbol{P})^{-1} \partial_t \boldsymbol{q} + v \begin{bmatrix} \boldsymbol{I} & \cdot \\ \cdot & \boldsymbol{0} \end{bmatrix} (\boldsymbol{R}\boldsymbol{P})^{-1} \partial_x \boldsymbol{q} &= (\boldsymbol{R}\boldsymbol{P})^{-1} \bar{\boldsymbol{s}}. \end{aligned}$$

Now, define a transformation $T(x) = (\boldsymbol{R}\boldsymbol{P})^{-1} x$, then $\widetilde{\boldsymbol{q}} \equiv T(\boldsymbol{q})$, $\widetilde{\boldsymbol{s}} \equiv T(\bar{\boldsymbol{s}})$ and

$$\partial_t \widetilde{\boldsymbol{q}} + v \begin{bmatrix} \boldsymbol{I} & \cdot \\ \cdot & \boldsymbol{0} \end{bmatrix} \partial_x \widetilde{\boldsymbol{q}} = \widetilde{\boldsymbol{s}}$$

is in a normal monocharacteristic form (4.9). □

4.2.3.1. Method formulation

Consider a problem (4.1) with a monocharacteristic property (4.8) without a loss of generality in the monocharacteristic form (4.10)

$$\begin{aligned}
\partial_t \boldsymbol{q}_{\mathrm{a}} + v\partial_x \boldsymbol{q}_{\mathrm{a}} &= \boldsymbol{s}_{\mathrm{a}}\left(\boldsymbol{q}_{\mathrm{a}},\boldsymbol{q}_{\mathrm{s}},\boldsymbol{u}\right) &\quad (4.11\mathrm{a})\\
\partial_t \boldsymbol{q}_{\mathrm{s}} &= \boldsymbol{s}_{\mathrm{s}}\left(\boldsymbol{q}_{\mathrm{a}},\boldsymbol{q}_{\mathrm{s}},\boldsymbol{u}\right) &\quad (4.11\mathrm{b})\\
\boldsymbol{q}_{\mathrm{a}}(0,t) &= \boldsymbol{b}(t) &\quad (4.11\mathrm{c})\\
\boldsymbol{q}_{\mathrm{a}}(x,0) &= \boldsymbol{q}_{\mathrm{a},0}(x) &\quad (4.11\mathrm{d})\\
\boldsymbol{q}_{\mathrm{s}}(x,0) &= \boldsymbol{q}_{\mathrm{s},0}(x), &\quad (4.11\mathrm{e})
\end{aligned}$$

where $\boldsymbol{u}(t)$ are external inputs, initial spatial profiles for advected states and static states are $\boldsymbol{q}_{\mathrm{a},0}(x)$, $\boldsymbol{q}_{\mathrm{s},0}(x)$, respectively and $v(t) \geq 0$. Define an equidistant grid of N elements with a grid spacing Δx. The stationary grid Ξ_{s} resembles the one of FVM

$$\Xi_{\mathrm{s}} = \left\{ x_{\mathrm{s}}^i \middle| \; i \in \mathbb{Z}, 0 \leq i \leq N, \Delta x = \frac{1}{N}, x_{\mathrm{s}}^i = \left(i - \frac{1}{2}\right)\Delta x \right\}, \tag{4.12}$$

but the advected grid differs importantly. The basic idea behind the MMFVM is to allow the grid of advected states to flow along the stationary states with the characteristic velocity v.

Definition 3 (Relative cell shift)**.** A relative stationary-to-advected grid shift p is a distance a tracer would travel with a velocity v in a time interval $\langle t_0, t_0 + \tau\rangle$ taken relative to one grid length Δx

$$p(t) = \frac{1}{\Delta x}\int_{t_0}^{t_0+\tau} v(s)\,\mathrm{d}s, \tag{4.13}$$

where the integration start t_0 will be specified later on.

Definition 4 (Advected grid)**.** Grid positions of the advected states are

$$\Xi_{\mathrm{a}} = \left\{ x_{\mathrm{a}}^i \middle| \, i \in \mathbb{Z}, 0 \leq i \leq N, x_{\mathrm{a}}^i = x_{\mathrm{s}}^i + p\Delta x \right\}, \tag{4.14}$$

where p is given by (4.13).

Remark 3. Note that there is always at least one upwind “ghost” cell for the advected states at position $x_{\mathrm{a}}^0 = (p - 1/2)\,\Delta x$, where a boundary condition is applied. Other ghost cells are added depending on the boundary conditions. See Fig. 4.1 for illustration. Also, note that there is a ghost cell at position x_{s}^0 that can be used to apply boundary conditions for static states, but this cell does not play any role and is only added for future use and simplification of the notation.

Theorem 1 (MMFVM step)**.** *Time evolution of a problem* (4.11) *discretized on grids* Ξ_{s}, Ξ_{a}, *is on a time interval* $\langle t_0, t_0 + \tau\rangle$ *given by*

$$\begin{aligned}
\frac{\mathrm{d}}{\mathrm{d}t}\begin{bmatrix} \boldsymbol{q}_{\mathrm{a}}^i \\ \boldsymbol{q}_{\mathrm{s}}^i \end{bmatrix} &= (1-p)\begin{bmatrix} \boldsymbol{s}_{\mathrm{a}}\left(\boldsymbol{q}_{\mathrm{a}}^i,\boldsymbol{q}_{\mathrm{s}}^i,\boldsymbol{u}\right) \\ \boldsymbol{s}_{\mathrm{s}}\left(\boldsymbol{q}_{\mathrm{a}}^i,\boldsymbol{q}_{\mathrm{s}}^i,\boldsymbol{u}\right) \end{bmatrix} \\
&\quad + p\begin{bmatrix} \boldsymbol{s}_{\mathrm{a}}\left(\boldsymbol{q}_{\mathrm{a}}^i,\boldsymbol{q}_{\mathrm{s}}^{i+1},\boldsymbol{u}\right) \\ \boldsymbol{s}_{\mathrm{s}}\left(\boldsymbol{q}_{\mathrm{a}}^{i-1},\boldsymbol{q}_{\mathrm{s}}^i,\boldsymbol{u}\right) \end{bmatrix} &\quad (4.15)\\
\frac{\mathrm{d}}{\mathrm{d}t}p &= \frac{v}{\Delta x}, &\quad (4.16)
\end{aligned}$$

where $\boldsymbol{q}_{\mathrm{a}}^i$, $\boldsymbol{q}_{\mathrm{s}}^i$, $i = 0,\ldots,N$, *denote centred cell average values of the advective and static grid, respectively, and* $\boldsymbol{s}_{\mathrm{a}}\left(\boldsymbol{q}_{\mathrm{a}}^0,\boldsymbol{q}_{\mathrm{s}}^0,\boldsymbol{u}\right) = \boldsymbol{0}$, $\boldsymbol{s}_{\mathrm{a}}\left(\boldsymbol{q}_{\mathrm{a}}^N,\boldsymbol{q}_{\mathrm{s}}^{N+1},\boldsymbol{u}\right) = \boldsymbol{0}$, $\boldsymbol{s}_{\mathrm{s}}\left(\boldsymbol{q}_{\mathrm{a}}^0,\boldsymbol{q}_{\mathrm{s}}^0,\boldsymbol{u}\right) = \boldsymbol{0}$, $\boldsymbol{s}_{\mathrm{s}}\left(\boldsymbol{q}_{\mathrm{a}}^{-1},\boldsymbol{q}_{\mathrm{s}}^0,\boldsymbol{u}\right) = \boldsymbol{0}$. *The length of the time interval* τ *is given by*

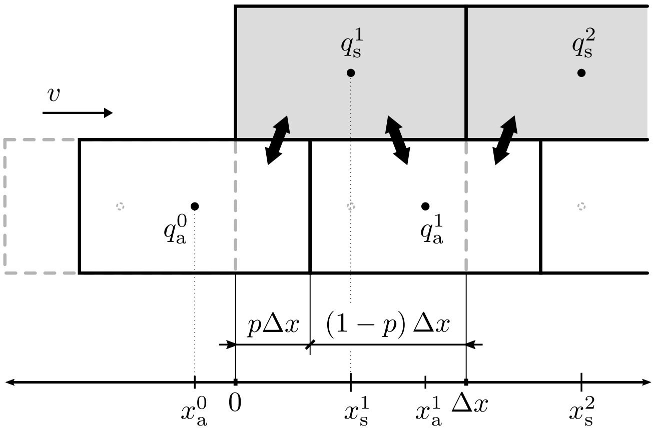

Figure 4.1.: Illustration of the advected grid movement against the static grid.

the relative cell shift to integrate from $p(t_0) = 0$ *to* $p(t_0+\tau) = 1$ *or equivalently*

$$\int_{t_0}^{t_0+\tau} v(t)\,\mathrm{d}t = \Delta x. \tag{4.17}$$

The initial conditions are

$$\begin{aligned} \boldsymbol{q}_\mathrm{a}^i(t_0) &= \overline{(\boldsymbol{q}_\mathrm{a}(x,t_0))}_{x_\mathrm{s}^i} && (4.18a)\\ \boldsymbol{q}_\mathrm{s}^i(t_0) &= \overline{(\boldsymbol{q}_\mathrm{s}(x,t_0))}_{x_\mathrm{s}^i} && (4.18b)\\ p(t_0) &= 0, && (4.18c) \end{aligned}$$

for $i = 1,\ldots,N$*. The boundary conditions are applied to the upwind ghost cell* $\boldsymbol{q}_\mathrm{a}^0(t_0) = \boldsymbol{b}(t_0)$ *at the beginning of the integration.*

Proof. Direct. Spatial discretization of (4.11), by applying cell average operator (4.4) about positions x_s^i, x_a^i, gives

$$\underbrace{\overline{(\partial_t\boldsymbol{q}_\mathrm{a})}_{x_\mathrm{a}^i}}_{(4.19a)} + \underbrace{\overline{(v\partial_x\boldsymbol{q}_\mathrm{a})}_{x_\mathrm{a}^i}}_{(4.19b)} = \underbrace{\overline{(\boldsymbol{s}_\mathrm{a})}_{x_\mathrm{a}^i}}_{(4.19c)} \tag{4.19}$$

$$\underbrace{\overline{(\partial_t\boldsymbol{q}_\mathrm{s})}_{x_\mathrm{s}^i}}_{(4.20a)} = \underbrace{\overline{(\boldsymbol{s}_\mathrm{s})}_{x_\mathrm{s}^i}}_{(4.20b)} \tag{4.20}$$

and to prove Theorem 1 we will deal with all the terms in (4.19) and (4.20) separately. Remember that $x_\mathrm{a}^i(t) = x_\mathrm{s}^i + p(t)\,\Delta x$.

The time differential term (4.19a) reads as

$$\overline{(\partial_t\boldsymbol{q}_\mathrm{a})}_{x_\mathrm{a}^i} = \frac{1}{\Delta x}\int_{x_\mathrm{a}^i(t)-\frac{\Delta x}{2}}^{x_\mathrm{a}^i(t)+\frac{\Delta x}{2}} \partial_t\boldsymbol{q}_\mathrm{a}(x,t)\,\mathrm{d}x,$$

where using the Leibnitz's integral rule the order of integration and differentiation can be switched to obtain

$$\begin{aligned}\overline{(\partial_t \boldsymbol{q}_\mathrm{a})}_{x^i_\mathrm{a}} &= \frac{1}{\Delta x}\frac{\mathrm{d}}{\mathrm{d}t}\int_{x^i_\mathrm{a}(t)-\frac{\Delta x}{2}}^{x^i_\mathrm{a}(t)+\frac{\Delta x}{2}} \boldsymbol{q}_\mathrm{a}(x,t)\,\mathrm{d}x - \\ &\quad \frac{1}{\Delta x}\boldsymbol{q}_\mathrm{a}\left(x^i_\mathrm{a}(t)-\frac{\Delta x}{2},t\right)\frac{\mathrm{d}}{\mathrm{d}t}\left(x^i_\mathrm{a}(t)-\frac{\Delta x}{2}\right) + \\ &\quad \frac{1}{\Delta x}\boldsymbol{q}_\mathrm{a}\left(x^i_\mathrm{a}(t)+\frac{\Delta x}{2},t\right)\frac{\mathrm{d}}{\mathrm{d}t}\left(x^i_\mathrm{a}(t)+\frac{\Delta x}{2}\right).\end{aligned}$$

Now, first calculating the integral bounds derivative,

$$\begin{aligned}\frac{\mathrm{d}}{\mathrm{d}t}\left(x^i_\mathrm{a}(t)\pm\frac{\Delta x}{2}\right) &= \frac{\mathrm{d}}{\mathrm{d}t}\left(x^i_\mathrm{s}+p(t)\,\Delta x\right) \\ &= \Delta x\frac{\mathrm{d}}{\mathrm{d}t}\left(p(t)\right) \\ &= \Delta x\frac{\mathrm{d}}{\mathrm{d}t}\int_{t_0}^{\mathsf{T}}\frac{v(s)}{\Delta x}\mathrm{d}s \\ &= v(t),\end{aligned}$$

we obtain the first term as

$$\begin{aligned}\overline{(\partial_t \boldsymbol{q}_\mathrm{a})}_{x^i_\mathrm{a}} &= \frac{1}{\Delta x}\left(\Delta x\frac{d}{dt}\boldsymbol{q}^i_\mathrm{a} - v\left(\boldsymbol{q}^{i+1/2}_\mathrm{a}-\boldsymbol{q}^{i-1/2}_\mathrm{a}\right)\right) \\ &= \frac{\mathrm{d}}{\mathrm{d}t}\boldsymbol{q}^i_\mathrm{a} - \frac{v}{\Delta x}\left(\boldsymbol{q}^{i+1/2}_\mathrm{a}-\boldsymbol{q}^{i-1/2}_\mathrm{a}\right),\end{aligned} \tag{4.21}$$

where $\boldsymbol{q}^i_\mathrm{a}(t) = \overline{(\boldsymbol{q}_\mathrm{a})}_{x^i_\mathrm{a}}(t)$ is a cell average value and $\boldsymbol{q}^{i\pm1/2}_\mathrm{a}(t) \equiv \boldsymbol{q}_\mathrm{a}\left(x^i_\mathrm{a}\pm{}^{\Delta x}/_{2},t\right)$ denote cell face values.

The transport term (4.19b) reads as

$$\overline{(v\partial_x \boldsymbol{q}_\mathrm{a})}_{x^i_\mathrm{a}} = \frac{1}{\Delta x}\int_{x^i_\mathrm{a}-\frac{\Delta x}{2}}^{x^i_\mathrm{a}+\frac{\Delta x}{2}} v\partial_x\boldsymbol{q}_\mathrm{a}(x,t)\,\mathrm{d}x,$$

which using the Ostrogradsky's divergence theorem simplifies to

$$\overline{(v\partial_x \boldsymbol{q}_\mathrm{a})}_{x^i_\mathrm{a}} = \frac{v}{\Delta x}\left(\boldsymbol{q}^{i+1/2}_\mathrm{a}-\boldsymbol{q}^{i-1/2}_\mathrm{a}\right). \tag{4.22}$$

The time differential term (4.20a) reads as

$$\overline{(\partial_t \boldsymbol{q}_\mathrm{s})}_{x^i_\mathrm{s}} = \frac{1}{\Delta x}\int_{x^i_\mathrm{s}-\frac{\Delta x}{2}}^{x^i_\mathrm{s}+\frac{\Delta x}{2}} \partial_t\boldsymbol{q}_\mathrm{s}(x,t)\,\mathrm{d}x$$

which by substitution $\boldsymbol{q}^i_\mathrm{s}(t) = \overline{(\boldsymbol{q}_\mathrm{s})}_{x^i_\mathrm{s}}(t)$ immediately gives

$$\overline{(\partial_t \boldsymbol{q}_\mathrm{s})}_{x^i_\mathrm{s}} = \frac{\mathrm{d}}{\mathrm{d}t}\boldsymbol{q}^i_\mathrm{s}. \tag{4.23}$$

The static state source term (4.20b) reads as

$$\overline{(\boldsymbol{s}_\mathrm{s})}_{x^i_\mathrm{s}} = \frac{1}{\Delta x}\int_{x^i_\mathrm{s}-\frac{\Delta x}{2}}^{x^i_\mathrm{s}+\frac{\Delta x}{2}} \boldsymbol{s}_\mathrm{s}\left(\boldsymbol{q}_\mathrm{a}(x,t),\boldsymbol{q}_\mathrm{s}(x,t),\boldsymbol{u}(t)\right)\mathrm{d}x.$$

Given $\boldsymbol{s}_\mathrm{s}$ is spatially independent and inspecting Fig. 4.1 we observe, that the integral may be separated as

$$\begin{aligned}\overline{(\boldsymbol{s}_\mathrm{s})}_{x_\mathrm{s}^i} &= \frac{1}{\Delta x}\left(\int_{x_\mathrm{s}^i-\frac{\Delta x}{2}}^{x_\mathrm{s}^i-\frac{\Delta x}{2}+p(t)\Delta x} \boldsymbol{s}_\mathrm{s}\left(\boldsymbol{q}_\mathrm{a}(x,t),\boldsymbol{q}_\mathrm{s}(x,t),\boldsymbol{u}(t)\right)\mathrm{d}x\right.\\ &\left.+\int_{x_\mathrm{s}^i-\frac{\Delta x}{2}+p(t)\Delta x}^{x_\mathrm{s}^i+\frac{\Delta x}{2}} \boldsymbol{s}_\mathrm{s}\left(\boldsymbol{q}_\mathrm{a}(x,t),\boldsymbol{q}_\mathrm{s}(x,t),\boldsymbol{u}(t)\right)\mathrm{d}x\right),\end{aligned}$$

which, under a piecewise constant spatial profile approximation of $\boldsymbol{q}_\mathrm{a}$, $\boldsymbol{q}_\mathrm{s}$ is

$$\begin{aligned}\overline{(\boldsymbol{s}_\mathrm{s})}_{x_\mathrm{s}^i} &= (1-p)\,\boldsymbol{s}_\mathrm{s}\left(\boldsymbol{q}_\mathrm{a}^i,\boldsymbol{q}_\mathrm{s}^i,\boldsymbol{u}\right)\\ &+p\boldsymbol{s}_\mathrm{s}\left(\boldsymbol{q}_\mathrm{a}^{i-1},\boldsymbol{q}_\mathrm{s}^i,\boldsymbol{u}\right)\end{aligned} \tag{4.24}$$

and finally, following the same reasoning as above, we obtain the advected state source term (4.19c)

$$\begin{aligned}\overline{(\boldsymbol{s}_\mathrm{a})}_{x_\mathrm{a}^i} &= (1-p)\,\boldsymbol{s}_\mathrm{a}\left(\boldsymbol{q}_\mathrm{a}^i,\boldsymbol{q}_\mathrm{s}^i,\boldsymbol{u}\right)\\ &+p\boldsymbol{s}_\mathrm{a}\left(\boldsymbol{q}_\mathrm{a}^{i},\boldsymbol{q}_\mathrm{s}^{i+1},\boldsymbol{u}\right).\end{aligned} \tag{4.25}$$

The source term formulas are only valid for $0 \leq p(t) \leq 1$, which corresponds with (4.17). Note that higher-order spatial reconstructions are possible following that appropriate calculation of the source terms (4.24), (4.25) above is performed.

Now, by substitution of (4.21) to (4.25) into (4.19), (4.20) we get

$$\begin{aligned}\frac{\mathrm{d}}{\mathrm{d}t}\boldsymbol{q}_\mathrm{a}^i - \frac{v}{\Delta x}\left(\boldsymbol{q}_\mathrm{a}^{i+1/2}-\boldsymbol{q}_\mathrm{a}^{i-1/2}\right)&\\ +\frac{v}{\Delta x}\left(\boldsymbol{q}_\mathrm{a}^{i+1/2}-\boldsymbol{q}_\mathrm{a}^{i-1/2}\right) &= (1-p)\,\boldsymbol{s}_\mathrm{a}\left(\boldsymbol{q}_\mathrm{a}^i,\boldsymbol{q}_\mathrm{s}^i,\boldsymbol{u}\right)\\ &+p\boldsymbol{s}_\mathrm{a}\left(\boldsymbol{q}_\mathrm{a}^{i},\boldsymbol{q}_\mathrm{s}^{i+1},\boldsymbol{u}\right)\\ \frac{\mathrm{d}}{\mathrm{d}t}\boldsymbol{q}_\mathrm{s}^i &= (1-p)\,\boldsymbol{s}_\mathrm{s}\left(\boldsymbol{q}_\mathrm{a}^i,\boldsymbol{q}_\mathrm{s}^i,\boldsymbol{u}\right)\\ &+p\boldsymbol{s}_\mathrm{s}\left(\boldsymbol{q}_\mathrm{a}^{i-1},\boldsymbol{q}_\mathrm{s}^i,\boldsymbol{u}\right)\end{aligned}$$

moreover, we see that the velocity-dependent terms cancel out, and by aggregation of states, we obtain (4.15). Differentiation of the relative cell shift equation (4.13),

$$\frac{\mathrm{d}}{\mathrm{d}t}p(t) = \frac{v(t)}{\Delta x}$$

with $p(t_0) = 0$ gives (4.16) and concludes the statement. □

Corollary 1 (MMFVM step for systems with a linear source term)**.** *If a monocharacteristic hyperbolic system of Theorem 1 has a linear source term*

$$\boldsymbol{s}\left(\boldsymbol{q}_\mathrm{a},\boldsymbol{q}_\mathrm{s},\boldsymbol{u}\right) = \begin{bmatrix}\boldsymbol{A}_\mathrm{aa} & \boldsymbol{A}_\mathrm{as}\\ \boldsymbol{A}_\mathrm{sa} & \boldsymbol{A}_\mathrm{ss}\end{bmatrix}\begin{bmatrix}\boldsymbol{q}_\mathrm{a}\\ \boldsymbol{q}_\mathrm{s}\end{bmatrix} + \begin{bmatrix}\boldsymbol{B}_\mathrm{a}\\ \boldsymbol{B}_\mathrm{s}\end{bmatrix}\boldsymbol{u}, \tag{4.26}$$

then (4.15) *simplifies to*

$$\begin{aligned}\frac{\mathrm{d}}{\mathrm{d}t}\begin{bmatrix}\boldsymbol{q}_\mathrm{a}^i\\ \boldsymbol{q}_\mathrm{s}^i\end{bmatrix} &= \begin{bmatrix}\boldsymbol{A}_\mathrm{aa} & \boldsymbol{A}_\mathrm{as}\\ \boldsymbol{A}_\mathrm{sa} & \boldsymbol{A}_\mathrm{ss}\end{bmatrix}\begin{bmatrix}\boldsymbol{q}_\mathrm{a}^i\\ \boldsymbol{q}_\mathrm{s}^i\end{bmatrix}+\\ &\quad +p\begin{bmatrix}\mathbf{0} & \boldsymbol{A}_\mathrm{as}\\ \boldsymbol{A}_\mathrm{sa} & \mathbf{0}\end{bmatrix}\begin{bmatrix}\left(\boldsymbol{q}_\mathrm{a}^{i-1}-\boldsymbol{q}_\mathrm{a}^i\right)\\ \left(\boldsymbol{q}_\mathrm{s}^{i+1}-\boldsymbol{q}_\mathrm{s}^i\right)\end{bmatrix}+\\ &\quad +\begin{bmatrix}\boldsymbol{B}_\mathrm{a}\\ \boldsymbol{B}_\mathrm{s}\end{bmatrix}\boldsymbol{u} \end{aligned}\tag{4.27}$$

and the whole system of equations can be formulated as

$$\frac{\mathrm{d}}{\mathrm{d}t}\boldsymbol{x} = \left(\mathbf{A}_\mathrm{c}+p\mathbf{A}_\mathrm{cp}\right)\mathbf{x}+\mathbf{B}_\mathrm{c}\boldsymbol{u},\tag{4.28}$$

where the state vector $\boldsymbol{x}\in\mathbb{R}^{(N+1)\cdot n}$ *aggregates the advected states and stationary states as*

$$\boldsymbol{x}=\left[\left(\boldsymbol{q}_\mathrm{a}^0\right)^\mathsf{T},\ldots,\left(\boldsymbol{q}_\mathrm{a}^N\right)^\mathsf{T},\left(\boldsymbol{q}_\mathrm{s}^0\right)^\mathsf{T},\ldots,\left(\boldsymbol{q}_\mathrm{s}^N\right)^\mathsf{T}\right]^\mathsf{T}.$$

Proof. By construction. Substituting (4.26) into (4.15), after minor arrangements, gives (4.27). Defining now $\widetilde{\boldsymbol{A}}_\mathrm{c,1}\equiv\begin{bmatrix}\boldsymbol{A}_\mathrm{aa} & \boldsymbol{A}_\mathrm{as}\\ \boldsymbol{A}_\mathrm{sa} & \boldsymbol{A}_\mathrm{ss}\end{bmatrix}$, $\widetilde{\boldsymbol{A}}_\mathrm{c,2}\equiv\begin{bmatrix}\mathbf{0} & \mathbf{0}\\ \boldsymbol{A}_\mathrm{sa} & \mathbf{0}\end{bmatrix}$, $\widetilde{\boldsymbol{A}}_\mathrm{c,3}\equiv\begin{bmatrix}\mathbf{0} & \boldsymbol{A}_\mathrm{as}\\ \mathbf{0} & \mathbf{0}\end{bmatrix}$, $\widetilde{\boldsymbol{B}}_\mathrm{c}\equiv\begin{bmatrix}\boldsymbol{B}_\mathrm{a}\\ \boldsymbol{B}_\mathrm{s}\end{bmatrix}$, $M=N+1$ and aggregating the states as

$$\widetilde{\boldsymbol{x}}=\left[\left[\left(\boldsymbol{q}_\mathrm{a}^0\right)^\mathsf{T}\quad\left(\boldsymbol{q}_\mathrm{s}^0\right)^\mathsf{T}\right]^\mathsf{T},\ldots,\left[\left(\boldsymbol{q}_\mathrm{a}^{N+1}\right)^\mathsf{T}\quad\left(\boldsymbol{q}_\mathrm{s}^{N+1}\right)^\mathsf{T}\right]^\mathsf{T}\right]^\mathsf{T},$$

we can summarize (4.27) for $i=0,\ldots,M$ into a formula

$$\begin{aligned}\frac{\mathrm{d}}{\mathrm{d}t}\widetilde{\boldsymbol{x}} &= \left(\boldsymbol{I}^M\otimes\widetilde{\boldsymbol{A}}_\mathrm{c,1}\right)\widetilde{\boldsymbol{x}}\\ &+ p\left(\boldsymbol{K}_{-1}^M\otimes\widetilde{\boldsymbol{A}}_\mathrm{c,2}+\boldsymbol{K}_{+1}^M\otimes\widetilde{\boldsymbol{A}}_\mathrm{c,3}\right)\widetilde{\boldsymbol{x}}\\ &+ \left(\mathbf{1}^M\otimes\boldsymbol{I}^n\otimes\widetilde{\boldsymbol{B}}_\mathrm{c}\right)\boldsymbol{u},\end{aligned}\tag{4.29}$$

where $\boldsymbol{K}_{-1}^M=\left(\boldsymbol{I}_{-1}^M-\boldsymbol{I}^M\right)$, $\boldsymbol{K}_{+1}^M=\left(\boldsymbol{I}_{+1}^M-\boldsymbol{I}^M\right)$, $\boldsymbol{I}^k$ denotes an identity matrix of size $\mathbb{R}^{k\times k}$, $\boldsymbol{I}_{-1}^k$, $\boldsymbol{I}_{+1}^k$ are lower and upper shift matrices of size $\mathbb{R}^{k\times k}$, respectively, $\mathbf{1}^k\in\mathbb{R}^k$ is a column vector of ones and $\otimes$ denotes the Kronecker product. Now, define a permutation matrix $\boldsymbol{P}$ such that $\boldsymbol{x}=\boldsymbol{P}^\mathsf{T}\widetilde{\boldsymbol{x}}$

$$\boldsymbol{P}=\widetilde{\boldsymbol{P}}\otimes\mathbf{1}^2,\widetilde{\boldsymbol{P}}=\{p_{i,j}\}=\left\{\begin{array}{cc}1 & i\text{ odd}, j=\frac{i+1}{2}\\ 1 & i\text{ even}, j=\frac{i+2N}{2}\\ 0 & \text{otherwise}\end{array}\right.,\tag{4.30}$$

then (4.29) becomes (4.28) with

$$\begin{aligned}\boldsymbol{A}_\mathrm{c} &= \boldsymbol{P}^\mathsf{T}\left(\boldsymbol{I}^M\otimes\widetilde{\boldsymbol{A}}_\mathrm{c,1}\right)\boldsymbol{P} &\text{(4.31a)}\\ \boldsymbol{A}_\mathrm{cp} &= \boldsymbol{P}^\mathsf{T}\left(\left(\boldsymbol{K}_{-1}^M\otimes\widetilde{\boldsymbol{A}}_\mathrm{c,2}+\boldsymbol{K}_{+1}^M\otimes\widetilde{\boldsymbol{A}}_\mathrm{c,3}\right)\right)\boldsymbol{P} &\text{(4.31b)}\\ \boldsymbol{B}_\mathrm{c} &= \boldsymbol{P}^\mathsf{T}\left(\mathbf{1}^M\otimes\boldsymbol{I}^n\otimes\widetilde{\boldsymbol{B}}_\mathrm{c}\right). &\text{(4.31c)}\end{aligned}$$

□

Theorem 2 (Mixed Mesh Finite Volume Method, MMFVM)**.** *A numerical solution to a monocharacteristic hyperbolic system is obtained by a repetitive solution of the MMFVM step (Theorem 1/ Corollary 1).*

There is a delay τ in the solution

$$\tau^i(t): \begin{cases} \int_{t-\tau^i(t)}^{t} v(s)\,\mathrm{d}s = \frac{\Delta x}{2}; & x = x_\mathrm{s}^i, i = 1,\ldots,N \\ \int_{t-\tau^i(t)}^{t} v(s)\,\mathrm{d}s = \Delta x; & x = x_\mathrm{s}^i, i = N+1 \end{cases} \tag{4.32}$$

caused by the fact that there is an additional $(N+1)^{st}$ cell in the advected grid.

Proof. During the MMFVM step, the cell average values evolve by the governing PDE, as proved in the Theorem 1. Consider now a ghost cell $\boldsymbol{q}_\mathrm{a}^0$ initialized by an appropriate boundary condition. It takes $N+1$ MMFVM steps to move this cell along all the stationary cells. Only after $N+1$ MMFVM steps, the cell has interacted with all the stationary cells and its value stops evolving.

The solution delay of the cell inside the spatial domain ($x = x_\mathrm{s}^i, i = 1,\ldots,N$) is caused by the length the MMFVM solution has to travel further opposed to a true analytic solution. More precisely, the true analytic residence time $\varsigma_\mathrm{T}^i(x,t)$ is by the method of characteristics given as

$$\varsigma_\mathrm{T}^i\left(x_\mathrm{s}^i,t\right): \int_{t-\varsigma_\mathrm{T}^i}^{t} v(s)\,\mathrm{d}s \quad = \quad x_\mathrm{s}^i = \left(i - \frac{1}{2}\right)\Delta x. \tag{4.33}$$

The MMFVM solution, however, has to travel a longer path (see Fig. 4.1) and its residence time $\varsigma_\mathrm{A}^i(x,t)$ is given by

$$\varsigma_\mathrm{A}^i\left(x_\mathrm{s}^i,t\right): \int_{t-\varsigma_\mathrm{A}^i}^{t} v(s)\,\mathrm{d}s = x_\mathrm{s}^i + \frac{\Delta x}{2} = i\Delta x,$$

which can be, due to the linearity of the integral operator, also written as

$$\int_{t-\varsigma_\mathrm{A}^i}^{t-\varsigma_\mathrm{A}^i+\varsigma_\mathrm{T}^i} v(s)\,\mathrm{d}s + \int_{t-\varsigma_\mathrm{A}^i+\varsigma_\mathrm{T}^i}^{t} v(s)\,\mathrm{d}s = \left(i - \frac{1}{2}\right)\Delta x + \frac{\Delta x}{2}. \tag{4.34}$$

Defining a solution delay as $\tau^i(t) = \varsigma_\mathrm{A}^i(t) - \varsigma_\mathrm{T}^i(t)$ and identifying (4.33) in (4.34) we conclude the first part of (4.32)

$$\int_{t-\tau^i(t)}^{t} v(s)\,\mathrm{d}s = \frac{\Delta x}{2}, i = 1,\ldots,N.$$

Similarly, for $i = N+1$, the analytic residence time $\varsigma_\mathrm{T}^{N+1}$ is given by

$$\int_{t-\varsigma_\mathrm{T}^{N+1}}^{t} v(s)\,\mathrm{d}s = 1.$$

The MMFVM residence time $\varsigma_\mathrm{A}^{N+1}$ is given by

$$\begin{aligned} \int_{t-\varsigma_\mathrm{A}^{N+1}}^{t} v(s)\,\mathrm{d}s &= \left(N + 1 - \frac{1}{2}\right)\Delta x + \frac{\Delta x}{2} \\ &= 1 + \Delta x, \end{aligned}$$

from which we can, by the same manipulation as above, conclude the remaining part of (4.32)

$$\int_{t-\tau^{N+1}(t)}^{t} v(s)\,\mathrm{d}s = \Delta x.$$

□

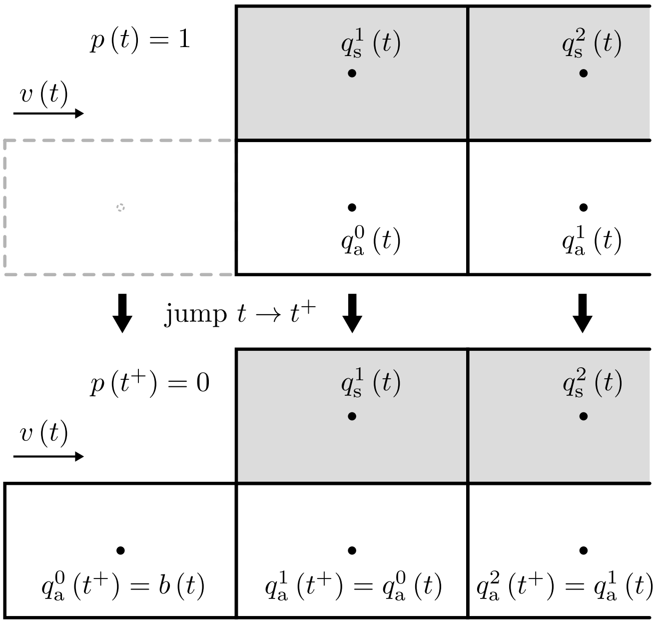

Figure 4.2.: Illustration of a discrete state jump in otherwise continuous state evolution.

Corollary 2 (State jump). *When a consecutive MMFVM step is being initialized (at $p(t) = 1$ from the preceding step), then the initial averaging of states* (4.18) *over the stationary grid Ξ_s (instead of the fully shifted Ξ_a grid) effectively performs a state shift/jump*

$$\boldsymbol{q}_a^i(t^+) = \boldsymbol{q}_a^{i-1}(t) \tag{4.35a}$$

$$\boldsymbol{q}_s^i(t^+) = \boldsymbol{q}_s^i(t) \tag{4.35b}$$

$$p(t^+) = 0, \tag{4.35c}$$

where t^+ denotes the just-after-jump instance at time t. Note that this relation holds only for a piecewise constant spatial profile approximation. Analogous relations can be derived for higher-order reconstructions.

Proof. Integration of (4.18) at $p = 1$ gives (4.35). See Fig. 4.2 for illustration.

□

Note that in the case of a simple transport equation $\partial_t \boldsymbol{q} + v\partial_x \boldsymbol{q} = s(\boldsymbol{q})$, $s(\boldsymbol{q}) = \boldsymbol{A}\boldsymbol{q} + \boldsymbol{b}$, the solution delay (4.32) of MMFVM for the position x_s^{N+1} (corresponding to the analytic solution at $x = 1$) can be compensated by a modification to the velocity $\widehat{v} = (N+1/N)\, v$ and modification to the source term $\hat{s}(\boldsymbol{q}) = N+1/N\, (\boldsymbol{A}\boldsymbol{q} + \boldsymbol{b})$. This statement can be shown to be true, but as it does not apply to the more general case considered, the proof is omitted.

Remark 4. There is a minor numerical diffusion caused by the cell homogeneity (constant spatial profile over a cell). Imagine an advected cell being halfway shifted ($p = 1/2$), as it interacts with its left stationary cell, its state value changes and this, by cell homogeneity, in turn, affects the interaction with its right stationary cell and vice versa. This effect is, however, minor compared to FVM, where the cell homogeneity affects the greater advective flux.

In FVM, the sampling in time is bounded by the CFL condition (and possibly other stability conditions) but otherwise can be chosen freely. Sampling instances t_k in MMFVM are, however, rigidly defined by the grid refinement and the actual characteristic velocity; in particular by

$$\int_{t_0}^{t_0+t_k} v(t)\,\mathrm{d}t = k\Delta x, k \in \mathbb{N}.$$

Those are the instances where the stationary and advected grid, (4.12) and (4.14), coincide ,and when the last advected cell is done interacting with the stationary cell, its value remains unchanged from there on. The advected state boundary condition is sampled at this rate. Homogeneity assumption (piecewise constant spatial profile reconstruction) disallows free time sampling at fixed spatial positions due to passing discontinuities. Free time sampling is in general possible, but the quality of the solution strongly depends on the quality of the spatial profile reconstruction.

When the characteristic velocity tends to zero, the sampling intervals tend to infinity; this is not a desired property. To prevent this scenario, the following step is advised.

Remark 5. When the sampling interval exceeds an allowed threshold, switch the solution method to FVM. I.e., stop the advected grid and incorporate the advective flux as is usual in FVM. It may also be beneficial to refine the grid momentarily.

Note that for low velocities, the relative importance of the advective flux decreases, and any numerical advection artifacts of FVM decrease. Also, as the velocity increases, the solution delay of MMFVM decreases. The MMFVM method is in a sense complementary to FVM, and its advantages prevail in highly-advective scenarios.

Remark 6. For systems with no static grid, apply the boundary condition directly to the first advected cell (and the upwind cells in the case of boundary conditions on the derivatives). MMFVM reduces to a system of ODEs with state shifts and solves the problem without transport delays in the solution.

Remark 7. The problem (4.11) can be imagined as time and spatial evolution of an infinite number of infinitesimally small slices/points. For illustration, in a cooled water pipe, we can imagine infinitely many slices of water of width dx travelling by a defined input velocity through a pipe consisting again of infinitely many, now static, slices. For increasing N, MMFVM approximates ever so closely the continuum of the governing PDE; the solution delay of Theorem 2 diminishes and so does the numerical diffusion introduced in Remark 4.

Two example implementations will be given now: a simple transport-decay equation, for which an analytic solution is known and a plug-flow heat exchanger, for which a comparison to a fine-grid FVM solution will validate the solution.

4.2.4. Advection-decay test system

A simple transport equation with decay

$$\begin{aligned} \partial_t q(x,t) + v\partial_x q(x,t) &= -sq(x,t) \\ q(0,t) &= b(t) \\ q(x,0) &= 0 \end{aligned}$$

has by the method of characteristics an analytical solution that is only a time-shifted initial or boundary condition with exponential decay along the transport,

$$q(x,t) = \begin{cases} 0 & t < \frac{x}{v} \\ b\left(t - \frac{x}{v}\right) e^{-\frac{s}{v}x} & t \geq \frac{x}{v}. \end{cases}$$

This analytic solution is compared to an FVM solution with a first order upwind scheme, an FVM solution with a ‘superbee’ limiter [35] and finally to the MMFVM.

According to the Theorem 2, the MMFVM solution is obtained by repetitive solution of the MMFVM step, i.e.

integrate the following system in time

$$\begin{aligned}\frac{\mathrm{d}}{\mathrm{d}t}q &= -sq\\ \frac{\mathrm{d}}{\mathrm{d}t}p &= Nv\end{aligned}$$

for $p \in \langle 0,1 \rangle$ and perform a state jump according to Corollary 2 at $p = 1$,when $b(t)$ is assigned to the first volume state.

Fig. 4.3 shows the results for $q(1,t)$, with a simulation setting $N = 5$, $v = 0.1$ and $s = -v \ln(0.6)$. A number of elements $N = 5$ is set low to highlight low-dimensional behaviour of the said methods. Time integration is performed by BS23 [36] method with event location [37] (at $p = 1$) . The analytic solution is $q(1,t) = 0.6 \times b(t - 10), t \geq 10$. Fig. 4.3 also contains the input signal $b(t)$.

Notably, the FVM solution with first order profile approximation brings great numerical diffusion to the solution. Using the superbee slope limiter [35] improves the behaviour but still under-performs in advecting discontinuities. The MMFVM solution is capable of truly advecting the input. The sampling is, however, dictated by the advection speed and is rather sparse in the case of only few elements ($N = 5$). The solution preserves the shape of input but suffers from the solution delay, as analysed in Theorem 2 and its proof.

Note that the problem contains no static states and therefore Remark 6 applies. However, in order to highlight the properties of the method for general scenarios, the boundary condition has been applied to a first upwind ghost cell in order to generate the transport delay in the solution (N+1 integration steps instead of N). The source term had to be altered as $s' = s\frac{N}{N+1}$ to account for this modification.

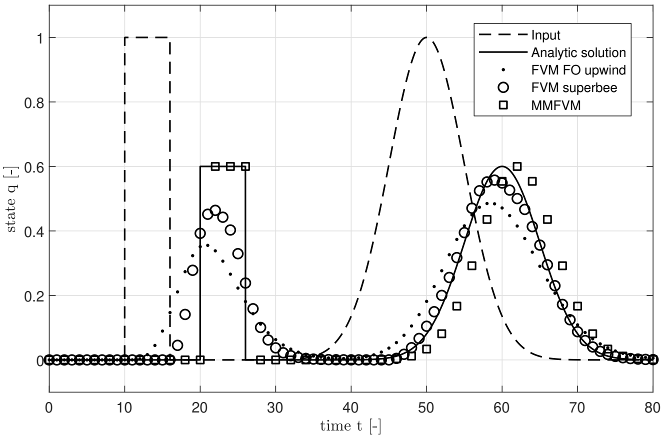

Figure 4.3.: Method comparison for the advection-decay test at $x = 1$; the number of volumes for all methods is $N = 5$.

4.2.5. Water-to-air heat exchanger thermal model

A plug-flow heat exchanger is a plug-flow reactor where no reaction, only a heat exchange occurs. Its model captures a distributed parameter, distributed time delay behaviour and can be used for simplified modelling of, for example, water-to-air heat exchangers.

A water-to-air heat exchanger is considered a tubular single-pass cross-flow heat exchanger with the following assumptions:

A.1 Heat transfer rates are constant in space, time and temperature. They solely depend on flow velocities.

A.2 There is only one phase in both fluids, i.e. no condensation nor evaporation occurs.
A.3 Fluids are incompressible and of constant density and specific heat capacity.
A.4 Heat conduction (dispersion, diffusion) in the direction of flow is negligible.
A.5 Water flow is radially coherent. The heat exchanger is thin in the airflow direction.
A.6 Airflow has no dynamics and is ideally mixed at the inlet and outlet. The air temperature acting on the heat exchanger body is assumed constant and equal to the air inlet temperature.
A.7 Water velocity (mass flow) is known.

The model is derived using the Fourier's and conservation laws. The resulting system of partial differential equations is first order hyperbolic

$$\begin{aligned}\partial_t T_\mathrm{w} + v\partial_x T_\mathrm{w} &= \alpha\left(T_\mathrm{b} - T_\mathrm{w}\right)\\ \partial_t T_\mathrm{b} &= \beta_1\left(T_\mathrm{w} - T_\mathrm{b}\right) + \beta_2\left(T_\mathrm{a} - T_\mathrm{b}\right),\end{aligned}$$

where the state variables $T_\mathrm{w} = T_\mathrm{w}(x,t)$ [°C] and $T_\mathrm{b} = T_\mathrm{b}(x,t)$ [°C] denote the water and metal body temperature, respectively, and $v(t) = {}^{\dot m(t)}/_{m_\mathrm{w}}\left[\mathrm{s}^{-1}\right]$ is a normalized transport speed, where $\dot m$ [$^\mathrm{kg}/_\mathrm{s}$] is a water mass flow and m_w [kg] a weight of water in the heat exchanger. The space variable was normalized using $x = {}^{\xi}/_{L}$ [−], where ξ [m] is the space variable along the length of the heat exchanger, L [m] denotes the length of the heat exchanger.

The boundary conditions are

$$\begin{aligned}T_\mathrm{w}(t,0) &= T_\mathrm{w,in}(t)\\ T_\mathrm{a}(t,x) &= T_\mathrm{a,in}(t),\ x \in \langle 0,1\rangle\end{aligned}$$

moreover, initial conditions are

$$\begin{aligned}T_\mathrm{w}(0,x) &= T_{w,0}(x)\\ T_\mathrm{b}(0,x) &= T_\mathrm{b,0}(x),\ x \in \langle 0,1\rangle\end{aligned}$$

where $T_\mathrm{w,0}(x)$ and $T_\mathrm{b,0}(x)$ are initial temperature profiles in the water and body, respectively, and $T_\mathrm{w,in}(t)$, $T_\mathrm{a,in}(t)$ [°C] are water and air inlet temperatures, respectively. The coefficients are

$$\alpha = \frac{H_\mathrm{wb}(\dot m)}{C_\mathrm{w}}, \beta_1 = \frac{H_\mathrm{wb}(\dot m)}{C_\mathrm{b}}, \beta_2 = \frac{H_\mathrm{ba}\left(\dot V\right)}{C_\mathrm{b}},$$

where $H_\mathrm{wb}(\dot m)$ [$^\mathrm{W}/_\mathrm{K}$], $H_\mathrm{ba}(\dot V)$ [$^\mathrm{W}/_\mathrm{K}$] are flow dependent heat exchange coefficients and C_w [$^\mathrm{J}/_\mathrm{K}$], C_b [$^\mathrm{J}/_\mathrm{K}$] are total heat capacities of water and metal body, respectively. Air volumetric flow is denoted $\dot V$ [$^{\mathrm{m}^3}/_\mathrm{s}$]. The outputs of the model are a heat flow from body to air

$$Q(t) = \int_0^1 UA_\mathrm{ba}\left(T_\mathrm{b}(x,t) - T_\mathrm{a,in}(t)\right)\mathrm{d}x\ [\mathrm{W}] \tag{4.36}$$

and an outlet water temperature $T_\mathrm{w,out}(t) = T_\mathrm{w}(1,t)$.

FVM is applied in a standard way; the CFL condition is $\dot m(t)\,\tau_\mathrm{s}(t)\,N \le m_\mathrm{w}$, where $\tau_\mathrm{s}(t)$ is a sampling period.

For the application of MMFVM, first define advected and static state variables $q_\mathrm{a} = T_\mathrm{w}$, $q_\mathrm{s} = T_\mathrm{b}$ and boundary conditions $b(t) = T_\mathrm{w,in}(t)$, $u(t) = T_\mathrm{a,in}(t)$. Quick observation of the source terms

$$\begin{aligned}s_\mathrm{a}(q_\mathrm{a},q_\mathrm{s}) &= -\alpha q_\mathrm{a} + \alpha q_\mathrm{s}\\ s_\mathrm{s}(q_\mathrm{a},q_\mathrm{s}) &= \beta_1 q_\mathrm{a} - (\beta_1 + \beta_2)\,q_\mathrm{s} + \beta_2 u,\end{aligned}$$

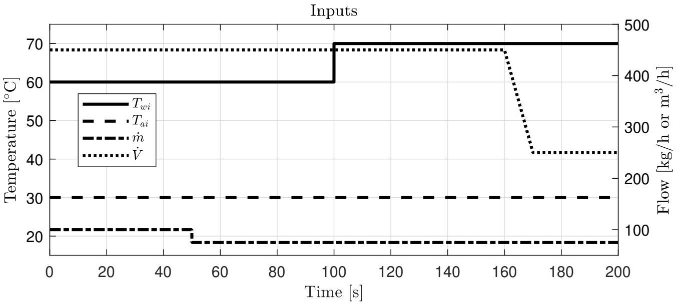

Figure 4.4.: Time sequence of inlet water temperature $T_{\mathrm{w,in}}$, inlet air temperature $T_{\mathrm{a,in}}$, water mass flow $\dot{m}$ and air volumetric flow $\dot{V}$.

reveals their linearity. By application of the MMFVM step (4.26) we get the following evolution of volume averages

$$\frac{\mathrm{d}}{\mathrm{d}t}\begin{bmatrix} q_{\mathrm{a}}^{i} \\ q_{\mathrm{s}}^{i} \end{bmatrix} = \begin{bmatrix} -\alpha & \alpha \\ \beta_1 & -(\beta_1+\beta_2) \end{bmatrix}\begin{bmatrix} q_{\mathrm{a}}^{i} \\ q_{\mathrm{s}}^{i} \end{bmatrix} + p\begin{bmatrix} 0 & \alpha \\ \beta_1 & 0 \end{bmatrix}\begin{bmatrix} q_{\mathrm{a}}^{i-1} - q_{\mathrm{a}}^{i} \\ q_{\mathrm{s}}^{i+1} - q_{\mathrm{s}}^{i} \end{bmatrix} + \begin{bmatrix} 0 \\ \beta_2 \end{bmatrix} u$$

and a relative shift equation

$$\frac{\mathrm{d}}{\mathrm{d}t} p = \frac{v}{\Delta x}.$$

Solving now this system according to Theorem 2 we obtain the solution. Time integration is performed by BS23 [36] method with event location [37] at $p = 1$.

Setting of the experiment was: $H_{\mathrm{wb}}(\dot{m}) = 43.1\,(\dot{m}/3600)^{0.292}\ \mathrm{W/K}$, $H_{\mathrm{ba}}\left(\dot{V}\right) = 1.68 \times 10^{-3}\dot{V}^2 - 0.87\dot{V} + 260\,\mathrm{W/K}$, $C_{\mathrm{w}} = 2.41 \cdot 10^3\ \mathrm{J/K}$, $C_{\mathrm{b}} = 2.26 \times 10^3\ \mathrm{J/K}$, $m_{\mathrm{w}} = 0.577\,\mathrm{kg}$, $T_{\mathrm{w},0} = T_{\mathrm{b},0} = 20\,°\mathrm{C}$. The time sequence of all four inputs is depicted in Fig. 4.4. Fig. 4.5 shows body and water volume temperatures at four equidistant spatial positions $x = [0.125, 0.375, 0.625, 0.875]$ (from top to bottom). Fine FVM solution ($N = 1004$) with HCUS limiter [38] mimics the role of the true solution. In order to have a comparison with the two consecutive solutions with $N = 4$, the states of the fine solution are averaged in space over $\Delta x = 1/4$. Fig. 4.6 depicts the outputs. An interesting comparison begins with the FVM simulation with only four volumes ($N = 4$) and HCUS flux limiter. Both state and output figures show how numerical diffusion alters the solution. The inlet temperature step at $t = 100\,\mathrm{s}$ is smeared out, whereas the true solution is a sharp-moving front. MMFVM with only four volumes ($N = 4$) is able to advect the sharp front. However, the time sampling is tightly defined by the problem setting and transport velocity, as also is the solution delay. Considerable quality enhancement is achieved by having more volumes; a low number of volumes has been chosen to intensify the distinction in properties of the compared methods. Nevertheless, the MMFVM still performs reasonably well in this highly convective scenario.

4.2.6. Thermal model solution method summary

A numerical solution method for systems with a dominant advective component has been presented. The method utilizes an Eulerian grid for stationary states and a Lagrangian grid for states with a characteristic velocity. Formulation of the interaction of the two grids is the main contribution. The employment of the Lagrangian grid removes advection flux from the cell-to-cell flux for its volumes as derived in the proof to Theorem 1. A solution to this problem formulation can contain discontinuities and the numerical diffusion is significantly decreased. Since no finite numerical method can give a perfect numerical solution, there also is a price to pay for the MMFVM. The time sampling intervals are advection velocity dependent, and there is a velocity-dependent delay in the solution. It

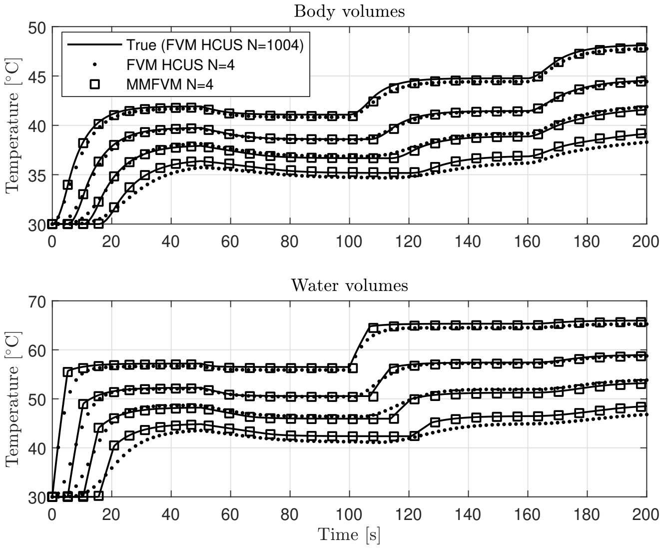

Figure 4.5.: Time evolution of the body and water temperatures T_b, T_w at $x = [0.125, 0.375, 0.625, 0.875]$ (from top to bottom). The fine FVM solution was spatially averaged to the cell size of the latter two solutions.

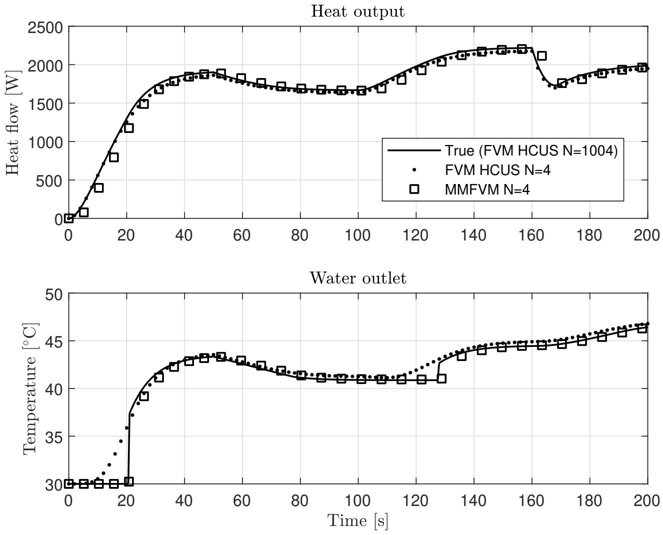

Figure 4.6.: Time evolution of the heat output Q and the water outlet temperature $T_\mathrm{w,out}$(at $x = 1$).

is reasonable to resort to the classic FVM for low-to-zero range velocities, where diffusion/dispersion/conduction prevails over the convection anyway. The MMFVM method should be used as complementary to the FVM in highly advective conditions (Pe $\gg$ 10). A low-order simulation model of a heat exchanger was implemented using both methods; the model implementation in MATLAB® is publicly available at [39].

Part II.

Load power control

The sole purpose of a heat distribution network is to deliver heat from a heat source to zones in a desired quantity. Heat exchange is a natural phenomenon that takes place whenever a temperature gradient exists. To control the heating power of a heat terminal (e.g. FCU etc.), one has to either alter the temperature gradient or limit the quantity of the heat exchange fluid. Both approaches are used in reality, heat source supply temperature is controlled as low as possible to sustain the heat demand of zones under full load (an equithermic regulation) and individual needs of the zones are regulated by adjusting heat transfer fluid flow rate (a quantitative regulation).

The equithermic regulation is based on the fact that heat losses through a building envelope are a linear function of the outside temperature and heat gains from heat terminals are a linear function of the supply temperature. Heat sources have built-in supply temperature regulation based on the outside temperature and the selected equithermic curve.

The ultimate goal of a heating system is to maintain thermal comfort for tenants. User comfort is a complex task [40], mainly translated into maintaining a set air temperature in a zone.

Fig. 4.7 provides three different architectures of zone temperature control; a direct zone temperature feedback loop, a zone control with an independent pressure controller and a cascade control with an inner power feedback loop. The direct temperature feedback (Fig. 4.7 (a)) is the standard for zone control: a controller regulates the flow rate through a heat exchanger by adjusting an opening x of a hydraulic flow regulation device (a throttling valve (CV) in a supply-oriented network or a control pump in a demand-oriented network, for details see Part III). The heat flow q is affected by changes in available differential pressure Δp and a supply-to-zone temperature difference $\Delta T = T_\mathrm{s} - T_\mathrm{z}$ and heat exchanger (HX) fan speed. The system input-output gain (x to q) varies with Δp and ΔT making it difficult to tune the controller. Furthermore, if the CV does not have an exact inverse characteristics of the HX, the system is non-linear. Any variation in the disturbance variables is propagated through the zone prior to being attenuated by the temperature controller TC. Any change in the CV opening causes pressure variation for all other units in the network.

The advent of pressure-independent control valves (PICV) brought pressure variations to rest since they employ an independent pressure control loop (Fig. 4.7 (b)) via mechanical regulator. Pressure difference over a control valve is constant, therefore the flow through the PICV is only a function of the CV opening. Each heat terminal unit is thus decoupled in pressure from all other units. The system input-output gain is, however, still affected by ΔT, which together with the non-linearities make the tuning of the zone controller not trivial. The PICV carries pressure ports by which the flow may be manually sensed for commissioning and diagnostic purposes.

This thesis advocates for an architecture with power-feedback control devices for supply-oriented networks (Chapter 5 and Fig. 4.7(c)) and for demand-oriented networks (Chapter 6). Such devices use the HX temperature-drop and other sensoric measurements to determine heat exchanger power and stabilize the power output by an inner power-feedback loop. The heat exchanger input-output system is thus linearized from the perspective of the cascade zone controller whose tuning may be in turn fixed and optimized. The HX temperature measurements may be used for remote hydraulic and thermal diagnostics. Furthermore power tracking of a known power reference q_SP allows for easier modelling of the thermal zone behaviour, which is an essential component for energy optimizing model predictive control (MPC).

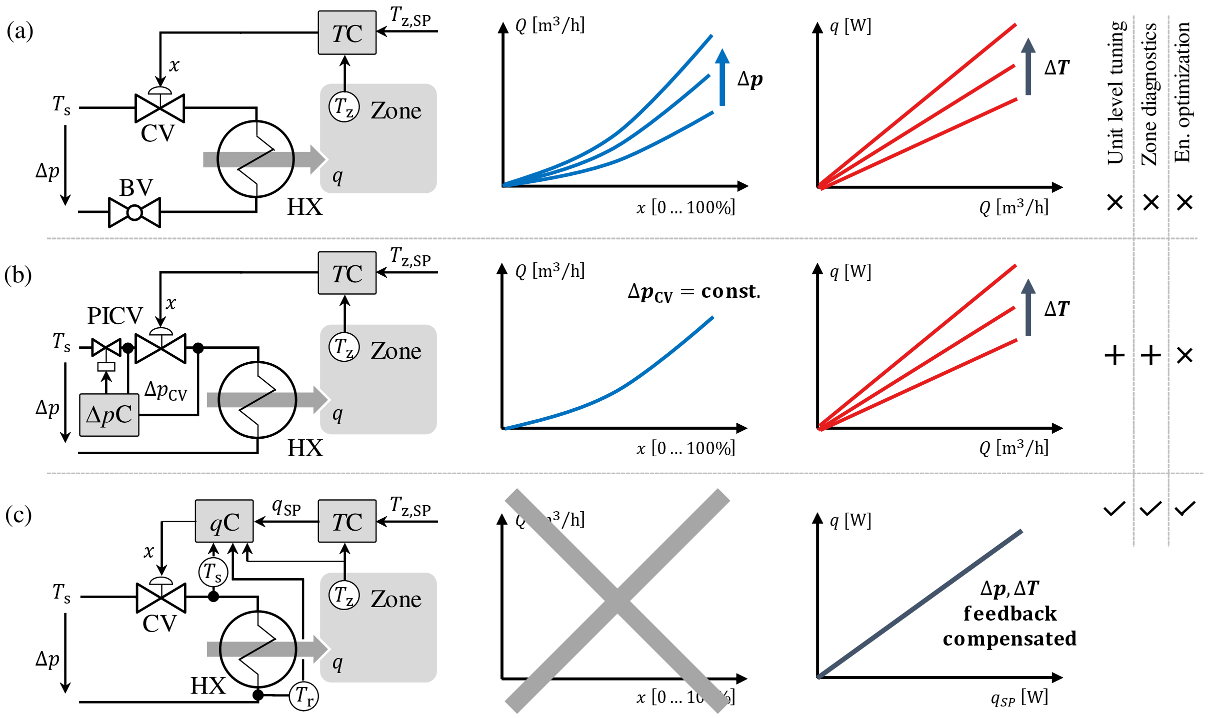

Figure 4.7.: Direct zone temperature control loop (a), zone control with an independent pressure-feedback loop (b) and zone control with an inner power-feedback loop (c).

5. Power control valve[1]

Power delivery through a hydronic load - a heat exchanger - depends on inlet temperature and flow rate in both streams. An ideal control device makes use of one of the inlet variables to control power output regardless of variations in the rest of the variables. In hydronic networks, the water flow rate is used to control the output power locally in the low power region. When the water flow is saturated, the airflow rate is controlled to increase the power output further. The water source temperature is used to set the max. heat output globally in the whole network based on the extent of losses to the exterior. The inlet air temperature, i.e. the zone temperature, is the controlled variable for which the heat is being delivered.

The water flow through a heat exchanger, as mentioned in Chapter 2, depends on the pressure difference over the hydraulic resistance the HX represents; usually adjusted by varying the hydraulic resistance of an accompanied valve.

The branch source pressure difference is, however, not constant and varies due to openings in other branches. The inlet water temperature also varies with the total flow due to heat losses along the transport. A solution is to employ a mechanical spring-type pressure regulator as in the pressure-independent control valve (PICV), or use an electronic flow meter in line with the valve. Another solution, termed “power control valve” (QCV), is to use temperature feedback, as proposed in the co-authored patent [41], and stabilize directly the power output.

The basis of the patented idea is to observe the ratio of delivered power to available power as depicted in Fig. 5.1. Regardless of heat exchanger size, there is a flow rate where an increase in flow does not increase power output sufficiently, i.e. the heat exchanger is saturated on the waterside.

The power ratio

$$\frac{q}{q_{\max}} = \frac{Qc_{\mathrm{p,w}}\left(T_{\mathrm{wi}} - T_{\mathrm{wo}}\right)}{Qc_{\mathrm{p,w}}\left(T_{\mathrm{wi}} - T_{\mathrm{ai}}\right)} = \frac{T_{\mathrm{wi}} - T_{\mathrm{wo}}}{T_{\mathrm{wi}} - T_{\mathrm{ai}}} = \epsilon_{\mathrm{w}},$$

maybe observed from water inlet and outlet temperature, T_{wi} and T_{wo}, respectively and inlet air temperature T_{ai}. The flow rate Q does not need to be known. The power ratio is also known as thermal effectiveness ϵ_{w} (on the water stream), or normalized temperature drop [42].

An important feature of the power control valve is the overflow avoidance, which is realized by controlling the valve position such that the power ratio does not undergo a preset limit. Therefore, regardless of inlet temperatures and air stream flow rate, the heat exchanger is always kept out of the saturation region.

The hydronic network, where no branch is in overflow is called balanced. The advantage of this balancing method is that it is free of any flow settings, which are heat exchanger capacity dependent.

Remark. The power control below the saturation limit and other details are subject to a business secret and may not be disclosed.

---

[1] Based on the co-authored original patent: Pavel Trnka, Jiří Dostál, Václav Prajzner, and Christoph Sturm. “Method for operating a hydronic heating and/or cooling system, control valve and hydronic heating and/or cooling system”. European pat. EP3073205. Sept. 2016. URL: `https://register.epo.org/application?number=EP15161449`

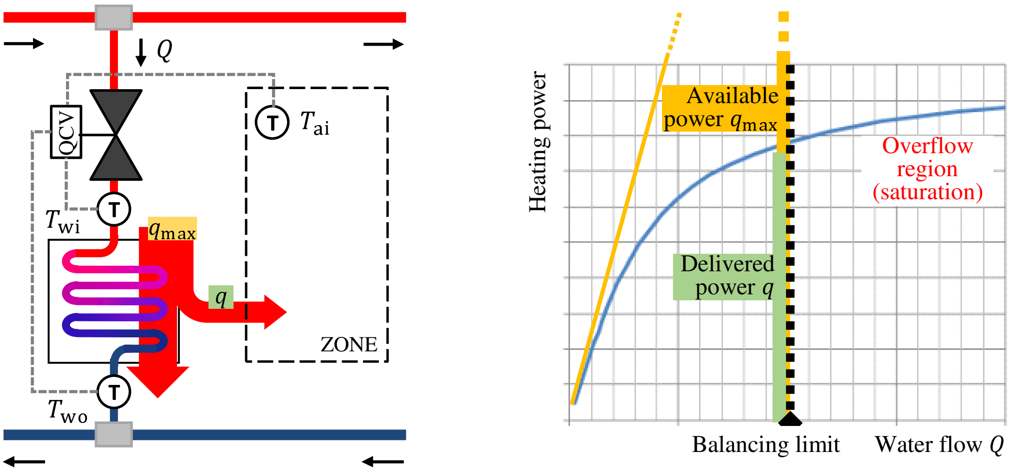

Figure 5.1.: Power control valve essential principle.

6. Power control pump[1]

This chapter presents the development and algorithms behind an active control device for pumping one-pipe (or primary-secondary pumping, see Part III) systems. The main feature of such a system is the series connection of thermal loads/sources and a small pump by each load/source for control, as opposed to classical two-pipe systems with a parallel connection and throttling control valves. The main contribution is an integration of all necessary components into one device and the ability to infer mass flow in a secondary circuit without a flow meter. By also measuring the temperature drop, we can estimate and control heat flow and provide remote thermal and hydraulic diagnostics of a connected heat terminal. It is powered and communicates through the Ethernet and contains a wet-rotor BLDC pump controlled by the field-oriented control method. A Kalman filter provides a mass flow estimate, and a robust distributed parameter system controller regulates the heat flow.

6.1. Introduction

As described earlier, the regular way to control a hydronic system is to impose resistance to flow by a throttling valve. However, an alternative way is to pump heat transfer liquid where needed instead of throttling it where not required. This solution is already available on the market [44, 45] and uses a small pump for each heat terminal. Let us call systems with throttling valves *passive* or *throttling* and systems using the pumps *active* or *pumping*. Wilo AG has also established a terminology where throttling systems are called *supply-oriented* and those with pumps *demand-oriented*. It is also possible to meet the term *centralized* for systems with a central pump and *decentralized* for the decentralized pumping systems.

Although there is also a two-pipe variant of a decentralized pumping system [44, 46], this chapter expands only on the one-pipe pumping hydronic network and its designated control device.

This chapter presents the development, algorithms and real-life validation of a pumping one-pipe network control device.

6.2. Functional principle

The pumping one-pipe hydronic system is fully described in the introduction to Part III . In short, however, there is a main pipe routed from the heat source and the main circulator. Two closely spaced T-fitting are mounted to the main pipe near a heat terminal. The free terminals of the T-fittings form a base of the secondary piping, where a secondary, tiny pump with a heat source/terminal is looped; see Fig. 6.1a. Consecutive heat terminal branches are connected to the primary piping all in series. The main (primary) piping loops throught all heat terminal branches back to the heat source.

The power output of the heat terminal is controlled by the secondary flow. As there is no variable hydraulic resistance in the secondary circuit (only pipes, HX, but no valves) and there is no additional pressure source (the T-fittings are close together), the secondary flow is governed solely by the pump speed.

Such conditions enable us to infer flow from pump power readings, as Fig. 6.1b ideologically depicts. Knowing the pump speed, power, and power-flow characteristics is the main predisposition to estimate the absolute liquid flow

---

[1] Based on the original paper: Jiří Dostál, Tomáš Bäumelt, and Jiří Cvrček. “Control device for pumping one-pipe hydronic systems”. In: *The REHVA European HVAC Journal* (June 2022), pp. 45–51. ISSN: 1307-3729. URL: `https://www.rehva.eu/rehva-journal/chapter/control-device-for-pumping-one-pipe-hydronic-systems`

rate through the pump and therefore through the whole secondary circuit including the heat terminal. The flow rate estimate is, in general, a function of pump power and pump speed

$$\hat{Q} = f(P, S, \theta),$$

where θ represents a vector of parameters. Heating/cooling power can be obtained by adding a pair of temperature sensors, one on a HX supply pipe and the other on a HX return pipe. The HX thermal power estimate is

$$\hat{q} = \hat{Q} c_\mathrm{p} \Delta T_\mathrm{HX}.$$

The functional principle is protected by multiple patents [47–51].

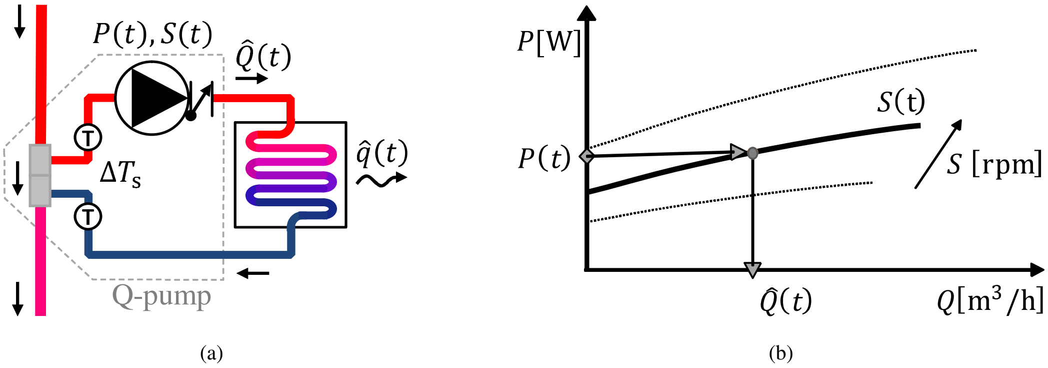

(a)

(b)

Figure 6.1.: Power control pump scheme (a) and basic functional principle (b).

6.3. Device design

The subject of our other patent family [52–54] is a one-pipe hydronic heating control device. It is an advantageous composition of the two closely-spaced T-fittings, pump housing, check-valve, two temperature sensors and electronics in one compact device. See Fig. 6.1a for a schematic depiction and Fig. 6.2 for an illustrative physical resemblance. The same device is or was historically also called a power control pump (PCP), a Q-pump (QP) or an IQ-pump (IQP, used historically).

6.3.1. Pipe sizing

The device contains primary and secondary piping; both shall be designed to allow a desired energy throughput, pose reasonable operating cost and minimize raw material needs (investment cost). Flow velocity and diameters are to be designed.

Flow speed in an HVAC pipe should neither be too low nor too high. An increased speed results in lower solid deposition, lower air deposition, smaller pipe size – and hence lower material cost, less liquid volume in the system, faster power delivery time and decreased risk of secondary circuit self-recirculation for small installations. On the other hand an increased speed increases pressure drop – and hence the pumping power costs, increases fatigue on fittings, increases noise risks. A survey conducted from available sources and questionnaires by practitioners at

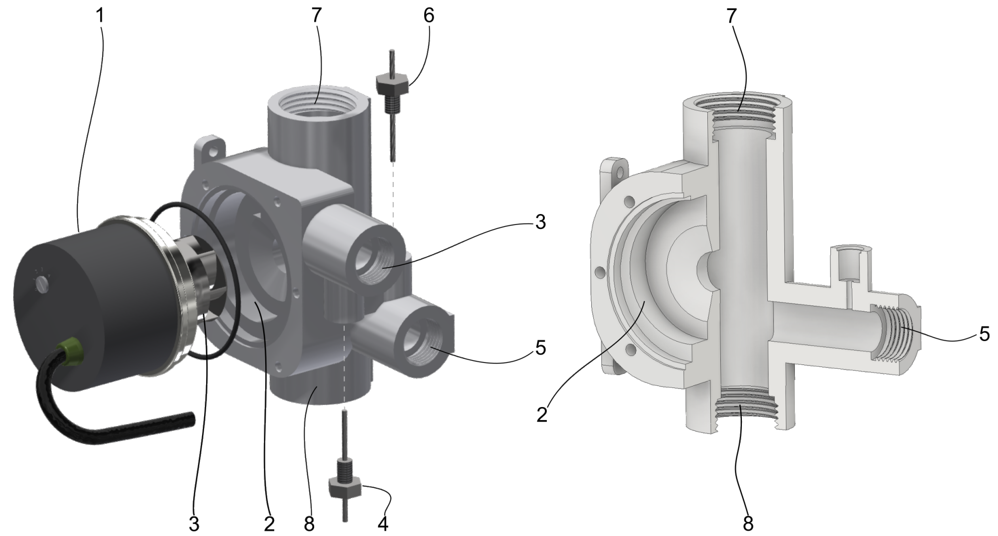

Figure 6.2.: The power control pump device consists of a circulator motor (1), pump housing (2), where impeller (3) works and pumps liquid into secondary outlet (3) featuring a supply temperature sensor (4). A heat terminal is connected between the secondary outlet (3) and the secondary inlet (5) featuring a return temperature sensor (6). The device connects to the heat source primary piping through the primary inlet (7); thereafter the heat transport liquid branches into the pump housing (2) and continues to be mixed with the heat terminal return only to leave through the primary outlet (8).

"Školení topenářů, Pilsen, 2019" have resulted in the velocity recommendation of 0,2 − 1,2 m/s for any HVAC piping [55].

The primary pipe loop is considered to run horizontally in each floor, where the primary loops in all floors are supplied by two-pipe risers (see Fig. 9.19). The EU directive [56] recommends designing heat sources for a typical (average) building load instead of the maximal load, with a complimentary heat source to cover extreme conditions. Applying the principle of designing for typical conditions also to heat distribution, the main pipe size has been chosen DN32 with G5/4 threads. It renders an economic pressure drop 392 Pa/m (4 ft head/100 ft)[19] for supplying one floor (63.7 kW/loop at 15°C temp. drop and max. velocity 1.2 m/s) of 77% of commercial buildings in the EU. The per-floor power needs were modelled by a Gamma distribution (mean 851 $\mathrm{m^2} \times 55\ \mathrm{W/m^2} = 46.8$ kW [57], shape factor 3, see Fig. 6.4). The rest of 23% of establishments with higher loads shall, but only for 6% of operation time [58], experience higher main pipe velocities. It should, however, be noted that according to our survey the max. velocity recommendations vary greatly depending on the situation. It is estimated that 95% of heating needs (~100 kW/floor) shall be satisfied by a DN32 copper pipe (or PEX equivalent) with the velocity of 1.8 m/s. Such velocity is permissible for a piping not routed directly through offices. A minimum recommended velocity 0.2 m/s yields minimum per-floor load of 11 kW. The control option for the power throughput in the primary pipe are described in Sec. 10.1.1.

The secondary piping of the power control pump is sized to accommodate connected heat terminals. Fig. 6.5 depicts a thermal and hydraulic analysis of randomly selected heat terminal manufacturers and their product lines (normalized using EN 442-1:1995 to the 70/55/20°C conditions). The average weighted hydraulic conductivity is 1.6 bar → $\mathrm{m^3/h}$. The majority of heat terminals make use of G1/2 threaded connections typical for DN15 pipe size. Such pipe is capable of delivering 12.4 kW at 1.2 m/s and 15°C temperature drop.

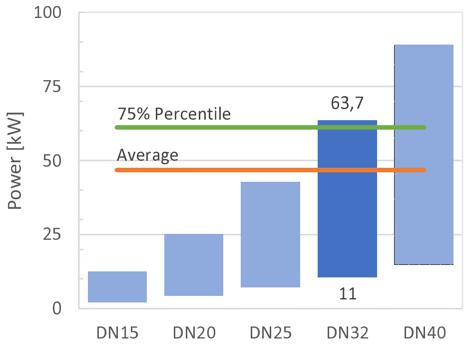

Figure 6.3.: Maximum heat throughput of a pipe (CTS-M, velocity 1.2 m/s, temperature drop 15°C).

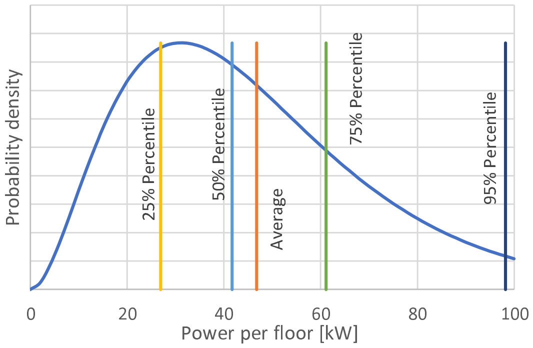

Figure 6.4.: Per-floor power needs of EU commercial buildings (Gamma dist., mean 46.8 kW[57], shape f. 3).

6.3.2. Secondary pump selection

The secondary pump is the most important element of the power control pump device. Its ability to create pressure potential gives an upped bound on maximum flow to deliver through the secondary circuit with the heat terminal and, therefore, also on the maximum thermal power output.

At first, designing a pump for the PCP was considered in cooperation with the Brno University of Technology, but it is a relief I didn’t pursue this development line. Such a pump, should it have better characteristics, would certainly prove prohibitively expensive and very difficult to do subsequent research with. Research through 20+ small circulators has been conducted [55] for an off-the-shelf solutions. The selected pump is a D5 type (Fig. 6.6) circulator produced by several manufacturers. It is a canned spherical wet-rotor pump with a metal casing used in hot water recirculation, solar thermic installations, computer cooling etc. The pump is 60 mm in diameter and has 32 mm rotor-tip-stator-tip height. The rotor has four magnetic poles and is magnetically fixed on a ceramic ball bearing; lubrication and cooling of both the rotor and the stator are provided by the pumped liquid. For PCP, the D5 pump was stripped of all control electronics down to stator winding. Electronic commutation of the rotor-impeller is held by the PCP electronics (Sec. 6.3.4).

The power and pressure characteristics of a selection of the researched small circulators are depicted in Fig. 6.8. For comparison, there is also the hydraulic performance of the power control pump (line *QP2023*). It shows that for secondary circuits having hydraulic conductivity no less than $K = 1.25$, the PCP is capable of serving a 10 kW heat terminal at the 70/55/20°C conditions; the electric power drawn by the PCP is at the 25 W power-over-ethernet maximum power delivery limit for a powered device. Note that the secondary circuit is considered to have 14 m of DN15 copper piping in series with the heat terminal.

6.3.3. Body design

The PCP body consists of the main pipe, from which a pump housing extends with its suction hole. The secondary pump outlet is directed perpendicularly away from the main pipe axis. The secondary outlet port houses a spring check valve and a secondary supply temperature sensor. From the same direction comes the secondary inlet, where the secondary return temperature sensor is housed and that connects back to the main pipe.

The PCP body was made as symmetrical as possible from the primary-pipe point of view to enable mounting the PCP facing with the secondary ports to the right or to the left, regardless of the flow direction in the main pipe. I.e. the direction of flow in the main pipe does not alter hydraulic conditions in the secondary piping.

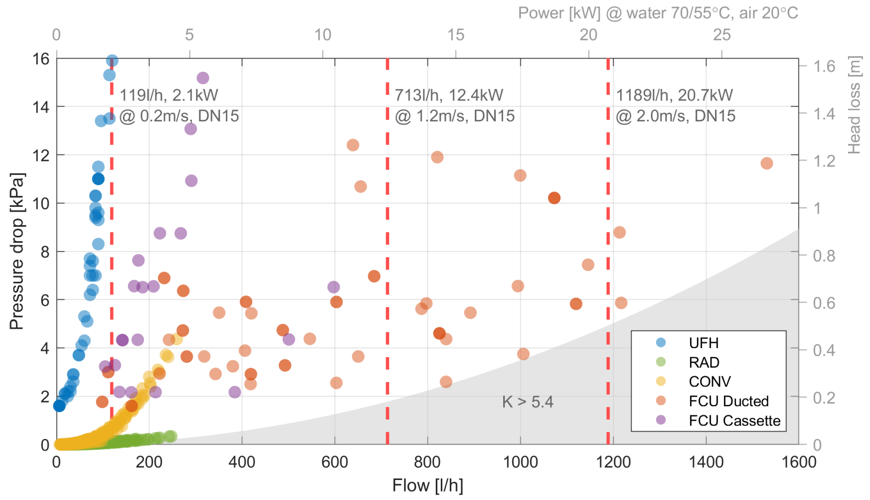

Figure 6.5.: Thermal and hydraulic analysis of heat terminals. All terminals were normalized to 70/55°C water temperature, 20°C air temperature using EN442-1:1995. Red vertical lines mark design velocities, black line average weighted conductivity.

One of the PCP assumptions is that the secondary circuit is hydraulically separated from the primary circuit. A measured primary-to-secondary piping influence is 4,5 l/h per 1000 l/h change in the primary circuit.. There is a divider plate in the primary pipe to prevent recirculation of the secondary return. There were four variants produced, tested and optimized for the least primary-secondary dependence.

There were eight different gradually evolving body designs developed and manufactured over the years [59]. The prototypes were first manufactured using ABS 3D printing and cured for water tightness. Later, a resin bracing was used to improve pressure-temperature ratings. The final 3D printed prototypes were manufactured using thermal sintering from Nylon 12. Finally, brass prototypes were cast using ceramic moulds created on top of 3D printed masters and machined using CNC. The final design is fully brass-castable and machinable by standard techniques. See Fig. 6.7 for a glimpse of the body design.

There has been performed a CFD analysis to help optimize the pump volute and four variants have been manufactured and tested.

The first prototypes used wet temperature wells; the final design utilizes custom designed dry temperature wells with minimized thermal convection bridges.

There were three different types of electronic covers designed to provide IP44 and cable-pull protection. The final design is injection-mouldable without using special cores.

Remark. The design details are intentionally left out of the thesis; they are development outcomes rather than research, and they are subject to business secret.

6.3.4. Electronics and firmware

There was a multitude of control electronics developed throughout the device development since 2014. The first hardware made use of STMelectronics Nucleo board. Later, a version based on Raspberry Pi Compute Module was developed (Fig. 6.9).

Several BLDC motor drivers were designed and built, from 6-step controllers to integrated field oriented control (FOC) solutions in the final electronics. Power measurements proved problematic when not performed on the chip.

Figure 6.6.: A D5-type shaftless canned spherical wet-rotor pump selected for the power control pump.

Figure 6.7.: Final brass-casted PCP prototype with the D5 pump stripped of electronics.

The pre-final electronics utilizes an NXP i.MX-RT microchip with built-in motor control features (hardware sine-wave commutation, 10-bit ADC, timing circuits). The pump speed and electrical power acquisition is performed by vector control methods [61], allowing for efficient pump speed control in the whole range from zero to maximal flow.

The device is powered by Power-over-Ethernet with a 24 V switching power supply. Two PT1000 temperature sensors are used.

The processor runs FreeRTOS, temperature readings, mass flow estimation, heat flow control and communications run in separate threads.

Final electronics have been schematically proposed, see Fig. 6.10.

6.4. Mass flow estimation

Mass flow estimation without the need of a flow meter is the key innovation of the power control pump device. Being able to determine flow enables cost-effective implementation of the following features:

- Heat flow estimation
- Heat flow control
- Hydraulic diagnostics
- Thermal diagnostics

Looking at the schematic of the secondary circuit (Fig. 6.1a), one can observe in the secondary circuit the double T-fitting (connection to the primary circuit), the pump with a check-valve and the hydraulic load – the heat terminal with its piping. The T-fittings are spaced closely together so as not to create a pressure source for the secondary circuit – hence, the two circuits are hydraulically separated. This simplifies the secondary hydraulic circuit to just two components: the pump and the load.

The PCP device always has full control authority over the heat terminal, as it directly controls the flow. Precision speed control of the pump enables precise flow control (up to $1\,\mathrm{l/h}$ steps). Therefore, the PCP body with its pump housing, check valve and ports has one fixed size, and the hydraulic performance can be described precisely by one set of head-flow (HQ) and power-flow (PQ) characteristics.

Pump characteristics were discussed in Sec. 3.2. Although the affinity scaling is generally true, better precision may be achieved by a polynomial model in two input dimensions, flow and speed, as discussed in Sec. 3.3. The polynomial model used has a full set of monomials up to the order 3 for both the HQ and the PQ characteristics

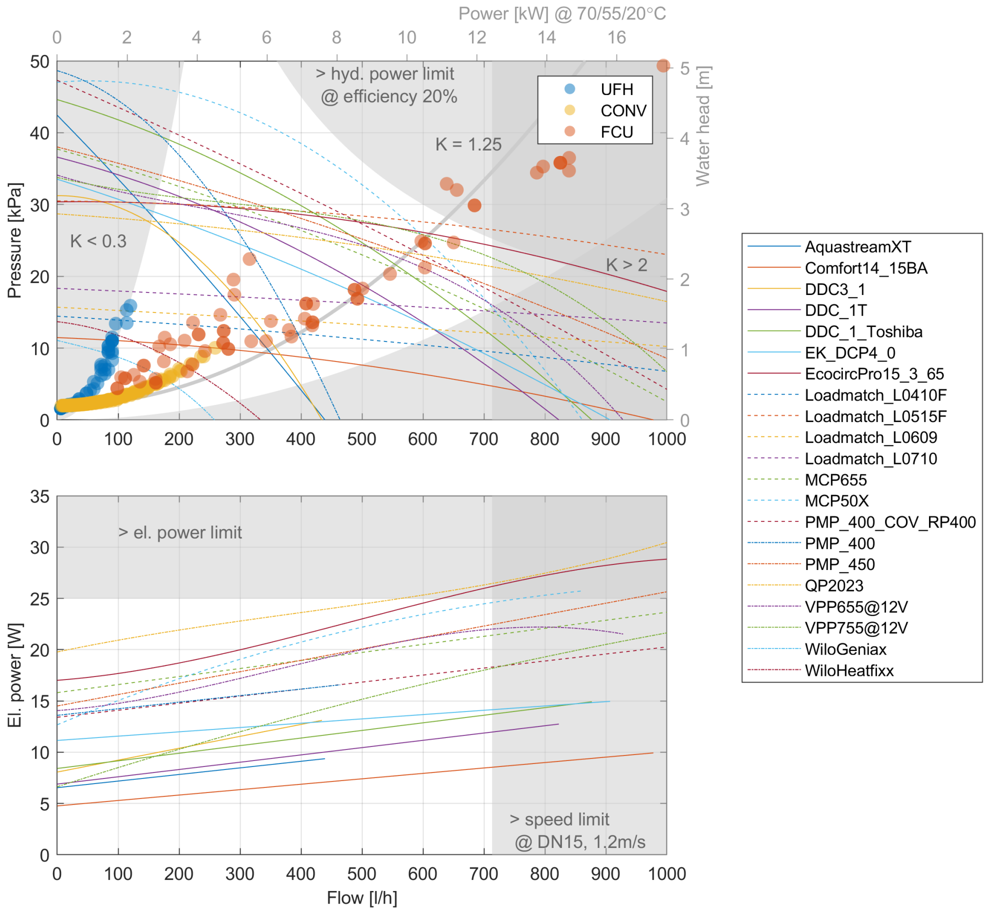

Figure 6.8.: Pressure and power characteristics of researched off-the-shelf small circulators. The hydraulic loads depicted consist of a heat terminal and 14 m of DN15 copper pipe.

$$H(Q,S) = \mathrm{pol}_{\mathrm{HQ}}(Q,S) = \sum_{i=0}^{3}\sum_{j=0}^{3} a_{i,j} Q^i S^j \tag{6.1}$$

$$P(Q,S) = \mathrm{pol}_{\mathrm{PQ}}(Q,S) = \sum_{i=0}^{3}\sum_{j=0}^{3} b_{i,j} Q^i S^j. \tag{6.2}$$

Fig. 6.11 illustratrates the polynomial model fit in normalized coordinates. The fitting was performed under an L1 norm with shape constraints (details in Sec. 3.3). The residuals are in absolute non-scaled values in [m] and [W], respectively.

Where should the residuals be normalized by the variation over the flow range (for $K = 1$)

$$\tilde{H}(S_{\text{data}}) = \frac{H_{\text{data}} - H(Q_{\text{data}}, S_{\text{data}})}{\max_Q H(Q, S_{\text{data}}) - \min_Q H(Q, S_{\text{data}})}$$

and similarly for $\tilde{P}$,we get Fig. 6.12 from which signal-to-noise ratios (SNR) may be observed. For high speed, the residuals over many pump samples and their measured datasets with respect to a mean pump model have a maximum

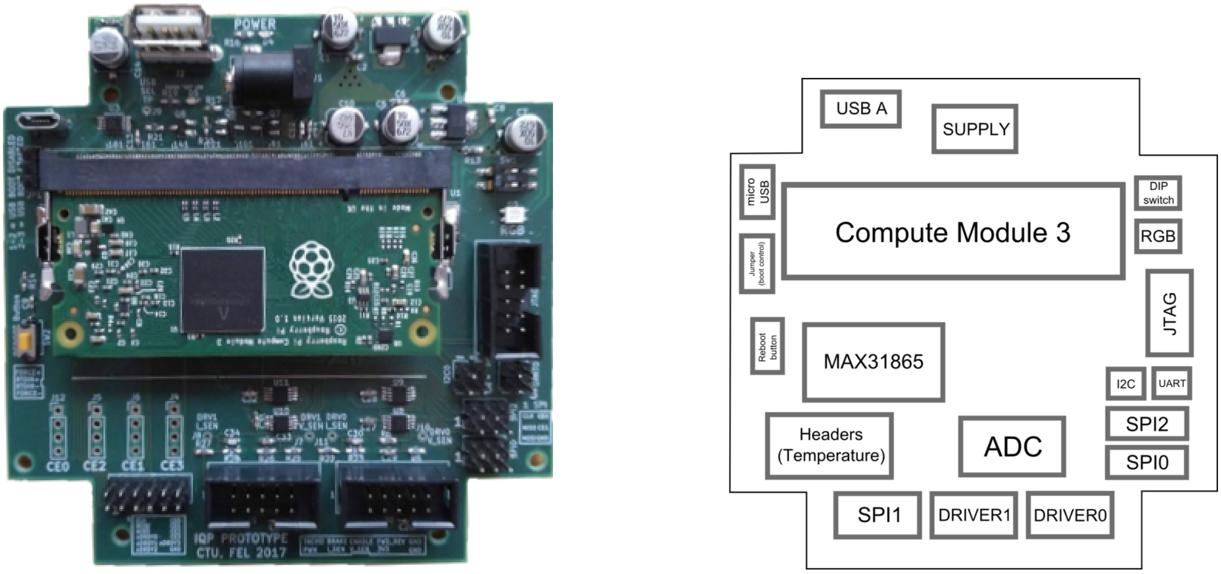

(a) (b)

Figure 6.9.: PCP electronics using RPi Compute module 3 (a) and its overview PCB layout (b) [60].

of 10% noise. The noise is gradually bigger than the valid signal magnitude for low speeds.

Mass flow estimation is based on the underlying mathematical model of the circuit (Fig. 6.13) consisting of a pump and a load model.

The pump model is mainly given by the head and power polynomials (6.1), (6.2). The dynamic behaviour is primarily governed by the speed controller, flow inertia and impeller inertia. The latter are, however, fast enough to enable approximation by first-order dynamics. The pump model inputs are $\boldsymbol{u}_\mathrm{P} = [Q, S_\mathrm{REF}]^T$, the state is $x_\mathrm{P} = [S]$ and the outputs are $\boldsymbol{y}_\mathrm{P} = [H, P, S]^T$. The state space model reads

$$\begin{aligned} \dot{S} &= \tau_\mathrm{P}(S_\mathrm{REF} - S) \\ H &= (Eq. 6.1) \\ P &= (Eq. 6.2)\,, \end{aligned}$$

where S_REF is a speed reference set by a heat flow controller.

The quadratic Darcy-Weisbach law (Sec. 2.1) mainly governs the model of the load

$$H_\mathrm{L} = \frac{c_\mathrm{L}}{K^2} Q\,|Q| \tag{6.3}$$

The hydraulic conductivity K is unknown and considered not changing; however it is mildly dependent on the mean water temperature. The dynamic flow model is derived from thre hydraulic inertance model, where the head difference between input and load is the flow change driving potential. The load model input is $u_\mathrm{L} = [H]$, the state is $x_\mathrm{L} = [Q]$ and the output is $y_\mathrm{L} = [Q]$. The state space model is

$$\dot{Q} = \tau_\mathrm{L}(H - H_L)\,,$$

where the load head H_L is given by (6.3).

The overall model for estimation is non-linear due to the Darcy-Weisbach law, has one input $u = [S_\mathrm{REF}]$, three states $\boldsymbol{x} = [S, Q, K]^T$ and two measured outputs $\boldsymbol{y} = [P, S]$, where the state and output equations are constructed by merging

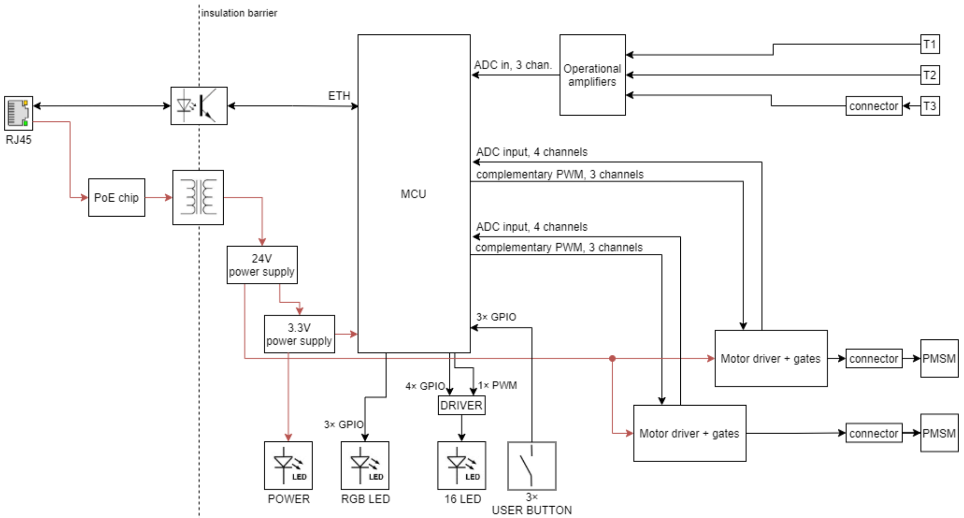

Figure 6.10.: Proposed high-level electronics scheme.

the pump and load models as per Fig. 6.13 into the standard form

$$\begin{aligned} \dot{\boldsymbol{x}} &= f_c(\boldsymbol{x}, u) \\ \boldsymbol{y} &= g(\boldsymbol{x}, u). \end{aligned}$$

The pump speed and, most importantly, the flow, altogether with the hyd. conductance of the load are estimated by an extended Kalman filter (EKF) [62] through a standard process of discretization (forward Euler with subsampling) and linearization (using automatic differentiation) at each step. The [63] implementation has been utilized. The resulting flow estimate is denoted $\hat{Q}$.

Fig. 6.14 depicts the filter performance after initialization. There are three calibration steps at high speeds, where the power characteristics gradient is the greatest and the relative noise magnitude is the smallest. The calibrated hydraulic conductivity then enables accurate flow rate estimates at low speeds, where the power characteristic is flat and any meaningful information is hidden in the noise. There is an actuated valve connected in series with the HX, which was randomly positioned to represent an unknown hydraulic load. Steady-state comparison of the estimated mass flow rate vs. measurement is depicted in Fig. 6.15; the standard deviation in the whole range was 3.91 l/h.

6.5. Heat flow control

Once the mass flow rate is known, an instantaneous apparent heat flow estimate $\hat{q}$ [W] may be obtained as

$$\hat{q} = \hat{Q} c_{\mathrm{V,w}} \left(T_{\mathrm{w,i}} - T_{\mathrm{w,o}}\right), \tag{6.4}$$

where a mass flow estimate $\hat{Q}$ [$\mathrm{m^3/s}$] is translated into appropriate units, $c_{\mathrm{V,w}}$ [$\mathrm{J/m^3K}$] is specific heat capacity of a working liquid and $T_{\mathrm{w,i}}, T_{\mathrm{w,o}}$ are inlet and outlet temperatures on the heat exchanger liquid side, respectively. The PCP has a liquid temperature measurements integrated, therefore all the necessary information the available to the PCP to perform the heat flow estimate.

Remark. Water is almost always the working liquid. Its utilization may be automatically detected by the PCP by spinning the rotor below check-valve opening speed/pressure and employ statistical detection methods. The supervised diploma thesis [64] covers the topic.

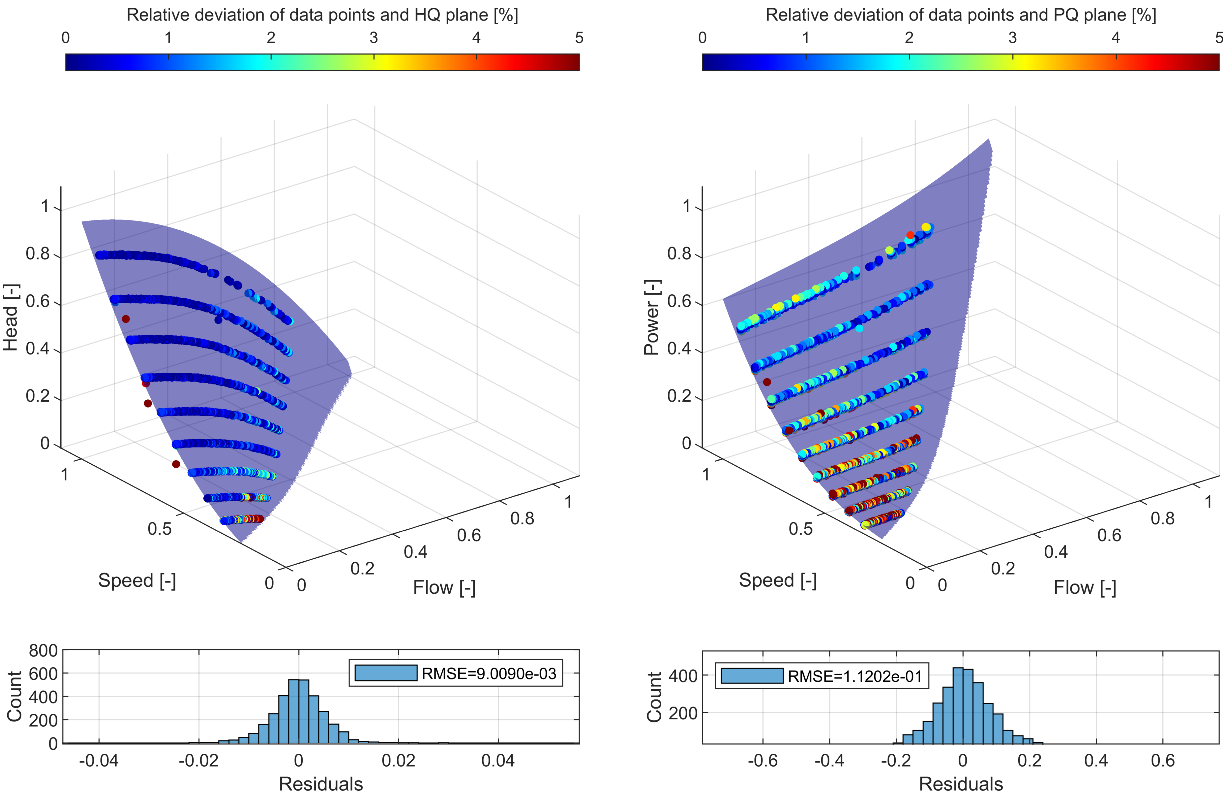

Figure 6.11.: Pump polynomial model data fit. The residuals are in absolute non-scaled values in meters of head and watts, respectively.

A heat terminal, e.g. FCU, behaves thermally as a distributed parameter, distributed time-delay system governed when simplified by a one-dimensional hyperbolic PDE (see Sec. 4.2 or [20]). The heat flow that is desired to control is the heating power transferred to the air side. The instantaneous heat flow (6.4) is a coarse estimate of a liquid-to-body power, which only equals the body-to-air side after an attenuation of any transients; the main complication being the flow-dependent transport delay in the HX piping and PCP-to-HX connection piping.

The MMFVM method (Sec. 4.2.3) was developed to obtain low-order HX models with convection accurate properties, e.g. the variable transport delay. As a quick reminder: liquid volumes (i.e. temperature states) are not fixed but travel at the speed of the fluid from inlet to outlet with respect to body volumes. Nevertheless, the MMFVM model still needs accurate parameters (volume of liquid in the piping, heat transfer coefficients, heat capacities) to simulate heat flow precisely. Even though automatic identification should be possible using the known mass flow rate and temperature readings, it has never been pursued.

Instead, a simple, robust approach of filtering out spikes at transients has been utilized. See the top graph of Fig. 6.17 for a measured instantaneous apparent heat flow rate (red) and filtered estimate (violet).

Standard PID feedback control is not suitable for systems with unknown variable transport delay. However, a controller by Sandoval [65] has been specifically designed for robust velocity control of convective spatially distributed systems, e.g. heat terminals. The control law (simplified)

$$\begin{aligned}\dot{\zeta} &= k_{\mathrm{I}} \mathrm{sg}\left(e\right) \left(\left| u\zeta - \zeta^2 \right| + |\dot{e}| \right) \\ u &= k_{\mathrm{P}} e + \zeta,\end{aligned}$$

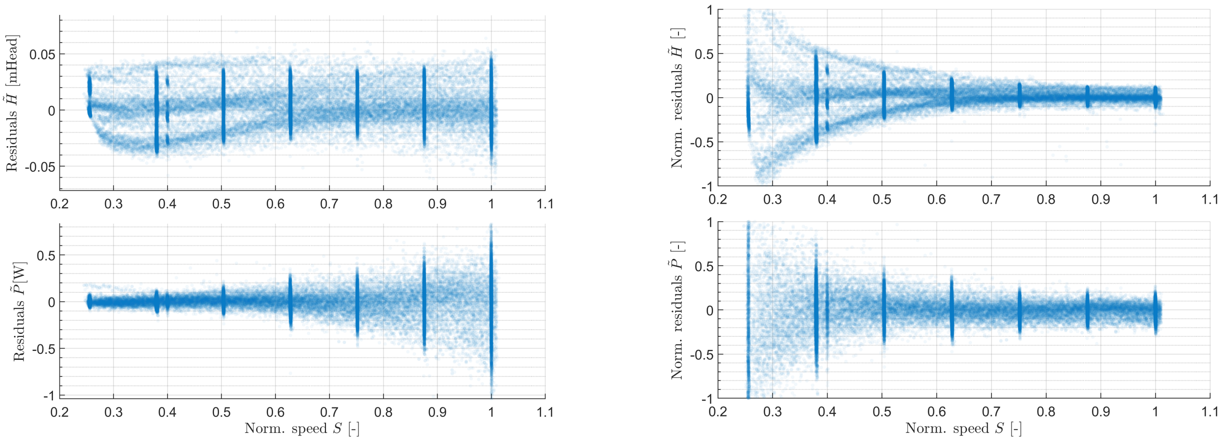

(a) (b)

Figure 6.12.: Data fit residuals over many pump samples and their characteristics (a) and normalized residuals to reveal signal-to-noise ratios (b).

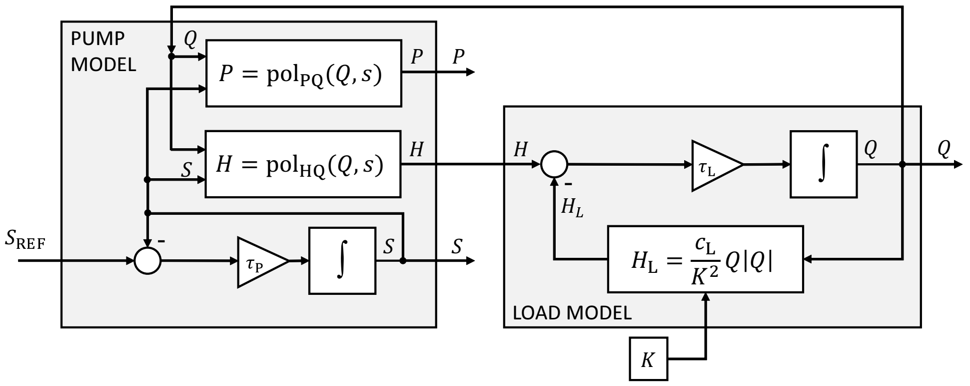

Figure 6.13.: Mass flow estimation model.

is designed to stabilize the governing hyperbolic PDE and drive the control error

$$e = q_{\mathrm{REF}} - \hat{q}$$

to the origin, where q_{REF} [W] is a heat reference assigned by a supervisory zone controller, e.g. simple temperature feedback wall module or MPC from Sec. 13.2). The controller can be considered a PI controller with a variable integral gain, where the two constants k_{P} and k_{I} are tuning parameters for proportional and integral action, respectively. A clamping anti-windup has been utilized to prevent integrator wind-up. The control error derivative is filtered and

$$\mathrm{sg}\,(e) = \begin{cases} 1 & e \geq 0 \\ -1 & e < 0. \end{cases}$$

Fig. 6.17 depicts the dynamics of the heat flow rate tracking; measured power in the air and the instantaneous power water are overlaid for comparison.

Fig. 6.16 presents steady state reference tracking performance on the water-to-air heat exchanger. The results were obtained by ramping up and down the absolute heat reference value. The standard deviation over the whole range of the heat terminal was 158 W. However, there were a few factors affecting the tracking precision especially at low

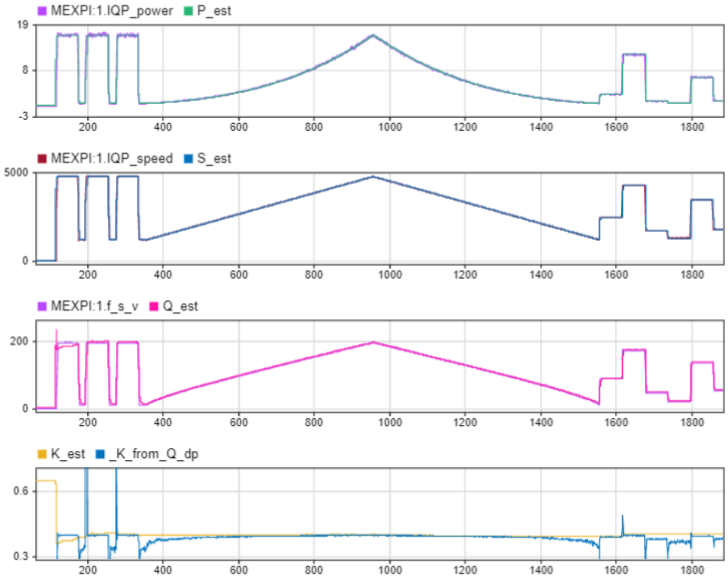

Figure 6.14.: Mass flow estimation filter test. The hydraulic conductance parameter has been intialized to 0.65. Three identification steps at high speeds were performed, followed by a slow ramp and random steps.

heat flows. The slope of the ramp will always be for some heat flow too steep where the results cannot be assumed steady state any more; however, the error in mass flow estimation has a bigger impact. Second, the delivered (real) heat is calculated from wet-well water temperature sensors positioned directly on the heat exchanger inlet and outlet. In contrast, the estimated power is calculated from dry-well temperature sensors onboard the PCP device; there is a notable portion of uninsulated piping in between them. The heat flow controller tracks the heat estimate to the reference without any error. However, the but the estimated power is higher than the reference measurement due to heat emission in the piping. The systematic power control error in the higher flows is likely due to the same heat losses and bias in temperature readings.

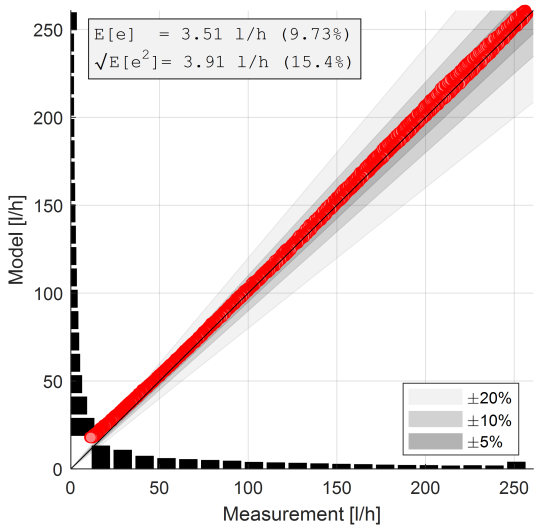

Figure 6.15.: Estimate to measurement correspondence of mass flow rate.

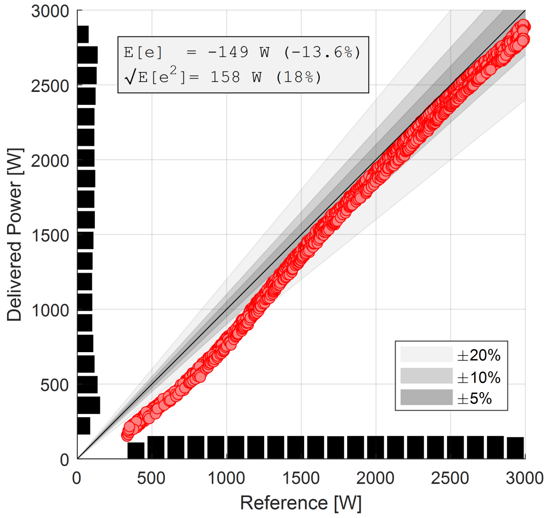

Figure 6.16.: Reference to thermal power delivery correspondence.

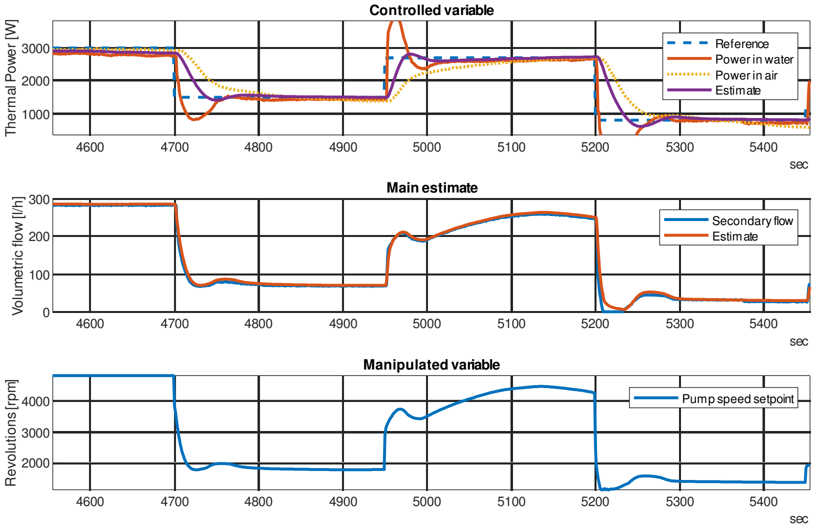

Figure 6.17.: Heat flow control. Heat flow rates on top, power in water and air measured from the testbed using flow meters and separate sets of temperature sensors. Mass flow estimate in the middle. Pump speed at the bottom.

7. Testbed

Theoretical advances made throughout the realization of the power control valve and power control pump devices would not have any practical utility without a proper feedback from real-life application. The Hydronics 4.0 project [11] enabled the realization of the temperature-feedback hydronic control device testbed, which builds upon experience gained building the preceding two test-stands of significantly smaller scale and budget.

The testbed contains three connected circuits. A primary hydronic circuit starts with the main pump and passes through a hot water tank, the primary side of the PCP device, set of PT1000 temp. sensors and electromagnetic flow meter prior to routing back to the main/primary pump. A secondary circuit starts at the PCP device's secondary outlet port and passes through an actuated valve, where QCV can reside, and further to a Coriolis flow meter, a set of PT1000 temp. sensors to a water-to-air heat exchanger and back to the PCP secondary inlet. A precise differential pressure sensor can be connected to either PCP secondary ports, primary ports or to the QCV ends. A third circuit contains a small tank holding water of significantly distinct temperatures to realize sharp temperature changes in the primary circuit prior to the PCP and QCV hardware. The third circuit is connected to the primary pipe and actuated via an old PCP prototype in a one-pipe manner. There is a short-circuit connection by which the secondary circuit may be transitioned from a one-pipe configuration (hydraulically independent "parallel" circuit) into a two-pipe configuration (secondary and primary connected into one "series" circuit). A hot water tank with a heat source is connected to the primary circuit via an actuated 3-way valve. See Fig. 7.2 for a full P&ID diagram.

An airstream starts with a straight duct employing a filter and a Wilson grid flow meter and continues through a controlled centrifugal fan and a set of PT1000 temp. sensors into the water-to-air heat exchanger, from where it leaves the testbed back to the thermal zone (room), where it is positioned in.

The physical realization of the testbed is depicted in Fig. 7.2.

7.1. Controllers

The testbed contains the following local control loops:

- Primary flow controller - PI type, no time delay, min. pump actuation limit
- Air flow controller - PI type, static time delay, min. fan actuation limit
- Hot tank controller - ADRC type Han [66], flow-dependent transport delay (stratification), open-loop heat loss estimator + closed-loop state observer on an identified model
- Cold tank controller - on/off + hysteresis type

There is also a centralized non-linear MPC controller designed in the supervised thesis Zelenka [67] for the purpose of tracking simulation inputs. A receding horizon MIMO controller is needed for tracking building simulation in the cyber-physical testbed concept (see Sec. 7.4). The controller has been designed and validated in simulations and the implementation on the real testbed is yet to come.

7.2. Data management

I have learned that a test stand is not a fixed appliance, but rather a dynamic machine morphing with an evolution of the tested unit. Difficulties with keeping multiple ledgers with signal names, units and bounds for each data bus quickly turned intractable.

To tackle the issue, a rapid prototyping data management system named "Matlab EXperiment Prototyping Interface", or MEXPI, in short, has been designed and developed under the supervised thesis [68].

The ideology is to have one configuration file communicated at each client connection. The clients set the inputs and outputs dynamically according to the configuration file.

The I/O configuration page, as well as, a I/O monitoring page and server configuration and logging are available through an embedded webserver in a target PLC running Linux.

The advantage of MEXPI is that controllers designed and tested via remote I/O communication can be, for research purposes, automatically embedded for stand-alone deployment into the PLC via a Matlab/Simulink Coder. All the controllers mentioned in Sec. 7.1 were implemented via automated embedding.

7.3. Experiments

This section serves only to display the amount of effort involved in constructing and using the testbed.

The following types of experiments have been performed on the testbed:

- Pump characteristics (speed, hydraulic load, temperature)
  - detailed HQ, PQ measurements
  - repeatability
  - fouling
  - pump-to-pump variability
- Primary-secondary dependence
- Load temperature model
- Motor coil temperature
- Flow estimation
- Heat flow control
- Valve characteristics
- Deadzone, deadband
- Glycol concentration estimation
- Peltier cooling
- Primary flow estimation with a flow meter in a parallel branch
- Primary flow control
- Air flow control
- Supply temperature control

Selected operational statistics are listed in Tab. 7.1.

Parameter	Value	Unit
Completion duration	2	years
In operation	5	years
Saved logged experiments	2137	-
Total saved experiment length	5284 (220.2)	hours (days)
Total size of “.mat” logged data	5.75	GB
Secondary circuit pumped weight	2 218 267	litres
Primary circuit pumped volume	10 819 556	litres
Total electricity consumption	6880	kWh

Table 7.1.: Testbed operation statistics.

7.4. Cyber-physical hydronic testbed

A cyber-physical appliance has its part simultaneously simulated, while the rest react to real-world environment. The concept of a cyber-physical hydronic testbed, depicted in Fig. 7.4, revolves around having a simulated building with a simulated hydronic heating network, from which any of the heat loads with its actuation may be realized in the physical testbed using a real-world components.

The building simulation may be with advantage performed by co-simulation between the EnergyPlus [69] building energy simulation program and Matlab [70] using the authored EnergyPlus co-simulation toolbox for Matlab (see Sec. 11.1, [71]). The hydronic network may be simulated using the authored software Hydronic heating toolbox (see Sec. 11.2, [72]). The simulation is at every sampling time run for the length of the prediction horizon to get actual and future conditions for the physically tested assembly. The simulation outputs over the prediction horizon are fed into a simulation tracking controller.

The simulation tracking controller is the main component connecting the simulated and real world and, as such, is the main focus of the supervised thesis [67]. The simulation tracking controller is responsible for controlling the primary flow (1-pipe)/primary pressure (2-pipe), the supply water temperature and ideally, the inlet air temperature. The air temperature, however, cannot be controlled and thus, the effect of different inlet temperature must be compensated for in the measurement conditioning block (see Fig. 7.4).

The main complexity is in supply water temperature tracking, as there are limited means to change the supply temperature. The means of temperature actuation are the small cold water tank and the primary circuit 3-way valve. Sudden temperature changes may only be realized by separating the primary circuit from the hot water tank (via the 3-way valve) and pumping the cold tank into the primary circuit. Long-term temperature decrease may only be realized by continuous cooling via the cold tanks liquid-to-liquid heat exchanger and via the water-to-air heat exchanger heat load itself.

The testbed model results in a system of DAE. The receding horizon non-linear control has been realized using the CasADi framework [73] with the IPOPT solver [74].

While the tracking controller has been designed, the entire cyber-physical testbed still needs to be assembled.

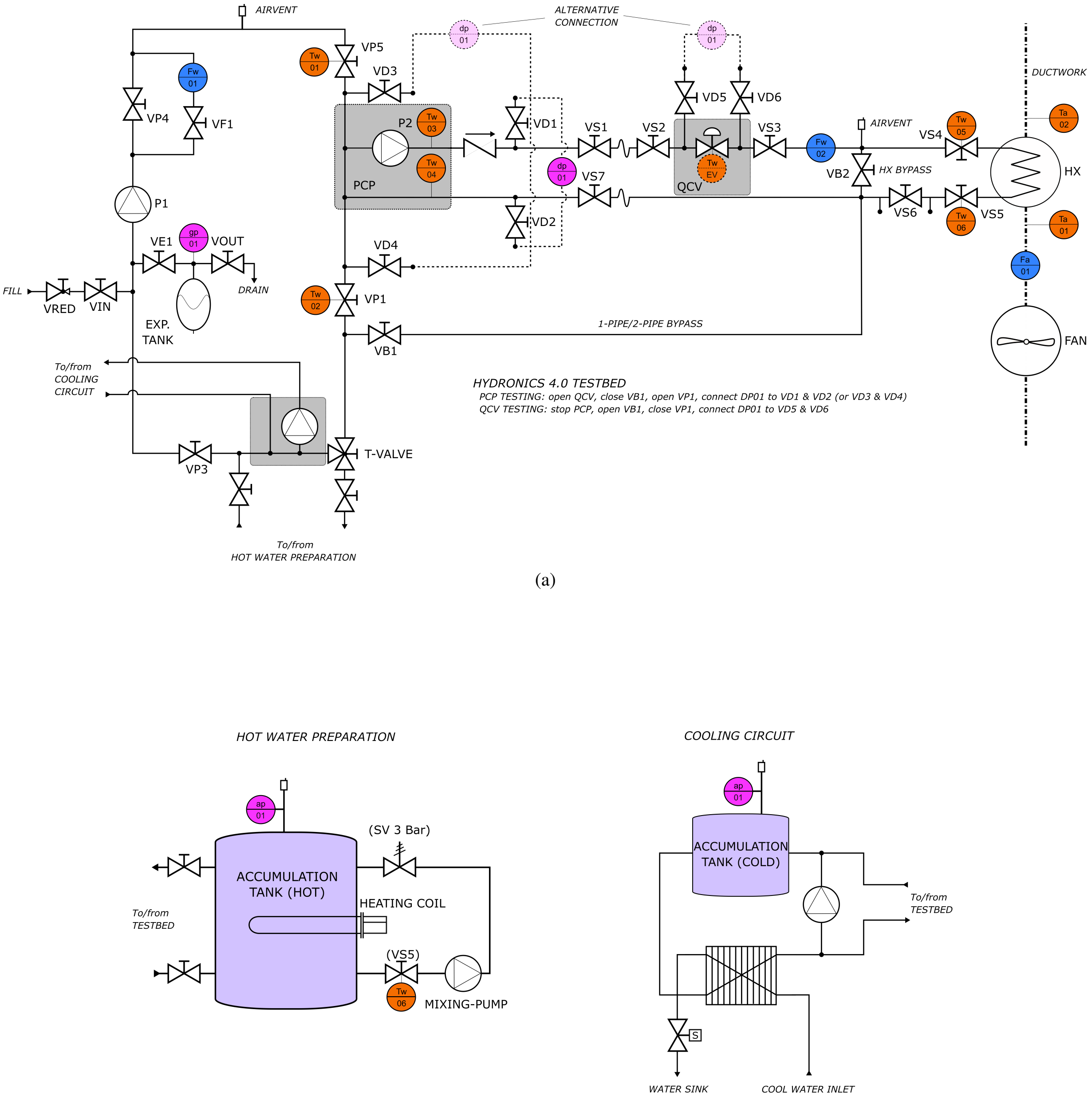

HYDRONICS 4.0 TESTBED

PCP TESTING: open QCV, close VB1, open VP1, connect DP01 to VD1 & VD2 (or VD3 & VD4)

QCV TESTING: stop PCP, open VB1, close VP1, connect DP01 to VD5 & VD6

(a)

(b)

Figure 7.1.: Temperature-feedback hydronic control device testbed P&ID scheme; main circuit (a), temperature preparation circuits (b).

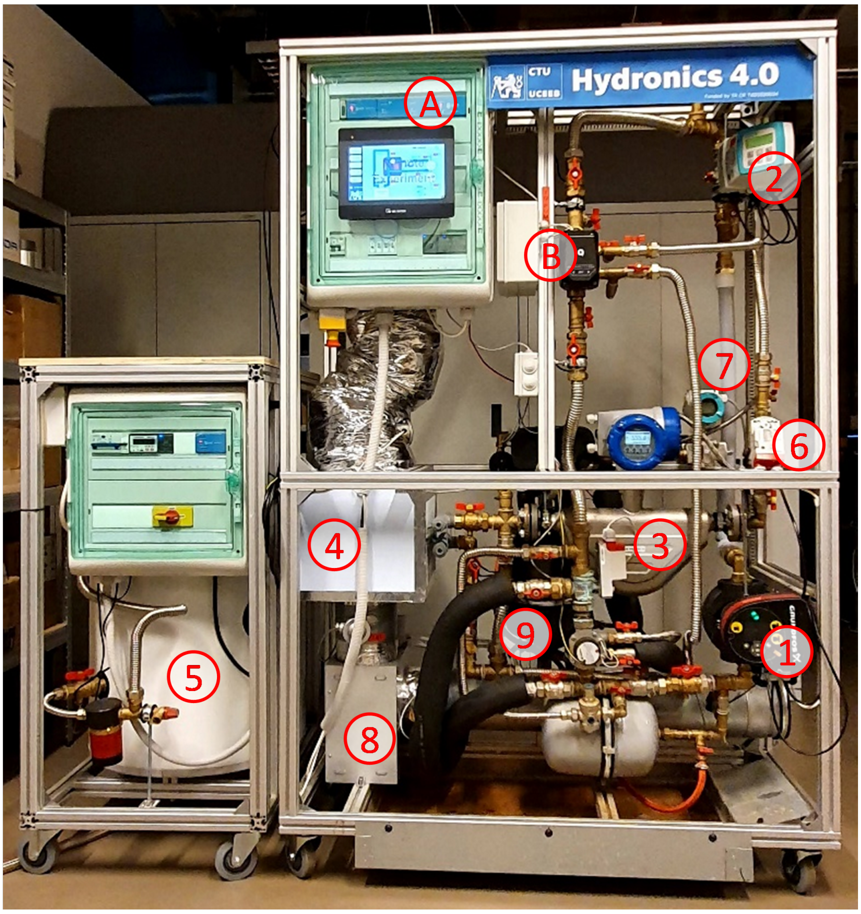

Figure 7.2.: Temperature-feedback hydronic control device testbed realization. The testbed parts are: A) controller PLC, B) power control pump, 1) primary pump, 2) primary induction flow meter, 3) secondary Coriolis flow meter, 4) water-to-air heat exchanger, 5) main tank, 6) actuated valve/power control valve, 7) differential pressure sensor, 8) controlled fan, 9) small tank for sudden temperature changes.

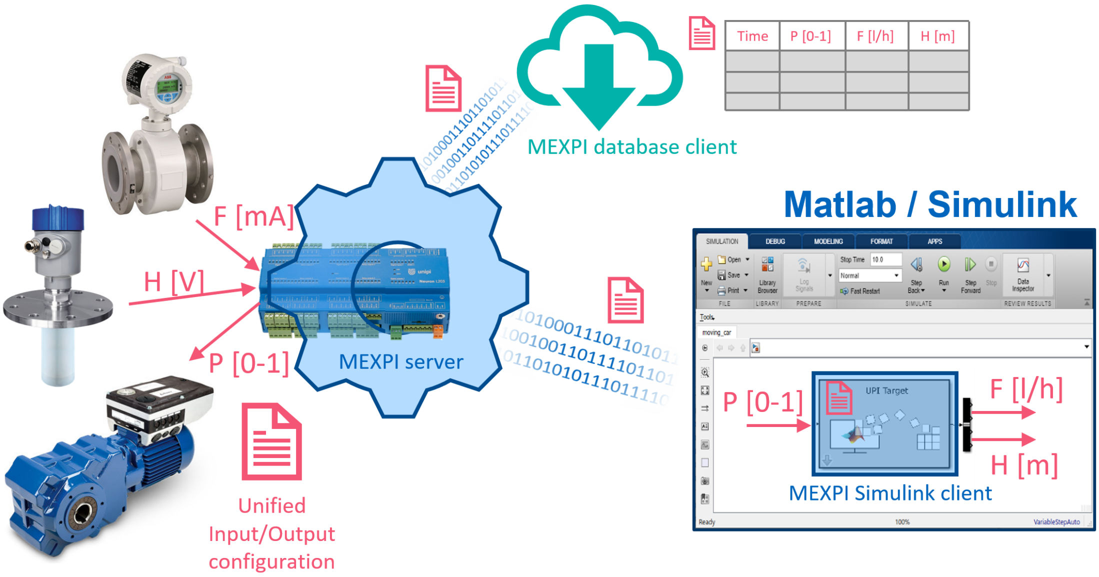

Figure 7.3.: Matlab EXperiment Prototyping Interface (MEXPI).

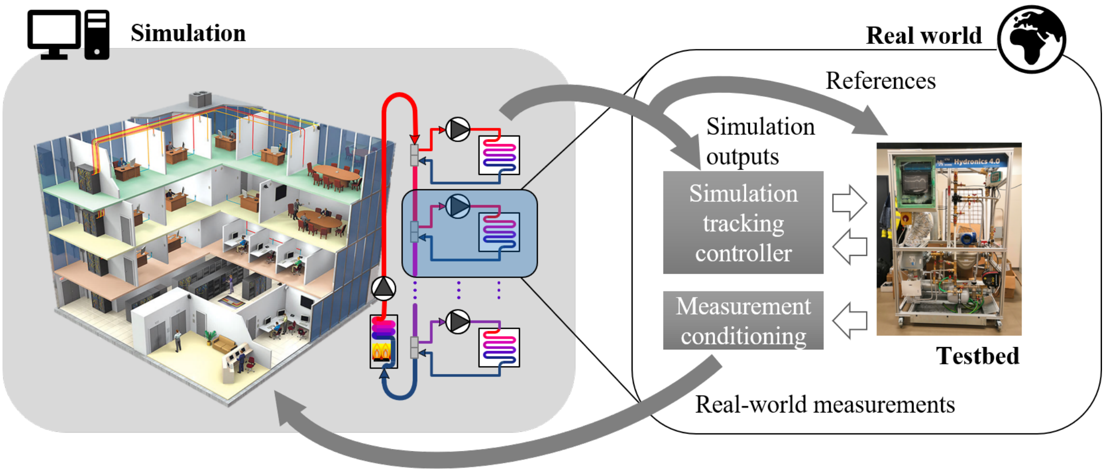

Figure 7.4.: Cyber-physical testbed concept.

Part III.

Hydronic networks

A heat distribution network is a technical system built to transport heat from a heat source to designated zones/processes; and it should do so efficiently, reliably, economically, and invisibly. There are multiple plausible choices for heat transfer fluid used, mainly air-, steam-, liquid- or refrigerant-based systems, and we are going to briefly cover the history of space heating and how the technology progressed.

Over millennia, the heating of occupied spaces was ensured by a fire burning directly in the heated room or by a hot air conveyed from the fireplace. It all changed at the beginning of the 18th century, when a Swede Marten Trifvald, in 1716, designed the first central hydronic heating system, which was utilized in a greenhouse [75]. However, it took almost another 150 years till the central hydronic heating systems spread among resident houses significantly.

In the 18th century dozens of steam heating systems used to be in operation; in many cases, these systems exploited waste heat from steam engines. Radiators were connected by a single pipe, which had both the steam supply and the condensate drainage function. Drawbacks of the steam heating systems such as noise, complexity and also the health hazard of users inhibited the extension of those systems into resident buildings and at the end of the 19th century, they were no longer competitive with - at that time - more and more succeeding hydronic heating systems.

Nevertheless, the massive spread of hydronic heating came in the second half of the 19th century. At first, gravity systems were built (no circulator pumps existed in those days); since the 50s of the 20th century electrical circulator pumps had been utilized, which allowed designers to use pipes of smaller diameters and to install heating systems into broader range of buildings. In the 70s and 80s, the number of one-pipe systems increased significantly, mainly due to the material savings during an installation. One-pipe networks from that period were sensitive to inaccuracies in design and realization and to changes in the system, which could rapidly decrease the efficiency and functionality of such systems [76]. There are, however, modern pressure and temperature balancing solutions available [77].

We can now identify four principally distinct hydronic network topologies: throttling systems utilizing valves to reject flow, pumping systems using small pumps to induce flow, and for each its two-pipe and one-pipe variants. An example of a control device - actuator for each system is given in Fig. 7.5.

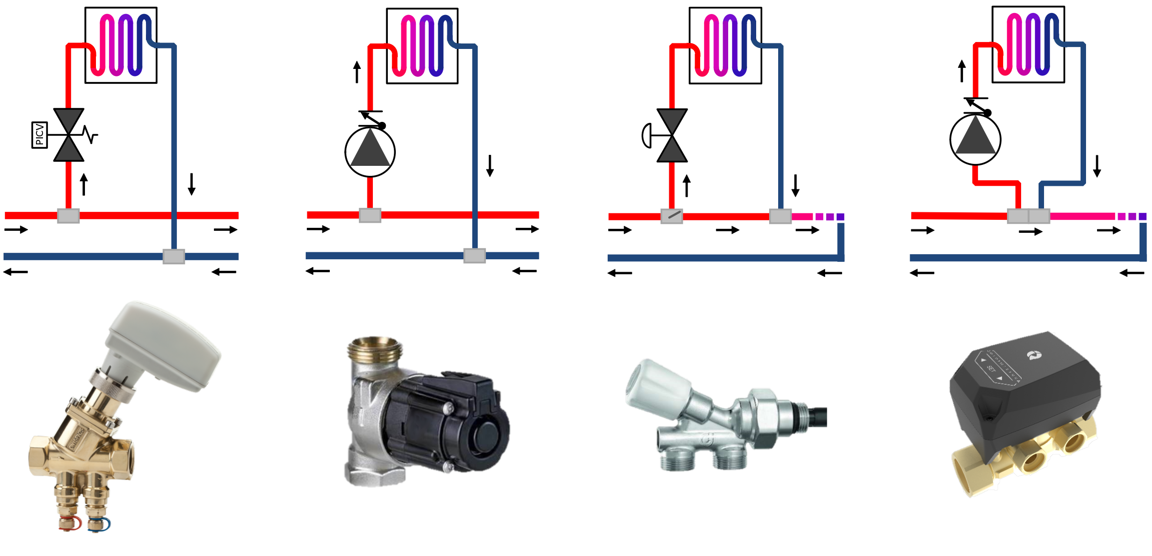

(a) (b) (c) (d)

Figure 7.5.: Piping scheme and actuator for a) throttling 2-pipe, b) pumping 2-pipe, c) throttling 1-pipe, d) pumping 1-pipe system.

By far the most predominant topology used today is the throttling two-pipe network (Fig. 7.5a), which despite surpassing the one-pipe throttling setup (Fig. 7.5c) in robustness, modifiability and control still pertain difficulties, mainly:

- Need for hydraulic balancing of loads or often poorly set in practice [78, 79]

- Dynamic pressure interactions between loads
- Pumping energy dissipation on control elements [78].

Pumping hydronic networks overcome these issues. The 2-pipe version (Fig. 7.5b) was developed by Wilo SE [44] in years 2001-2015 and is available in the market as Empur® Geniax (formerly Wilo Geniax). Full research reports are available on hydronic system analysis [79], field-testing [80] and reliability improvements [81]. An overview article [78] states the pumping 2-pipe system to be up to 90% more efficient in terms of pumping power and about 20% more efficient in thermal power (mainly due to better room control accuracy and proper night set-back). It also presents an advantage of a "demand driven" hydronic network to be the possibility of optimizing the supply water temperature - as opposed to "supply driven" networks, where the heating power has always to be prepared and is just rejected when not needed (valve closure). A different study of a comparative field test [82] confirms electricity savings of 53% (even with the electronic control system running as well in summer) and 21% gas savings. The pumping 2-pipe system usually requires an installation of hydraulic separation between the primary heat generator circuit and the secondary heat distribution circuit [79]. This technology had/has patents for the US [83] and Europe [84].

Other studies on distributed pumping [46, 85, 86] state savings in pumping energy up to 55%. The decentralized pump system suffers from more extensive wiring for pumps and controllers in retrofit cases [87]. Need-based or "demand driven" approach is the key energy saving principle by [88] and ISO52120 [89].

Significant progress has been made in residential heating/cooling over the last decade. New materials and fabrication technologies gave birth to slim copper pipes, plastic and composite flexible tubing, opening new opportunities and challenges in the field. Hydronic networks formed by this type of piping exhibit different hydraulic behaviour, and thus there is space for new piping concepts and pumping strategies. A close-tee hydraulic separation [19] is a good example of a novel piping scheme, and decentralized pumping is a revolutionizing concept of active media distribution. These and other new concepts prove that even a well-established field of study, such as hydronic heating, is still evolving.

Ideal hydronic network

Hydronic systems, in a modern European form have served our buildings for the last 50 years without any major innovation. It is worth stepping aside from the beaten track for a moment and considering what an ideal hydronic network should look. In my view, an ideal hydronic network is

- low on investment,
  - least amount of pipe length and pipe sizes
  - minimum number of fittings
- easily installed,
  - least number of piping connections
  - no manual pre-settings
- self-commissioning,
  - self-organised
  - remote diagnostics
- easily maintained,
  - robust
  - self-diagnostics
  - low-barrier extensibility
- efficient,
  - low pipe pressure loss
  - minimum pumping power
  - low heat loss
- self-optimizing,
  - local decoupling
  - edge-to-edge decentralized optimization.

Its closest real-life resemblance is the pumping one-pipe hydronic network with temperature-feedback actuators.

8. Simulation of hydronic networks

Hydronic networks merge together hydraulics and heat transfer fields. A variety of tools is available at the moment to simulate hydronic networks, for example:

- Building Library for Modelica [90]. This open-source library for the simulation of building energy and control systems is based heavily on the Modelica Fluid library. Even though the Modelica object-oriented modelling language and the building library are free, the necessary Dymola development environment is not. A nice example of the use of the Dymola/Modelica simulation environment is presented in [91]. See Fig. 8.1 for other illustrative examples.
- Base Circuit Methodology (BCM) Library [92]. This hydronic network simulation library is based on the idea, that any network can be decomposed into a number of "base circuits". These two or three-port building blocks cover a variety of possible network settings. Even though the library itself is distributed as open source, the simulation engine Engineering Equations Solver (EES) is not. See Fig. 8.1 for an illustrative example.
- THERMOSYS toolbox for Matlab Simulink. A toolbox developed by the University of Illinois at Urbana-Champaign, where the hydronic part was developed in the thesis [93]. The thesis also contains useful control-oriented model linearizations for predictive control of hydronic networks. The THERMOSYS toolbox is a commercial product.
- XRG Hydronics Library. Commercial product by XRG company developed in collaboration with multiple German universities.
- Matlab Simulink. Simulink is one of the most powerful continuous-time dynamic simulators. It employs efficient numerical integration solvers to simulate the evolution of differential systems. However, when fast dynamics of hydraulic networks is neglected, algebraic loop emerge and the generic solver algorithms begin to struggle. A specialized algorithm for solving hydraulic network loops is called a Hardy Cross method [94]. A numerical solution can be obtained by Newton-Raphson iterations [95].
- A list of building simulation toolboxes is given in [96].

There are certainly more simulation tools available, but none of them is free, provides flexibility and pairs well with Matlab for analysis. These reasons led me to create tools presented in the following sections, the Hydronic network solver (Sec. 8.1), the Hydro toolbox (Sec. 8.2) and the Hydronic heating toolbox (Sec. 11.2), which is also a building simulation tool.

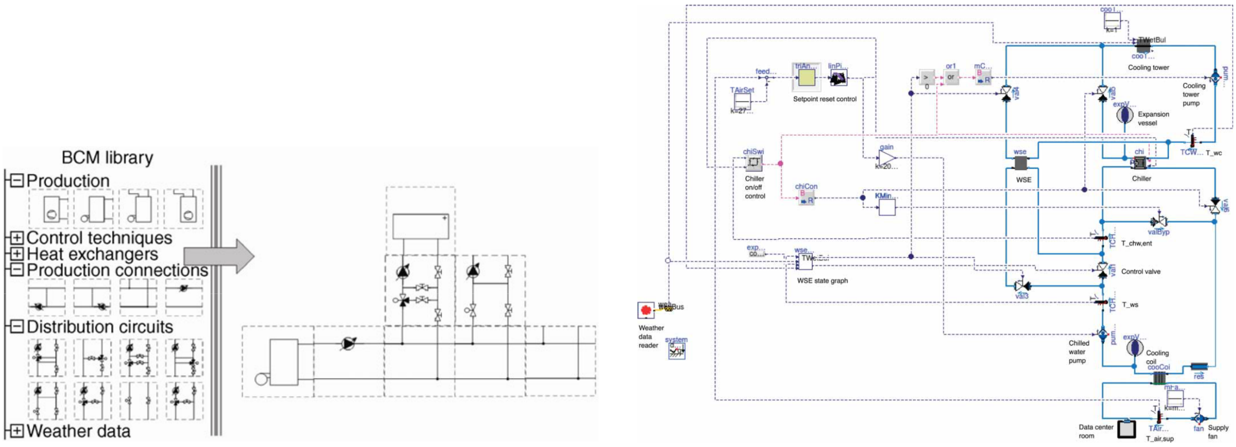

(a) BCM Library [92]

(b) Modelica Building Library [90]

Figure 8.1.: Illustrations of available hydronic network simulation tools.

8.1. Hydronic network solver[1]

Hydronic networks may contain dynamic elements (digraphs, etc.) and the propagation velocity is finite with the speed of sound (as seen in the water hammering, for example). However, these transient hydraulic phenomena diminish orders of magnitude quicker than what may be a practical timescale in hydronic (i.e., hydraulic-thermal) networks. Therefore, we are interested in quasi-steady-state solutions for any practical purpose of delivering heat through hydronic networks.

This hydronic network solver was developed to analyse network-wide properties of the throttling two-pipe vs. the pumping two-pipe control. The solver may be used to simulate 1-pipe networks as well, but in the case of pumping 1-pipe network, the problem simplifies into a number of separated elementary source-and-load circuits.

The solver employs a graph-based modelling approach using one unified building block to calculate the network solution, i.e. all pressures and flows in the network.

8.1.1. Hydraulic network simplification

All of the components of a hydronic network act, for the quasi-steady-state purposes, as either hydraulic sources or hydraulic resistances. A hydraulic scheme can be greatly simplified using the hydraulic-electric component analogy detailed in the following sections.

8.1.1.1. Hydraulic-electric analogy

Hydraulic circuits can be advantageously seen as equivalents to electric circuits, which, especially for electrical engineers, are natural and intuitive. The analogy between through and across variables is listed in Tab. 8.1. A non-exhaustive list of electric-hydraulic component analogies is given in Tab. 8.2.

An example of the hydraulic-electric analogy transformation is depicted in Fig. 8.2.

---

[1] Based on the original paper: Jiří Dostál and Vladimír Havlena. “Modeling, optimization and analysis of hydronic networks with decentralized pumping”. In: *CACS 2014 - 2014 International Automatic Control Conference, Conference Digest*. 2014, pp. 269–274. DOI: `10.1109/CACS.2014.7097200`

Hydraulic domain	Electric domain
Pressure	Potential
Pressure difference	Voltage
Flow rate	Current

Table 8.1.: Hydraulic analogy variables.

Hydraulic domain	Electric domain
Pipe, valve, etc.	Non-linear resistor
Pump	Source
Diaphragm fixed in a tank	Capacitor
Paddle wheel	Inductor
Check-valve	Diode

Table 8.2.: Hydraulic analogy elements.

8.1.1.2. Network simplification

A simplification of the hydronic network is possible by creating equivalent circuits with compound components. In other words, to collect all serial-parallel connections of resistances into one equivalent resistance and all serial-parallel connections of the pump into an equivalent pump model.

Recall from Sec. A.1 that for a series connection of hydraulic resistances it stands

$$R_{1\text{—}2} = R_1 + R_2,$$

and for a parallel connection

$$R_{1\|2} = \frac{R_1 R_2}{\left(\sqrt[2]{R_1} + \sqrt[2]{R_2}\right)^2}.$$

For pumps, recall from Sec. A.3.5 that for a series connection, the pressures add up; for a parallel connection, the flows add up.

8.1.2. Graph based modelling approach

A two-pipe hydronic network piping is formed by a main supply/return line from which individual heat exchangers with their piping and controls branch out. This is a pattern that replicates throughout the whole network. Realization of this fact sparked an idea expressed in the following proposition.

Proposition 1. *A hydronic network can be modelled as an interconnection of identical hydronic sub-network elements.*

The basic modelling sub-network element is called *basic hydronic network element,* and it is introduced in the following section. Each basic hydronic network element represents one node in a graph and the hydronic network may be modelled by a directed interconnection between these nodes.

8.1.2.1. Basic hydronic network element

A common pattern can be recognized in two-pipe hydronic networks. Usually, there is a supply and return pipe of a certain length leading to a junction where a heat exchanger with its piping branches out. This basic pattern, accompanied with a pump on the supply line and a pump by the heat exchanger, represents the generic construction block of the presented modelling approach.

Hydraulic resistance of the supply and return line can be equivalently substituted by one serial hydraulic resistance. Any valves present on the supply/return line are also incorporated into the serial hydraulic resistance. Parallel

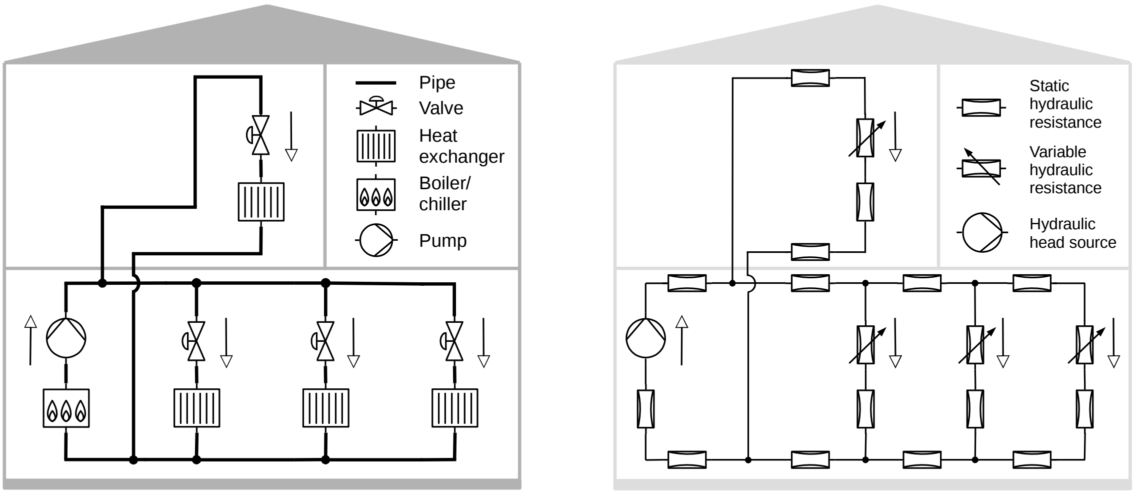

(a)

(b)

Figure 8.2.: Hydronic circuit (a) and its hydraulic-electric analogy representation (b).

hydraulic resistance aggregates any heat exchanger (boiler/chiller) hydraulic resistances, auxiliary piping resistances and resistances of any valves present by the heat exchanger (boiler/chiller). Any boosting pump would be represented by a serial pump, a main circulator pump or decentralized heat exchanger pumps are represented by a parallel pump. The basic hydronic network element is schematically depicted in Fig. 8.3.

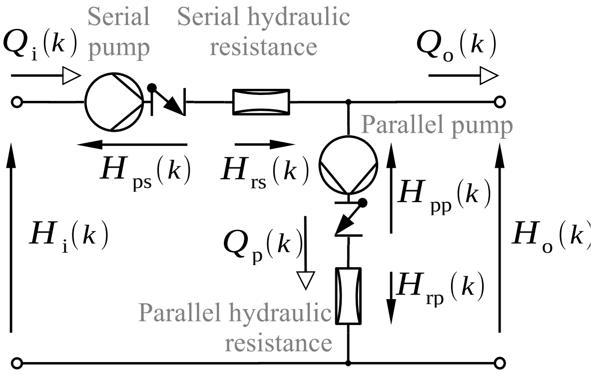

Figure 8.3.: Generic construction block of the modelling approach: the basic hydronic network element.

It follows from the water head balance in a k-th node that

$$\begin{aligned} H_o(k) &= H_{pp}(k) - H_{rp}(k), & (8.1)\\ H_i(k) &= H_{ps}(k) - H_{rs}(k) + H_o(k), & (8.2) \end{aligned}$$

where H_o denotes outlet water head potential of the basic hydronic element, H_{pp} denotes parallel pump head gain, H_{rp} parallel hydraulic resistance head loss, H_i denotes element's inlet water head potential, H_{ps} denotes serial pump head gain and H_{rs} denotes serial hydraulic resistance head loss. The mass conservation law governs the flows in the

k-th node as

$$Q_{\mathrm{i}}(k) = Q_{\mathrm{p}}(k) + Q_{\mathrm{o}}(k), \tag{8.3}$$

where Q_{i} is an inlet flow of the basic hydronic network element, Q_{p} is a flow through the parallel branch in the element and Q_{o} denotes an outlet flow.

The head gains and losses of the serial and parallel sources and resistances have non-linear polynomial representations given in Part I .

8.1.2.2. Network interconnection

An important step in the presented modelling framework is to properly identify the basic hydronic network elements in a hydronic network at hand. There will rarely be a complete basic hydronic network element present in a hydronic network, but instead, there will be segments where some of the components are missing. The next section explains the most important part of the approach - identifying basic hydronic network elements in the network and a translation into a graph.

Identification of basic hydronic network elements Note that leaving out the serial pump, serial hydraulic resistance or one of the parallel components by setting its respective heads to zero still leaves the modelling approach tractable. The only necessary component to be present in every basic hydronic network element is one of the parallel components. The following list will help with the translation from a piping network into a node graph.

- Substitute serial/parallel connections of hydraulic resistances with one equivalent hydraulic resistance. Substitute serial/parallel connections of pumps with one equivalent pump model.
- There is usually a basic hydronic element for each heat exchanger.
- Boiler/chiller is modelled as a parallel hydronic resistance and a central pump, if present, as a parallel pump in the same element. This hydronic element will only be connected by its outlet to the network.

Commonly encountered modifications of the basic hydronic network element are listed in Fig. 8.4.

Once basic hydronic network elements are identified in the hydronic network, they can be represented by a set of numbered nodes (the node containing a heat source is preferably given number 1). The interconnection graph is always a directed tree graph. The adjacency matrix $\mathbf{A}_{\mathrm{g}} \in \mathbb{R}^{n \times n}$ of the graph is

$$\mathbf{A}_{\mathrm{g}} = \{a_{u,v}\}_{u,v \in \mathcal{V}}, \text{ where } a_{u,v} = \begin{cases} 1 & \text{if edge } (u,v) \text{ exists} \\ 0 & \text{otherwise,} \end{cases} \tag{8.4}$$

where n is the number of nodes in the network and $\mathcal{V}$ represents the set of all nodes. An example hydronic network with its graph representation is depicted in Fig. 8.5.

Traditional 2-pipe hydronic networks form path graphs or sparsely branched tree graphs. Hydronic networks with decoupling manifolds translate into tree graphs with a star subgraph for each manifold. Hydronic networks with hydraulic separators form disconnected graphs with as many graphs as the hydraulically separated sections.

8.1.2.2.1. Flow and head balance It is straightforward that the outlet head and inlet head of subsequent connected elements must cohere together, i.e. be equal at every time instant. This head equality among all network nodes is, using the graph structure information, represented as

$$\mathbf{H}_{\mathrm{i}} = \mathbf{A}_{\mathrm{g}}^{T}\mathbf{H}_{\mathrm{o}}, \tag{8.5}$$

where $\mathbf{H}_{\mathrm{i}}$ is a vector of stacked node inlet heads and $\mathbf{H}_{\mathrm{o}}$ is a vector of stacked node outlet heads.

Outlet flow of one element divides at an interconnection into inlet flows of subsequent connected elements. For all nodes, this fact is represented as

$$\mathbf{Q}_{\mathrm{o}} = \mathbf{A}_{\mathrm{g}}\mathbf{Q}_{\mathrm{i}}, \tag{8.6}$$

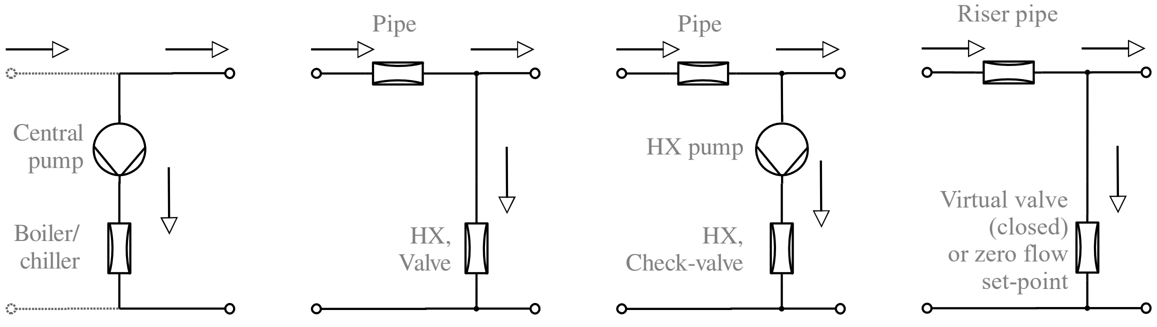

(a) (b) (c) (d)

Figure 8.4.: Commonly encountered hydronic network sections (basic hydronic network elements): a) boiler/chiller and central pump, b) heat exchanger with a control valve, c) heat exchanger with a decentralized pump, d) riser.

where $\mathbf{Q}_\mathrm{o}$ is a vector of stacked node outlet flows and $\mathbf{Q}_\mathrm{i}$ is a vector of stacked inlet flows. The flows through parallel branches are

$$\mathbf{Q}_\mathrm{p} = \mathbf{Q}_\mathrm{i} - \mathbf{Q}_\mathrm{o}. \tag{8.7}$$

For the example network from Fig. 8.5, the adjacency matrix is

$$\mathbf{A}_\mathrm{g} = \{a_{u,v}\}\,;\ a_{1,2} = 1, a_{2,3} = 1, a_{3,4} = 1, a_{1,5} = 1$$

and the head balance equation (8.5) correctly represents that, for example, the inlet head of the second and fifth element is equal to the outlet head of the first element, which may be best seen from

$$\boldsymbol{H}_\mathrm{i} = \begin{bmatrix} \cdot & \cdot & \cdot & \cdot & \cdot \\ 1 & \cdot & \cdot & \cdot & \cdot \\ \cdot & 1 & \cdot & \cdot & \cdot \\ \cdot & \cdot & 1 & \cdot & \cdot \\ 1 & \cdot & \cdot & \cdot & \cdot \end{bmatrix} \boldsymbol{H}_\mathrm{o}.$$

The flow continuity (8.6) also correctly represents the fact that, for example, the flow from the first element is a sum of the second and fifth element flow

$$\boldsymbol{Q}_\mathrm{o} = \begin{bmatrix} \cdot & 1 & \cdot & \cdot & 1 \\ \cdot & \cdot & 1 & \cdot & \cdot \\ \cdot & \cdot & \cdot & 1 & \cdot \\ \cdot & \cdot & \cdot & \cdot & \cdot \\ \cdot & \cdot & \cdot & \cdot & \cdot \end{bmatrix} \boldsymbol{Q}_\mathrm{i}.$$

That illustrates the simplicity of network head and flow balance definition and anticipates network solvers formulation.

8.1.2.3. Hydraulic network solvers

Three natural problems are emerging when dealing with hydraulic networks:

1. Network flow problem - Given an opening of every control element, what is the flow and hydraulic head at every point of the network?
2. Network control problem - Given a set of demand flows (references), what are the actuator openings ensuring

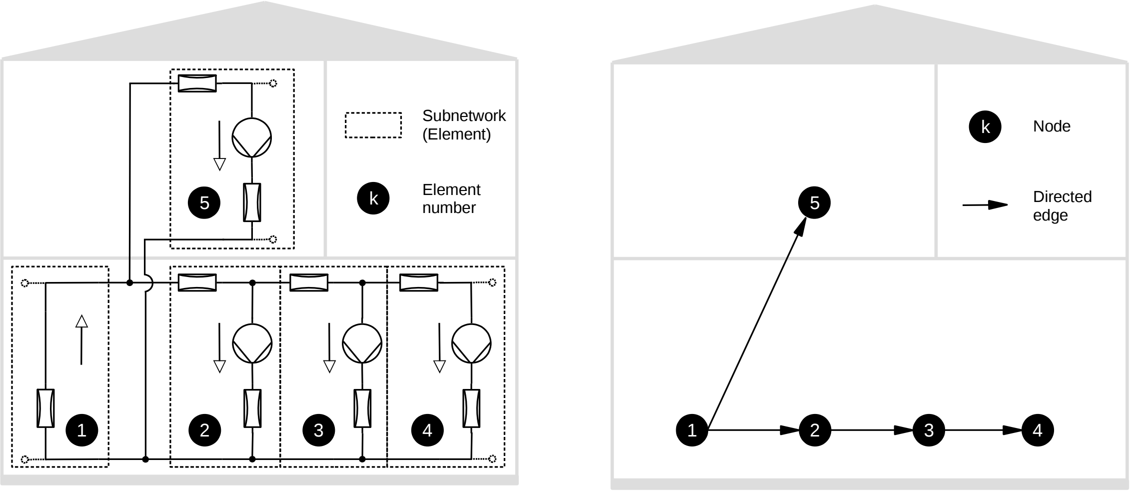

(a) (b)

Figure 8.5.: Identified basic hydronic network elements in a hydronic network with decentralized pumping (a) and its graph representation (b).

the flows?

3. Pumping energy optimization - Whenever there is a degree of freedom in the network, what is the control problem solution with a minimal electric power consumption?

The following subsections describe the solutions to the three problems. A graph structure plays a major role in all the solvers and enables a fast, non-iterative solution to the network control problem, which in turn speeds up the third optimization problem, where the network control problem is a sub-step of every iteration.

8.1.2.3.1. Network flow problem Lets first introduce a diagonal matrix of node in-degrees. As hydronic networks always form directed tree networks; the in-degree matrix $\mathbf{B}_\mathrm{g} \in \mathbb{R}^{n \times n}$ is defined as

$$\mathbf{B}_\mathrm{g} = \operatorname{diag}(b_u)_{u \in \mathcal{V}}, \text{ where } b_u = \begin{cases} 1 & \text{if inlet } u \text{ unconnected} \\ 0 & \text{otherwise.} \end{cases}$$

Let the flows in parallel branches of nodes with nonzero in-degree be the unknown variables, denoted $\mathbf{Q}_\mathrm{x}$. The number of unknown variables is denoted n_x and the following inequality holds

$$n_\mathrm{x} < n.$$

The flow in all parallel branches, i.e. also, the flow in a heat source node, is given by

$$\mathbf{Q}_\mathrm{p} = \left(\mathbf{I} - \mathbf{B}_\mathrm{g}\left(\mathbf{I} - \mathbf{A}_\mathrm{g}\right)^{-1}\right)\mathbf{C}_\mathrm{g}\mathbf{Q}_\mathrm{x}, \tag{8.8}$$

where $\mathbf{C}_\mathrm{g} \in \mathbb{R}^{n \times n_\mathrm{x}}$ is

$$\mathbf{C}_\mathrm{g} = \text{non-zero columns of } \left(\mathbf{I} - \mathbf{B}_\mathrm{g}\right)$$

and $\mathbf{I}$ is an identity matrix of a proper dimension.

The inlet flows, using (8.6), (8.7), are calculated as

$$\mathbf{Q}_\mathrm{i} = \left(\mathbf{I} - \mathbf{A}_\mathrm{g}\right)^{-1}\mathbf{Q}_\mathrm{p}. \tag{8.9}$$

The solution to the network flow problem must satisfy (8.5), (8.6) , and the solution procedure is iterative. At each iteration, $\mathbf{q}_{\mathrm{p}}$ and $\mathbf{q}_{\mathrm{i}}$ are calculated from $\mathbf{q}_{\mathrm{x}}$ and therefore, all flows in the network are known and head across all network components can be computed. Any gradient solver algorithm may be used to find $\mathbf{q}_{\mathrm{x}}$ such that head equality (8.5) is satisfied. Flow equality between the nodes is inherently satisfied by the flow calculation process. The most computationally expensive part of the calculation is the head loss/gain across all network components. However, it can be easily parallelized due to the nature of the formulation of the problem.

8.1.2.3.2. Network control problem It is assumed for simplicity that each node, except the nodes containing a boiler, contains a heat exchanger and a flow controlling element (control valve/pump) is present by each heat exchanger; flow reference (setpoint) through all heat exchangers is known and is denoted $\mathbf{Q}_{\mathrm{x}}^{\mathrm{SP}}$.

The inlet and parallel flows, $\mathbf{Q}_{\mathrm{i}}$ and $\mathbf{Q}_{\mathrm{p}}$ respectively, can be calculated from $\mathbf{Q}_{\mathbf{x}}^{\mathbf{SP}}$ using (8.9), (8.8). A head loss/gain across all non-actuator components than can be calculated using their respective head models.

A head across control actuator is then calculated from the loop equations (8.2), (8.1). And as the head and flow for each control actuator is now known, it is possible to determine the exact actuator opening x_{c} (valve stroke or pump speed) satisfying the given hydraulic conditions. For example, the speed of an actuated heat exchanger pump in a k-th node is determined from equations

$$\begin{aligned} H_{\mathrm{pp}}(k) &= H_{\mathrm{i}}(k) + H_{\mathrm{rs}}(k) + H_{\mathrm{rp}}(k) - H_{\mathrm{ps}}(k) \\ x_{\mathrm{c}}(k) &= \mathrm{pol}_{\mathrm{HQ}}^{-1}\left(H_{\mathrm{pp}}(k), Q_{\mathrm{x}}^{\mathrm{SP}}(k)\right), \end{aligned}$$

where x_c is the speed ratio of a heat exchanger pump (parallel pump) and $\mathrm{pol}_{\mathrm{HQ}}^{-1}$ is an inverse of the HQ characteristics of the pump.

A network control problem solution algorithm is detailed in Alg. 8.1. An illustration of the algorithm steps is depicted in Fig. 8.6.

Algorithm 8.1 Network control problem forward-calculation algorithm.

```
Determine flows $\mathbf{Q}_{\mathrm{i}}$, $\mathbf{Q}_{\mathrm{p}}$ from $\mathbf{Q}_{\mathrm{x}}^{\mathrm{SP}}$.
for $e = 1$ to $n$ do
    $e_p$ = predecessor of $e$ in the graph.
    $H_{\mathrm{i}}(e) = H_{\mathrm{o}}(e_p)$.
    Calculate the heads of all components in $e$ except for the control actuator.
    if actuator present in $e$ then
        Determine the head across the actuator.
        $x_c(e) \leftarrow$ calculate opening of the actuator from its characteristics.
    end if
    Calculate $H_{\mathrm{o}}(e)$.
end for
```

8.1.2.3.3. Pumping energy optimization A system with the same number of heat exchangers, i.e. flow setpoints, as the number of flow-controlling devices is well determined - has zero degrees of freedom. Any extra actuator on top of the basic count opens a degree of freedom for optimization; a variable speed main circulator may be the most common case.

There is a wide variety of hydronic network optimization problem formulation options. The approaches generally differ in cost function and constraint formulation. The first option is formulating the optimization problem, where the cost function is the total electrical power consumption and let the network head and flow balance, as well as, the flow reference be equality constraints. Flow direction in the heat exchangers is forced by inequality constraints and the range of actuators by box constraints. An interior-point solver computes the solution considerably fast, but finding a feasible initial solution is difficult.

Another possibility is to set the cost function as the total pumping power plus the squares of reference flow deviations. The network flow problem is then solved at each iteration separately. Actuator positions are the optimization values, but not all of their combinations pose a feasible solution to the network flow problem. This approach does not guarantee finding an optimal solution because each time there is infeasibility in the network flow problem, a new starting point must be randomly picked.

A numerically efficient approach to the network optimization problem, however, exists and is the following: the set of all available actuator variables (valve stroke, pump speed) is divided into two sets: a control variable set C and an optimization variable set O; the set of all actuator is be denoted as $\mathcal{A}$, the set of all pumps $\mathcal{P}$. The cardinality of the control variable set must be equal to the number of flow references in the network ($|C| = n_{\mathrm{x}}$) The control variables will typically be the position of actuators controlling the flow through heat exchangers, i.e. control valve strokes or heat exchanger pump speeds. All the remaining actuators form the set of optimization variables whose cardinality is $|O| = |\mathcal{A}| - n_{\mathrm{x}}$. Each network node must contain at most one control actuator, the rest of the actuators in the node are assigned to the optimization variable set.

The cost function is the total electric power consumption plus a heavily weighted norm of the network head and flow balance. The optimization problem is formulated as

$$\begin{aligned} &\min_{\mathbf{x}_o} \sum_{\alpha\in\mathcal{P}} P_e(\alpha) + \gamma \left\| \begin{matrix} \mathbf{H}_{\mathrm{i}} - \mathbf{A}_{\mathrm{g}}^T \mathbf{H}_{\mathrm{o}} \\ \mathbf{Q}_{\mathrm{o}} - \mathbf{A}_{\mathrm{g}} \mathbf{Q}_{\mathrm{i}} \end{matrix} \right\|^2 \\ &\text{s.t.} \quad 0 < x_o(i) < 1; \; i \in O \\ &\qquad \mathbf{x}_c \leftarrow \begin{matrix} \text{solution of the network control} \\ \text{forward-calculation algorithm} \end{matrix} , \end{aligned} \tag{8.10}$$

where $\mathbf{x}_o$ is a vector of the optimization variables, $P_e(\alpha)$ is an actual electric power of a pump α, γ is a relatively high penalization constant and the control variables $\mathbf{x}_c$ are computed by the network control forward-calculation algorithm (Alg. 8.1). The objective is to minimize electric consumption; yet, some combinations of the optimization variables make the network control problem infeasible. Infeasibility of the control problem results in network head/flow imbalance, whose penalization steers the optimization variables towards a feasible region.

The presented hydronic solver is used in the analysis presented in Sec. 9.2.

8.2. Hydro toolbox

The hydro toolbox [97] is a set of classes and functions in MATLAB developed to facilitate the work and analysis of components and circuits in the hydronic domain. There are four main classes:

- `fluid` - a wrapper class for the coolprop package [98] providing thermodynamic properties of fluids (water, humid air, refrigerants, etc.), which are utilized within the `pump` and `load` classes.
- `pump` - a class and a package providing tools to fit, manipulate and analyze pump characteristics in flow, pressure, power, and speed.
- `load` - a class and a package providing tools to fit, manipulate and analyze hydraulic loads.
- `heatload` - a package providing tools to analyze, fit and design heat exchangers.
- `circuit` - a class used for solving hydraulic circuits defined by `pump` and `load` objects.

The pump and load classes are ‘system objects’, which can be used in Simulink as well. The power control valve (Chapter 5) and the power control pump (Chapter 6) have been designed with the help of this toolbox.

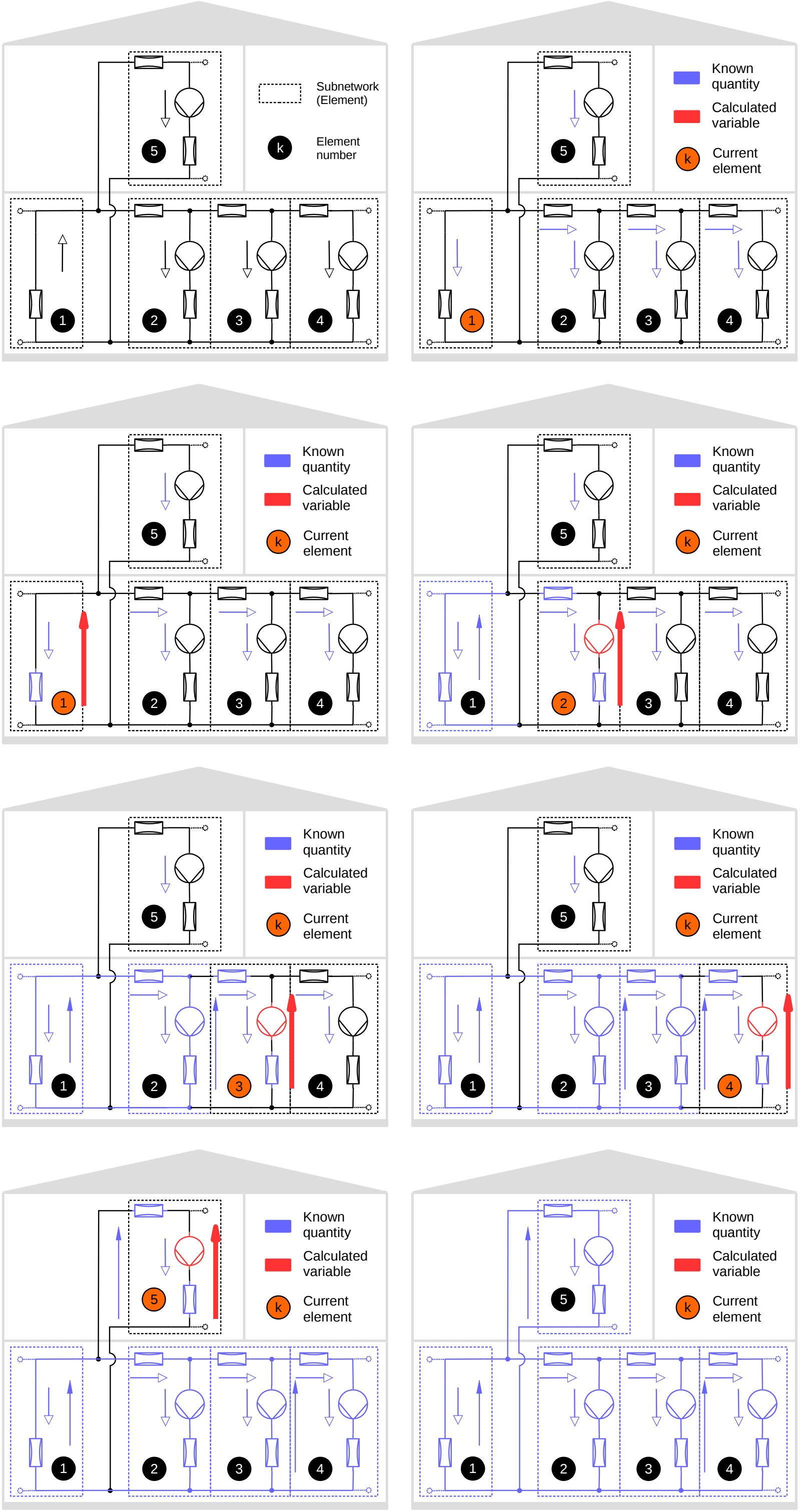

Figure 8.6.: Illustration of the network control problem forward-calculation algorithm steps.

9. Hydronic network analysis

This section presents results in the stability (Sec. 9.1) and effectivity (Sec. 9.2) of two-pipe network, as well as analysis of the pumping one-pipe network (Sec. 9.3).

9.1. Throttling two-pipe system stability[1]

Many HVAC systems are implemented using one heat source, the power of which is distributed to individual zones using a pipe network. Each zone can be independently controlled using its own zone controller. Due to the hydronic network interconnection, the zone controllers interact by pressure/flow changes. This study addresses the question when and under what conditions the overall system is a stable system. We use a simplified linearized model with linear heat exchangers and linear hydraulic resistances. Moreover, all heat exchangers are supposed to be the same. A closed-form formula for linearization of the interconnection is provided. Using these simplifications, we provide simple guidelines which the controller for each zone should satisfy. The main result is that from stability point of view, the interconnection does not bring any new design limitation. An extensive simulation verification is provided.

9.1.1. Introduction

Human kind has lost during the evolution the ability to endure rough weather, but gained in exchange greater mental ability. This ability catalyzed the pursuit for conditioning living environment, which lasts until the present-day. HVAC (heating, ventilation and air conditioning) systems the field of study continuing the comfort seeking endeavor also comprise an important part of the total energy consumption of modern society. Since the price for energy is increasing as is the comfort expectations, the control of HVAC systems are getting more and more sophisticated and complex.

Often, in a building environment there are, for heating/cooling purposes, several zones (for instance, rooms), which might set their own request onto the zone temperature. Purpose of the HVAC system is to closely follow the request regardless the everchanging inside and outside conditions. In order to accomplish this, each zone has to be supplied by an exact amount of heat energy, though a heat exchanger (for instance, a radiator), from a heat source (boiler/chiller) by a distribution piping system and its control mechanism. This article is treating hydronic systems in particular, there the heat distribution medium is one-phase liquid [19].

Hydronic control systems are either demand oriented, where there is a flow-controling pump aside each heat exchanger [46]. Or traditionally supply oriented, where there is there is only one pressure source in the hydronic network—a central pump. The pressure potential is turned into the right flow by a control throttling valve at individual heat exchanger. For automatic control of the temperature in the zone, zones are fitted with a temperature controller - a thermostat.

There are several control strategies for maintaining the desired temperatures in the zones, which differ based on the number of sensors, actuators and computation units. The simplest to implement is to control the heat source by one thermostat in one zone and have thermo-regulating valves in the remaining zones. Based on [100], this is still the most commonly implemented strategy.

Another centralized strategy is a model predictive control (MPC), where the setting for each valve can be optimally computed in a central computer [93, 101]. There also exist distributed implementations for MPC [102]. A fuzzy MPC framework, which was able to both heat and cool the building, was presented in [103].

The strategy, which is used in this study, is when a heat source is assumed ideally controlled (not purpose of this study) and an independent temperature controller, regulating the stroke of the control valve, is present in every zone.

---

[1] Based on the co-authored paper: Ivo Herman, Štefan Knotek, Jiří Dostál, and Václav Prajzner. “Stability of hydronic networks with independent zone controllers”. In: *IEEE Transactions on Control Systems Technology* 26.6 (Nov. 2018), pp. 2214–2222. ISSN: 1063-6536. DOI: `10.1109/TCST.2017.2753179`

However, due to the common pressure source (pump), when one valve changes its setpoint, there is a pressure change at the other valves [100].

The effect we investigate in this study is how the action of one controller affects, through the hydraulic network, the other controllers. For instance, when the controller i closes its valve, it results in an increase of pressure at all other valves. Consider the zone j. The increase in pressure over valve j means that with the given valve stroke, the flow increases and so does the heat flux delivered to the zone. Subsequently, the temperature in the zone j increases and the controller has to decrease the stroke x_j of its valve. However, this change propagates further to other valves. The question is: under what conditions is this interaction stable?

A similar problem of hydraulic interactions between different branches was considered in ventilation in mines. In the paper by [104] a centralized controller for the whole network was designed. Later, [105] designed a nonlinear decentralized controller. Unlike our study, in those two papers the nonlinear resistance and fluid inertia was considered. However, the authors assumed known plant model (just the fluid itself) and designed a complicated nonlinear control law. Instead, here we deal with a general plant model (zone and heat exchanger) and try to find a requirements on the controller (often a simple PI controller).

In order to analyze stability of the interconnected system, we are going to use tools from distributed control theory. Stability of a set of (identical) linear systems interconnected through network was analyzed in many works, e.g. [106–108]. The method used there was based on block diagonalization, after which the eigenvalues of the matrix describing the subsystem interconnection appeared as a gain in the closed-loop feedback system. The interconnection matrix in these works was mostly the graph Laplacian—that is, a relative interconnection was assumed. Although the hydronic interconnection does not have a structure of relative interactions, we can still use the results of these works and apply them for stability analysis.

Even though in this study we mainly speak about zone controllers (those are currently most widely used), our theory and results would hold even when a faster control loop is implemented: the loop for controlling the *heat flux* delivered to the zone. If this can be estimated, it allows faster detection of pressure change across the valve and therefore better control. On the other hand, faster control means higher risk of instability. Hence, our results would be even more important for this type of control.

9.1.2. System model

The system under consideration consists of several parts: a main pump (the pressure source for the hydraulic circuit), a boiler/chiller (in the following we will only assume heating, so only boiler will be used), N heat exchanger (HX) units used for heating/cooling of zones, N valves used to control the flow in the HXs and the pipe network connecting the HXs.

The schematic of the hydronic part is in Fig. 9.1. The flow goes through the supply water pipe, to which there are connected N HXs with their valves and the connection is parallel. The flow through the HXs is then collected at the return pipe and led back to the pump.

The valve at each HX is controlled based on the temperature θ_i in the ith zone and the reference temperature $\theta_{\mathrm{ref},i}$. The schematic of the valve control is in Fig. 9.2. This control loop is the same for all HXs. The controller sets the valve state—its stroke x. This stroke, based on the given differential pressure p_i over the valve, sets the mass flow Q_i. Based on the mass flow the HX generates, after some transient, the heat flow heating the zone and thus changing its temperature θ_i.

However, due to the common pressure source and parallel branch interconnection, the flow in each branch is not only given by x_i, but also by all other $x_j, j \neq i$. Thus, all the control loops are interconnected and we can write a vector form

$$\boldsymbol{Q} = f(\boldsymbol{x}, p_{\mathrm{in}}), \tag{9.1}$$

where $f : \mathbb{R}^N \to \mathbb{R}^N$, $\boldsymbol{Q} = [Q_1, \ldots, Q_N]^{\mathrm{T}}, \boldsymbol{x} = [x_1, \ldots, x_N]^{\mathrm{T}}$ and p_{in} is the pressure generated by the pump.

The hydraulic system can be depicted as the corresponding network in Fig. 9.3. The pump is analogous to a pressure source. The pipes were replaced by hydraulic serial resistances $r_{\mathrm{s}i}$ – combined resistance of the sections of the supply and return pipe between branch $i-1$ and i and r_{p_i} – resistance of the pipes in the i^{th} branch. The inertia of the fluid in the pipes was neglected. The valve was replaced by a variable hydraulic conductance g_{v_i}. Since we model only

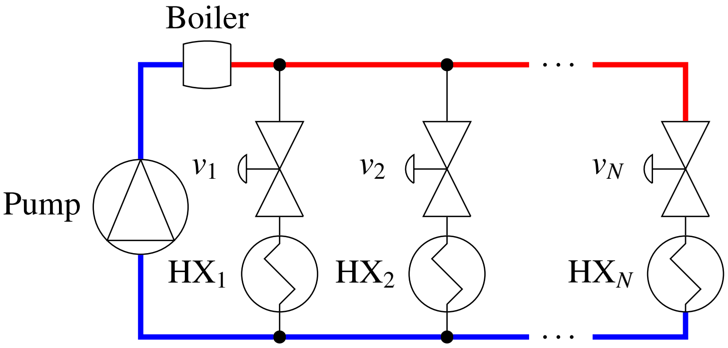

Figure 9.1.: A simplified schematics of the hydronic network. There are N parallel branches consisting of the valve and heat exchanger. The red (blue) line is the supply (return) pipe.

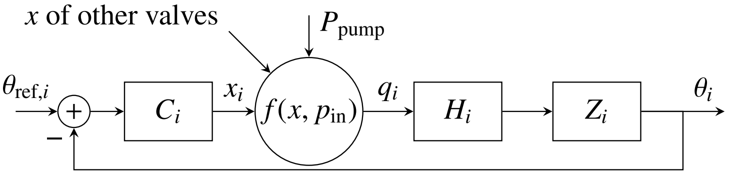

Figure 9.2.: Control loop schematics. H_i is the ith HX, Z_i is the ith zone and C_i is the ith zone controller.

the hydraulic network, the boiler and the heat exchanger are modelled by resistances r_{b} and $r_{\mathrm{h}i}$, respectively. In our analysis, we will simplify the notation by introducing the serial resistance r_i and parallel conductance g_i. The serial resistance in section one is comprised of a series combination of r_{b} and $r_{\mathrm{s}1}$; in all other sections it is just $r_{\mathrm{s}i}$. The parallel conductance is given as a variable conductance of a series combination of r_{p_i},$r_{\mathrm{h}i}$ and g_{v_i}. That is, the conductance is bounded as $g_i \in [0,\ 1/(r_{\mathrm{p}_i} + r_{\mathrm{h}i} + 1/g_{i,\max})]$, where $g_{i,\max}$ is the maximal conductivity of the valve.

9.1.2.1. Assumptions

In order to do a tractable analysis, we make the following simplifying assumptions.

1. We analyze only the hydraulic interactions—we assume that the inter-zone thermal interactions (e.g., heat flows through walls) are much slower and less important than the hydraulic ones.
2. The relation between pressure drop across the pipe and flow is linear. That is, we assume viscous laminar steady flow in a circular tubes [109, eq. 2.14]. Then the resistances in the network are linear and the relation is

$$p_i = r_i Q_i. \tag{9.2}$$

3. The model of the heat exchanger is linear and given by a transfer function $H(s)$. In an operating point, a simple linear model was used for instance in [110]. Also the model of the zone is assumed to be linear and given as $Z(s)$.
4. The model of the controller is linear and given by a transfer function $C(s)$.
5. All controllers, heat exchangers and zone models in the network are identical, that is, $C_i(s) = C(s), H_i(s) = H(s), Z_i(s) = Z(s)$ for all i.
6. There is a linear relation between the valve stroke x and the valve conductivity g, that is, $g_{\mathrm{v}_i} = h_i x_i$.

Thus, the only nonlinearity in the system is the mapping from strokes to flows. However, in order to test stability of the equilibrium, in the following section we will linearize also this nonlinear function.

In Sec. 9.1.6 we compare our simplified model with a fully nonlinear one to show that for analysis of stability, the simplified model gives a reasonable performance.

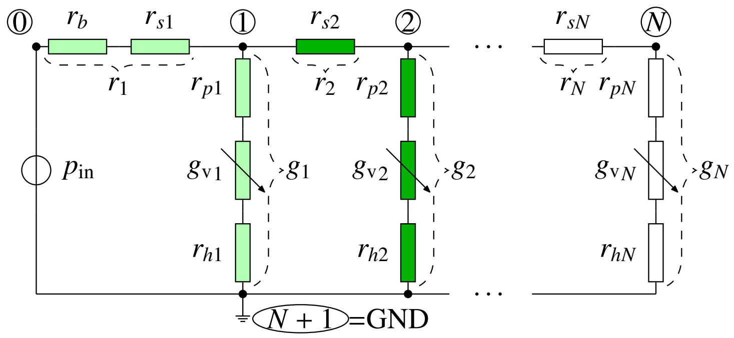

Figure 9.3.: A hydraulic circuit for modelling of the network. In light (dark) green is the first (resp. second) section of the ladder structure. 'GND' denotes the reference ("ground") node. In circles are number of nodes—places with different pressures.

9.1.3. Hydraulic network analysis

Let us calculate a function $f(\boldsymbol{x}, p_{\text{in}})$, relating the flows in the branches (through the conductances) to the conductivity of the valves. In order to do that, we will use results from the circuits theory [111]. Although the reference [111] describes electrical circuits, the same results can be applied in linear hydraulic networks. It is known from [111] that the external flow $\boldsymbol{Q}_{\text{ext}}$ applied to the network is tied to pressures in the network as

$$\boldsymbol{G}\bar{\boldsymbol{p}} = \boldsymbol{Q}_{\text{ext}}, \tag{9.3}$$

where $\boldsymbol{G} \in \mathbb{R}^{N+2\times N+2}$ is the conductance matrix and $\bar{\boldsymbol{p}}$ are pressures at the nodes of the circuit (each node in the circuit with different pressure is considered). $\boldsymbol{Q}_{\text{ext}}$ is a vector of the applied (external) flows. The elements of $\boldsymbol{Q}_{\text{ext}}$ are zeros if the corresponding node is not connected to the flow source, they are $+1$ (as flow $1\,\mathrm{kg/s}$) if the external flow enters the node and it is -1 if the flow leaves the node. In our setting the flow enters the node 0 and leaves the node $N+1$. The matrix $\boldsymbol{G}$ is a symmetric Laplacian (see [107] for some of its properties), hence it is a singular matrix. However, when the $(N+1)^{\text{th}}$ node (pressure at the return pipe in Fig. 9.3) is considered as a reference, then we might exclude this node from the conductivity matrix $\boldsymbol{G}$ and the reduced (grounded [112]) Laplacian $\tilde{\boldsymbol{G}}$ becomes non-singular. For instance, if the graph in Fig. 9.3 had two branches (light and dark green), the corresponding matrices would have a form

$$\boldsymbol{G} = \begin{bmatrix} \frac{1}{r_1} & -\frac{1}{r_1} & 0 & 0 \\ -\frac{1}{r_1} & g_1 + \frac{1}{r_1} + \frac{1}{r_2} & -\frac{1}{r_2} & -g_1 \\ -0 & -\frac{1}{r_2} & g_2 + \frac{1}{r_2} & -g_2 \\ 0 & -g_1 & -g_2 & g_1 + g_2 \end{bmatrix}, \bar{\boldsymbol{p}} = \begin{bmatrix} \bar{p}_0 \\ \bar{p}_1 \\ \bar{p}_2 \\ \bar{p}_3 \end{bmatrix}, \boldsymbol{Q} = \begin{bmatrix} 1 \\ 0 \\ 0 \\ -1 \end{bmatrix}. \tag{9.4}$$

Setting as reference the node $N+1$, the reduced matrices are

$$\tilde{\boldsymbol{G}} = \begin{bmatrix} \frac{1}{r_1} & -\frac{1}{r_1} & 0 \\ -\frac{1}{r_1} & g_1 + \frac{1}{r_1} + \frac{1}{r_2} & -\frac{1}{r_2} \\ -0 & -\frac{1}{r_2} & g_2 + \frac{1}{r_2} \end{bmatrix}, \tilde{\boldsymbol{p}} = \begin{bmatrix} \tilde{p}_0 \\ \tilde{p}_1 \\ \tilde{p}_2 \end{bmatrix}, \tilde{\boldsymbol{Q}}_{\text{ext}} = \begin{bmatrix} 1 \\ 0 \\ 0 \end{bmatrix}, \tag{9.5}$$

where $\tilde{\boldsymbol{p}}$ is the vector of pressure differences ($\tilde{p}_i = \bar{p}_i - \bar{p}_{N+1}$) when the input is the unit source of flow. Note also that the reduced connectivity matrix $\tilde{\boldsymbol{G}}$ can be written as

$$\tilde{\boldsymbol{G}} = \operatorname{diag}\left(\left[0, \boldsymbol{g}^T\right]\right) + \boldsymbol{L}, \tag{9.6}$$

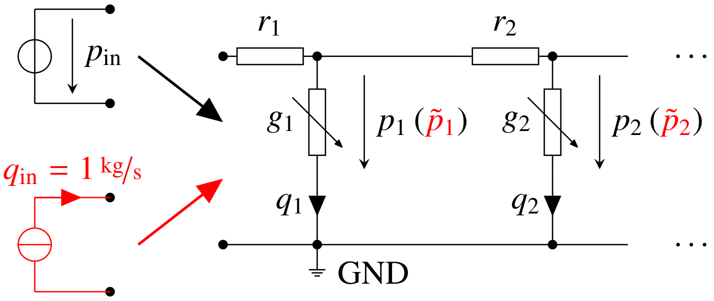

Figure 9.4.: Hydraulic network with either pressure source (black), or unit flow source (red). The corresponding pressure loss on ith branch is p_i for pressure source and $\tilde{p}_i$ for current source. We use the flow Q_i only for pressure source.

where the symmetric matrix $\boldsymbol{L}$ is a standard weighted Laplacian of an undirected path graph, given as

$$\boldsymbol{L} = \begin{bmatrix} \frac{1}{r_1} & -\frac{1}{r_1} & 0 & \dots & 0 \\ -\frac{1}{r_1} & \frac{1}{r_1} + \frac{1}{r_2} & -\frac{1}{r_2} & \dots & 0 \\ \vdots & \vdots & \vdots & \ddots & \vdots \\ 0 & \dots & 0 & -\frac{1}{r_N} & \frac{1}{r_N} \end{bmatrix} \tag{9.7}$$

and $\boldsymbol{g} = [g_1, g_2, \dots, g_N]$ is a vector of conductances.
Generally, since the reduced matrix has an inverse [111], we can calculate the pressures $\tilde{\boldsymbol{p}}$ as

$$\tilde{\boldsymbol{p}} = \tilde{\boldsymbol{G}}^{-1} \tilde{\boldsymbol{Q}}_{\text{ext}} \tag{9.8}$$

Unlike the flow source in the example, in the heating system we usually have a pressure source. Note that $\tilde{p}_0$ is the pressure difference which the flow source gives when the total flow is $Q_{\text{in}} = 1\ {}^{\text{kg}}/_{\text{s}}$, hence it is also the resistance of the circuit between nodes 0 and GND. The pressure p_i over the parallel conductance g_i, when the source is a pressure source, can therefore be calculated as

$$p_i = \frac{\tilde{p}_i(g)}{\tilde{p}_0(g)} p_{\text{in}}. \tag{9.9}$$

Introducing $\boldsymbol{p} = [p_1, p_2, \dots, p_N]^{\mathrm{T}}, \tilde{\boldsymbol{p}}_{\text{b}} = [\tilde{p}_1, \tilde{p}_2, \dots, \tilde{p}_N]^{\mathrm{T}}$, the flows through the branches can be calculated from pressures in a vector form as

$$\boldsymbol{Q} = \operatorname{diag}(\boldsymbol{g})\boldsymbol{p}(g) = \operatorname{diag}(\boldsymbol{g}) \frac{\tilde{\boldsymbol{p}}_{\text{b}}(g)}{\tilde{p}_0(g)} p_{\text{in}}. \tag{9.10}$$

The individual quantities and their role in the network are depicted in Fig. 9.4. Note that both $\tilde{p}(g)$ and $\boldsymbol{p}(g)$ are nonlinear functions of the resistances and conductances in the network. This follows from the matrix inverse $\tilde{\boldsymbol{G}}^{-1}$. The nonlinearity can be also easily seen from the law of parallel connection of resistances.

This allows us to calculate the flows in the individual branches, once all conductances are known. First the matrix $\tilde{\boldsymbol{G}}$ as in (9.5) is formed and then its inverse is calculated. Take the first column of the inverse to get pressures (9.8). Then normalize them by (9.9) and multiply by conductance as in (9.10) to get the flows through the heat exchangers. The individual quantities and their role in the network are depicted in Fig. 9.4.

9.1.4. Stability analysis

In this section we prove stability of an equilibrium of the hydronic system. Assume that a reference temperature $\theta_{\text{ref}\,i}$ is set for each zone. For the given reference temperatures $\boldsymbol{\theta}_{\text{ref}} = [\theta_{\text{ref}\,1}, \dots, \theta_{\text{ref}\,N}]^{\mathrm{T}}$, there is a *unique* equilibrium (denoted by superscript $(\cdot)^{\mathrm{e}}$). We are interested in stability of this equilibrium. The reference temperature in each zone, when in steady-state, corresponds to the unique flow Q_i^{e} through each heat exchanger and in turn to a unique branch conductivity g_i^{e} and valve stroke x_i^{e}.

As was mentioned earlier, the only nonlinearity assumed is the mapping $\boldsymbol{Q} = f(\boldsymbol{g}, p_{\mathrm{in}})$ (by assumption $g_i = h_i x_i$). We linearize this mapping in an equilibrium. Hence, around the equilibrium, we do a Taylor expansion of $\boldsymbol{Q} = f(\boldsymbol{g}, p_{\mathrm{in}})$ as

$$f(\boldsymbol{g}, p_{\mathrm{in}}) \approx f(\boldsymbol{g}^{\mathrm{e}}, p_{\mathrm{in}}) + \frac{\partial f(\boldsymbol{g}, p_{\mathrm{in}})}{\partial \boldsymbol{g}}\bigg|_{\boldsymbol{g}=\boldsymbol{g}^{\mathrm{e}}} (\boldsymbol{g}^{\mathrm{e}} - \boldsymbol{g}) + \dots . \tag{9.11}$$

Define $\Delta\boldsymbol{Q} = \boldsymbol{Q} - \boldsymbol{Q}^{\mathrm{e}} = f(\boldsymbol{g}, p_{\mathrm{in}}) - f(\boldsymbol{g}^{\mathrm{e}}, p_{\mathrm{in}})$, $\Delta\boldsymbol{Q} \in \mathbb{R}^N$ and $\Delta\boldsymbol{g} = \boldsymbol{g} - \boldsymbol{g}^{\mathrm{e}} \in \mathbb{R}^N$. Neglecting higher order terms, we can rewrite (9.11) as

$$\Delta\boldsymbol{Q} \approx \frac{\partial f(\boldsymbol{g}, p_{\mathrm{in}})}{\partial \boldsymbol{g}}\bigg|_{\boldsymbol{g}=\boldsymbol{g}^{\mathrm{e}}} \Delta\boldsymbol{g} = \boldsymbol{J}\Delta\boldsymbol{g} \tag{9.12}$$

where the *interconnection matrix* (or Jacobian) $\boldsymbol{J}$ is given as

$$\boldsymbol{J} = \frac{\partial f(\boldsymbol{g}, p_{\mathrm{in}})}{\partial \boldsymbol{g}}\bigg|_{\boldsymbol{g}=\boldsymbol{g}^{\mathrm{e}}} = \begin{bmatrix} \frac{\partial Q_1(g)}{\partial g_1} & \dots & \frac{\partial Q_1(g)}{\partial g_N} \\ \vdots & \ddots & \vdots \\ \frac{\partial Q_N(g)}{\partial g_1} & \dots & \frac{\partial Q_N(g)}{\partial g_N} \end{bmatrix}, \tag{9.13}$$

All partial derivatives in (9.13) are evaluated at the equilibrium. The $(k, j)^{\mathrm{th}}$ element in $\boldsymbol{J}$ can be calculated as follows from (9.10) as

$$\frac{\partial Q_k(g)}{\partial g_j} = \begin{cases} p_{\mathrm{in}} \left[\frac{\tilde{p}_k(g)}{\tilde{p}_0(g)} + g_k \frac{\frac{\partial \tilde{p}_k}{\partial g_j} \tilde{p}_0(g) - \tilde{p}_k \frac{\partial \tilde{p}_0}{\partial g_j}}{\tilde{p}_0^2(g)} \right] & \text{for } j = k, \\ p_{\mathrm{in}} \left[g_k \frac{\frac{\partial \tilde{p}_k}{\partial g_j} \tilde{p}_0(g) - \tilde{p}_k \frac{\partial \tilde{p}_0}{\partial g_j}}{\tilde{p}_0^2(g)} \right] & \text{for } j \neq k. \end{cases} \tag{9.14}$$

9.1.4.1. Properties of the interconnection matrix

The interconnection matrix can be calculated in a closed form using the following result, proved in Sec. B.

Theorem 3. *Let $\tilde{\boldsymbol{G}}_{22}$ be obtained be obtained from $\tilde{\boldsymbol{G}}$ by deleting the first row and the first column. Then the matrix $\boldsymbol{J}$ in* (9.13) *is*

$$\boldsymbol{J} = p_{\mathrm{in}} \left[\boldsymbol{I} - \mathit{diag}\,(\boldsymbol{g})\, \tilde{\boldsymbol{G}}_{22}^{-1}(g) \right] \mathit{diag} \left(\frac{\tilde{\boldsymbol{p}}_{\mathrm{b}}(g)}{\tilde{p}_0(g)} \right), \tag{9.15}$$

where $\tilde{\boldsymbol{G}}_{22}$ is

Note that the post-multiplication by $\mathrm{diag}\left(\frac{\tilde{\boldsymbol{p}}_{\mathrm{b}}(g)}{\tilde{p}_0(g)}\right)$ makes the matrix non-symmetric. The structure of $\boldsymbol{J}$ is such that there are positive signs on the diagonal and negative everywhere else.

We are also interested in the eigenvalues of $\boldsymbol{J}$.

Theorem 4. *The interconnection matrix $\boldsymbol{J}$ is diagonalizable and all the eigenvalues $\lambda_1 \leq \lambda_2 \leq \ldots \leq \lambda_N$ of $\boldsymbol{J}$ are real and positive. Further, the eigenvalues are bounded as $0 < \lambda_i < p_{\mathrm{in}}$.*

Although the $\boldsymbol{J}$ is not symmetric, it has real and positive eigenvalues. The proof is in Sec. B.

9.1.4.2. Stability

Consider the following SISO open loop $C(s)H(s)Z(s)$ and assume $\theta_{\mathrm{ref}} = {\theta_{\mathrm{ref}}}^{\mathrm{e}}$. The control loop around the operating point is shown in Fig. 9.5. The input to the open loop is the difference in flow ΔQ_i, the output is the difference in conductance Δg_i. There is also an external input δ_i, which is the disturbance in heat flow to the zone. The vector of outputs can be calculated from the vector of inputs using (9.12) as

$$\Delta\boldsymbol{g}(s) = -C(s)Z(s)H(s)\Delta\boldsymbol{Q}(s) + C(s)Z(s)\boldsymbol{\delta}(s), \tag{9.16}$$

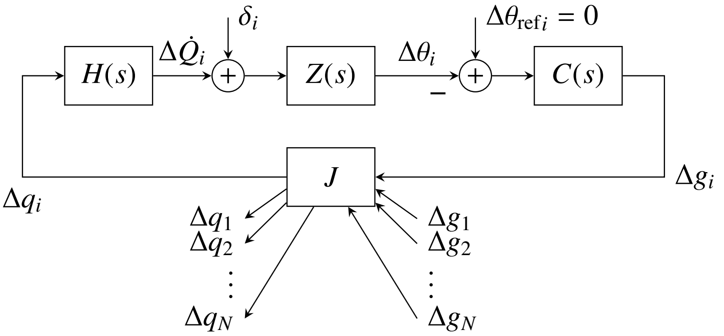

Figure 9.5.: Linearized system around the operating point. Identical, independently working controllers and zones are coupled through the interconnection matrix $\boldsymbol{J}$. $\Delta\dot{q}_i$ is the difference from the equilibrium of the heat flow delivered by the HX to the zone.

where $\boldsymbol{\delta} = [\delta_1, \ldots, \delta_N]^{\mathrm{T}}$. Plugging (9.12) to (9.16) and separating $\Delta\boldsymbol{g}$, we get

$$\Delta\boldsymbol{g}(s) = \left(\boldsymbol{I} + C(s)Z(s)H(s)\boldsymbol{J}\right)^{-1} C(s)Z(s)\ \boldsymbol{\delta} \tag{9.17}$$

So the system is stable if and only if the transfer function matrix $(\boldsymbol{I} + C(s)Z(s)H(s)\boldsymbol{J})$ has zeros in the left half-plane (provided that there is no pole-zero cancellation). Let us use the following state transform $\Delta\hat{\boldsymbol{g}} = \boldsymbol{V}^{-1}\Delta\boldsymbol{g}, \hat{\boldsymbol{\delta}} = \boldsymbol{V}^{-1}\boldsymbol{\delta}$, where $\boldsymbol{V}$ is the matrix of eigenvectors of $\boldsymbol{J}$. By Theorem 4, $\boldsymbol{J}$ is diagonalizable and $\boldsymbol{\Lambda} = \boldsymbol{V}^{-1}\boldsymbol{J}\boldsymbol{V}$ is diagonal matrix. This transformation was used, for instance, in [113] or [106]. Then the system gets a form

$$\Delta\hat{\boldsymbol{Q}} = \left(\boldsymbol{I} + C(s)Z(s)H(s)\boldsymbol{\Lambda}\right)^{-1} C(s)Z(s)\ \hat{\boldsymbol{\delta}}. \tag{9.18}$$

Since $\boldsymbol{\Lambda}$ is a diagonal matrix, (9.18) is a block diagonal system, which implies the following result.

Theorem 5. *The equilibrium of the hydronic system is stable if and only if all the following closed-loop systems are stable*

$$T_i(s) = \frac{C(s)Z(s)}{1 + \lambda_i C(s)Z(s)H(s)}, \quad \forall i. \tag{9.19}$$

All such systems $T_i(s)$ are SISO transfer function, analysis of which is quite easy. Hence, analysis of stability of overall network system with N units (9.17) was converted into analysis of N *single*-branch closed loops (9.19) with varying, but bounded gains.

9.1.5. Implications for controller design

In this section give some guidelines on how to design controllers which do not destabilize the hydronic system. A sufficient condition for stability of an equilibrium is the following.

Corollary 3. *If the closed loop* $\frac{C(s)Z(s)}{1+kC(s)Z(s)H(s)}$ *is stable for any* $k \in (0, p_{\mathrm{in}}]$*, then every equilibrium of the hydronic network is stable, regardless of the number of branches N.*

This easily follows from Theorem 5, since by Theorem 4 the eigenvalues $0 \leq \lambda_i \leq p_{\mathrm{in}}$. Note also that the poles of the closed loops (9.19) are identical as the poles obtained from a root-locus of the open loop $\lambda C(s)Z(s)H(s)$, where λ is gain for the open loop $C(s)Z(s)H(s)$. Hence, a root locus can be used for analysis.

It follows from Corollary 3 that stability depends on the value of the pressure source. We can eliminate the dependence on the pressure value by the next result.

Corollary 4. *If the open loop* $C(s)Z(s)H(s)$ *has infinite gain margin, then every equilibrium of the hydronic network is stable.*

So the requirements on the controller are

- Try to achieve infinite gain margin for the plant given as $H(s)Z(s)$.

- If it is not possible, guarantee stability of single-zone closed loop (9.19) for any gain λ in $[0,p_{\text{in}}]$.

Tuhs, it is the range λ for a single-zone closed loop in Theorem 5, which is the main factor in determining stability. If neither of the conditions above is satisfied, the controller might destabilize the network of multiple zones. This can happen even though one zone is stable. Another interesting fact is that if the system does not achieve infinite gain margin, the network can be destabilized just by changing (increasing/decreasing) the source pressure. For instance, suppose that the closed loop is not stable below some small gain $\lambda_{\text{crit}} > 0$. Then by decreasing the pump pressure (e.g. by a pump failure) below λ_{crit}, the system does not satisfy the condition of Theorem 5 and is unstable.

Remark 8. Using [114], results of Theorem 5 can be applied also to systems with time delay. The time delay might occur in the model of the heat exchanger or due to some estimation or measurement algorithm.

Remark 9. In real situations, different zones might have different heat exchangers. In such a case the restriction that all zone models are the same might be too restrictive. In this case a robust stability analysis, as shown in [108], might be used.

9.1.5.1. Comparison with one zone

Let us compare the conditions in Corollaries 3 and 4 with conditions for a system with one zone only. Currently, the controllers are usually designed only for such a single zone. In a network with a single zone, the change in the flow through the valve is given as $\Delta Q \approx p\Delta g$, considering only small changes in g. g is varied based on the controller, so the "gain" of the valve is $k = p$ – the pressure loss over this valve. If the valve is only slightly open (g very small) and the supply and return pipe have comparably low resistance, then the pressure loss over the valve is almost equal to the pump pressure. Hence, the "gain" $p \approx p_{\text{in}}$ and the controller, of course, has to guarantee stability for this case. If, on the other hand, the valve is almost fully open and the supply pipe has a high resistance, the pressure loss over the valve is small. Then, also the gain of the valve is small $k = p_{\text{in}}$. Again, the controller has to guarantee stability the closed loop for this gain. In summary, because the pressure loss over the valve can vary from almost 0 to p_{in}, the controller has to guarantee stability of the following system

$$\frac{p_{\text{in}}C(s)H(s)Z(s)}{1 + kC(s)H(s)Z(s)} \tag{9.20}$$

for $k \in [0,p_{\text{in}}]$. This is exactly the same condition as in Corollary 3. Hence, every equilibrium in the network is stable if the single-zone network is stable for any valve stroke. Nevertheless, the transients in a more complicated network can be worse than in the single-zone control.

9.1.6. Comparison with nonlinear model

For the testing we use a three-zone model, which can be downloaded at `www.matlabcentral.com`. Each zone consists of a heat exchanger (radiator), a valve and a room, which is not connected to any other room. All radiators are supplied from the same pump and the same boiler. In this section we show that the linearized system gives a good estimate of the system behavior near the operating point, hence also the stability analysis is justified.

9.1.6.1. Nonlinear model

The models of the radiator and the zone are taken from [110]. For convenience we repeat the model here. The radiator is modelled as a spatially discretized nonlinear PDE. The discretization has N_{rad} sections, where the temperature η_i in each section evolves as

$$\dot{\eta}_j = \frac{N_{\text{rad}}c_{\text{w}}}{C_{\text{r}}} Q_i(\eta_{j-1} - \eta_i) - \frac{K_{\text{r}}}{C_{\text{r}}}(\eta_j - \theta), \quad j = 1,2,\ldots,N_{\text{rad}} \tag{9.21}$$

where the parameters are given in Tab. 9.1, θ [°C] is temperature in the room and Q_i [kg/s] is the water mass inflow to the radiator in the i^{th} zone. The temperature in the zero$^{\text{th}}$ section η_0 is the inflow water temperature η_{w} [°C]. The heat

Label		Value
N_{rad}	Number of sections in radiator	45
c_{w}	Specific heat capacitance of water	$4186\,\mathrm{J/kg{\cdot}K}$
C_{r}	Thermal capacitance of water and radiator	$3.1 \times 10^4\,\mathrm{J/K}$
K_{r}	Radiator equivalent heat transfer coefficient	$33.65\,\mathrm{W/K}$
U_{e}	Thermal transmittance of the room envelope	$1.2\,\mathrm{W/m^2{\cdot}K}$
A_{e}	Area of the room envelope	$50\,\mathrm{m}^2$
C_{a}	Thermal capacitance of the room air	$7.2 \times 10^4\,\mathrm{J/K}$
C_{e}	Thermal capacitance of the room envelope	$4.0 \times 10^4\,\mathrm{J/K}$
θ_{amb}	Outdoor temperature	$-10\,^\circ\mathrm{C}$
r_{b}	Resistance of the boiler	$1.29 \times 10^7\,\mathrm{Pa/(kg{\cdot}s)^2}$
r_{s}	Resistance of the serial pipes	$4.24 \times 10^6\,\mathrm{Pa/(kg{\cdot}s)^2}$
r_{p}	Resistance of the parallel pipes	$4.67 \times 10^5\,\mathrm{Pa/(kg{\cdot}s)^2}$
p_{in}	Pressure of the pump	$1 \times 10^5\,\mathrm{Pa}$
ξ	Valve parameter	$1.25 \times 10^{-2}\,\mathrm{kg/s{\cdot}Pa^{-0.5}}$

Table 9.1.: Parameters of the radiator, room and hydraulic network. The parameters of radiator and room are taken from [110] and [116].

delivered by the radiator to the i^{th} room is

$$\dot{q}_i = \frac{1}{N_{\mathrm{rad}}} \sum_{j=1}^{N_{\mathrm{rad}}} K_{\mathrm{r}}(\eta_j - \theta). \tag{9.22}$$

The i^{th} room is modelled as a two-state system as follows

$$\begin{aligned} \dot{\theta}_i &= \frac{U_{\mathrm{e}}A_{\mathrm{e}}}{C_{\mathrm{a}}}(\theta_{\mathrm{e}i} - \theta_i) + \dot{q}_i \\ \dot{\theta_{\mathrm{e}i}} &= -\frac{U_{\mathrm{e}}A_{\mathrm{e}}}{C_{\mathrm{e}}}(\theta_{\mathrm{e}i} - \theta_i) + \frac{U_{\mathrm{e}}A_{\mathrm{e}}}{C_{\mathrm{e}}}(\theta_{\mathrm{amb}} - \theta_{\mathrm{e}i}) \end{aligned} \tag{9.23}$$

where $\theta_{\mathrm{e}i}$ is temperature of the room envelope, θ_{amb} is the outdoor temperature. Other parameters are in Tab. 9.1.
For the simulation with nonlinear hydraulic resistances $\bar{r}$ and conductances $\bar{g}$, we used quadratic laws [109, eq. 2.15]

$$p = \bar{r}Q^2 \Leftrightarrow Q = \bar{g}\sqrt{p} \tag{9.24}$$

with $\bar{r} = \frac{1}{\bar{g}^2}$ and $\bar{g} = \sqrt{\frac{1}{\bar{r}}}$. Then the law for parallel connection of two conductances $\bar{g}_1$ and $\bar{g}_2$ becomes $\bar{g}_{\mathrm{par}} = \bar{g}_1 + \bar{g}_2$. Similarly, for a series connection of two resistances $\bar{r}_1$ and $\bar{r}_2$ we have $\bar{r}_{\mathrm{ser}} = \bar{r}_1 + \bar{r}_2$. These laws allowed to us to calculate the flows in the branches in the network. The values of the quadratic resistances are in Tab. 9.1.
The valve conductance is given by the following law

$$\bar{g}_{\mathrm{v}} = 0.1 Q_{\max}\xi\,(\xi^{x/x_{\max}} - 1), \tag{9.25}$$

where ξ is a parameter of the valve [115]. This law describes an equal-percentage valve.

9.1.6.2. Linearized system

The nonlinear network describeb above is linearized in an equilibrium point, corresponding to the given temperatures θ_{ref}. The parameters at operating point are given in Tab. 9.2.
The radiator model (9.21) is linearized in the equilibrium to the standard state-space description with states

	Zone 1	Zone 2	Zone 3
θ_{ref} [°C]	23	23	23
Q^{e} [kg/s]	$1.08{\cdot}10^{-2}$	$1.08{\cdot}10^{-2}$	$1.08{\cdot}10^{-2}$
x^{e} [0 – 1]	0.258	0.258	0.258
h^{e} [kg/s·Pa$^{0.5}$]	$8.50{\cdot}10^{-7}$	$8.51{\cdot}10^{-7}$	$8.52{\cdot}10^{-7}$

Table 9.2.: Parameters at the operating point.

$\Delta\boldsymbol{\eta} = \eta - \eta^e$, $\boldsymbol{\eta} = [\eta_1, \ldots, \eta_{N_{\mathrm{rad}}}]^{\mathrm{T}}$ and inputs $\Delta\boldsymbol{u} = \boldsymbol{u} - \boldsymbol{u}^{\mathrm{e}}$ with $\boldsymbol{u} = [Q, \theta, \eta_{\mathrm{w}}]$. The model is $\Delta\dot{\boldsymbol{\eta}} = \boldsymbol{A}\Delta\boldsymbol{\eta} + \boldsymbol{B}\Delta\boldsymbol{u}$, $\Delta\dot{\boldsymbol{q}} = \boldsymbol{C}\Delta\boldsymbol{\eta} + \boldsymbol{D}\Delta\boldsymbol{u}$ with matrices

$$\begin{aligned} \boldsymbol{A} &= \frac{N_{\mathrm{rad}} c_{\mathrm{w}}}{C_{\mathrm{r}}} Q_{\mathrm{e}} \boldsymbol{M} - \frac{K_{\mathrm{r}}}{Cr} \boldsymbol{I}, \quad \boldsymbol{B} = [\boldsymbol{B}_{\mathrm{Q}}, \boldsymbol{B}_{\theta}, \boldsymbol{B}_{\eta_{\mathrm{w}}}] \\ \boldsymbol{C} &= \frac{K_{\mathrm{r}}}{N_{\mathrm{rad}}} [1, 1, \ldots, 1]^{\mathrm{T}}, \boldsymbol{D} = 0 \end{aligned} \tag{9.26}$$

with $\boldsymbol{B}_{\mathrm{Q}} = (N_{\mathrm{rad}} c_{\mathrm{w}})/C_{\mathrm{r}}\, \boldsymbol{M} \eta^{\mathrm{e}} + \eta_{\mathrm{w}}{}^{\mathrm{e}}\, (N_{\mathrm{rad}} c_{\mathrm{w}})/C_{\mathrm{r}} \cdot [1,0,\ldots,0]^{\mathrm{T}}$, $\boldsymbol{B}_{\theta} = Kr/Cr \cdot [1,\ldots,1]^{\mathrm{T}}$, $\boldsymbol{B}_{\eta_{\mathrm{w}}} = Q^{\mathrm{e}}(N_{\mathrm{rad}} c_{\mathrm{w}})/C_{\mathrm{r}} \cdot [1,0,\ldots,0]^{\mathrm{T}}$ and $\boldsymbol{M} \in \mathbb{R}^{N_{\mathrm{rad}} \times N_{\mathrm{rad}}}$ is a bidiagonal matrix with -1 on the diagonal and 1 on the first subdiagonal.

To use our linearization of the hydronic network, we need linear resistances. The following is used to get the linear resistance r from the quadratic $\bar{r}$:

$$r_i = \bar{r}_i Q_i^{\mathrm{e}}, g_i = \frac{1}{r_i} \tag{9.27}$$

That is, the linear resistance has such value which produces the same flow as the nonlinear one.

The valve is approximated by a simple gain. The value of the gain is obtained numerically as

$$h_i \approx \frac{g_{\mathrm{v}}(x_i^{\mathrm{e}}) - g_{\mathrm{v}}(x_i^{\mathrm{e}} + \delta x)}{\delta x} \tag{9.28}$$

$g_{\mathrm{v}}(x_i^{\mathrm{e}})$ is obtained using (9.25) and (9.27). Having the linear resistances, we can use Theorem 3 to calculate $\boldsymbol{J}$. The parameters at operating point are given in Tab. 9.2.

9.1.6.3. Simulations

We designed a PI controller, identical for all zones. It is given in a transfer function form as

$$C_1(s) = \frac{0.145s + 7 \cdot 10^{-5}}{s}. \tag{9.29}$$

This controller satisfies the infinite gain margin for the open loop consisting of the linearized radiator in (9.26), and gain (9.28). Therefore, it stabilizes the system for any number of radiators, every pump pressure and in every equilibrium.

In Fig. 9.6 we show a comparison of the nonlinear and linearized model. There was a step change with value 0.01 °C in the desired temperature of zone 2 at time 500 s. It can be seen that the linearized temperatures match the nonlinear ones. Hence, the linear analysis allow reasonable conclusion about stability of the equilibrium of the nonlinear system.

In Fig. 9.7 a step of 1 °C is shown. It can be seen that the linearized temperatures match the nonlinear ones quite well; hence the linear analysis allows a reasonable conclusion about stability of the equilibrium of the nonlinear system.

We designed also another controller

$$C_2(s) = \frac{1.139s + 0.004}{s}. \tag{9.30}$$

This is a very bad controller, nevertheless, it allows us to show that although the equilibrium of the network with only one branch is stable, the network with three branches is not. Location of eigenvalues of the close loop near imaginary axis is shown in Fig. 9.8. It is clear that one eigenvalue of the network with three branches is in the right-half plane,

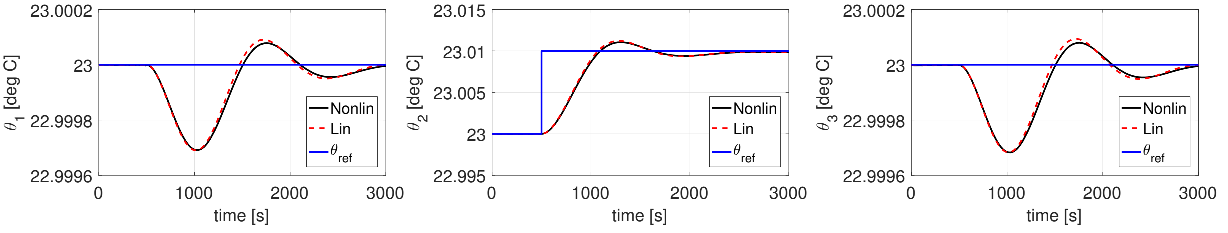

(a) Zone 1 (b) Zone 2 (c) Zone 3

Figure 9.6.: Temperatures in all zones for a step in reference from $\theta_{\text{ref}2} = 23.0\,°\text{C}$ to $\theta_{\text{ref}2} = 23.01\,°\text{C}$.

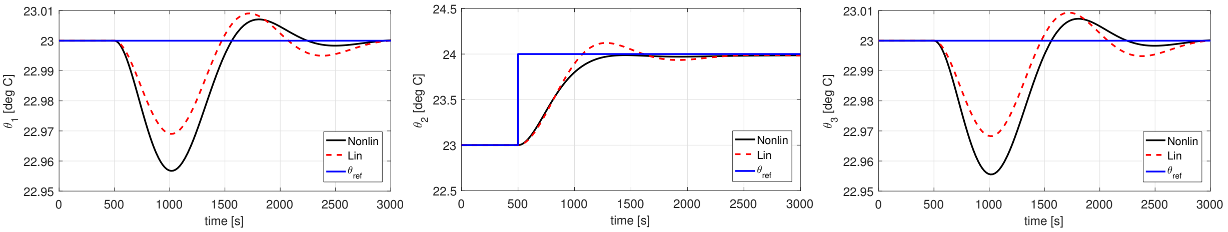

(a) Zone 1 (b) Zone 2 (c) Zone 3

Figure 9.7.: Temperatures in all zones for a step in reference from $\theta_{\text{ref}2} = 23\,°\text{C}$ to $\theta_{\text{ref}2} = 24\,°\text{C}$.

i.e. the network is unstable.

9.1.7. Summary

In this chaper we investigated the stability of two-pipe heating system, where all zones control their temperatures independently, but they share a common pressure source. We derived a matrix form of a linearization of the interconnecting network in a closed form. Then, we proved that this matrix has real and positive eigenvalues which are less than the pressure of the pump.

This allowed us to state simple stability criterion – the single-zone system has to be stable for any gain between 0 and p_{in}. This is a condition which also a controller designed only for a single zone has to satisfy. Thus, the interconnection does not bring any new design requirement. In addition, infinite gain margin guarantees stability of any network interconnection and for any pressure of the pump.

9.2. Two-pipe system analysis[1]

Throttling two-pipe hydronic system needs a central pump to provide pressure for the entire network. The pump can either have a fixed speed or the speed is controlled. Fixed speed pump has one fixed head-flow (HQ) characteristic, and it is designed to provide maximal (nominal) flow for all heat exchangers. When the flow demand is lower, the excess head must be discharged by throttling at control valves, which results in pumping energy waste and decreased controllability. Variable speed pump, on the other hand, has a variable HQ curve, and therefore, the head output can be varied.

Claim 1. The most efficient speed control method of a central pump in a throttling system is to always have one control valve (the most hydraulically disadvantaged) just fully opened.

Instead of using a central pump, local heat exchanger pumps instead of control valves may be employed to provide

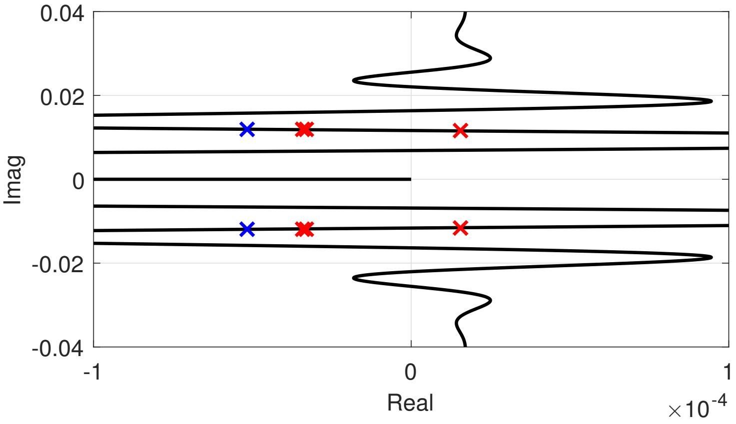

Figure 9.8.: Location of eigenvalues of the linearized system with only one branch (blue) and three branches (red). The black curve is the root-locus curve of the open loop - the radiator, room and the controller $C_2(s)$.

the pumping power [82]. The heat exchanger pumps replace the central pump, and the throttling valves HQ and PQ characteristics (hence also efficiency) of the local pump play a major role in the resulting efficiency of the decentralized system. Pump efficiency is the ratio between the generated hydraulic power and the electrical power consumed. Hydraulic power downscales with speed by a third power according to affinity laws (Sec. 3.1). However, electrical consumption downscales for real pumps in a lower rate due to the presence of losses. For example, a local HX pump model used in this n has pump characteristics as shown in Fig. 9.9. Peak pump efficiency depends on pump size and technology. According to [117], small circulation glandless pumps up to 100W, which is the case of heat exchanger pumps, range in total efficiency between 5-25%.

Claim 2. Decentralized pumping systems have lower hydraulic losses than centralized pumping systems with throttling.

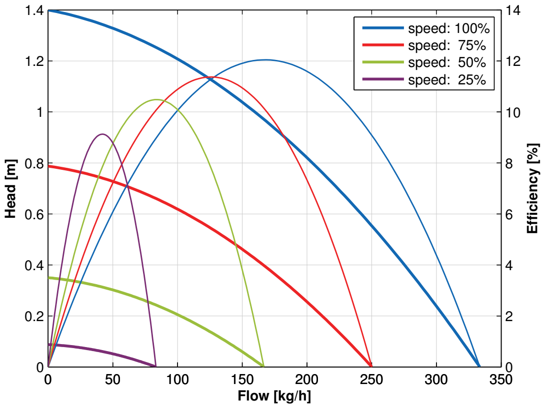

Figure 9.9.: Local HX pump head-flow (HQ) and efficiency characteristics (based on Wilo Geniax small HX pump [81]).

Combined flow through all heat exchangers implies a net flow through transportation piping. Hydraulic friction in the piping altogether with the heat exchangers and heat sources creates a hydraulic power loss, which in turn is the minimal hydraulic power pressure sources (pumps) have to deliver. Throttling valves, either control or balancing, inserted into the circuit pose additional hydraulic power losses to be covered by a pumping system. Decentralized pumping system lacks throttling valves, and therefore it only needs to generate the baseline hydraulic power.

From another point of view, a pump in the decentralized pumping hydronic systems covers only a flow range of the heat exchanger; which means it can be very small. A flow through a central pump in the centralized pumping system is the sum of all heat exchanger flows, i.e. it is much bigger in size than the heat exchanger pump. As the peak value of the pump efficiency generally increases with pump size [117], a central pump will have better efficiency than a heat exchanger pump.

Claim 3. A central pump will generally have better electric-to-hydraulic energy efficiency compared to a local heat exchanger pump.

The statements in Claim 2 , and Claim 3 give contradictory predictions in terms of power consumption, and it is therefore not straightforward which pumping strategy has a lower electric energy consumption. A necessary and sufficient condition for a decentralized pumping system to consume less electric power than centralized system is stated by Theorem 6.

Theorem 6. *A decentralized pumping hydronic system electric power consumption $P_{e,D}$ is lower than a centralized pumping system electric power consumption $P_{e,C}$ operating on the same hydronic network*

$$P_{e,C} > P_{e,D},$$

when

$$\eta_D > \frac{P_{h,\ piping}}{P_{h,\ piping} + P_{h,\ valves}} \eta_C,$$

where η_D is an overall efficiency of the decentralized system, η_C overall efficiency of the centralized system, $P_{\mathrm{h,\ pipes}}$ is an aggregate hydraulic power loss in transportation piping and $P_{\mathrm{h,\ valves}}$ is an aggregate hydraulic power loss across valves in the central pumping system that are not present in the decentralized system.

Proof. The efficiency of a pumping system is defined as the ratio of hydraulic power generated to the electric power consumed by pumps

$$\eta = \frac{P_\mathrm{h}}{P_\mathrm{e}}.$$

The hydraulic power produced by pumps is always entirely consumed by the hydraulic network

$$P_{\mathrm{h,\ pumps}} = P_{\mathrm{h,\ network}}.$$

The hydraulic power is a product of pressure Δp ($\Delta p = \rho g H$) and flow Q

$$P_\mathrm{h} = \Delta p Q = \frac{1}{\rho g} H Q.$$

The hydraulic power loss in a network is a sum of all power losses

$$P_{\mathrm{h,\ network}} = \sum_{c \in \mathcal{M}} P_\mathrm{h}(c), \quad \mathcal{M} = \{\text{all hydraulic resistances}\}.$$

The flows in the centralized and decentralized setting are the same, and therefore, the head losses are also the same, and thus the hydraulic power losses also the same

$$\begin{gathered} Q_\mathrm{C}(c) = Q_\mathrm{D}(c) \\ H_\mathrm{C}(c) = H_\mathrm{D}(c) \\ \Rightarrow \\ P_\mathrm{h,C}(c) = P_\mathrm{h,D}(c) \equiv P_\mathrm{h}(c), \forall c \in \mathcal{M}. \end{gathered}$$

The difference is, however, in the set $\mathcal{M}$ of all hydraulic resistances. In the centralized pumping scenario, the set contains the passive network and the valves

$$\mathcal{M}_\mathrm{C} = \{\text{piping, valves}\},$$

whereas the decentralized setting the set lacks the valves

$$\mathcal{M}_\mathrm{D} = \{\text{piping}\}.$$

The electric power consumed in the decentralized pumping system

$$P_{\mathrm{e,D}} = \frac{\sum_{c \in \mathcal{M}_{\mathrm{D}}} P_{\mathrm{h}}(c)}{\eta_{\mathrm{D}}} \equiv \frac{P_{\mathrm{h,\,piping}}}{\eta_{\mathrm{D}}}$$

will be lower than consumption of centralized pumping system

$$P_{\mathrm{e,C}} = \frac{\sum_{c \in \mathcal{M}_{\mathrm{C}}} P_{\mathrm{h}}(c)}{\eta_{\mathrm{C}}} \equiv \frac{P_{\mathrm{h,\,piping}} + P_{\mathrm{h,\,valves}}}{\eta_{\mathrm{C}}},$$

when

$$\begin{aligned} P_{\mathrm{e,C}} &> P_{\mathrm{e,D}} \\ \frac{P_{\mathrm{h,\,piping}} + P_{\mathrm{h,\,valves}}}{\eta_{\mathrm{C}}} &> \frac{P_{\mathrm{h,\,piping}}}{\eta_{\mathrm{D}}} \\ \eta_{\mathrm{D}} &> \frac{P_{\mathrm{h,\,piping}}}{P_{\mathrm{h,\,piping}} + P_{\mathrm{h,\,valves}}} \eta_{\mathrm{C}}. \end{aligned}$$

□

The Theorem 6 states that the total efficiency of the decentralized system, which is solely influenced by the efficiencies of the local HX pumps at their design operating points maybe a fraction of centralized pumping efficiency to still consume less electric energy. See the following case study for more details.

9.2.1. Case study: A bungalow

A residential hydronic network in a fictional bungalow has one boiler/chiller and main supply/return piping from which individual heat exchangers branch out one after another throughout the house. A schematic diagram of such a network with the centralized pumping system is depicted in Fig. 9.10a, with decentralized pumping in Fig. 9.10b. When translated into a graph by identifying the basic hydronic elements (Fig. 8.3), the result is a path graph depicted in Fig. 9.10c. An adjacency matrix of the graph contains ones on the first super-diagonal

$$\mathbf{A} = \begin{bmatrix} 0 & 1 & 0 & \cdots & 0 \\ 0 & 0 & 1 & \ddots & \vdots \\ \vdots & & \ddots & \ddots & 0 \\ & & & 0 & 1 \\ 0 & & \cdots & 0 & 0 \end{bmatrix}.$$

There are ten nodes in the network, and each has a 10 m-long serial pipe of diameter 25 mm (sum of supply and return pipe) and a 5 m-long parallel pipe of diameter 15 mm. Boiler in the first node is modeled as a 2 m-long pipe of diameter 20 mm and the head loss over heat exchangers is modeled as $H\,[\mathrm{m}] = 1.18 \cdot 10^8 \left(Q\,[\mathrm{m^3/s}]\right)^2$ [118, 119]. The nominal flow demand at each heat exchanger is set to 100 $\mathrm{kg/h}$ and the control valves have $K_{\mathrm{vs}} = 1.6$, authority 28%. The central pump characteristics are based on a Wilo BS 8 pump. The local HX pumps are based on the Wilo Geniax pumps [81], where the zero-flow head is tweaked to get different peak efficiencies.

Five different pumping scenarios are analyzed:

1. Fixed speed centralized pumping - pump peak efficiency 10.2%,
2. Minimized speed centralized pumping - pump peak efficiency 10.2%, speed is optimized for one of the valves to be always fully opened.
3. Decentralized pumping - local HX pumps peak efficiency 12%,
4. Decentralized pumping - local HX pumps peak efficiency 10%,
5. Decentralized pumping - local HX pumps peak efficiency 8%.

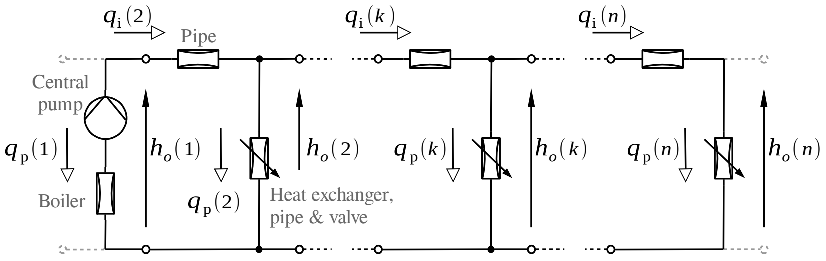

(a) Hydronic network with centralized pumping.

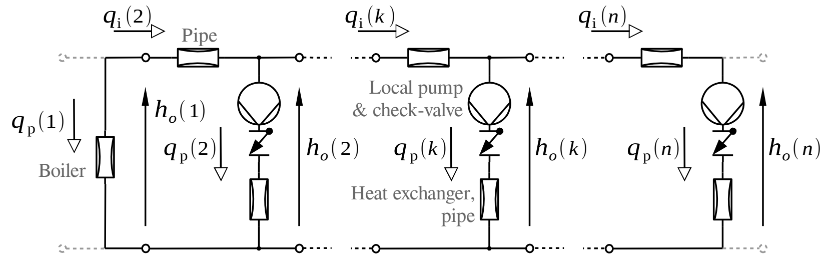

(b) Hydronic network with decentralized pumping.

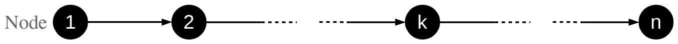

(c) Hydronic network interconnection graph.

Figure 9.10.: Case study: bungalow.

Electric power consumption of the five scenarios for unified flow demands ranging from 30-100% of the nominal is plotted in Fig. 9.11. Overall system efficiencies are depicted in Fig. 9.12. The case of a central pump with constant speed has, as probably foreseen, poor overall efficiency at low flow demands because the electrical power consumption remains almost constant throughout the setpoint range. The decentralized scenario ‘10%’ has, despite having similar maximal efficiency as the central pump, worse overall efficiency in the entire flow range when compared to the variable speed central pump scenario. The electrical consumptions of the two scenarios are, however, similar. This is a demonstration of the fact defined by Theorem 6.

The valve strokes and pump speeds for a unified 50% flow demand is depicted in Fig. 9.13. It can be observed that in the fixed-speed centralized scenario, all the control valves are throttling the flow, while in the speed-optimized scenario the pump speed is reduced to maintain the control valve in the node 11 fully opened (node 11 is the most hydraulically disadvantaged in this case).

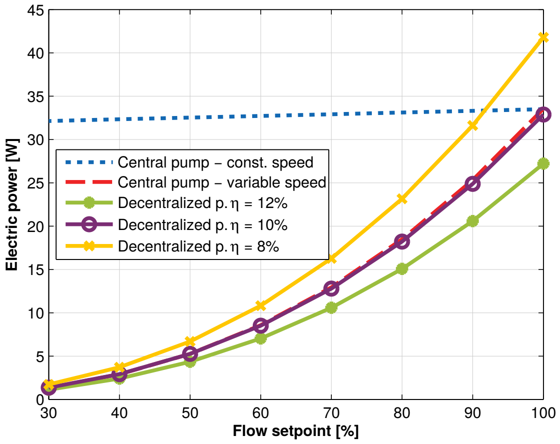

Figure 9.11.: Electric power consumption (pumping vs. ideal throttling 2-pipe network).

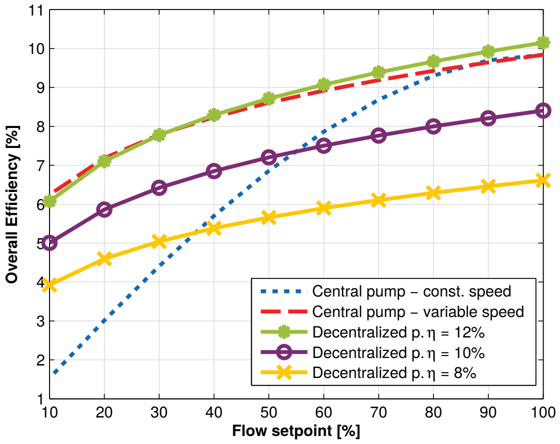

Figure 9.12.: Efficiency (pumping vs. ideal throttling 2-pipe network).

9.3. Pumping one-pipe system analysis

Pumping one-pipe systems, also referred to as "primary-secondary pumping" [120], are mostly used to connect heat sources but can also be utilised on the load side. The pumping one-pipe network is a demand-driven hydronic network with its associated energy saving benefits [88, 89]. The working principle is as follows: from the main pipe in the circuit branch out two closely-spaced T-fitting, where a secondary "small" pump with a heat source/terminal is looped around. The heat sources/terminals are connected in series on the main (primary) piping, that loops back to the main circulator and a heat load/source side, respectively. See Fig. 9.14 for a schematic depiction.

The system has several advantages [121–124]:

- generally, only two pipe sizes (primary, secondary),
- considerably fewer fittings (time and material savings),
- design simplicity (one secondary pump serves a wide range of load capacities),
- smaller primary pump (no valve and load resistance),
- lower pumping energy (no energy waste in throttling),
- no balancing (secondary circuits are hydraulically independent),
- lower heat losses (less piping surface, less liquid).

Single-pipe systems have up to 40% less pipes [125]. Simpler design saves 10-20% of mechanical contracts [124].

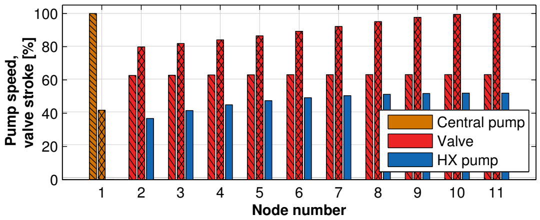

Figure 9.13.: Actuator openings at 50% flow demand. The single-hatched (\\) bars belong to the fixed-speed central pump system. The cross-hatched (xx) bars belong to the optimized variable speed central pump system and the solid(□) bars represent a decentralized pumping system (η = 10%).

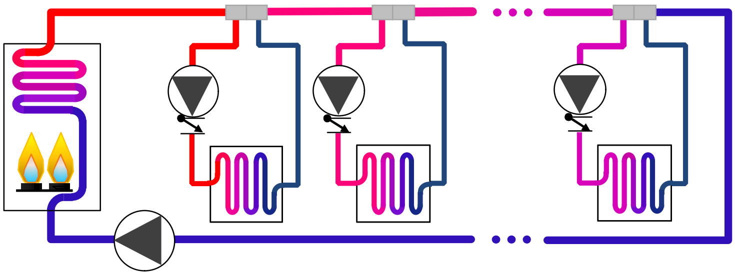

Figure 9.14.: Pumping one-pipe network: primary circuit with a heat source, secondary circuits with heat loads.

Piping installation cost is \$5.38 to \$16.15/m^2 lower compared to a conventional two-pipe system [122]. In one example, a relatively small building block consisting of 14 classrooms served by chilled beams operated by a pumping one-pipe hydronic network saved approximately \$3/ft^2 from a mechanical equipment budget [126]. In another study for supplying chilled beam heat terminals with cooling and heating, the installation cost of a traditional 4-pipe system is more than six times more expensive than a dual one-pipe system [126]. Pumping energy accounts for 20-30% of the total chilled water plant energy [85], in GCHP systems, fluid circulation represents significant energy consumption [122]. Pumping energy consumption is reported to be 4-53% lower [127] with the pumping one-pipe topology.

Variable speed pump injection mixing has been steadily increasing in North America in recent years, a 4-way mixing, however, remains the benchmark mixing method in the European market [128].

Throttling (valve) hydronic networks may be viewed as an equivalent of automatic transmission behaviour in a stationary car. The car always wants to drive forward, and the only way to stop it is to step on a brake, thus wasting energy. On the other hand, pumping hydronic systems are equivalent to a manual transmission in this analogy. One only shifts a gear in when forward motion is required. Thus no energy is wasted when standing still.

Among the disadvantages appear:

- bad reputation due to issues with old throttling one-pipe systems,
- temperature interactions between loads,
- generally lower temperature difference on a heat source.

Heat source temperature difference can maintained at its design value by a temperature-controlled primary circulation pump. The heat source return temperature is below but close to the last secondary branch design supply temperature. There are several ways to tackle temperature interactions between loads, which are described in depth in the next section.

9.3.1. Temperature interaction resolution methods

The inlet temperature decrease is the main concern, when it comes to 1-pipe hydronic systems. The first question that comes to mind is: “How can the heat terminals down the line deliver design power when their inlet temperature drops?”. To answer this question, we will first revise how heating systems are designed, what factors come into play, and how can the pumping 1-pipe system adapt to deliver the design load.

The most likely scenario for a 1-pipe system is in heating system refurbishments, as only about 10% of the building sector comprises new buildings or major renovations [129]. In the case of hydronic heating refurbishment, the heat loads (FCUs, convectors, etc.) are likely to already be installed in place and almost certainly designed for a 2-pipe throttling system. The following methods may address the temperature interaction, mainly the inlet temperature drop, between the units in 1-pipe systems.

9.3.1.1. Oversized heat terminals (retrofitting)

In retrofitting, the chances are the rule-of-thumb of floor area was used for heating capacity calculation. Such values are, for example, provided in [130]. To be robust, the rule-of-thumb should never fail, therefore, it provides coverage for worst case scenarios rather than average, and thus leads to oversizing for the majority of applications. This line of reasoning confirms the president of ASHRAE by saying: "Oversizing is common in commercial as well as residential applications because contractors use the rule-of-thumb sizing – a load calculation based on square footage" [131]. More than 50% of practitioners used to size HVAC by the rule-of-thumb methods in 1996 [132], but with the availability of computer aided calculations and BIM this percentage is expected to be diminishing for newer installations.

After defining design capacities, a safety factor of 10% is used by commercial designers [130, 133], and this is also the maximal safety factor value recommended by ASHRAE Standard 90.1-1989. Equipment units are then usually selected to the closest higher capacity, further adding to the safety factor. For the following discussion, we will use a conservative oversizing factor of 10%

$$\sigma_{\mathrm{SF}} = \frac{q_{\mathrm{design}}}{q_{\mathrm{load}}} = 1.1. \tag{9.31}$$

Furthermore, outside design temperatures are often taken for more extreme conditions than recommended. For example, the standard outside design temperature for Prague in the valid Czech norm ČSN383350 is -12°C; the norm has been valid since 1989. Looking into Tab. 9.3 we can see, that such temperature roughly equals the 99.6%-percentile design temperature by ASHRAE [134]. However, the ASHRAE recommended the design temperature to be the 99%-percentile temperature. The discrepancy is due to global warming and different national comfort standards. European-wide, however, the heating degree days values decreased by 11% between 1979 and 2021 in the EU [135]. Therefore even a right-sized equipment from a decade ago is oversized for today's outside conditions. We define an oversize factor due to outdoor design temperature as

$$\sigma_{\mathrm{OD}} = \frac{q_{\mathrm{design}}}{q_{\mathrm{real}}} = \frac{\mathcal{H}\Delta T_{\mathrm{design}}}{\mathcal{H}\Delta T_{\mathrm{real}}} \doteq \frac{T_{\mathrm{ID}} - T_{99.6}}{T_{\mathrm{ID}} - T_{99}}, \tag{9.32}$$

where $T_{99.6}$ and T_{99} are respective percentile design temperatures [134] that are used for σ_{DT} approximation. T_{ID} is the indoor design temperature (= 20°C). Tab. 9.3 lists the factor for some European capitals. The city of Strasbourg has standard European heating conditions according to the European heating index (EHI) [136] and will serve as a reference for outdoor-design-temperature based oversizing with a rough oversize value of $\sigma_{\mathrm{OD}} = 1.1$.

Location	$T_{99.6}$ [°C]	T_{99} [°C]	Difference [°C]	σ_{OD} [%]
Berlin	-11.8	-8.2	3.6	112.7
London	-2.6	-1.0	1.6	107.6
Prague	-12.1	-9.5	2.6	108.8
Stockholm	-12.6	-9.9	2.7	109
Strasbourg	-8	-5.5	2.5	109.8
Warsaw	-15.5	-12.2	3.3	110.3

Table 9.3.: Outside heating design temperatures for two standard design percentiles, 99.6% and 99%, in 2021 [134]. Oversize factor $\sigma_{\mathrm{D.T.}}$ calculated using (9.32) with a standard indoor temperature 20°C.

Now, writing the design load in the ψ-P form [42] and using (9.31) and (9.32) we derive

$$\begin{aligned} q_{\text{design}} &= h_{\text{desing}} \psi_{\text{design}} \Delta T_{\text{design}} \\ &= (\sigma_{\text{SF}} h_{\text{real}}) \cdot \psi_{\text{design}} \cdot (\sigma_{\text{OD}} \Delta T_{\text{real}}) \\ &= \sigma_{\text{SF}} \sigma_{\text{OD}} h_{\text{real}} \psi_{\text{design}} \Delta T_{\text{real}} \\ &= \sigma \cdot q_{\text{real}}, \end{aligned}$$

where $\psi = \epsilon \cdot \text{NTU}^{-1}$ defines how close is the heat exchanger to an ideal plate exchanger,

$$\sigma = \sigma_{\text{SF}} \cdot \sigma_{\text{OD}} \tag{9.33}$$

is the total oversize factor.

Now, we can calculate the water inlet temperature at which the oversized heat terminal will cover the real necessary load q_{real}. For one terminal unit x, we write the heat outputs in the P-NTU form [42]

$$\begin{aligned} q_{\text{design}} &= \sigma \cdot q_{\text{real}} \\ \mathcal{P}_{\text{w}} C_{\text{w}} \left(T_{\text{w,s}} - T_{\text{a,i}}\right) &= \sigma \cdot \mathcal{P}_{\text{w}} C_{\text{w}} \left(T^{x}_{\text{w,i}} - T_{\text{a,i}}\right) \end{aligned}$$

and considering a constant heat exchange coefficient, we can derive the lowered inlet water temperature as

$$T^{x}_{\text{w,i}} = \sigma^{-1} \cdot T_{\text{w,s}}. \tag{9.34}$$

Using the oversize factors $\sigma_{\text{SF}} = 1.1$ and $\sigma_{\text{OD}} = 1.1$, we get that the heat terminals are still able to deliver the necessary load q_{real} at 83% of the heat supply temperature. In 2-pipe systems, all heat terminals are supplied approximately by the heat supply temperature, for which they are designed; retrofitting the heating with a pumping 1-pipe system the real loads may be continuously covered by units having up to 17% lower inlet water temperature. Tab. 9.4 lists standard heat supply temperatures, typical 2-pipe return temperatures and inlet temperatures up to which the 1-pipe system delivers the same power to zones as a 2-pipe system.

Remark 10. Accounting for oversizing, all units in a pumping 1-pipe system having still approximately 83% of the heat supply temperature don't need any attention when retrofitted from a 2-pipe systems (see (9.34) and Tab. 9.4).

Heat supply temperature [°C]	Design 2-pipe return temperature [°C]	Sufficient 1-pipe inlet temperature [°C]
80	60	66.1
70	50	57.8
50	40	41.3

Table 9.4.: Comparison of a design 2-pipe return temperature to the 1-pipe temperature at which heat terminals are still able to deliver the necessary load.

Furthermore, in a 1-pipe distribution system , the heat terminals are temperature-dependent. At design outside conditions, the terminal in the 1-pipe chain will experience the lowest inlet water temperature; at partial load, however, 99% of the time, its inlet temperature may be significantly higher (depending on the main pipe flow control). Peak loads of heat terminals may not always coincide in time. Such a phenomenon is described by a diversity factor in the Code of Practice [137] and is given an approximate rule-of-thumb for heating applications. Non-coincidence of loading increases the inlet temperature for units downstream the primary pipe. Noting that heating systems are designed for a sum of peak loads across all heat terminals, we can estimate how diversity affects inlet temperature drop for units in the 1-pipe chain. We will use the rule-of-thumb by [137] as an approximation and define an oversize factor due to diversity for an x^{th} successive unit as

$$\sigma_{\text{Di}}^{x} = \frac{\sum_{i=1}^{x-1} q_{i,\text{design}}}{\sum_{i=1}^{x-1} q_{i,\text{real}}} \doteq (0.62 + 0.38/N_x)^{-1}$$

where N_x is the number of dwellings (independent users/zones) heated by the preceding $x-1$ units in the 1-pipe chain. It is worth noting that the first unit does not experience any diversity but has the highest (same as 2-pipe) heat transfer temperature potential. Further units have increasingly lower inlet water temperature but have increasingly higher diversity factor. The longer the 1-pipe chain is, the lower the probability of all units working at peak load [120]. For $N_x = 2$ the diversity oversize factor is already $\sigma_{\text{Di}} = 1.23$, which means that inlet water temperature maybe up to 18.7% higher than the design one.

Furthermore, heat sources are designed with at least 10% safety factor [133] increasing further the chance to deliver design heat load to any discriminated zone. The zone heat load may also be greatly reduced by a retrofitted building insulation.

Remark 11. Considering all oversizing factors, it is not uncommon that heat terminals designed for a 2-pipe system may perform well without any special consideration when retrofitted with a pumping 1-pipe system.

9.3.1.2. Increasing flow through heat terminal

Design rules for a heat exchanger differ with its type. A general design rule is given in [138]: “Optimally designed (with respect to first cost and operating cost) heat exchanger will be characterized by an NTU that is usually in the range of 1 to 2”.

According to P-NTU analysis [42], a heat exchanger heat output is

$$q = \mathcal{P}\,(\text{NTU},R,\text{arrangement})\,C\Delta T_{\text{i}}$$

where $\mathcal{P}\,(\ldots)$ is a known temperature effectiveness function, NTU is a number of heat transfer units, R is a heat capacity rate ratio, C is a heat capacity rate and ΔT_{i} is an inlet temperature difference (i.e. the maximal temperature difference). A multiple-tube-row-fin heat exchanger, such as in an FCU, the ’arrangement’ is “cross-flow both fluid unmixed” [42].

Remark. Note that the P-NTU effectiveness formulas for the “cross-flow both fluid unmixed” configuration are inaccurate in [42], instead [139] should be used; with the added value of also providing an explicit formulation to a $NTU\,(\mathcal{P},R)$ problem.

Now, for the first heat exchanger, the heat output is

$$q_1 = \mathcal{P}\,(\text{NTU}_1,R_1)\,C_{\text{w},1}\Delta T_{\text{i},1} \tag{9.35}$$

with $\text{NTU}_1 = {}^{\mathcal{H}}/{}_{C_{\text{w},1}}$, $R_1 = {}^{C_{\text{w},1}}/{}_{C_{\text{a},1}}$, where $C_{\text{w},1} = \dot{m}_{\text{w},1}c_{\text{p,w}}$ is the water heat capacity rate, $C_{\text{a}} = \dot{m}_{\text{a}}c_{\text{p,a}}$ is the air heat capacity rate and the inlet temperature difference is $\Delta T_{\text{i},1} = T_{\text{w,i},1} - T_{\text{a,i}}$.

The problem statement is the following: How much the flow rate through the heat exchanger must be increased to compensate for a water inlet temperature drop? We further consider these assumptions:

A.1 The 1-pipe system serves N identical zones with identical heat loads.
A.2 All heat exchangers have the same heat exchange properties (i.e. the same hardware realization).
A.3 There is a constant airflow $\dot{m}_{\text{a}}$ for all heat exchangers.
A.4 There is a constant inlet air temperature $T_{\text{a,i}}$ for all heat exchangers.
A.5 The specific heat capacity of water $c_{\text{p,w}}$ doesn’t change with temperature.
A.6 The heat conductivity of the heat exchanger’s metal body is omitted.
A.7 The heat transfer coefficient between water and body is velocity dependent (Gnielinsky correlation).

For an x^{th} heat exchanger down the primary pipe, the heat output is

$$q_x = \mathcal{P}\,(\text{NTU}_x,R_x)\,C_{\text{w},x}\Delta T_{\text{i},x},$$

where NTU_x, R_x, C_x are described below and $\Delta T_{\mathrm{i},x} = T_{\mathrm{w,i},x} - T_{\mathrm{a,i}} = \Delta T_{\mathrm{i},1} - T_{\mathrm{D},x}$ with $T_{\mathrm{D},x}$ being the inlet water temperature drop at terminal x. Therefore, we are looking for a flow multiplication factor

$$f_x = \frac{\dot{m}_{\mathrm{w},x}}{\dot{m}_{\mathrm{w},1}},$$

such that heat outputs are equal

$$q_1 \quad = \quad q_x\left(T_{\mathrm{D},x}, f_x\right).$$

Rewriting the heat capacity rate using the multiplication factor we get

$$C_{\mathrm{w},x} = \dot{m}_{\mathrm{w},x} c_{\mathrm{p,w}} = f_x \dot{m}_{\mathrm{w},1} c_{\mathrm{p,w}} = f_x C_{\mathrm{w},1},$$

then the number of transfered units is

$$\mathrm{NTU}_x = \frac{\mathcal{H}}{C_{\mathrm{w},x}} = \mathrm{NTU}\left(\dot{m}_{\mathrm{w},1}, f_x\right) = \frac{\mathcal{H}\left(f_x \dot{m}_{\mathrm{w},1}, \dot{m}_{\mathrm{a}}\right)}{f_x C_{\mathrm{w},1}}. \tag{9.36}$$

The overall heat transfer coefficient $\mathcal{H}$ varies with flow velocities on the air and water side of the heat exchanger

$$\mathcal{H}\left(\dot{m}_{\mathrm{w}}, \dot{m}_{\mathrm{a}}\right) = \left(\mathcal{H}_{\mathrm{w}}^{-1}\left(\dot{m}_{\mathrm{w}}\right) + \mathcal{H}_{\mathrm{a}}^{-1}\left(\dot{m}_{\mathrm{a}}\right)\right)^{-1},$$

where the water side heat transfer $\mathcal{H}_{\mathrm{w}}\left(\dot{m}_{\mathrm{w}}\right)$ was calculated using Nusselt number by a correlation of Gnielinsky [140] with Darcy friction factor correlation by Haaland [141]. If we calculate the air-side heat transfer coefficient for the base (1st) heat exchanger as

$$\mathcal{H}_{\mathrm{a}} = \left(\mathcal{H}^{-1}\left(\dot{m}_{\mathrm{w},1}, \dot{m}_{\mathrm{a}}\right) - \mathcal{H}_{\mathrm{w}}^{-1}\left(\dot{m}_{\mathrm{w},1}\right)\right)^{-1}$$

we can state the change in $\mathcal{H}$ due to flow increase as

$$\mathcal{H}\left(\dot{m}_{\mathrm{w},x}, \dot{m}_{\mathrm{a}}\right) = \mathcal{H}\left(\dot{m}_{\mathrm{w},1}, f_x\right) = \left(\mathcal{H}^{-1}\left(\dot{m}_{\mathrm{w},1}, \dot{m}_{\mathrm{a}}\right) - \mathcal{H}_{\mathrm{w}}^{-1}\left(\dot{m}_{\mathrm{w},1}\right) + \mathcal{H}_{\mathrm{w}}^{-1}\left(f_x \dot{m}_{\mathrm{w},1}\right)\right)^{-1}. \tag{9.37}$$

Unfortunately, the $\mathcal{H}_{\mathrm{w}}\left(\right)$ function is highly non-linear, therefore, (9.36) can't be simplified any further. The capacity rate ratio may be rewritten as

$$R_x = \frac{\dot{m}_{\mathrm{w,x}}}{\dot{m}_{\mathrm{a}}} = \frac{f_x \dot{m}_{\mathrm{w},1}}{\dot{m}_{\mathrm{a}}} = f_x R_1.$$

So, in order to achieve the same power output, the following needs to be true

$$\begin{aligned}
\mathcal{P}\left(\mathrm{NTU}_1, R_1\right) C_{\mathrm{w},1} \Delta T_{i,1} &= \mathcal{P}\left(\mathrm{NTU}_x, R_x\right) C_{\mathrm{w},x} \Delta T_{i,x} \\
\mathcal{P}\left(\mathrm{NTU}_1, R_1\right) \Delta T_{i,1} &= \mathcal{P}\left(\mathrm{NTU}\left(\dot{m}_{\mathrm{w},1}, f_x\right), f_x R_1\right) f_x \left(\Delta T_{i,1} - T_{D,x}\right)
\end{aligned}$$

and we can, using (9.36) and (9.37), numerically solve for f_x.

Fig. 9.15 depicts the multiplication factor dependence on the inlet water temperature drop under multiple scenarios. The base scenario (black line) represents a randomly selected 2-pipe heating system (no changeover, no cooling coil) FCU - Gea Basic-Geco, size 3, stage 2 with an output power 8.6kW, $\mathrm{NTU}_{\max} = 1.6$, $\mathcal{P}_{\max} = 0.65$. Fig. 9.15 shows how f_x varies when decreasing the base total heat exchange coefficient $\mathcal{H}_1$, the base inlet temperature difference $\Delta T_{\mathrm{i},1}$ (i.e. for the decrease in the inlet water temperature) or the base heat capacity rate R_1 (i.e. increasing air flow rate). In general, the bigger the heat exchanger, the inlet temperature potential, or the airflow the easier is to compensate for an inlet liquid temperature drop.

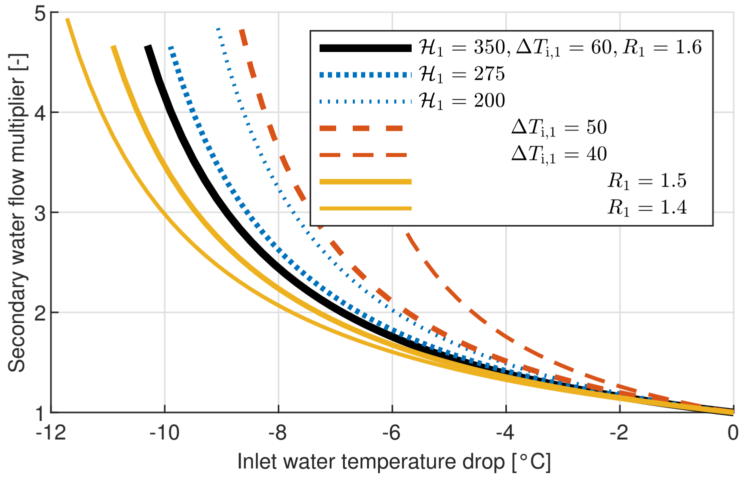

Figure 9.15.: Compensation of inlet temperature drop by increased liquid flow for multiple variations of important design properties.

Fig. 9.16 depicts how effectiveness ϵ and NTU vary for the selected FCU under inlet liquid temperature drop T_{D}.

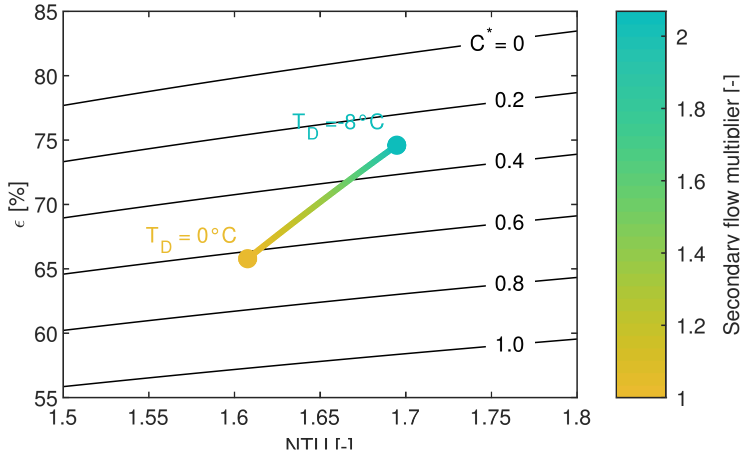

Figure 9.16.: Compensation of inlet temperature by increased liquid flow in NTU-effectiveness coordinates.

Remark 12. Increasing the liquid flow rate can compensate for decreasing inlet water temperature. Also note that the flow rate at peak load conditions is likely significantly lower than the design flow rate due to oversizing (see Sec. 9.3.1.1). Or in other words, the temperature drop compensable by the secondary pump is even larger due to oversizing.

Remark 13. A liquid temperature drop across a heat exchanger is not supposed to be as high as in the 2-pipe system. Any liquid HX temperature drop (even close to none) is valid for the 1-pipe system; the attention only needs to be paid to the primary pipe outlet temperature, which is channelled back to the heat source.

9.3.1.3. Supply temperature / primary flow increase

For an x^{th} heat terminal down the primary pipe, the heat output is

$$q_x = \mathcal{P}\left(\dot{m}_{\mathrm{w},x}, \dot{m}_{\mathrm{a}}\right) \dot{m}_{\mathrm{w},x} c_{\mathrm{p,w}} \left(T_{\mathrm{w,i},x} - T_{\mathrm{z},x}\right),$$

therefore, a qualitative control by the supply temperature linearly alters the heat output. In the pumping one-pipe system, the supply temperature for an x^{th} heat terminal is determined by the following heat balance

$$\dot{m}_{\text{w,p}} c_{\text{p,w}} T_{\text{s}} = \dot{m}_{\text{w,p}} c_{\text{p,w}} T_{\text{w,i},x} + \sum_{i=1}^{x-1} q_i$$

from which we can factor out the inlet temperature and its dependence on the heat supply temperature T_{s} and primary flow rate $\dot{m}_{\text{w,p}}$ as

$$T_{\text{w,i},x} = T_{\text{s}} - \frac{1}{\dot{m}_{\text{w,p}} c_{\text{p,w}}} \sum_{i=1}^{x-1} q_i. \tag{9.38}$$

For a constant heat output of preceding heat terminals, constant secondary water flow rate and airflow rate, the heat output on an x^{th} heat terminal is proportional to the heat source outlet temperature and inversely proportional to the primary flow rate

$$q_x = \mathcal{P}\left(\dot{m}_{\text{w},x}, \dot{m}_{\text{a}}\right) \dot{m}_{\text{w},x} c_{\text{p,w}} \left(T_{\text{s}} - \frac{1}{\dot{m}_{\text{w,p}} c_{\text{p,w}}} \sum_{i=1}^{x-1} q_i - T_{\text{z},x} \right). \tag{9.39}$$

9.3.1.4. Load sizing design

The design of a new 1-pipe hydronic heating system shall be made with respect to the predicted design inlet temperature drop. The publication [142] describes the whole process of optimizing system design, which has been implemented into the publicly available tool [143]. The main hurdle is the 1-pipe system chain affect that a heat exchanger affects all HXs down the line and the primary pipe flow and the supply temperature affect all HXs. Therefore, designing a 1-pipe chain, one must consider all the heat exchangers in one problem. The terminals are temperature dependent similarly as all terminals are pressure dependent in a 2-pipe system; only in the 2-pipe systems, the coupling global, i.e. also upstream.

Heat exchanger performance is always published for the 2-pipe system usage; datasheets state power ratings for specified inlet conditions and a fixed liquid temperature drop. Since for 1-pipe, the inlet temperature varies and any liquid temperature drop is valid (see 13), we need a way to calculate its power rating. The norm EN 442 (or DIN 4704-3) provides the formula for adjusting the nominal heat flow

$$q = q^{\text{n}} \left(\frac{\text{LMTD}}{\text{LMTD}^{\text{n}}} \right)^{c}, \tag{9.40}$$

where LMTD is the logarithmic mean temperature difference [141], nominal or considered, and c is an exponent accounting for heat transfer coefficient variation (for FCU $c \doteq 1.4$). The LMTD is calculated using $T_{\text{w,o}} = T_{\text{w,i}} - q / \dot{m}_{\text{w}} c_{\text{p,w}}$. The inlet water temperature of the $x^{\text{th}} + 1$ heat exchanger is calculated by mixing the x^{th} secondary outlet to the primary flow as

$$T_{\text{w,i},x+1} = \frac{\dot{m}_{\text{w},x} T_{\text{w,o},x} + \left(\dot{m}_{\text{w,p}} - \dot{m}_{\text{w},x} \right) T_{\text{w,i},x}}{\dot{m}_{\text{w,p}}}. \tag{9.41}$$

The primary flow may be calculated knowing all heat loads in the chain q_x and a desired heat source temperature difference ΔT_s as

$$\dot{m}_{\text{w,p}} = \frac{\sum_{\forall x} q_x}{c_{\text{p,w}} \Delta T_s}. \tag{9.42}$$

We can now construct the optimization problem to find all mass flows and nominal heat exchanger sizes

$$\begin{aligned} &\min_{\dot{m}_{\text{w},x},\, q_{\text{n},x},\, \dot{m}_{\text{w,p}}} \quad \Phi \\ &\text{s.t. } (9.40), (9.41), (9.42) \quad \forall x. \end{aligned} \tag{9.43}$$

The objective function is

$$\begin{aligned}\Phi =& w_1 \sum_{x=1}^{N} \operatorname{norm}\left(\frac{q_x}{q_x^{\mathrm{n}}} - \left(\frac{\mathrm{LMTD}_x}{\mathrm{LMTD}_x^{\mathrm{n}}}\right)^c\right) \\ &+ w_2\left(\dot{m}_{\mathrm{w,p}} + \sum_{x=1}^{N} \dot{m}_{\mathrm{w},x}\right) \\ &+ w_3\left(\sum_{x=1}^{N} q_x^{\mathrm{n}}\right),\end{aligned}$$

where w_1 is a relatively high weight constant assuring the heat loads are matched, w_2 sets weight on minimization of the flows and by w_3, the heat exchanger size is penalized. N is the number of heat terminals in the 1-pipe chain.

Solving the problem (9.43) puts optimal values on heat exchanger sizes, which are probably different from those any manufacture produces. Therefore, the design tool [143] performs a second step in which real heat exchangers are selected from provided datasheets. This selection problem is similar to (9.43), but with a known set of nominal heat flows $q_{\mathrm{n},x}$, i.e. the sizes. The problem has always many feasible combinations as a particular load q_x may be delivered by a smaller heat exchanger with higher mass flow and vice versa. In order to constrain the number of possible combination, only the closest higher and closest lower nominal power values are considered. Therefore, we get to solve 2^N-times the modified problem (9.43) from which a project designer may select. Any selected solution provides peak load mass flows through all heat exchangers and the primary mass flow rate.

Fig. 9.17 depicts an example 1-pipe system design for five zones with required loads 3.6, 1.7, 3.15, 1.85 and 2.3 kW, heat source temperatures 75 and 50°C, supply and return and a catalogue of four possible heat exchanger sizes. Designed terminals of nominal size 4, 2, 4, 2.8 and 4 kW deliver the peak load to its respective zone.

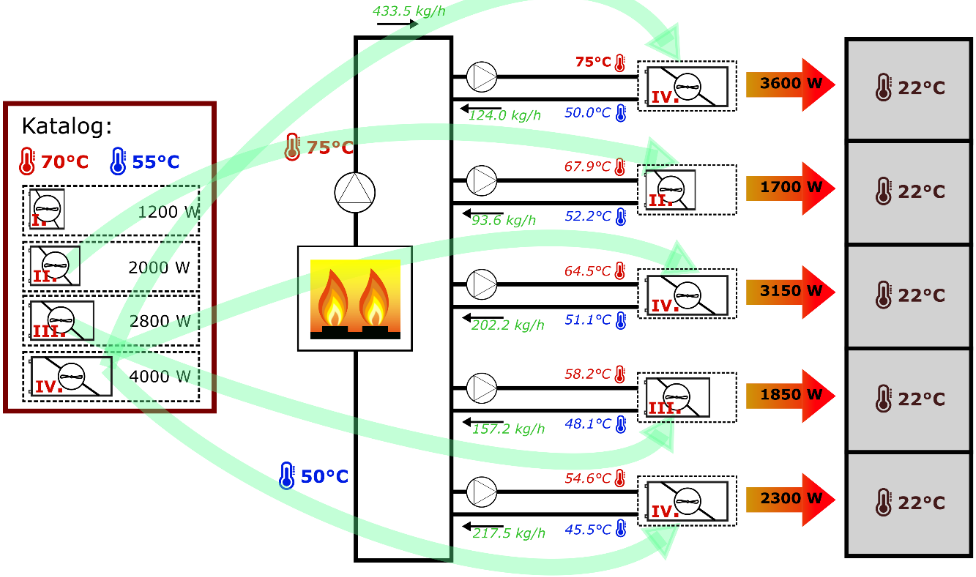

Figure 9.17.: Example 1-pipe system optimal design by the design tool [143].

Remark 14. Optimal sizing of heat exchangers for the pumping 1-pipe system results many HX sizes, which may not be practical from the manufacturing, delivery ,and installation point of view. Project designer may however oversize any heat exchanger to get fewer HX sizes. Ultimately, one could choose all heat exchanger sizes equal to the largest one.

Remark 15. Note that it is beneficial to position high-temperature-potential heat terminals, e.g. FCUs, at the beginning of the primary circuit and combine them with low-temperature-potential terminals, e.g. radiant floor heating, towards the end of the circuit. This may be a very effective design with regards to low primary return temperature, but the radiant floor heating needs to have temperature mixing installed.

9.3.1.5. Primary flow direction alternation

A typical multi-floor tertiary building has a multitude of supply and return pipe vertical risers with a horizontal distribution piping to heat terminals. Those are most probably designed for a fixed supply water temperature (2-pipe system) and oversized (see Sec. 9.3.1.1).

The main concern surrounding the 1-pipe distribution systems is whether the diminishing supply temperature in the chain will be sufficient for the power demand. Should there be a lack of heating power towards the end of the chain, we can alter the direction of the primary flow by one of the schemes of Fig. 9.18. This topology utilizes 2-pipe risers from which 1-pipe run-around piping branches. Such topology may be advantageous, especially for buildings, where floors are similar to each other, e.g. hotels, block of flats, office buildings, etc.

The flow through the primary pipe is controlled by the 3-way valve (Fig. 9.18a), alternatively the 4-way valve (Fig. 9.18b) or by a 2-way control valve inline on the primary pipe (not shown). The flow control may be realized such that there is certain return temperature returning from the 1-pipe chain (detailed description in Sec. 10.1.1) or to ensure a restricted flow value (as would be the case for 2-pipe balancing).

The switching control may be realized such that if there is an insufficient heat delivery towards the end of the chain, we should be able to preheat zones towards the beginning of the chain, by increased flow, and switch the primary flow direction to increase the heat potential in those now deprived zones. Once those are preheated, the direction is switched back, and a cycle is complete. This system is able to deliver the peak heat flow to all zones due to their thermal inertia.

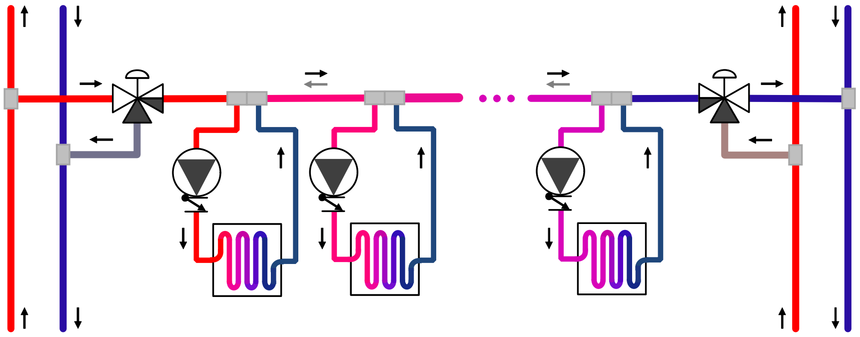

(a)

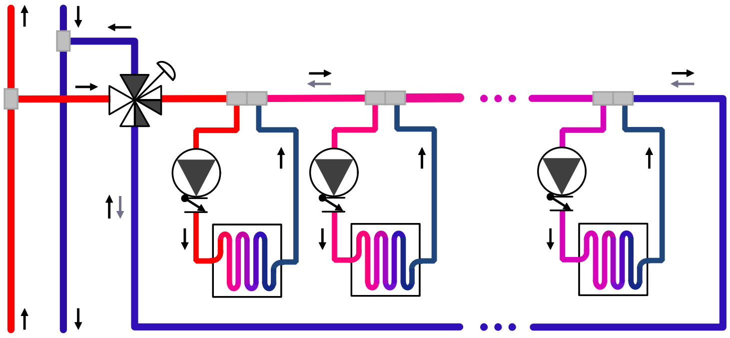

(b)

Figure 9.18.: Piping scheme for primary flow direction alternation with 3-way valves (a) and a 4-way valve (b).

9.3.2. Other topologies involving pumping one-pipe systems

Pumping one-pipe network offers many advantages but suffers from more complicated design and possibly non-uniform heat exchanger sizes due to inlet temperature decrease down the primary circuit. It is, therefore, beneficial to consider forming hybrid 2-pipe 1-pipe configurations such as the one depicted in Fig. 9.19. The 2-pipe part here brings a constant supply temperature to all 1-pipe chains, which are ultimately responsible for heating power delivery with all the advantages it offers (see Chapter 6). Balancing of the 2-pipe branches may favourably be performed using return temperature valves, which automatically adapt every branch flow to its power demand.

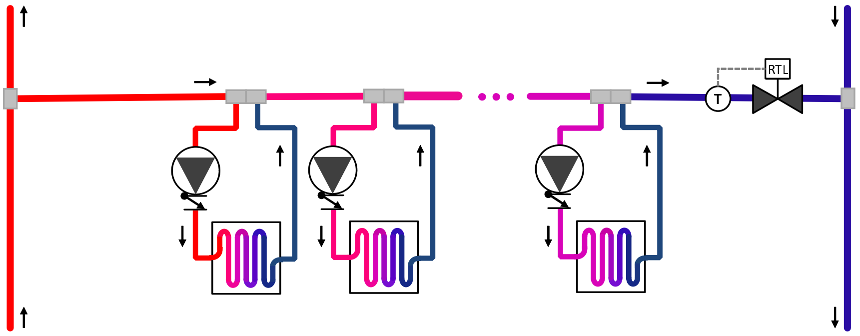

Figure 9.19.: Hybrid hydronic network composed of 2-pipe risers with 1-pipe branches. The branch primary flow may be controlled by a return temperature valve (RTL).

Another interesting application was conducted by Taco Comfort Solution and its pumping one-pipe system branded LoadMatch[45]. The 27-story high Council Tower Senior Apartments building in St. Louis, USA (Fig. 9.20a, 225 apartment units) has been refurbished using two 1-pipe networks in place of the old 2-pipe change-over system. Prior the renovation, the all the tenants in the building could either use heating or cooling depending on the seasonal change-over period. Such limitation proved impractical in the period between the seasons due to cooling needs on the south-facing facade during the day and heating demand on the north facade during the night. As Fig. 9.20b depicts, the solution was to refurbish the existing 2-pipe risers into two one-pipe networks, one to cover heating demands and the other to provide cooling. The vertical primary pipes are looped back to the technical room outside the apartments.

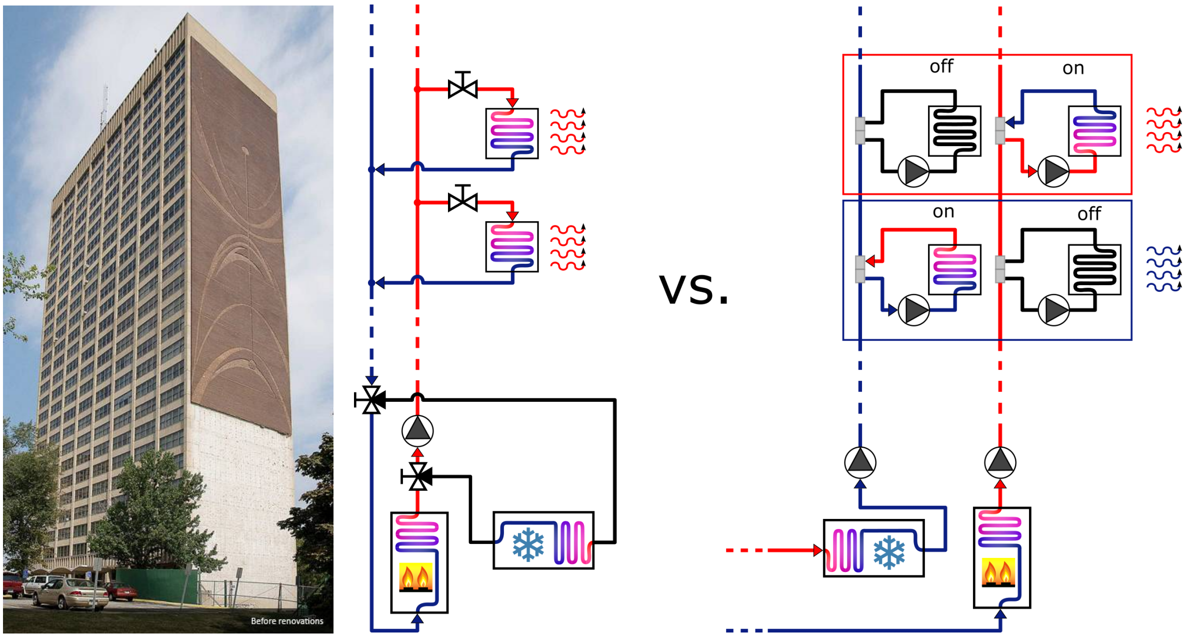

(a) source: EM Harris Construction

(b)

Figure 9.20.: Refurbishment of a change-over 2-pipe network into a double 1-pipe network for simultaneous heating and cooling; the renovated building (a) and the hydronic network renovation scheme (b).

10. Control of hydronic networks

A heat distribution network is a technical system that transports heat from a heat source to designated zones/processes. It should do so efficiently, reliably, economically, and 'invisibly'. For heating purposes in Europe, water-based heating is the most prominent; in particular, the throttling two-pipe water-based (hydronic) heating system.

The purpose of a hydronic network is to deliver heat from a heat source to thermal zones. The power delivery was already detailed in Part II .

Global means of control are the heat source supply temperature and the main flow/head. Local means of heat flow delivery are the heat transfer liquid flow rate and the air flow rate on the heat exchanger.

A throttling two-pipe network is usually sectioned into many hydraulically disconnected branches (risers) via generously sized low loss header, hydraulic separators or the riser base pressure is controlled by a differential pressure control valve. The hydraulic separation effectively separates the network into many subnetworks with independent virtual pressure sources. The local flow control is performed via a variable hydraulic resistance - the control valve. The control valves are designed to have the nominal pressure loss comparable to the pressure loss of the rest of a branch (branch piping, HX, etc.) [144, 145]. The local load control has already been detailed in Part II . The central pressure source should be controlled to provide the least pressure, such that the current flow demands are met (Claim 1).

The control of a pumping two-pipe network has been briefly outlined in Sec. 9.2. Usually there is a hydraulic separator employed to make circulation through a heat source independent, the secondary side – the distribution network – has as many local pumps as there are heat exchangers (flow demands). There are, therefore, zero degrees of freedom and the local pump speed is set to meet the demand flow (or similarly other zone controller reference signal) exactly.

The control of the throttling one-pipe network is irrelevant; this topology is phased out now.

10.1. Control of pumping one-pipe networks

A pumping 1-pipe system utilizes closely spaced double-tee arrangement to decouple the pressure source for one heat terminal from the rest of the heat terminals and network; the pressure/flow is exclusively controlled by the local pump. The power of preceding heat terminals, however, affects the inlet supply temperature, i.e. there is a thermal coupling. Fortunately, *temperature interactions are easy to measure and can be compensated for by a control system* as shown in Sec. 9.3.1.2 or Chapter 6.

10.1.1. Primary flow control strategy

The pumping one-pipe system has constant hydraulic conductance of the primary loop, i.e. the main pipe serving secondary circuits in the series does not contain any valve and is hydraulically independent from the secondary circuits. The differential pressure and consequently the pump speed needed to maintain a flow rate is thus constant. But what primary flow rate is optimal?

The optimal primary flow is the minimal flow for which all heat loads deliver necessary heat flow; any flow beyond that decreases the supply-return temperature difference on a heat source and hence also its efficiency. As already outlined in Sec. 9.3.1.3, the heat output of an x$^{\text{th}}$ terminal is

$$q_x = \mathcal{P}\left(\dot{m}_{\mathrm{w},x},\dot{m}_{\mathrm{a}}\right)\dot{m}_{\mathrm{w},x}c_{\mathrm{p,w}}\left(T_{\mathrm{w,i},x} - T_{\mathrm{z},x}\right) \tag{10.1}$$

$$T_{\mathrm{w,i},x} = T_{\mathrm{s}} - \frac{1}{\dot{m}_{\mathrm{w,p}}c_{\mathrm{p,w}}}\sum_{i=1}^{x-1} q_i, \tag{10.2}$$

so, should we know the thermal properties of all heat terminals and all flows and temperatures, the optimal primary flow rate would be

$$\begin{aligned} \dot{m}^{\star}_{\mathrm{w,p}} = \quad & \min_{\dot{m}_{\mathrm{w,p}}} && \dot{m}_{\mathrm{w,p}} \\ & \text{s.t.} && q_x \geq q_x^{\mathrm{SP}} \\ & && \dot{m}_{\mathrm{w},x} = \dot{m}_{\mathrm{w}}^{\max} \quad \forall x, \end{aligned}$$

which, however, mildly put, is a rather impractical approach. What is then the best suboptimal, yet practical approach to finding the primary flow rate?

We can't rely on knowing the exact thermal properties of the heat terminals nor should we consider knowing air flow rates. We know from (10.1), the heat output of a terminal is directly proportional to its primary inlet temperature. To satisfy the heat flow setpoint q^{sp} of the least favoured (the last in the chain) terminal, its primary inlet temperature may not drop below a minimal primary inlet temperature $T_{\mathrm{w,p}}^{\min}$ across all heat terminals in the one-pipe chain.

10.1.2. Decentralized control

In a completely decentralized - the least optimal - scenario, the primary flow controller does not pose any information other then its own local information. The primary flow may be controlled either by a variable speed circulator or by an actuated valve accompanied by some kind of a pressure source, see Fig. 10.1. As we don't know anything about the heat demands, we must assure that under all circumstances all heat terminals are able to deliver nominal heat flows, which is satisfied by having all inlet temperatures higher then their design values

$$q_x^{\max} \geq q_x^{\mathrm{design}} \iff T_{\mathrm{w,i},x} \geq T_{\mathrm{w,i},x}^{\mathrm{design}}, \quad x = 1 \dots N.$$

The above statement may be checked by (9.35) and noting that any secondary pump is always able to deliver secondary design flow, $\dot{m}_{\mathrm{w},x}^{\max} \geq \dot{m}_{\mathrm{w},x}^{\mathrm{design}} \quad \forall x$, as the secondary hydraulic resistance is constant since the network construction.

Supposing that we install the primary flow actuator on the heat source return pipeline, we can only measure the heat source return temperature $T_{\mathrm{s,r}}$. Therefore the best strategy we can deploy is to maintain the heat source return temperature at the nominal (design) inlet water temperature of the last (N^{th}) heat terminal in the one-pipe chain

$$\dot{m}_{\mathrm{w,p}} : T_{\mathrm{s,r}} = T_{\mathrm{w,i},N}^{\mathrm{design}} \Rightarrow q_x^{\max} \geq q_x^{\mathrm{design}}.$$

Then we know, that the inlet temperature of the last heat terminal is certainly higher than nominal which consequently applies to all upstream terminals which conclude the statement reasoning.

Note that measuring flow is possible and can be beneficial for calorimetric purposes, but its value for primary flow control is nil as the right flow reference is unknown. Equithermal heat supply outlet temperature control may be utilized, in which case, the return temperature reference should be calculated from the actual heat demand for the last heat terminal in order to minimize primary flow and increase heat source efficiency.

It is also important to note that return temperature control of the primary flow always reflects the actual heat output of all associated heat exchangers. Should the heat output sum be lower than nominal, the primary return temperature is higher than designed and the primary flow actuator reduces the flow. And the lower primary flow will result in lower primary output temperature in all the double-tees along the way matching the design return temperature at the end.

Fig. 10.1 depicts a return temperature control method a temperature controlled pump, in hybrid 2-pipe 1-pipe networks may the return temperature be controlled by a return temperature valve (see Fig. 9.19).

10.1.3. Distributed control

Let's consider now a distributed control scenario where we have the ability to communicate between active members of the hydronic network and where the power control pump actuators (PCP, Chapter 6) are installed with their internal heat flow estimations and self-diagnostics. Then the primary flow controller may utilize the information

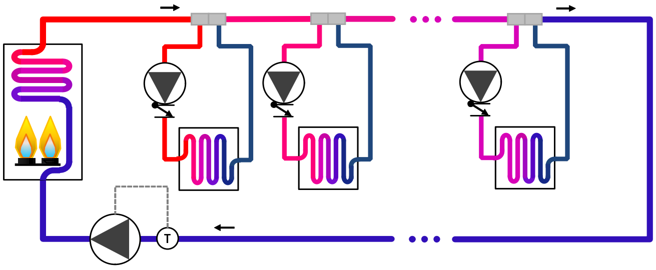

Figure 10.1.: Temperature-feedback primary flow control using a temperature-controlled pump.

about secondary flow saturation altogether with the information on how the heat demands are met. In the most basic setting, the primary flow (or heat source power) is stepped down until any of the PCP actuators flag unreachable heat flow setpoint in which case the primary flow (or heat source power) is stepped back up, see Alg. 10.1. This approach is similar to [146]. The system balances at a limit cycle where one heat terminal is operated at its limits and the primary flow (or heat source power) is the lowest possible. In this case, the heat source return temperature is also the lowest possible.

Algorithm 10.1 Primitive distributed primary flow control algorithm. Primary pump speed is denoted S, speed step s_{step} and node heat flows q. All nodes communicate heat flow demand fulfilment (binary).

```
$0 \leq S_{\text{p}} \leq S_{\text{p}}^{\text{max}}$.
while true
    if $(q_x^{\text{max}}(t) \geq q_x^{\text{SP}}(t)\ \ \forall x)$
        Decrease primary flow.
        e.g. for primary pump control $S_{\text{p}}(t+\Delta t) = S_{\text{p}}(t) - s_{\text{step}}$.
    else
        Increase primary flow.
        e.g. for primary pump control $S_{\text{p}}(t+\Delta t) = S_{\text{p}}(t) + s_{\text{step}}$.
    end
end while
```

10.1.4. Secondary pump control

Secondary flow is the only direct way to control the heat terminal power. The secondary circuit is intentionally hydraulically separated from the primary circuit and lacks variable throttling devices by design. All to make the pump impeller speed have 100% authority over the flow.

10.1.4.1. Direct zone temperature feedback

The hydronic network serves the ultimate goal of delivering thermal comfort to building zones. From here stems the basic control algorithm idea: temperature loo low, increase speed; temperature too high, reduce sped. Such an algorithm, implemented as a hysteresis controller for example is a robust way to control zone temperature.

When implemented via a PI controller, the issues from unknown non-linearity of the pump speed to heat power system; unknown inlet temperature disturbance and variable time delay arise. Heat terminals are also dynamically coupled in the downstream direction via primary inlet temperature.

10.1.4.2. Heat Flow Control

Fixed hydraulic resistance of the secondary circuit with no pressure source other than the secondary pump (hydraulic independence of the primary circuit) presents an interesting opportunity. Known pump pressure and power characteristics allow us to estimate liquid mass flow (see Sec. 6.4) and validate heat transfer fluid. Coupled with a temperature drop measurement, a heat flow through a heat terminal may be estimated and controlled (see Sec. 6.5).

Once the thermal power estimate exists, we can stabilize it under varying inlet temperatures and thus effectively thermally decouple the power influx into a said zone. The heat output is hydraulically and thermally independent from the rest of the network! The zone temperature controller is not affected by external disturbances and the heat flow delivery is linearized (power delivery tracks the demand demand 1:1).

Knowing thermal power enables also approximate energy metering, thermal modelling for optimization purposes (see Sec. 12.2) and thermal diagnostics.

10.1.5. Whole-system MIMO optimal control

The pumping one-pipe network heat output for each node may be incorporated into a building-wide optimal predictive controller. Such an approach is detailed in Sec. 13.2 and [147].

Part IV.

Building level control

Buildings are getting digitized. An ideal building control system should, according to my wit, feature the following:

- all datapoints (sensors, actuators) are available via standardized communication protocol and come with semantic metadata according to a standardized ontology,
- diagnostics is generated according to the semantic description,
- the diagnostics encompass all technical systems and runs regularly,
- a control structure is constructable & reconfigurable in a plug-and-play manner,
- the control employs optimization to maximize an objective under constraints,
- the control objective is tunable on demand (comfort, energy savings, HW preservation, energy flexibility services, energy community objectives),
- the control takes all known information into account (construction data, real-time data, predictions),
- the interactions between technical systems are considered.

Such an ideal may never be achievable due to the wide variety and complexity of the building control landscape, however, the transition of the building stock should nevertheless aim towards an ambitious goal/ideal.

Energy consumption of HVAC can form up to 30 % of the overall building consumption [148]. Fortunately, modern HVAC and BACS systems can decrease the consumption and costs by 17-24 % [101, 149], therefore they are being increasingly applied. The EU directive on energy performance of buildings (EPBD 3, [150]) enforces non-residential buildings (over 290 kW) to be equipped with a building automation and control system (BACS) by 2025. BACS enable continuous performance monitoring, which is the stepping stone for diagnostics and data analytics. BACS is also an elementary requirement for the development and deployment of an energy-effective control system.

There is no solution for a widely applicable optimal control of buildings yet as per the review [151]. The Hydronics 4.0 concept introduced in Sec. 1.2

I have had the opportunity to work on a project of automatic semantic model creation using machine learning techniques. While the value of metadata is still not very well understood in the building control community, we believe that diagnostics generated from semantic models will be the turning point for a wide-spread adoption of the concept. Proper diagnostics itself may provide up to 25% energy savings just by making the HVAC system work as originally intended [152].

This part first presents building energy simulation tools, a building control model calibration is treated next as it is the most important part of optimal control and a building control chapter comes last.

11. Building energy simulation tools

Increasing computational power in the late ’80s and early ’90s led to the development of many building energy simulation tools; 120 as of 1998 by the U.S. Department of Energy (DOE) [153]. There had been a precision discrepancy between the tools and therefore a Building Energy Simulation Test (BESTest) has been introduced. Since then, the computational engines have been validated against analytical closed-form solutions, empirical tests based on measured data and comparative tests. Among the BESTest validated tools are EnergyPlus [69], ESP-r [154] and TRNSYS [155] to name a few. These tools, categorized as building energy performance simulation (BEPS) tools, provide tailored algorithms for detailed building physics simulation. However, for control purposes, these tools are impractical mainly due to their non-explicit representation. Although attempts to use BEPS for control have been made [156–158], researchers tend to use low-order explicit models instead [6]. The high-fidelity BEPS tools are however extensively used for control strategy validation through co-simulation [159–162] for instance in [163–167]. A new generation tool is also being developed under IEA EBC Annex 60 [168].

The simulation of hydronic networks has been detailed in Chapter 8. However, the sole purpose of hydronic networks in buildings is to set zone comfort. To assess the comfort, here mainly thermal, a building energy simulation tool is needed.

There are many simulation tools available, but most notably the TRNSYS[155], Modelica [169], EnergyPlus [69]. A few work well with Matlab and are cheap/free, though. The motivation for using Matlab is its (optimal) control design capabilities. This chapter will present one co-simulation toolbox for Matlab and one toolbox made for Matlab directly.

11.1. EnergyPlus co-simulation toolbox

EnergyPlus [69] is a building performance simulation program developed by the National Renewable Energy Laboratory (NREL). There has been a set of Matlab scripts [161] suited to interconnect to EnergyPlus using the Building Controls Virtual Test Bed (BCVTB, [160]). There were, however, still manual steps necessary to interconnect the inputs and outputs (via writing a XML file). There was no Simulink extension for EnergyPlus available.

I have built upon the scripts of Nghiem [161] a Matlab toolbox called *EnergyPlus Co-simulation Toolbox* [71] to automate and simplify the co-simulation between the two programs.

The features of the toolbox include:

- Parsing of the IDF file to determine co-simulation inputs/outputs and sampling.
- Automatic socket communication configuration (on localhost).
- Background start of the EnergyPlus process with output to the Matlab command line.
- System Object implementation functional in Matlab & Simulink.
- Bus input/output integration for easy Simulink model setup.
- A ’mlep Bus Creator’ block to facilitate Simulink co-simulation input setup.

The download count of the toolbox at Matlab FileExchange is more than 1400 (Aug. 2023), the GitHub repository is not monitored. See Fig. 11.1 for an example.

11.2. Hydronic heating toolbox

Co-simulation with high-fidelity building simulation tools is one way to approach the issue, another is to build a building simulation tool inside the Matlab/Simulink itself.

I have created a Matlab toolbox called a *Hydronic heating toolbox* [72] used for the simulation of hydronic networks and the thermal simulations of buildings.

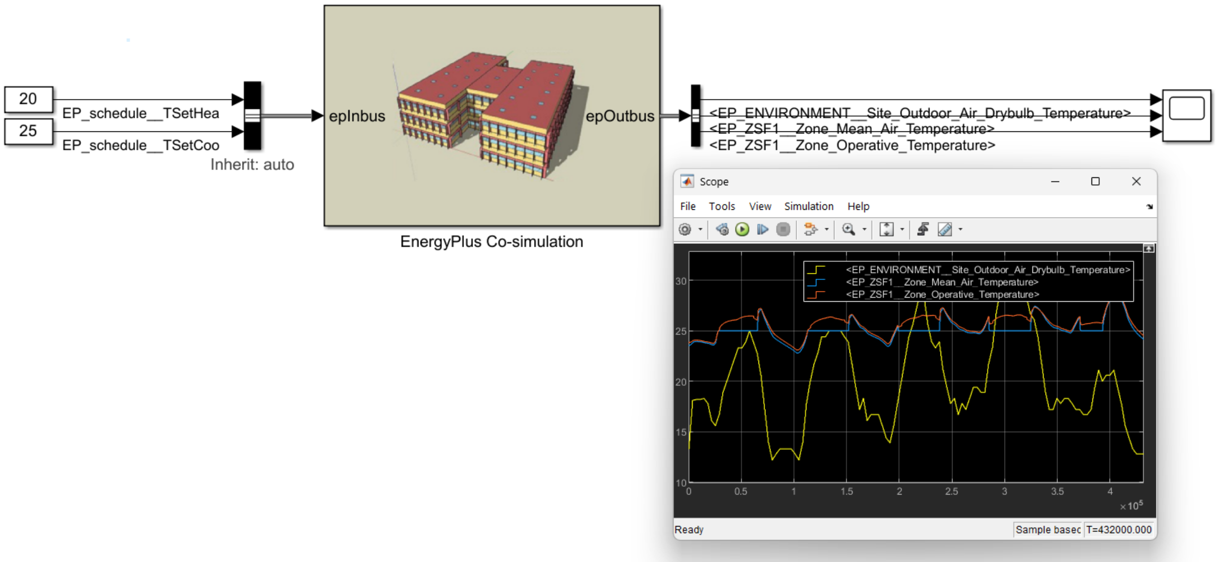

Figure 11.1.: EnergyPlus Co-simulation Toolbox basic example.

Hydronic component models were already presented in Part I . The heat exchanger model employs the developed minimum numerical diffusion approach presented in Sec. 4.2.3, the heat transfer coefficients may be fitted directly by specifying data-sheet ratings or other suitable measurements.

Building thermal components are to some extent presented in Sec. 12.2. Wall models have a thermal state for each layer (plaster, main construction material, insulation, etc.). The zone model is composed of the main two-state thermal inertial and a thin thermal layer state by each wall to capture the thermostat (wall module) temperature readings more accurately. Envelope walls are subject to solar gains (including direct zone gains through windows) and ambient temperature variations.

See Fig. 11.2 for an example of a one-story flat modelled using the toolbox.

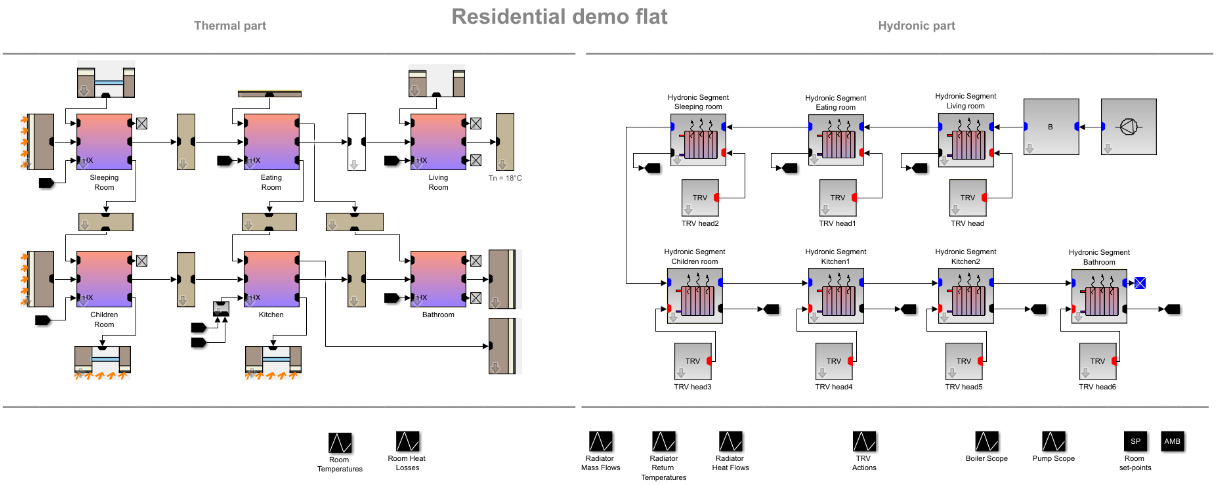

Figure 11.2.: Residential flat hydronic heating modeled by the Hydronic heating toolbox.

12. Building model calibration[1]

This chapter deals with the parameter calibration of a building thermal model. It describes a modelling issue and parameter identification approach. A distributed identification approach is presented. This approach uses the dual decomposition method, which decomposes a large optimization problem into smaller local ones which are then solved by local agents. The local models are found using a grey-box calibration, and coordinating agents' mutual shared parameters, a global consistency is obtained. The method is tested in two scenarios: one trivial demonstration case and the other a complex model of a building simulated in the EnergyPlus simulation program.

12.1. Introduction

A building model used for control should satisfy several requirements; it has to be explicit, of reasonable simplicity, estimate well important process dynamics, and agree to measurements in steady-state [171]. There are numerous reviews of building models used for control [172–176]; suitable control models shall be obtained by one of the following techniques: prediction-error-method (PEM) [149, 177], subspace identification (4SID) [148, 178, 179], deterministic grey-box modelling (GB) [180–182], stochastic grey-box modelling (SGB) [183–185] or lately by machine learning techniques [186–190]. A review on the state-of-the-art of control-oriented modelling techniques for buildings is most recently given in [191]. The paper brings on the practical aspects of model selection. It states that while white-box models can provide accurate outputs, they are challenging to obtain. The grey-box models are developed much faster, but their calibration also comes with challenges, specifically the lack of excitation of individual model dynamics in real data. The availability of a white-box model might as well solve this. The grey-box models cover the main physics aspects while retaining a relatively simple structure and low complexity. They are also not prone to give unphysical predictions as black-box approaches potentially can [171, 192]. This study focuses on the grey-box approach.

The GB approach is adopted by numerous principal laboratories [193–195]. It is popular mainly for its favourable properties such as a relatively low time consumption during creation (compared to white-box), exact or near physics-based interpretation. Also for capturing of prior information (structure known from basic physics postulates) and a relatively low number of parameters to be calibrated. The review composed by Serale et. al. [175] states that 48 % of all papers dealing with control-oriented building models adopt the GB approach. GB compared to ARX, ARMAX, gaussian process and artificial neural network in [176] wins in terms of handling uncertainties and commissioning cost. The quality of identified GB models is treated in [181]. Building grey-box models are most often based on the electrical resistance-capacitance analogy to the thermal processes. This approach is, in detail, presented, for example, in [196–198]. Grey-box calibration techniques range from linear regression [199, 200], non-linear programming [197, 198, 201], global optimization [202, 203], MPC relevant identification [204], particle swarm optimization [205] and also by agent-based optimization [206]. The agent-based approach is used in this chapter.

Even though grey-box calibration is relatively low computationally demanding [176], its calibration may become intractable in the case of large/complex buildings [163]. The sparsity of the thermal couplings advocates the usage of distributed/agent-based calibration, where the computational load, as well as data management, is distributed into many subsystems/agents [207]. Documented distributed calibration studies thrive on the primal/dual decomposition by [208] (later used in [209, 210]); this is the case for [206, 211]. There is, however, an abundance of distributed optimization techniques that can be used to solve the distributed grey-box calibration problem. See, for example, dual decomposition with parameter decomposition [212], alternating direction method of multipliers (ADMM) [213] or optimality condition decomposition (OCD) [214]. It should be noted that this study does not aim to compare multiple distributed optimization methods and resorts to dual-decomposition by Boyd [208]. To the best of authors' knowledge and research efforts, no other study of distributed GB applied to a control-oriented building model was

---

[1] Based on the co-authored original paper: Tomáš. Bäumelt and Jiří Dostál. "Distributed agent-based building grey-box model identification". In: *Control Engineering Practice* 101 (2020), p. 104427. ISSN: 0967-0661. DOI: `10.1016/j.conengprac.2020.104427`

found. It is, therefore, in authors' opinion, relevant to present first the notion of distributed model calibration and its formulation in the building scenario giving the space for later publication comparing distributed optimization techniques on the topic.

A development of a process model takes a large portion of time when implementing advanced control. Zhu [215] states that model preparation for MPC takes up to 80 % of the total effort. For building models, it was reported to take about 60 % to 80% when dealing with the MPC-oriented models [216]. The distributed GB approach is among the candidates to partially automate the model creation process and thus facilitate the application of MPC for buildings.

12.2. Building modelling

This section presents a complete derivation of a building control-oriented model. At first, the construction of a local zone grey-box model is described. Then, it follows a procedure of parameter estimation. At last, a distributed approach to building identification via the agent coordinated agents is presented.

12.2.1. Agent definition

The building is divided into individual zones (rooms) where corresponding agents operate. The agent's main goal is to identify a local grey-box model. For this purpose, the agent can access only measured data from its zone (alternatively to ambient measurements, in case of adjacency with the outside environment) and can also communicate with adjacent agents.

12.2.2. Grey-box modelling

The local grey-box model structure represents the most significant physical (thermal) effects that take part within the zone. The final model is created by merging smaller submodels representing the following objects:

- *Zone* with its thermal capacity,
- *Wall* with its thermal conductance or resistance,
- *Heat exchanger* with a possible inner dynamics,
- *Solar gains* as an ideal source of heat flow with a shading factor,
- *Outside environment* as an ideal source of temperature.

This grey-box modelling approach has the advantage that only these small simple submodels are at first defined and subsequently, the whole zone GBM (with walls etc.) is created automatically (in Matlab using object-oriented programming). Therefore, it is very simple to change the resulting zone "big" GBM by changing only a particular submodel structure.

12.2.3. Submodels

At first, the *zone* submodel, which represents a core part of the final grey-box model, will be discussed. It is assumed there is only a measurement of the air temperature T_z in the zone. A main element of this submodel is formed by the air heat capacity C_z, which is depicted using a thermal circuit in the Fig. 12.1.

For each submodel, it is defined which submodels can be connected to. In the case of the zone, an arbitrary number of walls and heat exchangers can be connected. A state space description is also defined for each model in the standard form

$$\dot{\mathbf{x}}(t) = \mathbf{A}\mathbf{x}(t) + \mathbf{B}\mathbf{u}(t), \tag{12.1a}$$

$$\mathbf{y}(t) = \mathbf{C}\mathbf{x}(t) + \mathbf{D}\mathbf{u}(t), \tag{12.1b}$$

where all matrices and vectors have appropriate dimensions.

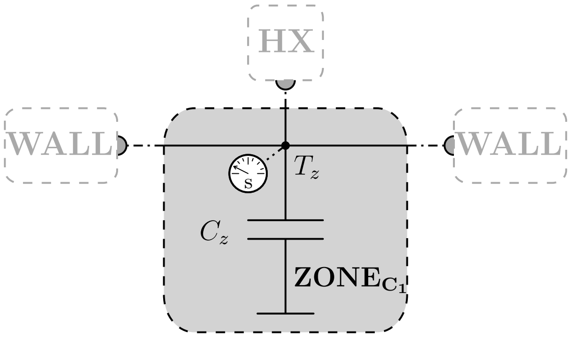

Figure 12.1.: Zone submodel with its one-capacity thermodynamic circuit. There can be seen other submodels connected (grey coloured). The submodel HX denotes a heat exchanger. The node T_z is considered a measured point (a sensor being applied), which is marked with a white analogue gauge.

Specifically, a state space description for the zone submodel is then given by matrices

$$A = 0, \quad \mathbf{B} = \begin{bmatrix} \frac{1}{C_z} & \dots & \frac{1}{C_z} \end{bmatrix}, \quad C = 1, \quad \mathbf{D} = \mathbf{0}^{\mathrm{T}} \tag{12.2}$$

with a state and input vector

$$x = T_z, \quad \mathbf{u} = \begin{bmatrix} q_1 & \dots & q_{N_z} \end{bmatrix}^{\mathrm{T}}. \tag{12.3}$$

The inputs $q_i, i = 1, \dots, N_z$ in (12.3) represent all modelled heat flows entering the zone, both from adjacent zones, outside and heat exchangers.

Let the objects be discussed in more detail. Despite the attractive simplicity of the one-capacity zone submodel, typically walls (generally all solid objects) have their own significant thermal capacity, i.e. they have their own inner states, which can, however, be hardly measured. On the other hand, if walls were modelled with capacities and resistances, the overall number of unknown parameters of the final grey-box model would significantly increase, which would make the identification problem very difficult to solve or it would require to have additional measurements available.

Therefore, a more complex model will be introduced. This model takes into account there exist other capacities which influence a zone (walls etc., as aforementioned). These other existing capacities are aggregated into one other heat capacity C_s, which is depicted in the zone circuit of this submodel in the Fig. 12.2.

Considering these two capacities (which implies two states), an air temperature measurement (i.e. the system output y) in real case is a non-negative combination of these two states

$$y = \alpha T_z + \beta T_s, \quad \{\alpha,\beta\} \in [0,1]\,.‘ \tag{12.4}$$

This system output (12.4) represents an "operative temperature" and is denoted further as T_{op} – as it can be seen in . Fig. 12.2.

The state space model of this submodel is then described as follows

$$A = \begin{bmatrix} -\frac{U_s}{C_z} & \frac{U_s}{C_z} \\ \frac{U_s}{C_s} & -\frac{U_s}{C_s} \end{bmatrix}, \tag{12.5a}$$

$$B = \begin{bmatrix} \frac{1}{C_z} & \dots & \frac{1}{C_z} & 0 & \dots & 0 \\ 0 & \dots & 0 & \frac{1}{C_s} & \dots & \frac{1}{C_s} \end{bmatrix}, \tag{12.5b}$$

$$C = \begin{bmatrix} \alpha & \beta \end{bmatrix}, \quad D = \mathbf{0}^{\mathrm{T}}, \tag{12.5c}$$

where the parameter U_s is a virtual thermal conductance between the two states representing a conductance between

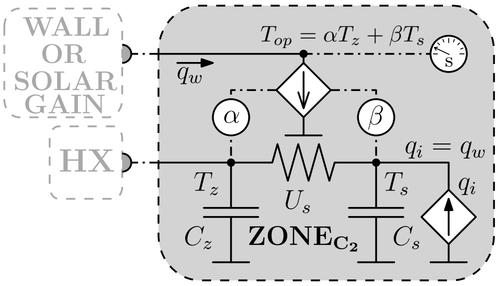

Figure 12.2.: Two-capacity zone submodel with its thermodynamic circuit. White squares with arrows up or down represent controlled sources (analogical to the electrical domain). The white square with the arrow heading up is a controlled source of heat flow and the one with the arrow down is a controlled source of temperature.

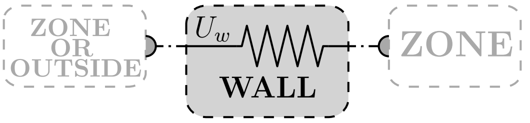

Figure 12.3.: Wall submodel with a thermodynamic circuit. The wall can divide off two adjacent zones or a zone with the outside environment.

zone air and solid objects.

A corresponding state and input vector are

$$x = \begin{bmatrix} T_\mathrm{z} \\ T_\mathrm{s} \end{bmatrix}, \quad u = \begin{bmatrix} q_{\mathrm{hx}_1} & \dots & q_{\mathrm{hx}_{N_\mathrm{hx}}} & q_{\mathrm{w}_1} & \dots & q_{\mathrm{w}_{N_\mathrm{w}}} \end{bmatrix}^\mathrm{T}. \tag{12.6}$$

Another important submodel which participates in the final grey-box model is a wall submodel.

Using its thermodynamic circuit in the Fig. 12.3, following state space model can be derived (in fact it is a simple static model, since there is no dynamic element)

$$A = \emptyset, \quad B = \emptyset, \quad C = \emptyset, \quad D = \begin{bmatrix} U_\mathrm{w} & -U_\mathrm{w} \end{bmatrix}, \tag{12.7a}$$

$$x = \emptyset, \quad u = \begin{bmatrix} T_{\mathrm{z}_\mathrm{n}} & T_\mathrm{z} \end{bmatrix}^\mathrm{T} \text{or} \begin{bmatrix} T_{\mathrm{s}_\mathrm{n}} & T_\mathrm{s} \end{bmatrix}^\mathrm{T}. \tag{12.7b}$$

The wall state space model (12.7) is considered from the view of the zone (zone C_2) submodel with the state T_z (T_s) neighbouring on the zone with the state $T_{\mathrm{z}_\mathrm{n}}$ ($T_{\mathrm{s}_\mathrm{n}}$), respectively.

The last three submodels, which leave, the heat exchanger, solar gain and outside, are modelled with no dynamics. The *heat exchanger* (Fig. 12.4) is just an ideal source of heat flow and the *outside* is an ideal source of temperature (Fig. 12.5). Therefore their state space model is simply following

$$A = \emptyset, \quad B = \emptyset, \quad C = \emptyset, \quad D = 1 \tag{12.8}$$

with no states $x = \emptyset$ and an input vector $u = q_\mathrm{hx}$ for the heat exchanger and $u = T_\mathrm{o}$ for the outside submodel.

The *solar gain* (Fig. 12.6) submodel is very similar to the *heat exchanger*. It has no dynamics either, the only difference is that the heat flow does not enter the zone in full extent but it is reduced by a so called shading factor s_f. This factor represents the fact that a certain portion of solar irradiation is shaded and does not influence the zone air

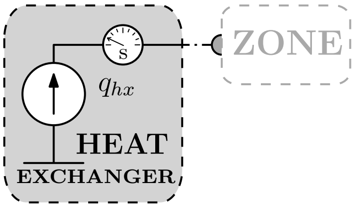

Figure 12.4.: Heat exchanger submodel with a thermodynamic circuit.

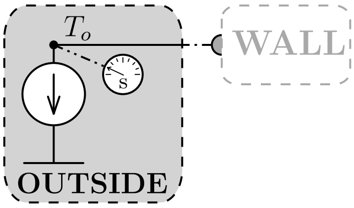

Figure 12.5.: Outside environment submodel with a thermodynamic circuit.

temperature. The state space model is thus given by

$$A = \emptyset, \quad B = \emptyset, \quad C = \emptyset, \quad D = s_\mathrm{f}, \tag{12.9}$$

with no states $x = \emptyset$ and an input vector $u = q_\mathrm{sg}$ for the solar gain, where the shading factor is naturally limited to: $s_\mathrm{f} \in [0,1]$.

12.2.4. Submodel merging

In general, in order to build a proper desired grey-box model, a set containing all submodels presented earlier is defined as

$$\mathcal{M} = \{Z_{\mathrm{c}_1}, Z_{\mathrm{c}_2}, W, H, S, O\}, \tag{12.10}$$

where Z_{c_1} stands for the one-capacity zone submodel (see (12.2), (12.3) and Fig. 12.1), Z_{c_2} stands for the two-capacity zone submodel (see (12.5), (12.6) and Fig. 12.2), W stands for the wall submodel (see (12.7) and Fig. 12.3), H stands for the heat exchanger submodel (see (12.8) and Fig. 12.4), S stands for the solar gain submodel (see (12.8) and Fig. 12.6) and O stands for the outside submodel (see (12.8) and Fig. 12.5).
Besides the set $\mathcal{M}$, there is also a set of rules, which defines what submodels may be interconnected.
Using the submodel set $\mathcal{M}$ (12.10) and the set of rules (presented at the Tab. 12.1) it is possible to create a grey-box model which models a zone. Such an example is pictured in Fig. 12.7.

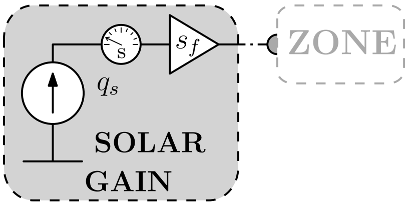

Figure 12.6.: Example of the solar gain submodel with a thermodynamic circuit consisting of the ideal source of heat flow, which is measured, and a shading factor that reduces this heat flow entering the zone.

Submodel (abbreviation)	Might be connected to	Maximal number of connections
One-capacity zone (Z_{c_1})	W, H	∞
Two-capacity zone (Z_{c_2})	W, H	∞
Wall (W)	Z_{c_1}, Z_{c_2}, O	2
Heat exchanger (H)	Z_{c_1}, Z_{c_2}	1
Solar gain (S)	Z_{c_1}, Z_{c_2}	1
Outside (O)	W	1

Table 12.1.: Set of interconnection rules for the submodels $\mathcal{M}$.

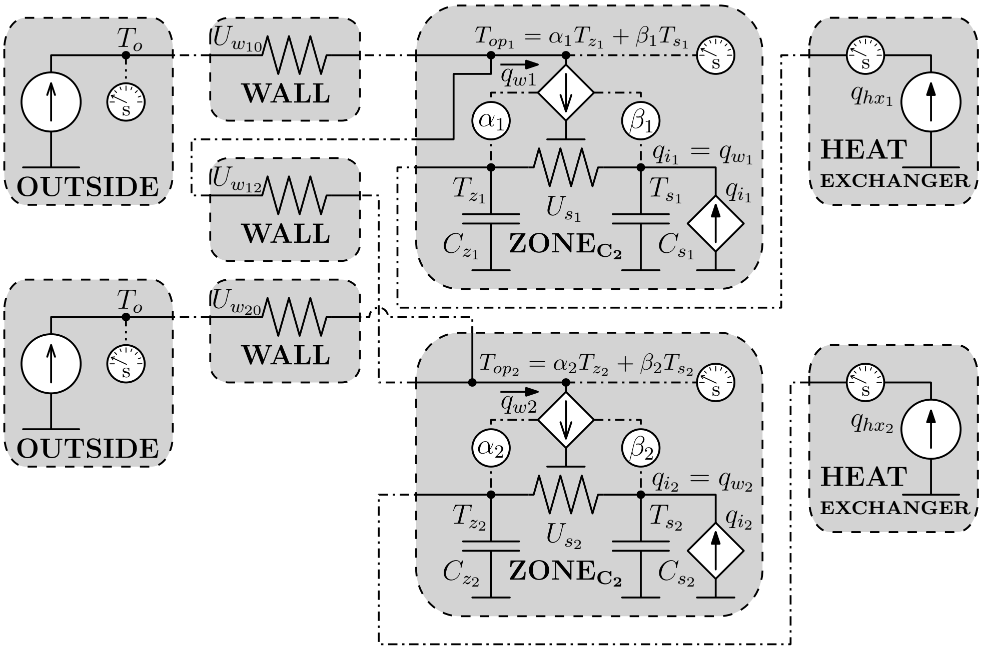

Figure 12.7.: Example of merged submodels forming a two-zone building.

As soon as the submodels are interconnected, their corresponding grey-box models are appropriately merged (using an interconnection matrix, which describes inner input-output connections) forming a new big grey-box model of the whole room (zone). The merging of linear submodels is dealt with in [217, 218]. The exact algorithm, developed independently, is listed in Chapter C.

Therefore, the upper zone's (labelled with number 1) continuous-time grey-box model in the Fig. 12.7 is described by

$$\mathbf{A}_\mathrm{c} = \begin{bmatrix} -\frac{U_{\mathrm{s}_1}}{C_{\mathrm{z}_1}} & -\frac{U_{\mathrm{s}_1}}{C_{\mathrm{z}_1}} \\ \frac{U_{\mathrm{s}_1}}{C_{\mathrm{s}_1}} & -\frac{1}{C_{\mathrm{s}_1}}\left(U_{\mathrm{w}_{10}} + U_{\mathrm{w}_{12}} + U_{\mathrm{s}_1}\right) \end{bmatrix}, \tag{12.11a}$$

$$\mathbf{B}_\mathrm{c} = \begin{bmatrix} \frac{1}{C_{\mathrm{z}_1}} & 0 & 0 \\ 0 & \frac{U_{\mathrm{w}_{12}}}{C_{\mathrm{s}_1}} & \frac{U_{\mathrm{w}_{10}}}{C_{\mathrm{s}_1}} \end{bmatrix}, \tag{12.11b}$$

$$\mathbf{C}_\mathrm{c} = \begin{bmatrix} \alpha_1 & \beta_1 \end{bmatrix}, \quad \mathbf{D}_\mathrm{c} = \begin{bmatrix} 0 & 0 & 0 \end{bmatrix}. \tag{12.11c}$$

The second grey-box zone model is very similar and analogous to the first one (12.11), thus it will not be presented.

12.3. Parameter estimation

The parameters U and C contained in state space models are naturally unknown and are to be identified. All the parameters are now incorporated into a vector form of the unknown parameters

$$\begin{aligned} &\boldsymbol{\theta} = \begin{bmatrix} C_\mathrm{z}, & (C_\mathrm{s}), & (U_\mathrm{s}), & U_{\mathrm{w}_1}, & \dots & ,U_{\mathrm{w}_{n\mathrm{w}}}, & s_\mathrm{f}, & (\alpha), & (\beta) \end{bmatrix}^\mathrm{T} \\ &\boldsymbol{\theta} \in \mathbb{R}^{n_\theta \times 1}, \quad \boldsymbol{\theta} \succ \mathbf{0}, \end{aligned} \tag{12.12}$$

where the elements in brackets are taken into account only in the two-capacity case (Fig. 12.2). The state space descriptions with particular parameters like (12.11) can now be generally parametrized by the parameter $\boldsymbol{\theta}$ (the matrix $\boldsymbol{D}$ is omitted since it is equal to a zero vector), hence the continuous time grey-box model is obtained in a form

$$\dot{\mathbf{x}}(t) = \mathbf{A}_\mathrm{c}(\boldsymbol{\theta})\mathbf{x}(t) + \mathbf{B}_\mathrm{c}(\boldsymbol{\theta})\mathbf{u}(t), \tag{12.13a}$$

$$y(t) = \mathbf{C}_\mathrm{c}(\boldsymbol{\theta})\mathbf{x}(t). \tag{12.13b}$$

Usually, the measured data are measured not continuously but with a discrete time step T_s. Therefore the model (12.13) is discretized as in [177], giving

$$\mathbf{x}_{k+1}(\boldsymbol{\theta}) = \mathbf{A}(\boldsymbol{\theta})\,\mathbf{x}_k(\boldsymbol{\theta}) + \mathbf{B}(\boldsymbol{\theta})\,\mathbf{u}_k, \tag{12.14a}$$

$$\hat{y}_k(\boldsymbol{\theta}) = \mathbf{C}(\boldsymbol{\theta})\mathbf{x}_k(\boldsymbol{\theta}). \tag{12.14b}$$

Substituting parameter $\boldsymbol{\theta}$ with particular real values, one obtains from (12.14) an output estimate (which equals to the zone temperature estimate). Naturally, the parameter values, for which the resulting estimate is the most closely to the actual measurement, are the ones which are searched for. Hence, the optimization problem can be formulated as a (non-linear) Least Square Estimation (LSE)

$$\boldsymbol{\theta}^* = \arg\min_{\boldsymbol{\theta}} V(\boldsymbol{\theta}) = \arg\min_{\boldsymbol{\theta}} \frac{1}{2}\mathcal{E}(\boldsymbol{\theta})^\mathrm{T}\,\mathcal{E}(\boldsymbol{\theta}), \tag{12.15}$$

where an error vector is given by

$$\mathcal{E}(\boldsymbol{\theta}) = \mathbf{Y} - \hat{\mathbf{Y}}(\boldsymbol{\theta}) = \mathbf{Y} - \left(\mathbf{C}(\boldsymbol{\theta})\hat{\mathbf{X}}(\boldsymbol{\theta})\right)^\mathrm{T} \tag{12.16}$$

and where the matrix of state predictions $\hat{\mathbf{X}}(\boldsymbol{\theta}) \in \mathbb{R}^{n\times K}$ is formed as

$$\hat{\mathbf{X}}(\boldsymbol{\theta}) = \begin{bmatrix}\hat{\mathbf{x}}_0(\boldsymbol{\theta}) & \dots & \hat{\mathbf{x}}_{K-1}(\boldsymbol{\theta})\end{bmatrix}. \tag{12.17}$$

The output estimate vector can be directly expressed as

$$\hat{\mathbf{Y}}(\boldsymbol{\theta}) = \begin{bmatrix}\hat{y}_1(\boldsymbol{\theta})\\ \hat{y}_2(\boldsymbol{\theta})\\ \vdots\\ \hat{y}_K(\boldsymbol{\theta})\end{bmatrix} = \begin{bmatrix}\mathbf{CA}\\ \mathbf{CA}^2\\ \vdots\\ \mathbf{CA}^K\end{bmatrix}\mathbf{x_0} + \\ + \begin{bmatrix}\mathbf{CB} & 0 & \dots & 0\\ \mathbf{CAB} & \mathbf{CB} & \dots & 0\\ \vdots & \vdots & \ddots & \vdots\\ \mathbf{CA}^{K-1}\mathbf{B} & \mathbf{CA}^{K-2}\mathbf{B} & \dots & \mathbf{CB}\end{bmatrix}\begin{bmatrix}\mathbf{u_0}\\ \mathbf{u_1}\\ \vdots\\ \mathbf{u_{K-1}}\end{bmatrix}, \tag{12.18}$$

where all three matrices **A**,**B** and **C** are function of $\boldsymbol{\theta}$.

It can be seen at (12.18) that the longer the measured data **Y** are, the more complex the estimation becomes. On the other hand, longer data carry more information about the system, thus it is always a trade-off between the data length and problem complexity. Another issue is that there is different sensitivity of a parameter change to the output estimation; the data must be such that with a single parameter variation, the final estimate varies as well.

Since the expected final numerical values of parameter $\boldsymbol{\theta}$ are completely in different scales (capacities vs conductances), the parameter values during an optimization search are normalized to be approximately in the same order of magnitude. Hence,

$$\boldsymbol{\theta} = \mathbf{N}\boldsymbol{\theta}_{\mathrm{n}}, \tag{12.19}$$

where $\mathbf{N} \in \mathbb{R}^{n_\theta\times n_\theta}$ is a diagonal matrix with scale values on its main diagonal.

The last enhancement, which makes the optimization problem (12.15) more likely to reach a true global optimum rather than local "false" ones, consists in restricting the individual elements of $\boldsymbol{\theta}$ to a certain search range based on prior knowledge of a building; i.e. it is expected that the capacities "fall" into a certain value range as well as the conductances. Therefore each parameter element is enclosed within a lower and upper bound for the optimization search, which can be formulated as

$$\begin{aligned} &\underset{\boldsymbol{\theta}}{\text{minimize}} && \frac{1}{2}\mathcal{E}(\boldsymbol{\theta})^{\mathrm{T}}\mathcal{E}(\boldsymbol{\theta}),\\ &\text{subject to} && \theta_i \in [\theta_{\mathrm{LB}_i},\theta_{\mathrm{UB}_i}], \quad i = 1,\dots,n_\theta. \end{aligned} \tag{12.20}$$

12.4. Distributed identification

In the previous sections the parameter estimation problem of a zone was described. However, the main goal is to identify or calibrate the model of the whole building.

There are parameters shared by more zones; specifically, it is a case of mutual walls' conductances. If separated local zone parameter estimations had been performed only, these shared parameters would have had different optimal values in adjacent zones. As a result, such a building model would have contained inconsistency.

Therefore, it is necessary to apply such additional measures that would ensure and bring back the desired model consistency. This is achieved by an equality requirement on the shared (public or complicating) variables. A so-called dual decomposition is used [208].

In general, there is an N-zone building identification problem in a form

$$\begin{aligned}
\min_{\boldsymbol{\Theta}} \quad & \sum_{i=1}^{N} V_i\left(\boldsymbol{\theta}_{i_l}, \boldsymbol{\theta}_{i_s}\right), \\
\text{s. t.} \quad & \boldsymbol{\Theta}_s = \mathbf{E}\mathbf{z}, && (12.21) \\
& \boldsymbol{\theta}_i \in \left[\boldsymbol{\theta}_{\mathrm{LB}_i}, \boldsymbol{\theta}_{\mathrm{UB}_i}\right], \quad i = 1, \ldots, N, && (12.22)
\end{aligned}$$

where the equation (12.21) represents consistency constraints, in which $\boldsymbol{\Theta}_s \in \mathbb{R}^{2n_z \times 1}$ is a vector of shared variables from all subsystems, $\mathbf{z} \in \mathbb{R}^{n_z \times 1}$ is a vector that gives the common values of the shared variables in each consistency constraint [208], finally, the matrix $\mathbf{E} \in \mathbb{R}^{2n_z \times n_z}$ is defined as

$$E_{ij} = \begin{cases} 1 & \Theta_{s_i} \text{ is in a constraint } j \\ 0 & \text{otherwise.} \end{cases} \tag{12.23}$$

Using Lagrange multiplicators it is possible to incorporate consistency constraints and formulate a dual optimization problem to the primal one (12.22), which yields completely separable local subproblems

$$\begin{aligned}
q_i(\boldsymbol{\lambda}_i) &= \min_{\boldsymbol{\theta}_i} F_i(\boldsymbol{\theta}_i) = \min_{\boldsymbol{\theta}_{i_l}, \boldsymbol{\theta}_{i_s}} V_i(\boldsymbol{\theta}_{i_l}, \boldsymbol{\theta}_{i_s}) + \boldsymbol{\lambda}_i^{\mathrm{T}} \boldsymbol{\theta}_{i_s}, \\
i &= 1, \ldots, N && (12.24)
\end{aligned}$$

and a dual global (master) problem

$$\begin{aligned}
\underset{\boldsymbol{\lambda}}{\text{maximize}} \quad & q(\boldsymbol{\lambda}) = \sum_{i=1}^{N} q_i(\boldsymbol{\lambda}_i), \\
\text{subject to} \quad & \mathbf{E}^{\mathrm{T}} \boldsymbol{\lambda} = \mathbf{0}. && (12.25)
\end{aligned}$$

The cost function of the local subproblem (12.24) contains a function $V(\boldsymbol{\theta})$, which is a cost function from the problem (12.20).

12.4.1. Analytic gradient computation

The local subproblems (12.24) can be solved by standard methods. However, since they are non-linear intrinsically, a computational cost can be reduced by providing the solvers with a gradient (Jacobian matrix). Therefore, an analytic form of the gradient will be derived.

A gradient (or generally a Jacobian matrix) of the cost function represents its sensitivity to parameter changes. Let's denote it as $\mathbf{J}(\boldsymbol{\theta}) \in \mathbb{R}^{1 \times n_\theta}$ and differentiate $F(\boldsymbol{\theta})$ from (12.24) with respect to $\boldsymbol{\theta}^{\mathrm{T}}$ (the transpose denotes here only that the differentiation by $\boldsymbol{\theta}$ is projected into the result row-wisely)

$$\mathbf{J}(\boldsymbol{\theta}) = \frac{\partial F(\boldsymbol{\theta})}{\partial \boldsymbol{\theta}^{\mathrm{T}}} = -\mathcal{E}(\boldsymbol{\theta})^{\mathrm{T}} \frac{\partial \hat{\mathbf{Y}}(\boldsymbol{\theta})}{\partial \boldsymbol{\theta}^{\mathrm{T}}} + \boldsymbol{\lambda}^{\mathrm{T}}. \tag{12.26}$$

It can be seen the red written term in (12.26) is essential for the gradient computation and needs to be further derived (the steps of derivation follow [219]). This matrix $\frac{\partial \hat{\mathbf{Y}}(\boldsymbol{\theta})}{\partial \boldsymbol{\theta}^{\mathrm{T}}} \in \mathbb{R}^{K \times n_\theta}$ represents output parameter sensitivity and using (12.16) it is obtained

$$\frac{\partial \hat{\mathbf{Y}}(\boldsymbol{\theta})}{\partial \boldsymbol{\theta}^{\mathrm{T}}} = \frac{\partial}{\partial \boldsymbol{\theta}^{\mathrm{T}}} \left(\mathbf{C}(\boldsymbol{\theta}) \hat{\mathbf{X}}(\boldsymbol{\theta})\right)^{\mathrm{T}} \simeq \hat{\mathbf{X}}(\boldsymbol{\theta})^{\mathrm{T}} \frac{\partial \mathbf{C}(\boldsymbol{\theta})^{\mathrm{T}}}{\partial \boldsymbol{\theta}^{\mathrm{T}}} + \frac{\partial \hat{\mathbf{X}}(\boldsymbol{\theta})^{\mathrm{T}}}{\partial \boldsymbol{\theta}^{\mathrm{T}}} \mathbf{C}^{\mathrm{T}}, \tag{12.27}$$

where the term $\frac{\partial \hat{\mathbf{X}}(\boldsymbol{\theta})^{\mathrm{T}}}{\partial \boldsymbol{\theta}^{\mathrm{T}}} \in \mathbb{R}^{K \times n \times n_\theta}$ would be a "cubic matrix" generally. Hence, the second part of the term in (12.27) with the state sensitivity matrix must be differentiated with respect to individual parameters separately

$$\frac{\partial \hat{\mathbf{X}}(\boldsymbol{\theta})^{\mathrm{T}}}{\partial \theta_i}\mathbf{C}(\boldsymbol{\theta})^{\mathrm{T}} = \boldsymbol{\mathcal{X}}_i(\boldsymbol{\theta})^{\mathrm{T}}\mathbf{C}(\boldsymbol{\theta})^{\mathrm{T}}, \quad i = 1, \dots, n_\theta \tag{12.28}$$

and then the output sensitivity vector is assembled as

$$\frac{\partial \hat{\mathbf{Y}}(\boldsymbol{\theta})}{\partial \theta_i} = \hat{\mathbf{X}}(\boldsymbol{\theta})^{\mathrm{T}}\frac{\partial \mathbf{C}(\boldsymbol{\theta})^{\mathrm{T}}}{\partial \theta_i} + \boldsymbol{\mathcal{X}}_i(\boldsymbol{\theta})^{\mathrm{T}}\mathbf{C}^{\mathrm{T}}. \tag{12.29}$$

The matrix $\boldsymbol{\mathcal{X}}_i(\boldsymbol{\theta}) \in \mathbb{R}^{n\times K}$ is formed from state sensitivities to a parameter θ_i

$$\boldsymbol{\mathcal{X}}_i(\boldsymbol{\theta}) = \begin{bmatrix}\boldsymbol{\xi}_1^i(\boldsymbol{\theta}) & \dots & \boldsymbol{\xi}_K^i(\boldsymbol{\theta})\end{bmatrix}, \quad \boldsymbol{\xi}_k^i(\boldsymbol{\theta}) = \frac{\partial}{\partial \theta_i}\hat{\mathbf{x}}_k(\boldsymbol{\theta}). \tag{12.30}$$

It is needed to express state sensitivities $\boldsymbol{\xi}_k^i(\boldsymbol{\theta})$. In order to achieve this, the discrete-time GBM predictor is utilized

$$\begin{aligned}\boldsymbol{\xi}_{k+1}^i(\boldsymbol{\theta}) &= \frac{\partial}{\partial \theta_i}\hat{\mathbf{x}}_{k+1}(\boldsymbol{\theta}) = \frac{\partial}{\partial \theta_i}\left(\mathbf{A}(\boldsymbol{\theta}) \cdot \hat{\mathbf{x}}_k(\boldsymbol{\theta})\right) + \frac{\partial \mathbf{B}(\boldsymbol{\theta})}{\partial \theta_i}\mathbf{u}_k \\ &= \frac{\partial \mathbf{A}(\boldsymbol{\theta})}{\partial \theta_i}\hat{\mathbf{x}}_k(\boldsymbol{\theta}) + \mathbf{A}(\boldsymbol{\theta})\underbrace{\frac{\partial \hat{\mathbf{x}}_k(\boldsymbol{\theta})}{\partial \theta_i}}_{\boldsymbol{\xi}_k^i(\boldsymbol{\theta})} + \frac{\partial \mathbf{B}(\boldsymbol{\theta})}{\partial \theta_i}\mathbf{u}_k \\ &= \mathbf{A}_i(\boldsymbol{\theta})\hat{\mathbf{x}}_k(\boldsymbol{\theta}) + \mathbf{A}(\boldsymbol{\theta})\boldsymbol{\xi}_k^i(\boldsymbol{\theta}) + \mathbf{B}_i(\boldsymbol{\theta})\mathbf{u}_k.\end{aligned} \tag{12.31}$$

The equation (12.31) can be understood as an extended discrete-time LTI system for the state prediction $\hat{\mathbf{x}}(\boldsymbol{\theta})$ and state sensitivity $\boldsymbol{\xi}^i(\boldsymbol{\theta})$. This extended system can be written in the standard state space matrix form

$$\begin{aligned}\begin{bmatrix}\hat{\mathbf{x}}_{k+1} \\ \boldsymbol{\xi}_{k+1}^i\end{bmatrix} &= \begin{bmatrix}\mathbf{A}(\boldsymbol{\theta}) & \mathbf{0} \\ \mathbf{A}_i(\boldsymbol{\theta}) & \mathbf{A}(\boldsymbol{\theta})\end{bmatrix}\begin{bmatrix}\hat{\mathbf{x}}_k \\ \boldsymbol{\xi}_k^i\end{bmatrix} + \begin{bmatrix}\mathbf{B}(\boldsymbol{\theta}) \\ \mathbf{B}_i(\boldsymbol{\theta})\end{bmatrix}\mathbf{u}_k, \\ i &= 1, \dots, n_\theta, \\ \hat{y}_k &= \begin{bmatrix}\mathbf{C}(\boldsymbol{\theta}) & \mathbf{0}^{\mathrm{T}}\end{bmatrix}\begin{bmatrix}\hat{\mathbf{x}}_k \\ \boldsymbol{\xi}_k^i\end{bmatrix}, \\ \begin{bmatrix}\hat{\mathbf{x}}_0 \\ \boldsymbol{\xi}_0^i\end{bmatrix} &= \begin{bmatrix}\mathbf{x}_0 \\ \mathbf{0}\end{bmatrix}.\end{aligned} \tag{12.32}$$

Using this extended system (12.32), both state predictions and state sensitivities can be computed. The last thing remaining to be determined are derivatives of discrete-time matrices $\mathbf{A}_i(\boldsymbol{\theta})$ and $\mathbf{B}_i(\boldsymbol{\theta})$.
An approach from [177] is applied to achieve discrete-time system matrices $\mathbf{A}(\theta)$,$\mathbf{B}(\theta)$ and their derivatives for the extended system (12.32)

$$\begin{aligned}&\left[\begin{array}{cc|c}\mathbf{A}(\boldsymbol{\theta}) & \mathbf{0} & \mathbf{B}(\boldsymbol{\theta}) \\ \mathbf{A}_i(\boldsymbol{\theta}) & \mathbf{A}(\boldsymbol{\theta}) & \mathbf{B}_i(\boldsymbol{\theta}) \\ \hline \mathbf{0} & \mathbf{0} & \mathbf{I}\end{array}\right] = \\ &= \exp\left(\left[\begin{array}{cc|c}\mathbf{A}_{\mathrm{c}}(\boldsymbol{\theta}) & \mathbf{0} & \mathbf{B}_{\mathrm{c}}(\boldsymbol{\theta}) \\ \mathbf{A}_{\mathrm{c}_i}(\boldsymbol{\theta}) & \mathbf{A}_{\mathrm{c}}(\boldsymbol{\theta}) & \mathbf{B}_{\mathrm{c}_i}(\boldsymbol{\theta}) \\ \hline \mathbf{0} & \mathbf{0} & \mathbf{0}\end{array}\right]T_{\mathrm{s}}\right), \\ &i = 1, \dots, n_\theta,\end{aligned} \tag{12.33}$$

where

$$\mathbf{A}_{\mathrm{c}_i}(\boldsymbol{\theta}) = \frac{\partial \mathbf{A}_{\mathrm{c}}(\boldsymbol{\theta})}{\partial \theta_i} \quad \text{and} \quad \mathbf{B}_{\mathrm{c}_i}(\boldsymbol{\theta}) = \frac{\partial \mathbf{B}_{\mathrm{c}}(\boldsymbol{\theta})}{\partial \theta_i} \tag{12.34}$$

are derivatives of continuous-time matrices with respect to individual parameters.

The ubiquitous parameter vector $\boldsymbol{\theta}$ in parentheses within this whole section emphasizes the fact that all the quantities are functions of $\boldsymbol{\theta}$. In particular, this means for them to be evaluated every time again for new parameter values during iterations of the local optimization problem (12.24).

12.4.2. Global optimization problem

The global problem (12.25) can be solved by a projected sub-gradient iterative method

$$\boldsymbol{\lambda}^{k+1} = \boldsymbol{\lambda}^k + \alpha^k \underbrace{\left(\mathbf{I} - \mathbf{E}\left(\mathbf{E}^{\mathrm{T}}\mathbf{E}\right)^{-1}\mathbf{E}^{\mathrm{T}}\right)}_{P}\boldsymbol{\Theta}_s^{k*}, \tag{12.35}$$

where P is a projection operator onto a feasible set $\mathbf{E}^{\mathrm{T}}\boldsymbol{\lambda} = \mathbf{0}$ and α^k is a step size in the k-th iteration. Various step size rules for α might be applied; more on that can be found in [220].

In the particular case of the proposed building identification the projector P in (12.35) reduces to a shared variable "difference from average" operator. It calculates an average of two local copies of a shared variable and this average is then subtracted from the local copy itself. This is then multiplied by a step factor α and added to a previous value of the price $\boldsymbol{\lambda}$. Hence, corresponding prices (dual variables) of one shared variable have always equal absolute value and only differ by a sign from each other.

A solution to the local subproblems (12.24) and the dual global problem (12.25) can be summarized and described by an algorithm (see Alg. 12.1).

Furthermore, there is a definition of a consistency constraint residual at the line 8 in the Alg. 12.1. This quantity can be used as a measure of the shared variables consistency

Algorithm 12.1 Dual decomposition - hypergraph form. More details can be found in [208].

Input: Initial dual variable vector λ^0 satisfying $E^{\mathrm{T}}\lambda = 0$ (e.g. $\lambda = 0$)

Output: Estimate λ^K at K-th iteration (and primal variables y^*)

```
 1: for $k = 0$ to $K$ do
 2:   for $i = 1$ to $N$ do
        % Distribute multipliers (prices) to subproblems
 3:     $\lambda^k \rightarrow \lambda_i^k$
        % Solve a subproblem and return its sub-gradient
 4:     Solve $q_i(\lambda_i^k)$ and return $\theta_{i_s}^{k*}$
 5:   end for
      % Compute average of shared variables over each net
 6:   $\hat{z}^k = \left(E^{\mathrm{T}}E\right)^{-1} E^{\mathrm{T}}\Theta_s^{k*}$
      % Update the dual variables (prices)
 7:   $\lambda^{k+1} = \lambda^k + \alpha^k\left(\Theta_s^{k*} - E\hat{z}^k\right)$
      % Compute the norm of consistency constraint residual
 8:   $r^k = \left\|\Theta_s^{k*} - E\hat{z}^k\right\|_2$
 9:   if $r^k < r_{\mathrm{THRES}}$ then
10:     break
11:   end if
12: end for
```

12.5. Results and discussion

Two examples are discussed and analysed.

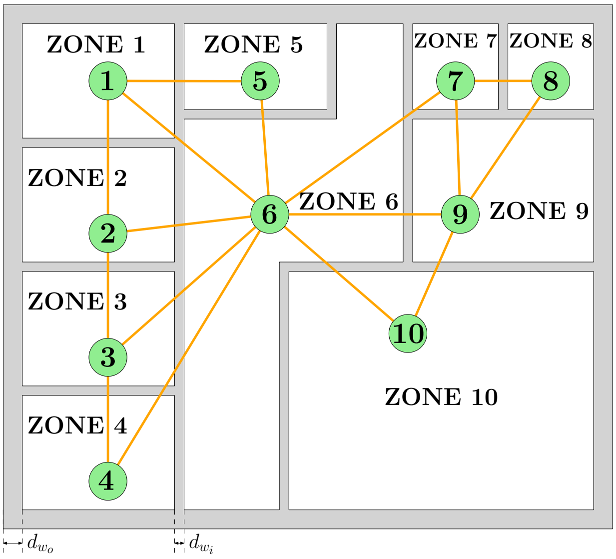

Figure 12.8.: Floor plan of the trivial case example building with its adjacency graph. Walls are grey coloured. Outer dimensions of this building are approximately 35 × 29 meters. Room dimensions and inner (outer) wall widths d_{w_i} (d_{w_o}) were used to calculate true parameter values.

12.5.1. Trivial case

The first one is a basic case which is formed by a Simulink 10-zone building model. Its thermodynamics is modelled using one-capacity zones, walls, heat exchangers and outside environment as it was presented in the Sec. 12.2.2. Since the used GBM structure exactly coincides with the simulation model, the found parameters should correspond very closely with the simulation ones. Therefore, this example is a trivial case which serves as a basic proof and illustrates the proper function of the distributed GBM calibration.

A floor plan of such a building can be seen in the Fig. 12.8. In this figure, there is also depicted a graph of zones' adjacency (interconnection) - ten green coloured nodes, which represent zones are interconnected with sixteen edges, which represent mutual walls.

Each edge (mutual wall) brings one more shared variable to the GBM calibration problem. The next logical step is the creation of local GBMs using the submodel merging. As aforementioned, a core of the local GBM is formed by a one-capacity zone submodel (Fig. 12.1), to which are connected inner or outer walls (Fig. 12.3) and a heat exchanger (Fig. 12.4). The final local GBMs, connected together, representing the whole building are pictured in the Fig. 12.9.

A state space description of zone 1, presented as an example (other zones have analogical model), is given by

$$\begin{aligned}\dot{T}_{\mathrm{z}_1} &= -\frac{1}{C_{\mathrm{z}_1}}\left(U_{12} + U_{15} + U_{16} + U_{10}\right) T_{\mathrm{z}_1} \\ &\quad + \frac{1}{C_{\mathrm{z}_1}}\begin{bmatrix} 1 & U_{12} & U_{15} & U_{16} & U_{10}\end{bmatrix}\begin{bmatrix} q_{\mathrm{hx}_1} \\ T_{\mathrm{z}_2} \\ T_{\mathrm{z}_5} \\ T_{\mathrm{z}_6} \\ T_{\mathrm{o}}\end{bmatrix}, \qquad (12.36\mathrm{a})\\ y &= T_{\mathrm{z}_1}. \qquad (12.36\mathrm{b})\end{aligned}$$

Blue-coloured variables correspond to blue submodels in the Fig. 12.9 and represent the shared variables.

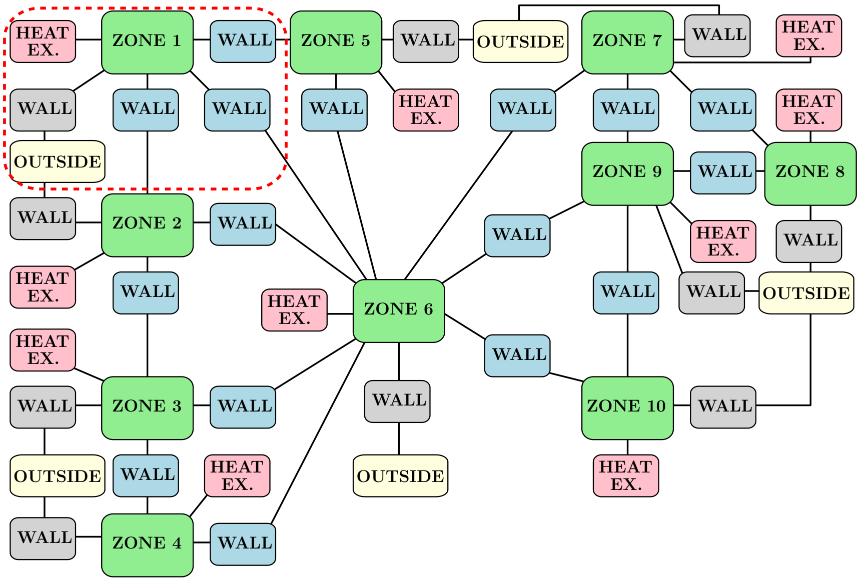

Figure 12.9.: The trivial case local GBMs, which were created by submodel merging. Mutual walls with shared variables are light blue highlighted. A model that pertains to Zone 1, is selected as a local GBM example and its borders are marked with a red colour. The corresponding state space description is presented at (12.36). Other local models are analogous.

θ_7	True	Identified	Difference [%]	θ_9	True	Identified	Difference [%]
C_{z_7}	34525	34743	0.63	C_{z_9}	136130	136953	0.61
U_{67}	44.38	44.31	0.16	U_{69}	87.49	87.20	0.33
U_{78}	44.38	44.42	0.09	U_{79}	44.38	44.39	0.02
U_{79}	44.38	44.39	0.02	U_{89}	44.38	44.42	0.09
U_{70}	16.64	16.65	0.06	U_{910}	88.76	88.85	0.10
–	-	-	-	U_{90}	32.81	32.83	0.06
θ_8	True	Identified	Difference [%]	θ_{10}	True	Identified	Difference [%]
C_{z_8}	34525	34814	0.84	$C_{z_{10}}$	468980	466868	0.45
U_{78}	44.38	44.42	0.09	U_{610}	247.25	247.16	0.04
U_{89}	44.38	44.42	0.09	U_{910}	88.76	88.85	0.10
U_{80}	33.28	33.29	0.03	U_{100}	125.53	125.54	0.01

Table 12.2.: True and identified values of GBM parameters (zones 7-10) with their corresponding relative differences in the trivial case. The capacities C are stated in J/K and conductances U in W/K.

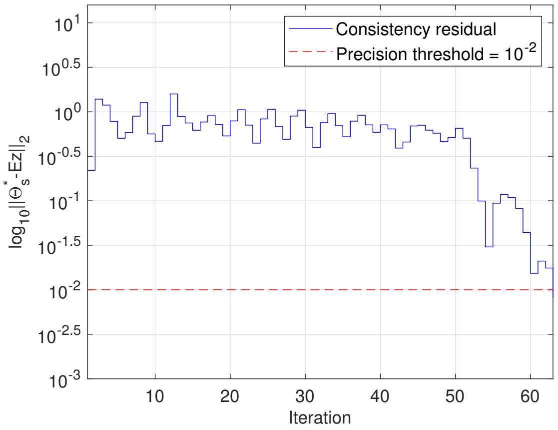

Figure 12.10.: Norm of consistency constraint residual evolvement in the trivial case (logarithmically scaled).

Zone number	Identification [%]	Validation [%]
1	98.10	94.15
2	97.26	95.44
3	97.66	96.50
4	97.71	95.07
5	98.03	95.76
6	97.03	93.91
7	97.71	95.81
8	97.80	94.33
9	97.09	94.89
10	97.46	95.02
Average	97.59	95.09

Table 12.3.: Identification and validation fit (NRMSE) of the ten zones in the trivial case.

Since now all ten zones' GBMs are at disposal, it is possible to calibrate them using distributed identification.

The distributed identification program stopped after 63 global iterations when its norm of consistency constraint residual reached a desired precision, which was equal to 10^{-2}. Its waveform can be seen in the Fig. 12.10.

The identification was performed using a two-day data (with a sampling period $T_s = 180$ s) burdened with measurement Gaussian noise. The overall goodness of fit will be expressed further by two well-known metrics – a root mean square error (for zone temperature)

$$\mathrm{RMSE} = \sqrt{\frac{1}{K}\left\|\mathbf{Y}-\hat{\mathbf{Y}}\right\|_2^2} \quad [^\circ\mathrm{C}] \tag{12.37}$$

and its normalized counterpart

$$\mathrm{NRMSE} = \left(1 - \frac{\left\|\mathbf{Y}-\hat{\mathbf{Y}}\right\|_2}{\left\|\mathbf{Y}-\frac{1}{K}\sum_{k=0}^{K-1}\hat{y}_k\right\|_2}\right)100 \quad [\%], \tag{12.38}$$

where in both metrics a euclidean norm is used. The identification fit reached in the trivial case is presented in the Tab. 12.3.

As the identification and validation fit suggests, the identified and true values of the model are very close to each other. This can be seen in the Tab. 12.2, where in the last column a relative parameter difference is calculated as

$$\theta_{\text{diff}} = \frac{|\theta_{\text{true}} - \theta_{\text{id}}|}{\theta_{\text{true}}} 100 \quad [\%]. \tag{12.39}$$

In the aforementioned Tab. 12.2, there are presented only parameters of the zones number 7-10 for illustration. Nevertheless, identified parameters of other zones reach very similar accuracy with respect to the true values.

12.5.1.1. Computational comparisons

In the previous sections, the grey-box model is identified using the distributed procedure. Now, a comparison with the centralized approach will be presented.

In the centralized approach case, at first a large grey-box model for the whole building (see Fig. 12.8) is created. In this particular case, the large GBM, a structure of which is given by the model in the Fig. 12.9 (except for no separation into local models), has 10 states, 11 inputs and 10 outputs. Subsequently, its parameters are estimated using the standard non-linear least squares method as in (12.15).

There were 20 executions of both the distributed and centralized grey-box model identifications. Performance times, which were reached on a computer with a CPU Intel® Core™ i7-8550U, were averaged and are following:

- Distributed approach: 161.2 s
  (potentially 161.2/10 = 16.12 s - in the parallel computation case as explained below),
- Centralized approach: 73.7 s.

First, it is necessary to mention that the quality of both models was very similar, i.e. identification and validation fits did not differ from each other (distributed vs. centralized case) more than a few tenths of a percent.

Second, although it might seem at first sight that the centralized approach is more than twice as fast, it is necessary to add that the distributed approach was performed serially. This means that the 10 local GBM identifications were executed one by one.

However, the nature of this approach promises to execute all the (10 in this case) local GBM identifications in parallel. Therefore, one might generally up to N-fold acceleration when using the parallelly performed distributed approach.

In the second part of this subsection there will be shown a comparison of performance between the numerically and analytically computed gradient when the distributed identification approach is applied.

The analytical gradient was calculated according to a derivation in the Sec. 12.4.1 and provided to the *fmincon* optimization solver, which ensured the local GBM identification (12.24). Furthermore, analytical gradient correctness was successfully verified by a solver option *CheckGradients*.

Again, 20 executions were carried out and performance times were averaged. The results are the following:

- Analytical gradient: 161.2 s,
- Numerical gradient: 318.9 s.

This time, there is no doubt that the analytical gradient brings very significant acceleration of the overall computation - in fact, almost twofold. Hence, extra implementation of the analytical gradient is meaningful and brings substantial computational time savings.

12.5.2. Fenix building - EnergyPlus model

This section is dedicated to the grey-box model creation and calibration of the *Fenix building* [221] (a sketch of which is in Fig. 12.11). According to this energy-efficient office building, which is located in Jesenik town in the Czech republic, a very accurate thermodynamic model using EnergyPlus software was created.

Operation of the building's HVAC system was simulated in the EnergyPlus program and output simulation data were used in the grey-box calibration procedure to obtain the building model. The procedure was implemented in Matlab using object-oriented programming and is publicly available as a GitHub repository [222] and Mendeley Data [223].

The communication between the EnergyPlus software and Matlab was ensured by the EnergyPlus Co-simulation Toolbox (Sec. 11.1, [71]).

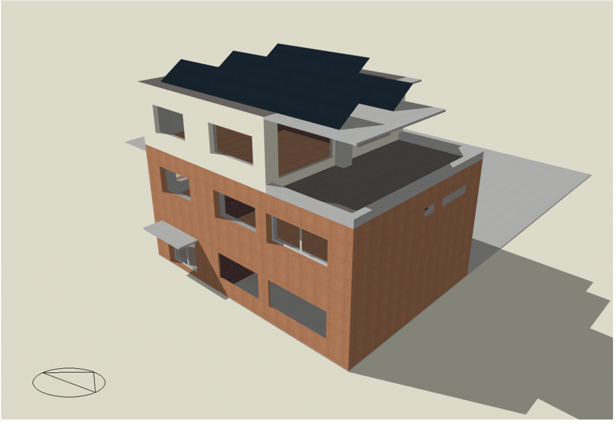

Figure 12.11.: 3D sketch of the Fenix building. Its second floor was chosen to be modelled.

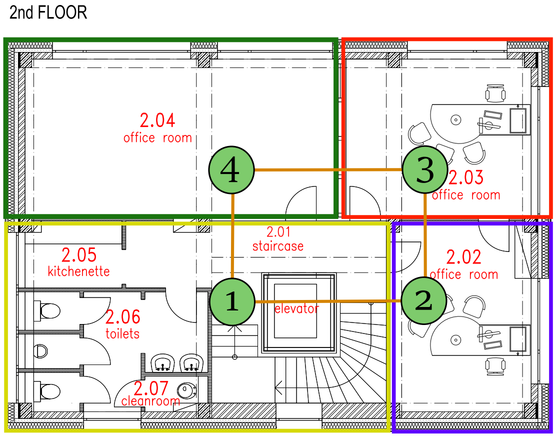

Figure 12.12.: The 2nd-floor plan of the Fenix building forms a "four-zone building". Coloured rectangles denote individual zones' borders and the four-vertex graph represents zones' topology.

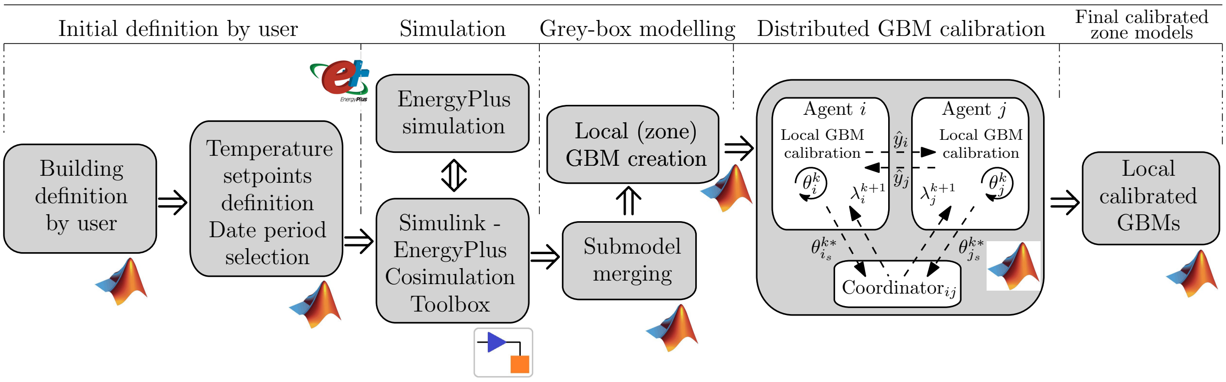

Figure 12.13.: Distributed grey-box model calibration framework used in the Fenix building case. Matlab®, Simulink® and EnergyPlus® software usage is marked with their logos. The distributed GBM calibration algorithm itself is described more thoroughly in the Alg. 12.1.

The second floor of this building was chosen to model, a floor plan of which with zoning can be seen in the Fig. 12.12. There are four zones and four mutual walls. Despite that the zone number one is adjacent to the zone number three, this fifth wall (edge in the graph) was omitted due to a negligible direct influence of these two zones.

A two-capacity zone submodel (see (12.5), (12.6) and Fig. 12.2) was used as a core for the grey-box zone model. Since state space grey-box models for individual zones are analogous to each other, it will be shown only the one for zone number 1:

$$\mathbf{A}_c = \begin{bmatrix} -\frac{U_{\mathrm{s}_1}}{C_{\mathrm{z}_1}} & \frac{U_{\mathrm{s}_1}}{C_{\mathrm{z}_1}} \\ \frac{1}{C_{\mathrm{s}_1}}\left(U_{\mathrm{s}_1} - \alpha_1 U_{1x}\right) & \frac{1}{C_{\mathrm{s}_1}}\left(-U_{\mathrm{s}_1} - \beta_1 U_{1x}\right) \end{bmatrix}, \tag{12.40a}$$

$$\mathbf{B}_c = \begin{bmatrix} \frac{1}{C_{\mathrm{z}_1}} & 0 & 0 & 0 & 0 \\ 0 & \frac{s_{\mathrm{f}1}}{C_{\mathrm{s}_1}} & \frac{U_{12}}{C_{\mathrm{s}_1}} & \frac{U_{13}}{C_{\mathrm{s}_1}} & \frac{U_{10}}{C_{\mathrm{s}_1}} \end{bmatrix}, \tag{12.40b}$$

$$\mathbf{C}_c = \begin{bmatrix} \alpha_1 & \beta_1 \end{bmatrix}, \quad \mathbf{D}_c = \mathbf{0}^{\mathrm{T}}, \tag{12.40c}$$

$$\mathbf{u} = \begin{bmatrix} q_{\mathrm{hx}_1} \\ q_{\mathrm{s}_1} \\ T_{\mathrm{op}_2} \\ T_{\mathrm{op}_3} \\ T_{\mathrm{out}} \end{bmatrix}, \quad \mathbf{x} = \begin{bmatrix} T_{\mathrm{z}_1} \\ T_{\mathrm{s}_1} \end{bmatrix}, \tag{12.40d}$$

where U_{1x} is a sum of conductances given by

$$U_{1x} = \sum_{i \in I} U_{1i}, \quad I = \{0,2,3\}, \tag{12.41}$$

where set I denotes indices of adjacent zones (number 0 means "Outside").

12.5.2.1. Grey-box calibration of the Fenix building

The local grey-box models (12.40), which were composed from the fundamental submodels (see Sec. 12.2.3) are now going to be calibrated.

The EnergyPlus Fenix building model was simulated with a 10-minute time step. The rooms on the second floor were heated up by electrical heating, a thermal power of which was used as an input data to the GBM calibration procedure. Temperatures of all zones were measured as well as ambient temperature with global solar irradiation

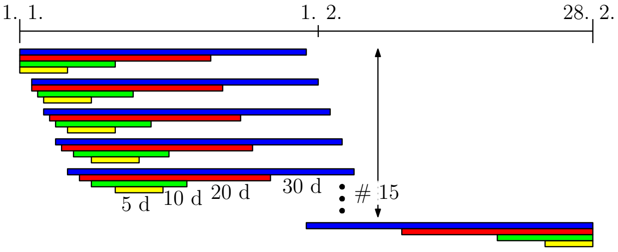

Figure 12.14.: Data sets used for the Fenix building GBM calibration.

RMSE [°C]	Calibration data length			
Zone number	5-day	10-day	20-day	30-day
1	0.42	0.59	0.61	0.77
2	0.56	0.75	0.78	0.95
3	0.53	0.79	0.86	1.15
4	0.52	0.60	0.79	1.11
Average	0.51	0.68	0.76	1.00

Table 12.4.: Average calibration fit (RMSE) in the four zones for different lengths of identification data. The last row shows mean values over the zones.

entering the building.

The air temperatures in the zones were controlled by simple PI controllers. Their setpoints formed a normally distributed pseudorandom sequence with parameters

$$\mu_T = 20\ ^\circ\mathrm{C}, \quad \sigma_T = 5\ ^\circ\mathrm{C}, \tag{12.42}$$

where one sequence step took 6 hours.

A fairly big set of both, distributed GBM calibration and validation procedures was prepared. The calibration was conducted on four different data lengths (5, 10, 20 and 30 days) and for each data length the GBM was calibrated fifteen times within different time periods, which is depicted in the Fig. 12.14. The Fenix building was identified on winter time data (1. 1. – 28. 2.).

In order to compare results from the whole set of calibrations, RMSE was calculated for each calibrated model. The results are depicted in the form of a multi box plot in the Fig. 12.15.

Every box plot consists of a median value within the coloured bar, horizontal edges of which mark the 25th and the 75th percentiles. Further, it consists of vertical dashed lines (often called "whiskers") which mark the minimal and maximal values. At last, the red crosses denote outliers.

In the Fig. 12.15 there is quite apparent a growing trend of the average RMSE for every room. Hence, the longer "training" period does not bring a more accurate model - the most accurate models were reached for the 5-day period. A comparison of averaged reached RMSE can be found in the Tab. 12.4.

Results of the particular calibrated distributed GBM will be now presented. A comparison of the zone temperatures between the simulated Fenix building and the calibrated GBM is in the Fig. 12.16. An average RMSE between the measured and estimated temperatures achieved 0.41 °C - thus, a fairly good agreement between the building and model might be observed.

The parameters that appeared in (12.40) were estimated after a distributed GBM calibration procedure and are presented in the Tab. 12.5.

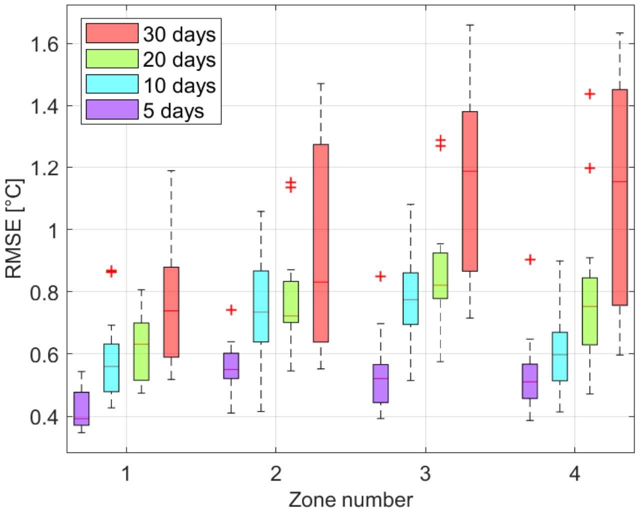

Figure 12.15.: GBM calibration of the Fenix building for different lengths of identification data. There are four box plots for each zone.

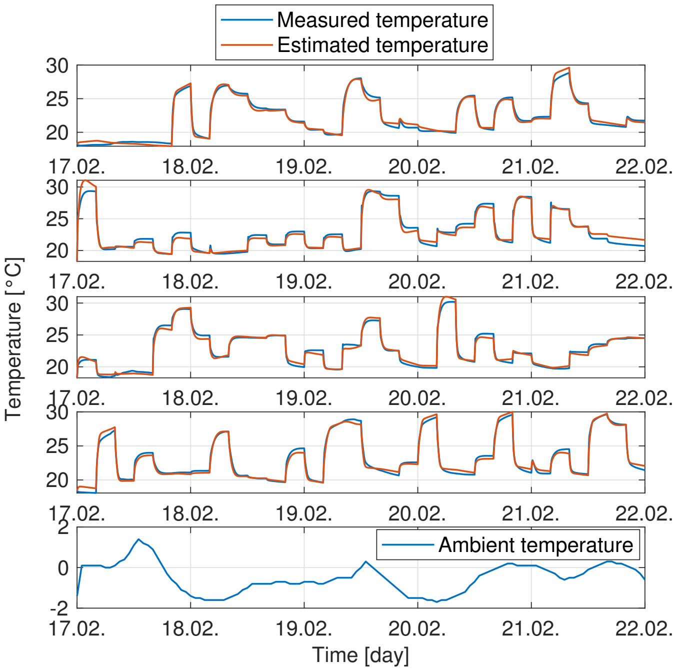

Figure 12.16.: Outputs comparison of the simulated Fenix building (blue line) with the calibrated distributed GBM (red line). The top four upper charts represent four building zones. The lowest chart shows ambient air temperature.

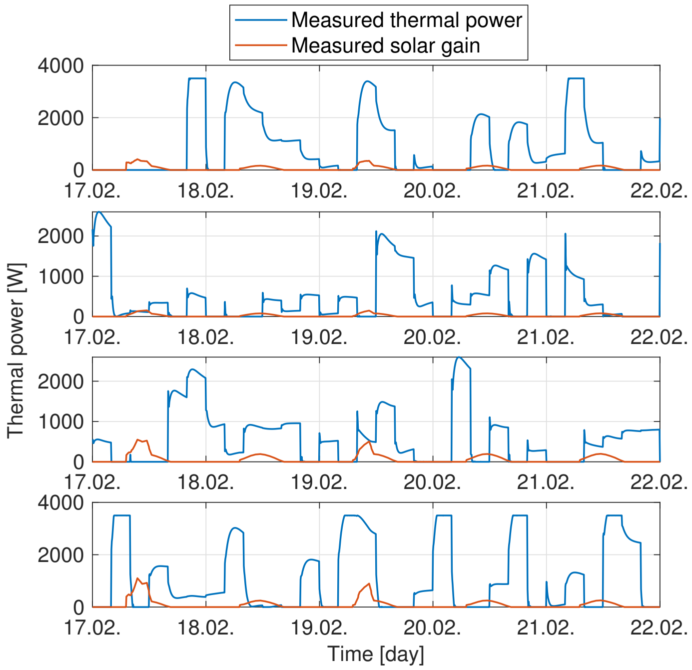

Figure 12.17.: Heat flows obtained by an EnergyPlus simulation which were used as input data to calibrate a distributed GBM. The uppermost chart shows the first zone data, the second most upper shows the data of the zone number 2 etc. The blue line waveform represents the thermal power of the electrical heating entering the corresponding zone. The red line shows the global solar irradiation which enters the zones.

Heat flows that were measured in the zones and served as input data for the GBM are in Fig. 12.17.

As for the distributed aspect of the whole GBM calibration, consistency constraints (12.22) play an important role. In other words, the shared variables must be equal each other to form a consistent mathematical model. This is ensured by their coordination via zone agents actions, thus after several tens of iterations an acceptable consensus is attained. Mutual developments of these shared variables are shown in the Fig. 12.18.

The last thing taht is related to the distributed aspect is a consistency constraint residual defined in the Alg. 12.1. Its evolution in 47 global iterations, when a precision threshold was reached is shown in the Fig. 12.19.

12.5.2.2. Grey-box validation of the Fenix building

The calibrated GBMs from the previous section were validated in the following manner. Since they are intended for control purposes (e.g. MPC), their behaviour were tested on an output prediction on different prediction horizons – 6, 12 and 24 hours ahead.

At first, the zone states T_z and T_s were estimated by a Kalman filter. Then, these estimated states served as initial conditions for open loop simulation of the calibrated GBMs on the aforementioned prediction horizons. GBMs were validated on a two-day data and RMSE was calculated for each of them.

Again, the temperature setpoints formed a normally distributed pseudorandom sequence, this time with parameters

$$\mu_T = 21\ ^\circ\mathrm{C}, \quad \sigma_T = 1.5\ ^\circ\mathrm{C}, \tag{12.43}$$

where one sequence step took 2 hours.

Capacity [J/K] $\times 10^3$		Conductance [W/K]		Cond. [W/K] or shading f. [-]		Others [-]	
C_{z_1}	166.5	U_{12}	81.23	U_{s_1}	241.54	α_1	0.55
C_{s_1}	20 803	U_{13}	50.18	s_{f_1}	1.00	β_1	0.47
C_{z_2}	10.8	U_{10}	40.57	U_{s_2}	17.53	α_2	0.08
C_{s_2}	17 642	U_{24}	7.41	s_{f_2}	1.00	β_2	1.00
C_{z_3}	133.3	U_{20}	15.39	U_{s_3}	246.46	α_3	0.98
C_{s_3}	7 382	U_{34}	58.55	s_{f_3}	1.00	β_3	0.09
C_{z_4}	233.0	U_{30}	26.12	U_{s_4}	335.70	α_4	0.77
C_{s_4}	24 644	U_{40}	42.93	s_{f_4}	1.00	β_4	0.27

Table 12.5.: Estimated values of the distributed grey-box model which forms a thermodynamic model of the Fenix building.

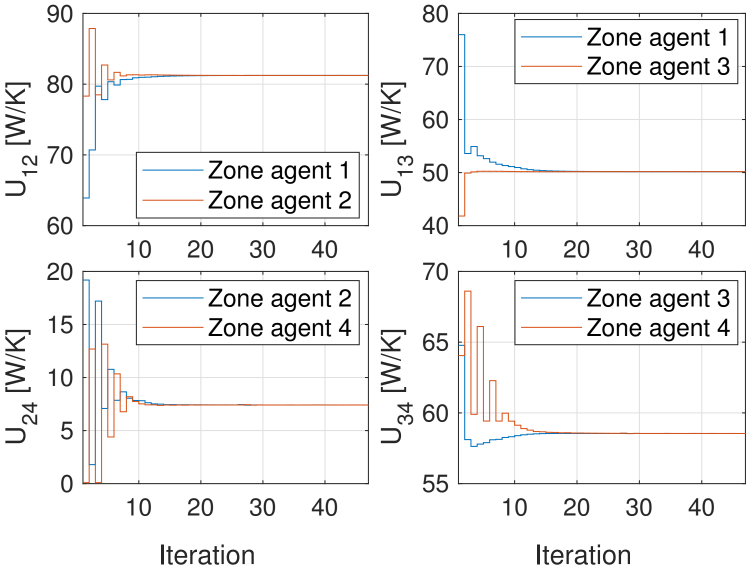

Figure 12.18.: Evolution of the shared parameters that represent mutual wall conductances. For instance, the parameter U_{12} is a conductance between the first and second zone. The zone agent number 1 controls a local GBM calibration in the first zone (blue line). Analogously, the similar stands for the zone agent number 2 (red line). After 47 global iterations, an acceptable consensus was reached for all the shared parameters.

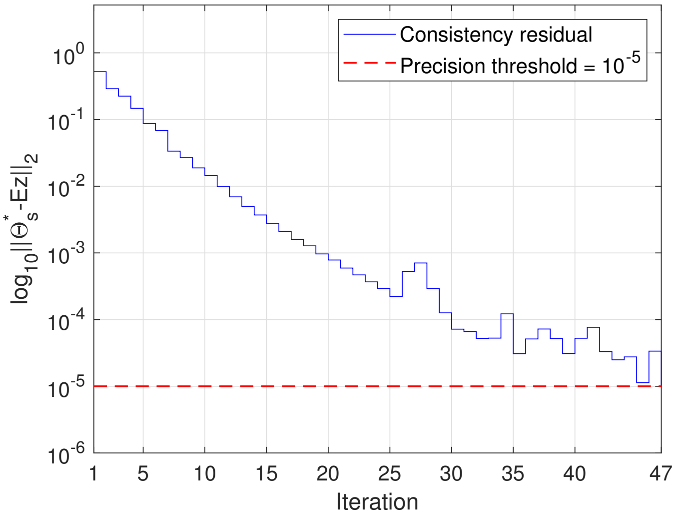

Figure 12.19.: Evolution of the consistency constraint residual before it overcame a precision threshold equal to 10^{-5} after 47 global iterations of the distributed GBM calibration. The values are in the logarithmic scale.

In total, there were carried out 50 validation procedures for each prediction horizon where were used GBMs calibrated on different data lengths (5, 10 and 20 days). For instance, a GBM calibrated on the 5-day data was subsequently validated on three different time periods - at the beginning of January, at the end of January and in the middle of February. This ensured a proper validation of the particular GBM since its dynamical behaviour was tested on different input data and ambient conditions.

The overall results achieved by all the validations are presented again in the box plot form (see Fig. 12.20). It is not a big surprise that the best validation results (according to RMSE) were attained on the shortest horizon, where the GBMs most accurately predicted the zone temperatures.

Furthermore, there is another point of view on how all the validations can be compared. It is focused on which GBMs provide the most accurate predictions if they are compared according to the calibration data length.

Again, a box plot was used for the comparison (see Fig. 12.21). This time, individual zones' RMSE were not considered since they were averaged to a single value for the whole building. Not surprisingly, one can see in this figure that the RMSE increases with the longer prediction horizon. However, there can be observed another notable phenomenon - the RMSE values (e.g. medians) are the lowest for the GBMs, which were calibrated on the 20-day data. This implies that the GBMs calibrated on the longer data are eventually more accurate despite their a bit worse calibration RMSE.

Therefore it can be said that the better calibration score (RMSE) does not automatically bring better validation results. Only after successful validation procedures, it can be decided if the GBM is a truly sufficiently accurate model of the building.

So far, only aggregated statistics about validation results were presented. Now, a validation performance of the GBM, calibration results of which are in the Fig. 12.16 and Tab. 12.5, will be shown. A comparison between estimated and measured zone temperatures can be seen in the Fig. 12.22.

Corresponding RMSE values for different prediction horizons are presented in the Tab. 12.6. An average RMSE over all the zones reached values 0.38 - 0.48 °C, which is very close to the calibration score (0.41 °C).

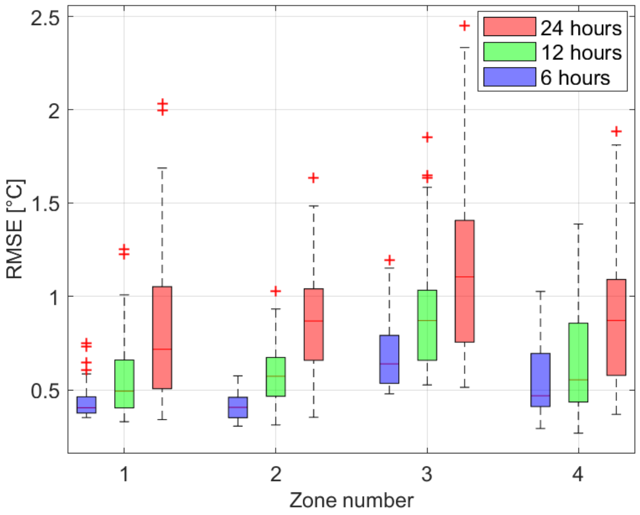

Figure 12.20.: Comparison of RMSE in four zones of the Fenix building achieved during 50 GBM validations, each on three different prediction horizons.

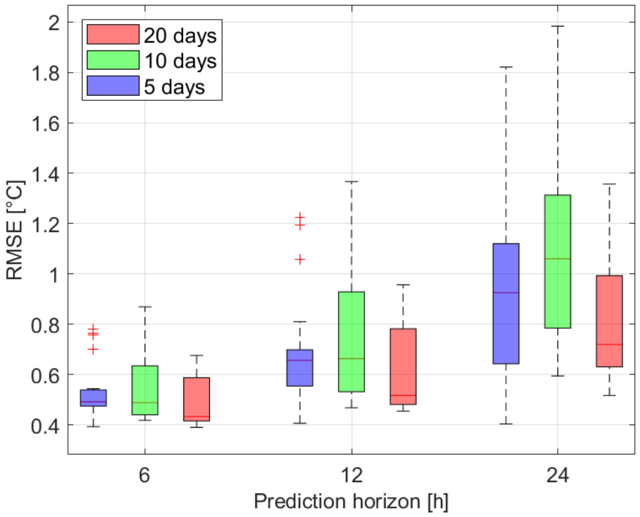

Figure 12.21.: Prediction accuracy comparison of validated GBMs. For every prediction horizon GBMs which were calibrated on three different data length are presented. The RMSE values are mean values of the four zones.

RMSE [°C]	Prediction horizon		
Zone number	6 hours	12 hours	24 hours
1	0.36	0.37	0.48
2	0.38	0.42	0.42
3	0.44	0.47	0.57
4	0.35	0.42	0.45
Average	0.38	0.42	0.48

Table 12.6.: Validation fit (RMSE) of the four zones for different prediction horizons (in the particular case).

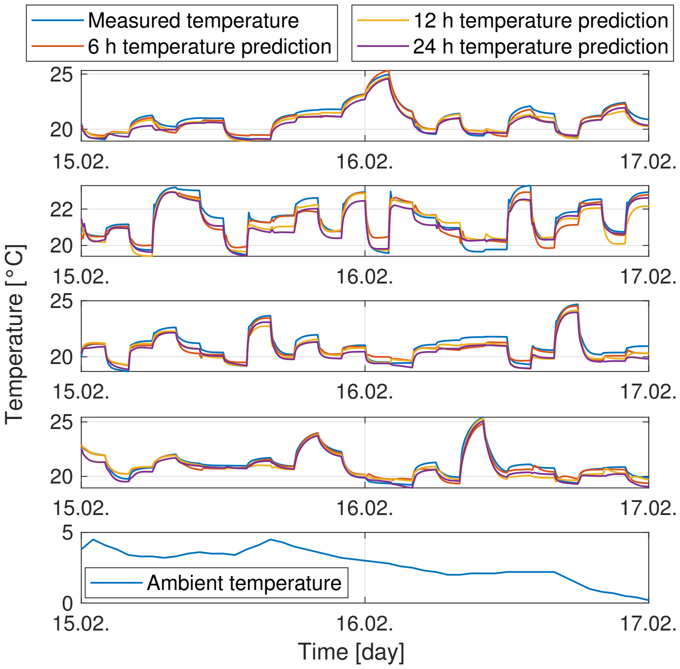

Figure 12.22.: Outputs comparison of the simulated Fenix building (blue line) with temperatures (red, orange and purple line) which were predicted by the calibrated GBM on different prediction horizons. The top four upper charts represent four building zones. The lowest chart shows ambient air temperature. Corresponding RMSE is stated in the Tab. 12.6.

12.6. Conclusions

In this chapter, there has been introduced a grey-box method to model buildings with thermal *RC* circuits. At first, the grey-box models have been composed from fundamental so called submodels, e.g. zones, walls, heat exchangers and so forth. This approach allows to quickly and smartly modify or add other submodels which then form grey-box local models of the building zones. This feature might be a good point for future development - to try and use different grey-box models in the presented distributed building identification framework.

Subsequently, the identification problem has been decomposed using the dual decomposition into the local optimization (model calibration) problems. Hence, a building identification can be approached in a fully distributive manner with the local coordination of the shared parameters.

The proposed method has been tested on two different building examples. The first one was just a trivial case to verify and illustrate a function of the whole algorithm. The latter dealt with a distributed GBM calibration of the Fenix building, which was simulated in the EnergyPlus program. The resulting building model was capable of predicting a zone air temperature on a prediction horizon from 6 to 24 hours ahead with RMSE from 0.38 to 0.48 °C, which might be considered a good result - especially for control purposes.

Considering an identification without the subsequent coordination, only a suboptimal model could be obtained. Therefore, the coordination of shared parameters is needed and the final calibrated model is very close to the model, which would be obtained by global calibration (i.e. when the whole building is identified in one stroke).

This method brings also a possibility to perform local calibrations using small local computational units purely in parallel.

Moreover, in case of a communication failure among zone computational units, there is still the local approximating model for the predictive control, even without the additional shared parameter coordination. The coordination, ergo ensures more precise models leading to generally higher energy savings.

13. Building control

A brief introduction to building control has already been given at the beginning of this part. This chapter is sectioned according to communication to topology. A decentralized system is one, where the controllers do not use information from other controllers in their control law. A distributed system on the other hand requires node-to-node communication and information exchange enters the local control law. In a centralized system, one detached controller serves all local loops. It shall be noted that this categorization represents a qualitative nature of the control approach and shall be applied with care to a particular control problem, e.g. a building comfort control.

Between the decentralized/distributed control structure advantages stand: robustness, reconfigurability, lower processing needs, no single point of failure; the centralized approach benefits from: lower communication needs, deployment simplicity,

The comfort control objectives were already mentioned to generally be: comfort, energy savings and possibly HW preservation, energy flexibility services, and energy community objectives.

This chapter briefly presents decentralized and distributed control of buildings and also a study on a centralized optimal control scenario with the one-pipe pumping hydronic network involved.

13.1. Decentralized & distributed control

The most prevalent hardware (HW) architecture of today's HVAC control is the topology with local/zone controllers (piece of HW), where locally close sensors and actuators are connected using either analogue or digital connection. The local controllers run the local control loops, which predominantly are on/off and PI controllers [224] and connect to supervisory controllers (or intermediate controllers) in a star configuration. Nowadays, the control strategy is decentralized with the robustness and simplicity that pertain it. There is however, no optimization involved and furthermore the local controllers are rarely tuned well.

I have had the opportunity to work on a project which dealt with local controller tuning [225]. A monotonically enhancing incremental tuning algorithm was developed and tested on hydronic heating loops. From another part of the project - the control performance diagnostics, it stemmed out that about 90% of controllers are left in default settings. The automatic tuning algorithm was tested on 38 hydronic heating control loops, where it improved the closed-loop performance on 70% of the circuits [226], the rest would not be possible to tune even by a human due to rough disturbances (caused by bad control performance of connected technology).

13.1.1. Hydronics 4.0 concept

The Hydronics 4.0 concept was introduced in Sec. 1.2. The concept stands on the following principles:

- edge-to-edge communication architecture (flat), control, and analytics computed at the edge,
- daisy-chained power-over-ethernet to allow connection of power and communication network using one cable,
- zero-commissioning decoupling hydronic actuators (see Chapter 5 and Chapter 6), remote hydraulic and thermal self-diagnostics,
- optimized hydronic network topology (see Sec. 9.3.2),
- distributed model-based optimization algorithm.

All the bullets except the last one are about field instrumentation. The Hydronics 4.0 major characteristic is, however, to enable optimal control for buildings. Considerable edge computation is readily available nowadays, which enables to run local optimization problems, namely the model parameter estimation and the model predictive control.

Depending on the amount of node-to-node communication and accuracy needs, the model calibration process may take one of the following scenarios:

M.1 predefined average model - no parameter estimation necessary, zone coupling neglected or modelled generically,

M.2 first principles model - based on physical dimensions, zone coupling from first principles,
M.3 local model identification - local zone model parameter estimation, zone coupling neglected,
M.4 distributed identification - local and coupling parameters estimated, consistency achieved via node-to-node communication (discussed in Chapter 12).

Note that the model parameter estimation task is greatly simplified due to known heat flows when the PCV or the PCP are used.

The model predictive control may, depending on the amount of communication and the nature of the model be:

C.1 local MPC - zone coupling omitted, no communication between nodes, no global constraints possible,
C.2 robust MPC - zone coupling treated as box uncertainty, no communication between nodes, no global constraints possible,
C.3 distributed MPC - multiple flavours possible, communication used to reach a consensus in global objective and constraints.

The advantage of the local MPC and robust MPC is that they does not need to iterate its optimization problem to reach a consensus with neighbours. The entire system is composed by adding nodes and may be freely reconfigured; on the other hand, it is not possible to add global constraints such as resource allocation. The combined performance is suboptimal due to the neglected interactions, but the approach is still superior to local PI control due to its prediction capabilities (weather forecast, dynamic behaviour, anticipation of setpoint changes).

Decentralized/distributed Model Predictive Control (DMPC) uses multiple controllers deployed across coupled subsystems. The subsystems are coupled either by physical interactions and/or by operation constraints (e.g. shared resources). The objective of the distributed model predictive control is to provide flexibility of the decentralized control topology (simplified commissioning, maintenance, reconfigurability) while delivering performance of a centralized controller.

DMPC coupled with DID (M.4 + C.3) as depicted in Fig. 13.1 is the ultimate control and modelling structure. The integration of coupling, in theory, pushes the performance to that of the centralized controller. And the optimization problem may be, for both, the modelling and control, composed in a modular fashion and run at the edge hardware (such at the PCV and PCP for hydronic networks).

The Hydronics 4.0 concept addresses numerous features of the ideal BACS presented at the beginning of Part IV , namely:

- the control structure is constructable and reconfigurable in a plug-and-play manner,
- the control employs optimization to maximize an objective under constraints,
- the control objective is tunable on demand (comfort, energy savings, HW preservation, energy flexibility services, energy community objectives),
- the control takes some known information into account: real-time data and predictions.

All that, on top of lower projected material cost, simplified installation, commissioning and maintenance brought by the rest of the concept elements.

Remark. Decentralized/distributed optimization is not in the scope of my thesis. I have supervised the thesis ‘Distributed predictive control of buildings’ [227], which explores possible implementations of distributed optimal control, but the real practical algorithms were developed in the Hydronics 4.0 project [11] by my colleagues [228]. This section is here to complete the description of the concept; my contribution in the DMPC domain is the application concept to building control and hydronic networks.

13.2. Centralized control[1]

As opposed to the distributed control layout, the centralized approach collects all data at one location, performs building-wide optimization and commands all actuators from there. Centralized approaches offer simplified deployment but suffer from poor maintenance [151].

This section presents one particular study of a model predictive control for a building with the one-pipe hydronic

---

[1] Based on the original paper: Jiří Dostál and Tomáš Bäumelt. “Model Predictive Control for Buildings with Active One-pipe Hydronic Heating”. In: ed. by S. I. Tanabe et al. Vol. 111. EDP Sciences, 2019, p. 04050. DOI: `10.1051/e3sconf/201911104050`

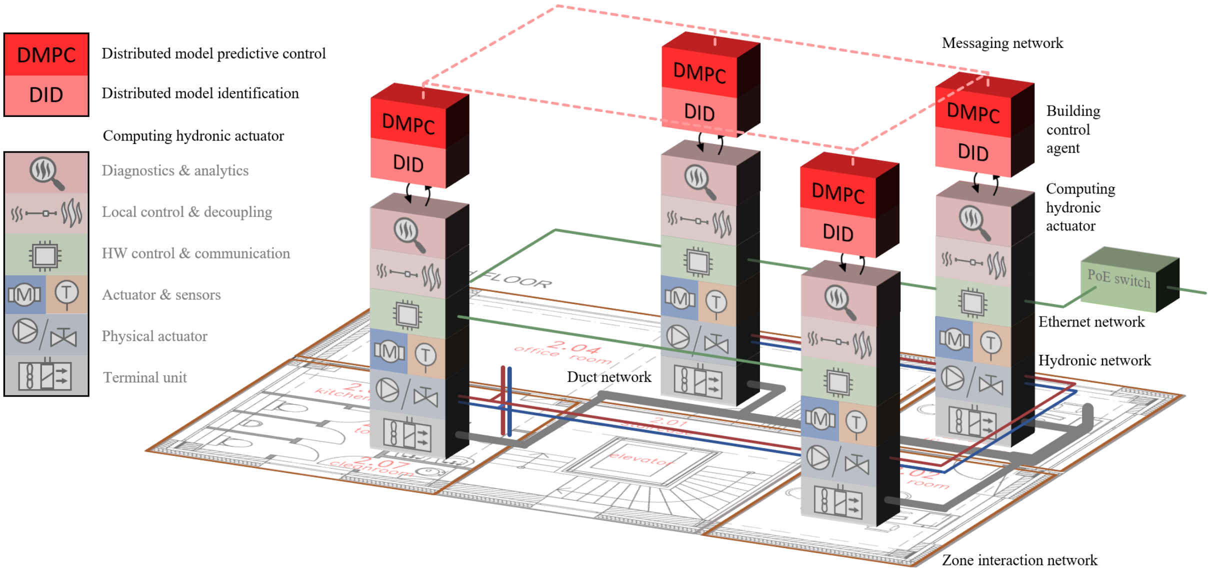

Figure 13.1.: "Hydronics 4.0" concept with the distributed identification (DID) and distributed MPC (DMPC) layers highlighted.

heating network. This control problem would need to be realized in a distributed manner for a possible implementation in the power control pumps involved.

The section is organized to present the control model used first, followed by the formulation of MPC and completed by simulation study and results.

13.2.1. Building control model

The building control model adopts the already described widely-used RC thermal-electric analogy approach (Sec. 12.5 and e.g. [14, 229]). The resulting dynamic model is linear and may be, after discretization, represented by the standard state space model

$$\mathbf{x}_{k+1} = \mathbf{A}\mathbf{x}_k + \mathbf{B}\mathbf{u}_k + \mathbf{B}_\mathrm{d}\mathbf{d}_k \tag{13.1a}$$

$$\mathbf{y}_k = \mathbf{C}\mathbf{x}_k, \tag{13.1b}$$

where $\mathbf{x}$ is a state vector, $\mathbf{u}$ is an input vector consisting of heat exchanger heat flows q^z_hx, $\mathbf{d}$ is a disturbance vector composed of solar gains $q^\mathrm{z}_\mathrm{sol}$ and an environment temperature T_env. Output vector $\mathbf{y}$ is a composition of zone temperatures T^z_z. The model discrete time steps are $t_k = t_0 + kT_\mathrm{s}$, where T_s is the step size and k is a sequence index. Matrices $\mathbf{A}$, $\mathbf{B}$, $\mathbf{B}_\mathrm{d}$, $\mathbf{C}$ may be found by standard calibration techniques such as the prediction error method (PEM), subspace identification (4SID) etc. The model in this study was calibrated by a distributed grey-box approach [170]. More on the topic in Chapter 12 or [196, 211].

This study focuses mainly on the incorporation of hydronic network capabilities into the building-wide optimization, in particular the one-pipe network described in the following section.

One-pipe hydronic system model

The active one-pipe hydronic network consists of the following components: pipe, pump, twin-tee, heat exchanger and a heat source.

The pipe (hydraulic resistance) and pump (pressure source) were given in 2 and 3, respectively. A twin-tee composed of two T-shaped fittings hydraulically separates primary and secondary circuits ($\Delta p_\text{twin-tee} = 0$). Heat exchanger's dynamics is neglected in the model as its settling time is short compared to a controller sampling time/ building dynamics. HX's steady-state behaviour is modelled by the P-NTU analysis [42]

$$q_{\mathrm{hx}} = P\left(h_{\mathrm{tot}}\right) c_{\mathrm{p}} \dot{m}_{\mathrm{s}} \left(T_{\mathrm{wi}} - T_{\mathrm{z}}\right), \tag{13.2}$$

where $P\,[-]$ is the temperature effectiveness of the water stream, $c_{\mathrm{p}}\left[\mathrm{J\,kg\,K^{-1}}\right]$ is the specific heat capacity of the heat transfer fluid, $\dot{m}_{\mathrm{s}}$ is the secondary flow (through the heat exchanger) and the heat exchange coefficient is

$$h_{\mathrm{tot}} = \left(h_{\mathrm{w}}^{-1} + h_{\mathrm{a}}^{-1}\right)^{-1}.$$

It is a series connection of two thermal conductances: the liquid-to-body coefficient $h_{\mathrm{w}}\ \left[\mathrm{W\ K^{-1}}\right]$ and the body-to-air coefficient $h_{\mathrm{a}}\ \left[\mathrm{W\ K^{-1}}\right]$. From the work of Nusselt and others [138], it follows that the heat exchange coefficient on the inner surface of a pipe can be modelled as

$$h_{\mathrm{w}} = \theta_1^{\mathrm{w}} \left(\dot{m}_{\mathrm{w}}\right)^{\theta_2^{\mathrm{w}}},$$

where $\boldsymbol{\theta}^{\mathrm{w}} = \left[\theta_1^{\mathrm{w}}, \theta_2^{\mathrm{w}}\right]^T$ are setup dependent parameters. The body-to-air heat exchange coefficient is modelled as a second-order polynomial in the air flow $\left(\dot{V}_{\mathrm{a}}\right)$

$$h_{\mathrm{a}} = \theta_0^{\mathrm{a}} + \theta_1^{\mathrm{a}} \dot{V}_{\mathrm{a}} + \theta_2^{\mathrm{a}} \dot{V}_{\mathrm{a}}^2,$$

where $\boldsymbol{\theta}^{\mathrm{a}} = \left[\theta_0^{\mathrm{a}}, \theta_1^{\mathrm{a}}, \theta_2^{\mathrm{a}}\right]^T$ are setup dependent parameters. For a thorough explanation and a heat exchanger coefficient fitting process see [32]. A heat source is an ideal heat source capable of maintaining any desired supply temperature regardless flow or return temperature variation. Its hydronic resistance is neither considered as the primary circulator is also idealized; i.e., considered to have the capability of setting the primary flow instantly to its reference value.

The branches in the one-pipe hydronic network are connected in series using twin-tees. This way, the secondary circuits are hydraulically separated, but consequently, also the primary supply stream loses its energy/temperature further down the pipe. This relation may be expressed as a simple loss of secondary energy in the primary stream. The primary outlet temperature of a z branch is

$$T_{\mathrm{po}}^{\mathrm{z}} = T_{\mathrm{po}}^{\mathrm{z}-1} - q_{\mathrm{hx}}^{\mathrm{z}} \left(c_{\mathrm{p}} \dot{m}_{\mathrm{p}}\right)^{-1}, \forall \mathrm{z} \in \mathcal{Z}, \tag{13.3}$$

where $T_{\mathrm{po}}^{0} = T_{\mathrm{bo}}$ [°C] is the heat supply (boiler) outlet temperature, $\mathrm{z} \in \mathcal{Z}$ is a specific zone out of the set of all zones/branches z, z − 1 stands for a preceding branch in the direction of the primary flow $\dot{m}_{\mathrm{p}}\ \left[\mathrm{kg\ s^{-1}}\right]$.

The primary flow is always considered greater than all secondary flows

$$\dot{m}_{\mathrm{p}} > \dot{m}_{\mathrm{s}}^{\mathrm{z}}, \forall \mathrm{z} \in \mathcal{Z}, \tag{13.4}$$

and each secondary inlet temperature equals the primary outlet temperature of the preceding branch...

$$T_{\mathrm{si}}^{\mathrm{z}} = T_{\mathrm{po}}^{\mathrm{z}-1}, \forall \mathrm{z} \in \mathcal{Z}. \tag{13.5}$$

13.2.2. Model predictive control

Heating control systems were traditionally on/off zone controllers switching an HVAC actuator. Nowadays also, proportional-integrational (PI) controllers are frequent. They control HVAC actuators in a continuous range 0–100 % to lessen the wear of hardware components and possibly to raise comfort levels.

In the past decades model predictive controllers (MPC) have been studied and tested. Some realizations hold their benefits for about 15 consecutive years now [152, 171, 216]. In contrast to the mentioned approaches, MPC integrates all the available sensor, actuators as well as weather and internal gain information together into a coherent mathematically-founded optimization problem. The controller seeks optimal actuator settings to minimize energy consumption while maintaining comfort levels or other constraints on the environment and the equipment itself. The optimization problem, in general, is

$$\begin{aligned} \boldsymbol{v}^{\star} = \arg\min_{\boldsymbol{v}} \quad & \mathcal{J} \\ \text{s.t.} \quad & \mathcal{C}, \end{aligned} \tag{13.6}$$

where $\mathbf{v}$ are the optimization variables (13.9) over which the objective functional $\mathcal{J}$ (13.7) is minimized subject to the constraint set $\mathcal{C}$ (13.8). Note that the boiler output temperature T_{bo} is considered fixed, but should the efficiency map of the heat source be known, the heat source should be included into optimization.

13.2.2.1. Objective function

The objective function

$$\mathcal{J} = \sum_{k=1}^{N} \sum_{i=1}^{4} \mathcal{J}_k^i \tag{13.7}$$

is composed of four functionals $\mathcal{J}^i$ shaping the optimization outcome over a prediction horizon of length N.
A reference funnel tracking functional is responsible for driving the model outputs to their reference ranges

$$\mathcal{J}_k^1 = \left\|\mathbf{y}_k - \mathbf{s}_k^{\mathrm{r}}\right\|_{\mathbf{Q}_1}^2,$$

where $||\alpha||_{\mathbf{Q}_i}^2 \equiv \alpha^{\mathbf{T}}\mathbf{Q}_i\alpha$ represents a second vector norm weighted over a matrix $\mathbf{Q}_i$ and $\mathbf{s}^{\mathrm{r}}$ is a reference slack vector defined later. An input effort (power) is minimized by the functional

$$\mathcal{J}_k^2 = ||\mathbf{u}_k||_{\mathbf{Q}_2}^2,$$

smooth operation is attained by penalizing an input change by

$$\mathcal{J}_k^3 = ||\mathbf{u}_{k-1} - \mathbf{u}_k||_{\mathbf{Q}_3}^2,$$

and the primary flow is minimized by

$$\mathcal{J}_k^4 = \left\|\dot{m}_{\mathrm{p},k}\right\|_{Q_4}^2.$$

13.2.2.2. Constraints

The objective function is utilized to shape the optimization outcome; the constraint set encodes the knowledge of the system behaviour and enables to bound the optimization/decision variables. The constraint set is composed of a multitude of constraints

$$\mathcal{C} = \bigcup_{\forall i,k} \mathcal{C}_k^i. \tag{13.8}$$

The first is an equality constraint establishing the model dynamics (13.1)

$$\mathcal{C}_k^1 : \ \mathbf{x}_{k+1} - \mathbf{A}\mathbf{x}_k - \mathbf{B}\mathbf{u}_k - \mathbf{B}_{\mathrm{d}}\mathbf{d}_k = \mathbf{0}.$$

The reference slack variable vector is constrained to a reference trajectory vector range

$$\mathcal{C}_k^2 : \underline{\mathbf{r}}_k < \mathbf{s}_k^{\mathrm{r}} < \overline{\mathbf{r}}_k,$$

where the underbar and overbar accents stand for lower- and upper-funnel limits, respectively.
Further constraints now encode the one-pipe hydronic network algebraic relations. The HX output equation (13.2) combined with the series connection of nodes (13.5) relates the heat output to the zone temperature and secondary mass flow

$$\mathcal{C}_k^3 : q_{\mathrm{hx}}^{\mathrm{z}} - P\left(h_{\mathrm{tot}}\right) c_{\mathrm{p}} \dot{m}_{\mathrm{s,z}} \left(T_{\mathrm{po}}^{\mathrm{z}-1} - T_{\mathrm{z}}^{\mathrm{z}}\right) = 0, \forall \mathrm{z} \in \mathcal{Z},$$

where $q_{\mathrm{hx}}^{\mathrm{z}}$ is a z^{th} element of the input vector **u.**
The branch-to-branch coupling, manifested by decaying primary flow energy, is captured by (13.3)

$$C_k^4 \quad : \quad T_{\mathrm{po}}^{\mathrm{z}} - T_{\mathrm{po}}^{\mathrm{z}-1} + q_{\mathrm{hx}}^{\mathrm{z}} \left(c_{\mathrm{p}} \dot{m}_{\mathrm{p}}\right)^{-1} = 0, \forall \mathrm{z} \in \mathcal{Z}.$$

For C^4 to hold, we must also constraint the primary flow to exceed secondary flows (13.4), which are also supposed to be non-negative

$$C_k^5 : 0 \leq \dot{m}_{\mathrm{s}}^{\mathrm{z}} < \dot{m}_{\mathrm{p}}, \forall \mathrm{z} \in \mathcal{Z}.$$

Note that while not stated explicitly the time instance for all variables in the constraints C^3, C^4, C^5 is t_k. Also, note that usual box constraints on the decision variables are also part of C.

13.2.2.3. Implementation

The control mechanism of the MPC is to find the optimal solution $\mathbf{v}^*$ to the problem (13.6) and to apply the first optimal input to the system; then after one sampling period, measure system outputs, optionally estimate the current system state and calculate optimal solution again.
The problem is non-linear due to the non-linear constraints involved.
The problem was implemented by the multiple shooting method [230], where the state at each sampling time is included as a decision variable. This approach generally improves convergence but also increases the NLP size considerably. The optimization variable vector is, therefore, composed of primary and secondary flows, states and the reference slack variables

$$\mathbf{v} = \bigcup_{k=1}^{N} \left\{ \dot{m}_{\mathrm{p},k}, \dot{\mathbf{m}}_{\mathrm{s},k}, \mathbf{x}_k, \mathbf{s}_k^{\mathrm{r}} \right\}, \tag{13.9}$$

where $\dot{\mathbf{m}}_{\mathrm{s},k} = \bigcup_{\mathrm{z} \in \mathcal{Z}} \dot{m}_{\mathrm{s}}^{\mathrm{z}}(k)$ is a vector of all secondary flows at time k.
The implementation was first carried out in the YALMIP framework [231] using the Gurobi solver [232]. This approach involving numerical gradients, however, provided insufficient results in terms of accuracy and timeliness. The second implementation using algorithmic differentiation of the CasADi framework [73] in combination with the IPOPT solver [233] yielded consistent, precise and prompt solutions. Further information may be found in [234].

13.2.3. Simulation study

The proposed control approach was validated using a building simulation scenario. The building of choice was the Fenix Trading office centre (Fig. 13.2) located in Jesenik, the Czech Republic. It is an NZEB building with hybrid PV panels and a yearly energy consumption of 27 kWh [221]. UCEEB (Czech technical university in Prague, University centre for energy efficient buildings) was active in energy system design and energy performance monitoring and analysis [221]. An EnergyPlus simulation model of the building (developed by M. Urban, UCEEB) that was used for energy predictions in [221] is without qualitative modifications utilized for this study. The MPC control is realized on a second floor with four thermal zones; see Fig. 13.3. The rest of the building is kept at a constant temperature range 20-25 °C by local decentralized PI controllers.
The heating appliances used in the building are electrical heaters. Their power is, for our purposes, set to the power obtained from the one-pipe hydronic heating network model (Simulink). The hydronic terminal sizes were designed by our open source design tool [143, 235] published in paper [142].
The design loads, for conditions $T_{\mathrm{env}} = -12°\mathrm{C}, T_{\mathrm{z}} = 22°\mathrm{C}, T_{\mathrm{bo}} = 60°\mathrm{C}, T_{\mathrm{bi}} = 40°\mathrm{C}$, are $q_{\mathrm{hx}}^{\mathrm{design}} = (1450, 650, 800, 1350)$ W for the staircase (Sc), director room (202), office assistant room (203) and office room (204), respectively. The design sizes for catalogue values 90/70/20°C are (2800,1550,2150, 4750) W. The heat exchangers are modelled by 20-state plug-flow model (Sec. 4.2). The flow through the secondary circuits is forced to be equal the flow reference $\dot{m}_{\mathrm{s}}^{\mathrm{z}}$. Note that the mass flow may be inferred from pump measurements (Sec. 6.4, [**woPatentDostal2016**]) and ,as such, may be, by varying pump speed, controlled to the reference level. Boiler supply temperature is 60°C.

Figure 13.2.: Fenix building. Credits :Fenixgroup, Miroslav Urban

Matlab/Simulink was used to perform the simulation; the simulation model is depicted in Fig. 13.4. Real-time co-simulation of the EnergyPlus model was executed by the EnergyPlus Co-simulation Toolbox (Sec. 11.1, [**EPcosim**]). The model timestep is 300 s.

Baseline control

The baseline control is performed by PI controllers; one for primary flow and four for each secondary flow (Fig. 13.4). The primary flow is controlled such that the boiler return temperature T_{bi} is always at least 40°C. This enforces a sufficient temperature potential for the last terminal unit to operate correctly. Primary flow is also overridden by the maximal secondary flow to prevent backflow at the secondary circuits. The integrator state is tracking the output to ensure bumpless control when the override is over.

Secondary PI controllers steer the temperature to the lower limit of the reference funnel (for comparison with the MPC). The flow-to-power characteristic of the heat exchangers is non-linear with a steep ascend from the low flow region. An inverse equal-percentage transformation curve (Sec. A.2) known from hydronic control valves have been added to linearize the characteristics and improve control performance.

The predictive controller uses the presented mathematical model to predict system behaviour and optimize control actions. The building model for control purposes here uses a CRC bridge structure for zone models and the simplest one-resistance R1C0 structure for wall models [170]. The model was calibrated on a 10-day interval and validated on a different 2-day interval; mean identification fit 86.6 % (NRMSE), mean validation fit for 6-hour predictions 82.9 % (NRMSE).

MPC also requires an initial state at each step. A Kalman filter with an unknown input observer extension estimates the system state. The control scheme is depicted in Fig. 13.5. MPC sampling time is 600 s, prediction horizon $N = 30$ (5 hours).

13.2.4. Results

Fig. 13.6 shows results for three simulation settings; the first column pertains to the baseline control, the second column to a setting, where the building is simulated by the building control model itself; the heat flows are, however, still generated by the one-pipe network model. The third column pertains to the MPC control of the one-pipe network and the actual EnergyPlus model. The building was warmed up by a 10-day warming period.

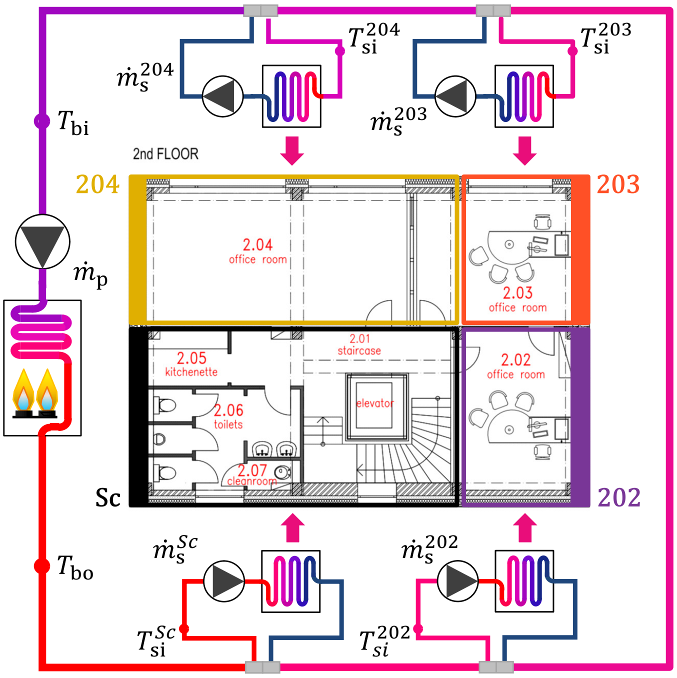

Figure 13.3.: One-pipe hydronic heating installation for the 2nd floor. Note the zone color frames match the line colors in the simulation results presented further.

The baseline primary controller is tracking the return temperature reference; it is overridden by the heat up of the room 203 at the time $t = 6\,\text{h}$. Such override, however, is not very realistic in real field conditions due to missing communication. This override increases the performance of the baseline control to a comparable level. All the room temperature references are eventually reached, but as there is no planning, the heat up time can't be decreased without increasing the return temperature reference and thus sacrificing heat source efficiency (the lower the return temperature, the better).

The anticipative capabilities of MPC are demonstrated on the interval $t = 1 - 6\,\text{h}$ of the MPC on the model scenario. At time $t = 1\,\text{h}$ the reference change of the room 203 appears at the end of the prediction horizon. The decision is to accumulate heat in all the zones so that when the reference change happens, all the preceding zones (Staircase & 202) can be shut off. Then the room 203 has the highest inlet temperature and is able to raise its temperature faster. Note that the reference funnel tracking weight was high to exaggerate this effect.

As the building control model is not precise in prediction, we can see at time $t = 6 - 8\,\text{h}$, that the MPC on EnergyPlus is struggling to raise the room 203 temperature. The primary and secondary flows are at their limits.

Tab. 13.1 presents cumulative energy consumption for the three scenarios, as well as, an average out-of-funnel root mean square tracking error (RMSE) across the four zones and an average boiler return temperature.

	Baseline	MPC(model)	MPC(EnergyPlus)
Energy [kWh]	32.18	32.39	35.07
RMSE [°C]	0.29	0.16	0.12
Boiler return temp. [°C]	42.40	31.40	32.09

Table 13.1.: Cumulative/mean results.

The tracking precision of the baseline control is inferior, but consequently, the energy consumption is also lower due to generally lower tracked temperatures. Despite having the MPC aggressively tracking the reference, the cumulated

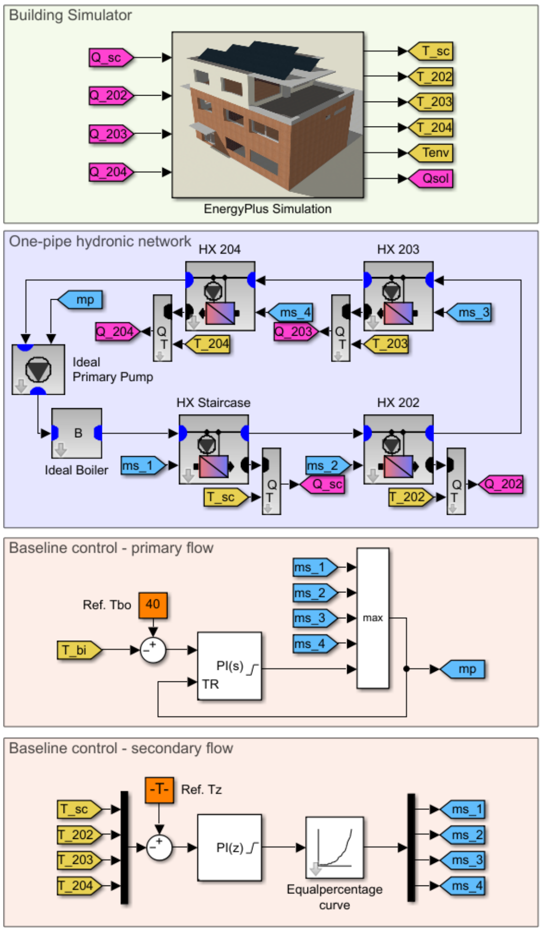

Figure 13.4.: Software realization of the proposed baseline control scheme. The building is simulated by EnergyPlus, the one-pipe hydronic network and controller by Matlab/Simulink.

energy consumption is comparable to the baseline in prediction (on the control model). Applied to the EnergyPlus model, the MPC consumption is 9% higher, but as mentioned, the energy consumption comparison is not completely fair.

The temperature at the boiler inlet ranks about 10 °C lower, which could significantly improve heat source efficiency should it be included in the study.

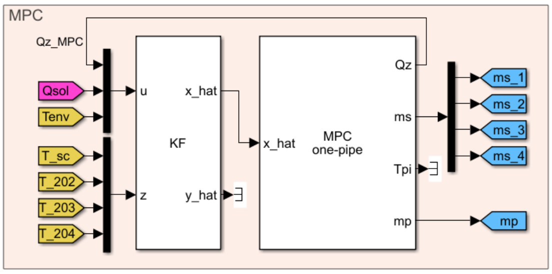

Figure 13.5.: Software realization of the proposed MPC control scheme (as a replacement for the control block in Fig. 13.4).

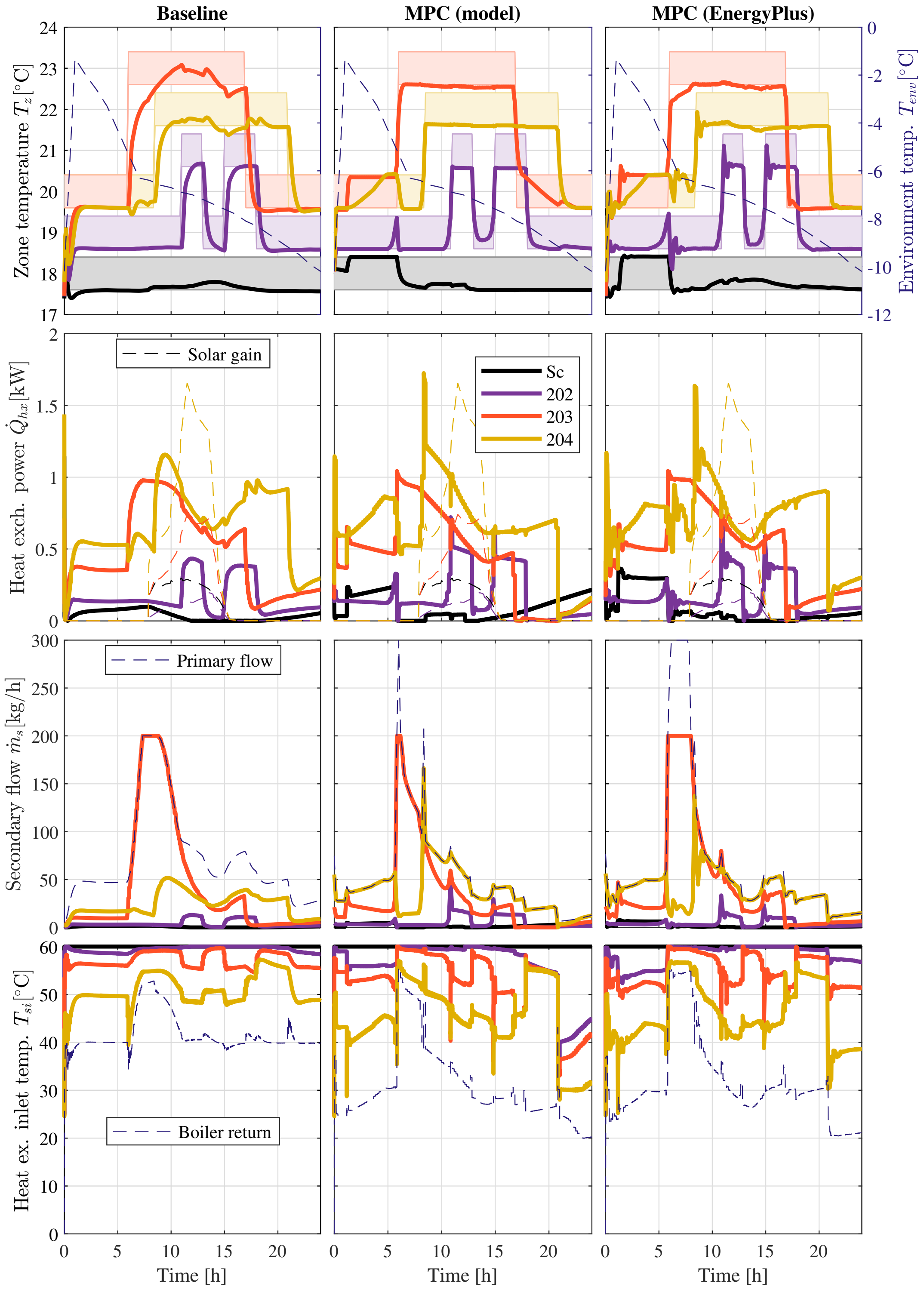

Figure 13.6.: Comparison of three control results: the baseline control by PI controllers (left), MPC controlling the identified state space model through the one-pipe network model (middle) and MPC controlling the EnergyPlus model accompanied by the Kalman state estimator (right). Note the y-axis for the environment temperature (dashed) positioned on the right of the first row. Solid lines represent the four zones: Staircase (Sc), room 202 (202), room 203 (203) and room 204 (204).

14. Conclusion

This thesis maps the theoretical results accomplished during the development of the Hydronics 4.0 concept and its related devices. The thesis goals from Sec. 1.1 were accomplished. Hydronic heating networks have been thoroughly studied, and the innovative Hydronics 4.0 concept was formulated. Simulation tools for heat exchangers, hydronic networks and building energy performance have been realized. Control and estimation algorithms for load power, building model and energy optimization were developed, implemented and validated; some by simulations, some in real life.

14.1. Original contribution

Original research and development contributions of the thesis are:

Part I – Hydronic components A solution to a system of hyperbolic transport PDEs, defining a heat exchanger, for example, suffers from artificial numerical diffusion when solved by the finite volume method with the state-of-the-art flux limiters. The proposed MMFVM method approximates the PDEs using a mixed Lagrange-Euler mesh to minimize the numerical diffusion. The method serves well for low-order heat exchanger simulation focusing on the convected stream, such as in temperature-feedback hydronic devices.

Part II – Load power control The heat flow stabilization is in today's hydronic networks accomplished by mass flow rate stabilization through a mechanical pressure regulator. The temperature-feedback solution presented in this part enables the direct stabilization of the heat flow; relative heat flow in the case of the Power Control Valve and absolute heat flow for the Power Control Pump.
The power control pump is an original patented device with a patented heat flow control method. The invention is to estimate the mass flow from pump power readings and, consequently, control the heat flow. The results are supported by real-life measurements on the testbed.
Practical contributions are within the design of the hardware and electronics of the devices and testbed.

Part III – Hydronic networks The solution to the network flow control by actuator opening is mostly achieved by the iterative gradient descent with pressure balance and flow continuity conditions. The solution method proposed in Sec. 8.1, employs unified virtual hydronic blocks and graph representation to solve the flow control problem in as few steps as there are actuators. This method speeds up related optimization problems when degrees of freedom are present.
The heating power is affected by pressure coupling from other zones in two-pipe systems. Proven in Chapter 9 , the hydronic network is stable when the individual zone controllers are locally stable for the zero to pressure-source input pressure; infinity gain margin ensures hydronic network stability for any source pressure.
This thesis provides the most comprehensive analysis of the previously unstudied pumping one-pipe hydronic network, from sizing and retro-fitting to control.

Part IV – Building level control The deployment of optimal control is prohibitively expensive; the usual centralized MPC suffers from maintenance issues. The Hydronics 4.0 concept enables optimization control deployment by edge computation, node-to-node communication and distributed optimization algorithms. The presented distributed building model identification provides a previously unpublished modular parameter calibration problem formulation by sub-model merging.
The contribution to the distributed MPC domain lies in its application to the building control domain.
The main practical contribution of this part is the much downloaded EnergyPlus co-simulation toolbox for Matlab.

14.2. Future research

The future research tasks stem mainly from the Hydronics 4.0 concept validation; either by the to-be-developed cyber-physical testbed or in physical field testing. The field testing was already prepared in a Horizon 2020 project but failed due to a re-structuralization of the at-the-time industrial partner. The focus is on finding a new industrial partner to validate, realize and commercialize the concept with.

Appendices

A. Hydronic components supplementary information

A.1. Series and parallel connection of hydraulic resistances

Series connection of hydraulic resistances When two hydraulic resistances are connected in series, the flow in both is the same and their head sum to the overall head

$$\begin{aligned} H &= H_1 + H_2 \\ Q &= Q_1 = Q_2, \end{aligned}$$

where the two hydraulic resistance share the same hydraulic model (Darcy-Weisbach formula for example), the particular resistance heads are

$$H_1 = R_1 Q_1^m \tag{A.1}$$

$$H_2 = R_2 Q_2^m. \tag{A.2}$$

So an equivalent resistance is derived by

$$H = R_1 Q_1^m + R_2 Q_2^m = (R_1 + R_2)\, Q^m = R_{1—2} Q^m,$$

and therefore

$$R_{1—2} = R_1 + R_2.$$

Parallel connection of hydraulic resistances Two hydraulic resistances connected in parallel share the same head loss and the flow divides into the two branches

$$\begin{aligned} H &= H_1 = H_2 \\ Q &= Q_1 + Q_2. \end{aligned}$$

Using (A.1), (A.2), the flow are expressed as

$$\begin{aligned} Q_1 &= \sqrt[m]{\frac{H_1}{R_1}} \\ Q_2 &= \sqrt[m]{\frac{H_2}{R_2}} \end{aligned}$$

and an equivalent resistance is derived as

$$Q = \sqrt[m]{\frac{H_1}{R_1}} + \sqrt[m]{\frac{H_2}{R_2}} = \left(\frac{1}{\sqrt[m]{R_1}} + \frac{1}{\sqrt[m]{R_2}}\right) \sqrt[m]{H}$$

$$Q^m = \left(\frac{1}{\sqrt[m]{R_1}} + \frac{1}{\sqrt[m]{R_2}}\right)^m H$$

$$H = \frac{R_1 R_2}{\left(\sqrt[m]{R_1} + \sqrt[m]{R_2}\right)^m} Q^m = R_{1\|2} Q^m.$$

The equivalent resistance of the parallel connection is under the assumption of the same flow exponent

$$R_{1\|2} = \frac{R_1 R_2}{\left(\sqrt[m]{R_1} + \sqrt[m]{R_2}\right)^m}.$$

Series connection of hydraulic conductivities Recall the hydraulic conductivity is defined by (2.3). A total pressure loss over two conductivities is

$$\Delta p = \Delta p_1 + \Delta p_2,$$

the pressure loss on each conductivity is

$$\Delta p_i = \frac{1}{K_i^m} Q^m, i = 1,2$$

therefore the total loss is

$$\Delta p = \left(\frac{1}{K_1^m} + \frac{1}{K_2^m}\right) Q^m$$

and converting back into the conductivity form (2.3) gives

$$Q = \left(\frac{1}{K_1^m} + \frac{1}{K_2^m}\right)^{-\frac{1}{m}} \sqrt[m]{\Delta p}.$$

The hydraulic conductivity of a series connection of conductivities is

$$K_{1—2} = \left(\frac{1}{K_1^m} + \frac{1}{K_2^m}\right)^{-\frac{1}{m}}.$$

Parallel connection of hydraulic conductivities In a parallel connection, the total flow is a sum of the parallel flows

$$Q = Q_1 + Q_2,$$

where each conductivity experiences the same pressure potential and thus

$$Q = K_1 \sqrt[m]{\Delta p} + K_2 \sqrt[m]{\Delta p}$$
$$Q = (K_1 + K_2) \sqrt[m]{\Delta p}.$$

A hydraulic conductivity of a parallel connection of conductivities is

$$K_{1\|2} = K_1 + K_2.$$

A.2. Common valve characteristic types

Linear

There is a linear dependency between stroke and the flow factor $K_v(x)$. When the valve is fully closed the flow corresponds to its minimal value $K_v(0) = K_{v0}$, when the flow is fully opened the flow gets its saturation value $K_v(1) = K_{vs}$. The describing function for the whole range is

$$K_v(x) = K_{v0} + x(K_{vs} - K_{v0}).$$

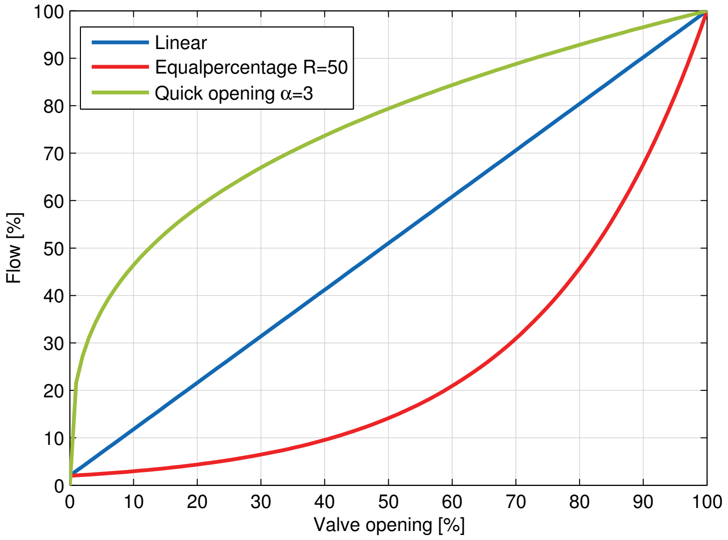

Figure A.1.: Valve characteristics.

Equalpercentage

Equalpercentage valve is mainly used in practice to linearize heat output of heat exchangers, i.e. approximately - in the first half of a stroke the flow increases slowly and in the second half quickly. The valve rangeability r is chosen such that the valve characteristic is complementary to that of a heat exchanger (usually R=50 [19]).The describing function is

$$K_{\mathrm{v}}(x) = K_{\mathrm{vs}} r^{x-1}, \tag{A.3}$$

where one shall notice in Fig. A.1 that for a closed valve the flow is no zero, but corresponds to K_{v0}. There is a modification called *semi-equalpercentage* valve, which starts with zero flow for a fully closed valve, but on the other hand it does not reach the flow corresponding to K_{vs} (as A.3 does). The modified characteristics is desribed by

$$K_{\mathrm{v}}(x) = K_{\mathrm{vs}}\left(r^{x-1} - r^{-1}\right).$$

Quick opening

For on-off functionality, a quick opening valve characteristics is often used. The flow here increases rapidly at the beginning of a stroke and after that the change in flow is rather mild. The describing function is

$$K_{\mathrm{v}}(x) = K_{\mathrm{vs}} x^{\frac{1}{\alpha}}, \quad \alpha > 0.$$

A.3. Pump characteristics manipulations

A.3.1. Speed scaling

Pump characteristics for nominal pump speed are defined in section 3.2. Using the affinity laws presented in section 3.1, the behavior of the of the pump when the angular velocity of the impeller varies from the nominal conditions.

Head-flow characteristics scaling

Varying the pump speed by a ratio

$$S = \frac{n}{n_\mathrm{n}}$$

results by the first and second affinity law in adapted pump head-flow polynomial

$$H(Q,n) = H(Q,n)|_\mathrm{n} S^2 = H(Q/S,n_\mathrm{n}) S^2 = \sum_{i=0}^{d_\mathrm{H}} a_{i,\mathrm{n}} \left(\frac{Q}{S}\right)^i S^2 = \sum_{i=0}^{d_\mathrm{H}} a_{i,\mathrm{n}} S^{2-i} Q^i,$$

and the speed-scaled coefficients are

$$a_i(S) = a_{i,\mathrm{n}} S^{2-i}. \tag{A.4}$$

This approximation holds close to the nominal conditions ($S \sim 1$). The speed scaling transformation preserves the characteristic shape. Scaled pump characteristics is displayed in Fig. 3.1. Head-flow characteristics of a real pump varies in shape for large speed variations; such a variation is no handled in the above approach, but could be handled by defining the pump polynomial in several working points.

Power characteristic scaling

The power consumption of a pump changes by affinity laws cubically with the speed. It holds if the efficiency of the pump is assumed to remain constant and the power characteristics polynomial coefficients scale in the following manner

$$P_\mathrm{e}(Q,n) = P_\mathrm{e}(Q,n_\mathrm{n}) S^3 = P_\mathrm{e}(Q/S,n) S^3 = \sum_{i=0}^{d_\mathrm{E}} b_{i,\mathrm{n}} \left(\frac{Q}{S}\right)^i S^3 = \sum_{i=0}^{d_\mathrm{E}} b_{i,\mathrm{n}} S^{3-i} Q^i.$$

The pump efficiency in reality deteriorates for pump speeds lower then in design conditions. When the decrease in efficiency is monotone, the above formula can be modified to account for the diminishing performance in the following way

$$P_\mathrm{e}(Q,n) = P_\mathrm{e}(Q/S,n) S^{3-\chi} = \sum_{i=0}^{d_\mathrm{E}} b_{i,\mathrm{n}} S^{(3-\chi-i)} Q^i,$$

where $\chi > 0$ is a performance reduction factor. Scaled power characteristic with the efficiency adaptation ($\chi = 0.2$) can be seen in Fig. 3.1. The speed-scaled coefficients are

$$b_i(S) = b_{i,\mathrm{n}} S^{(3-\chi-i)}. \tag{A.5}$$

A.3.2. Hydraulic power model

Hydraulic power in hydralic systems is given as

$$P_\mathrm{h}\left(\Delta p,\dot{V}\right) = \Delta p \cdot \dot{V},$$

where Δp [Pa] is pressure difference and $\dot{V}$ [$\mathrm{m^3/s}$] is a volumetric flow. Pump systems are usually defined in head H[m] and volumetric flow Q [$\mathrm{m^3/h}$] $= 3{,}6 \cdot 10^3 \cdot \dot{V}$. Then the hydraulic power is

$$P_\mathrm{h}(H,Q) = \left(\frac{1}{3{,}6 \cdot 10^3}\rho g\right) \cdot H \cdot Q.$$

Now, given that the H-Q characteristic is defined by a polynomial

$$H(Q) = \sum_{i=0}^{d_H} a_i Q^i,$$

then the hydraulic power model is

$$P_h(H,Q,S) = \frac{1}{3{,}6 \cdot 10^3}\rho g \sum_{i=0}^{d_H} a_i(S)\, Q^{i+1} = \sum_{i=0}^{d_H}\left(\frac{1}{3{,}6 \cdot 10^3}\rho g \cdot a_i(S)\right) Q^{i+1} = \sum_{i=0}^{d_H+1} c_i(S)\, Q^i, \tag{A.6}$$

and the hydraulic power polynomial coefficients are

$$\begin{aligned} c_i(S) &= \tfrac{1}{3{,}6 \cdot 10^3}\rho g \cdot a_{i-1}(S), i = 1 \ldots d_H + 1 \\ c_0 &= 0. \end{aligned}$$

A.3.3. Best efficiency point (BEP)

Efficiency of a pump is defined as a ratio of a hydraulic power P_h transfered to the fluid and electric power P_e consumed

$$\eta(Q,S) = \frac{P_h(Q,S)}{P_e(Q,S)}.$$

The hydraulic power function is defined by (A.6) and the electric power is defined by (3.5). The best efficiency point is located at the peak of the efficiency function, e.i. at a point where

$$\frac{\mathrm{d}\eta(Q,S)}{\mathrm{d}Q} = 0.$$

Substituting for the efficiency gives

$$0 = \frac{\mathrm{d}}{\mathrm{d}Q}\left(\frac{P_h(Q,S)}{P_e(Q,S)}\right) = \frac{\frac{\mathrm{d}}{\mathrm{d}Q}P_h(Q,S) \cdot P_e(Q,S) - P_h(Q,S) \cdot \frac{\mathrm{d}}{\mathrm{d}Q}P_e(Q,S)}{P_e(Q,S)^2}$$

which is equivalent to

$$\frac{\mathrm{d}}{\mathrm{d}Q}P_h(Q,S)\, P_e(Q,S) - P_h(Q,S)\, \frac{\mathrm{d}}{\mathrm{d}Q}P_e(Q,S) \overset{!}{=} 0.$$

Solving for Q gives the flow at BEP $Q_{BEP}(S)$. Head $H_{BEP}(S)$, power $P_{e,BEP}(S)$ and efficiency $\eta_{BEP}(S)$ are found by evaluating respective polynomials/functions.

Remark. Polynomial multiplication may be simplified by convolution on its coefficients. Define polynomials $p_1 : \sum_{i=0}^{N} a_i x^i, p_2 : \sum_{j=0}^{M} b_j x^j$, then their product is given by $p_1 \cdot p_2 = \sum_{i=0}^{N+M} c_i x^i$, where the coeffiecient vector is convolution of the two polynomial coefficient vectors $c = a * b$.

Remark. Derivative on a polynomial is a respective degree right-shift on the polynomial coeffiecients vector.

A.3.4. Energy efficiency index (EEI)

Energy efficiency index (EEI) is a measure of energy utilization efficiency of a pump. According to [19] 40% of pumping energy pertains to circulators. European parliament legislative Ecodesign-Directive (2009/125/EC) permits selling new standalone circulators only with EEI ≤ 0.27 since January 1st 2013 and since January 1st 2015 only with EEI≤ 0.23. The EEI is calculated, according to [58], as

$$\mathrm{EEI} = \frac{P_{e,avg.}}{P_{ref}} C_{20\%},$$

where $P_{e,avg}$ [W] is a weighted average electrical power input of the circulator, P_{ref} [W] is a reference power and $C_{20\%} = 0.49$ is a calibration factor ensuring that only 20% of a certain type have an EEI≤ 0.20 benchmark value. The reference power is calculated using hydraulic power of a circulator at hand as

$$P_{\mathrm{ref}} = 1.7 P_{\mathrm{h,max}} + 17 \left(1 - e^{-0.3 P_{\mathrm{h,max}}}\right) \quad 1\mathrm{W} \leq P_{\mathrm{h,max}} \leq 2500\mathrm{W},$$

where the maximal hydraulic power $P_{\mathrm{h,max}}$ [W] is calculated from a measured data at pump's full speed as

$$P_{\mathtt{h,max}} = \max_{h,Q} (H \cdot Q) = H_{\mathtt{max}} Q_{\mathtt{max}}.$$

Four operating points at 100%, 75%, 50% and 25% of Q_{max} and at heads defined by Fig. A.2 are measured on the actual pump. Electrical power consumption for each operating point is recorded and denoted $P_{\mathrm{e},100\%}, P_{\mathrm{e},75\%}, P_{\mathrm{e},50\%}, P_{\mathrm{e},25\%}$, respectively. The average weighted electrical power is then calculated as

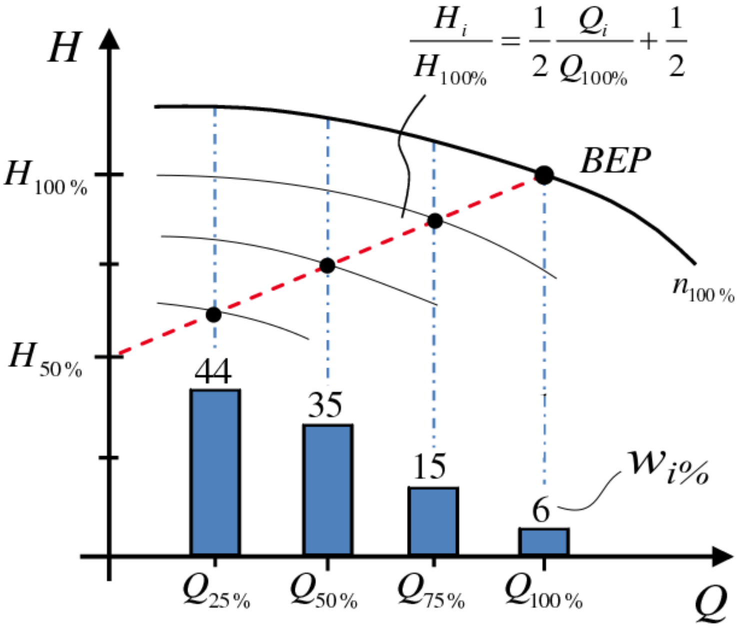

Figure A.2.: Energy Efficiency Index. Illustration of measurement points [58].

$$P_{\mathrm{e,avg}} = w_{100\%} P_{\mathrm{e},100\%} + w_{75\%} P_{\mathrm{e},75\%} + w_{50\%} P_{\mathrm{e},50\%} + w_{25\%} P_{\mathrm{e},25\%},$$

where the weighting coefficients represent average operating time at the stated power levels and the coefficient values defined by [58] are in Fig. A.2.

A.3.5. Series and parallel connections of pums

Serial connection of pumps A serial connection of pump shares the same basic dependences as a serial connection of resistances, i.e.

$$\begin{aligned} H(Q) &= H_1(Q_1) + H_2(Q_2) \\ Q &= Q_1 = Q_2. \end{aligned}$$

The head of the compound increases, while the max. flow remains unchanged. The pumps have at nominal speed the following polynomials

$$\begin{aligned} H_1(Q_1) &= \sum_{i=0}^{d_{\mathrm{H},1}} a_i Q_1^i \\ H_2(Q_2) &= \sum_{i=0}^{d_{\mathrm{H},2}} b_i Q_2^i. \end{aligned}$$

The equivalent pump model has therefore the following polynomial representation

$$H(Q) = \sum_{i=0}^{\max\left(d_{\mathrm{H},1}, d_{\mathrm{H},2}\right)} (a_i + b_i) Q^i.$$

Parallel connection of pumps Two pumps connected in parallel have the following total head and flow

$$\begin{aligned} H(Q) &= H_1(Q_1) = H_2(Q_2) \\ Q &= Q_1 + Q_2. \end{aligned}$$

Simple polynomial representation of the connection is not available in this case. The overall behavior is however predictable, the maximal produced head remains the same, while the total flow of the parallel connection is increased.

B. Two-pipe system stability proofs

Proof of Theorem 3. The Jacobian (9.13) can be written as

$$\begin{aligned} \boldsymbol{J} &= p_{\text{in}}\left[\operatorname{diag}\left(\frac{\tilde{\boldsymbol{p}}_{\text{b}}(g)}{\tilde{p}_0(g)}\right) + \operatorname{diag}(\boldsymbol{g})\left(\frac{\nabla_g\tilde{\boldsymbol{p}}_{\text{b}}(g)}{\tilde{p}_0(g)} - \frac{\tilde{\boldsymbol{p}}_{\text{b}}(g)\nabla_g^T\tilde{p}_0(g)}{\tilde{p}_0^2(g)}\right)\right] \\ &= \frac{p_{\text{in}}}{\tilde{p}_0^2(g)}\left[\tilde{p}_0\operatorname{diag}(\tilde{\boldsymbol{p}}_{\text{b}}(g)) + \operatorname{diag}(\boldsymbol{g})\left(\tilde{p}_0\nabla_g\tilde{\boldsymbol{p}}_{\text{b}}(g) - \tilde{\boldsymbol{p}}_{\text{b}}(g)\nabla_g^T\tilde{p}_0(g)\right)\right], \end{aligned} \tag{B.1}$$

where $\nabla_g f(g)$ denotes the operation of taking the Jacobian of the function $f(g)$ with respect to g.
The terms in the Jacobian (B.1) can be simplified. Let us start with $\nabla_g\tilde{\boldsymbol{p}}_{\text{b}}(g)$. Recall that $\tilde{p}_i = (\tilde{\boldsymbol{G}}^{-1})_{i+1,1}$, the ith element of the first column of $\tilde{\boldsymbol{G}}^{-1}$. Thus, to get $\frac{\partial\tilde{p}_i}{\partial g_j}$ we can use the derivative of the matrix inverse. Note that for the derivative of the inverse of any parametric matrix $\boldsymbol{A}(g)$ holds [236, Fact 10.11.20]

$$\frac{\partial\boldsymbol{A}^{-1}(g)}{\partial g_i} = -\boldsymbol{A}^{-1}(g)\left(\frac{\partial A(g)}{\partial g_i}\right)\boldsymbol{A}^{-1}(g). \tag{B.2}$$

So $\frac{\partial\tilde{\boldsymbol{G}}^{-1}(g)}{\partial g_i} = -\tilde{\boldsymbol{G}}^{-1}(g)\left(\frac{\partial\tilde{\boldsymbol{G}}(g)}{\partial g_i}\right)\tilde{\boldsymbol{G}}^{-1}(g)$. The derivative of the conductance matrix $\tilde{\boldsymbol{G}}$ is $\frac{\partial\tilde{\boldsymbol{G}}(g)}{\partial g_j} = \operatorname{diag}(\boldsymbol{e}_{j+1})$, where $\boldsymbol{e}_j = [0,\dots,0,1,0,\dots,0]^T$ is the jth canonical vector. In other words, $\frac{\partial\tilde{\boldsymbol{G}}(g)}{\partial g_j}$ is the matrix of zeros, with 1 on the $j+1$th element of the diagonal. Let h_{ij} be the (i,j)th element of $\tilde{\boldsymbol{G}}^{-1}$. Then we have using (B.2) and the fact that $\tilde{p}_i = h_{i+1,1}$

$$\frac{\partial\tilde{p}_i(g)}{\partial g_j(g)} = -h_{j+1,1}(g)h_{i+1,j+1}(g) = -\tilde{p}_j(g)h_{i+1,j+1}(g). \tag{B.3}$$

Partition the matrix $\tilde{\boldsymbol{G}}^{-1}$ as

$$\tilde{\boldsymbol{G}}^{-1} = \begin{bmatrix} H_{11} & \boldsymbol{H}_{12} \\ \boldsymbol{H}_{21} & \boldsymbol{H}_{22} \end{bmatrix}, \tag{B.4}$$

where $H_{11} = h_{1,1} = \tilde{p}_0$, $\boldsymbol{H}_{12}^{\text{T}} = \boldsymbol{H}_{21} = \tilde{\boldsymbol{p}}_{\text{b}}$ and $\boldsymbol{H}_{22}$ is the remaining $N-1\times N-1$ matrix. Note that $\boldsymbol{H}_{22}$ is symmetric, since it is a principal submatrix of a symmetric matrix $\tilde{\boldsymbol{G}}^{-1}$.
Using this partitioning and defining $\boldsymbol{V} = \operatorname{diag}\left(\frac{\tilde{\boldsymbol{p}}_{\text{b}}(g)}{\tilde{p}_0(g)}\right)$, from (B.3) we get

$$\nabla_g\tilde{\boldsymbol{p}}_{\text{b}}(g) = -\boldsymbol{H}_{22}(g)\,\boldsymbol{V}. \tag{B.5}$$

.
Similarly, consider $\tilde{\boldsymbol{p}}_{\text{b}}(g)\nabla_g^T\tilde{p}_0(g)$. Its (i,j)th element is

$$(\tilde{\boldsymbol{p}}_{\text{b}}\nabla_g^T\tilde{p}_0)_{ij} = \tilde{p}_i\frac{\partial\tilde{p}_0(g)}{\partial g_j} = -\tilde{p}_i\tilde{p}_jh_{1,j+1} = \tilde{p}_i\tilde{p}_jh_{j+1,1} = \tilde{p}_i\tilde{p}_j^2. \tag{B.6}$$

Then, we get

$$\tilde{\boldsymbol{p}}\nabla_g^T\tilde{p}_0 = -\tilde{\boldsymbol{p}}\tilde{\boldsymbol{p}}^T\boldsymbol{V}. \tag{B.7}$$

In (B.1), there is the term $\boldsymbol{M} = \tilde{p}_0\nabla_g\tilde{\boldsymbol{p}}_{\text{b}}(g) - \tilde{\boldsymbol{p}}_{\text{b}}(g)\nabla_g^T\tilde{p}_0(g)$. It can be written using (B.5) and (B.7) as

$$\begin{aligned} \boldsymbol{M} &= \tilde{p}_0\nabla_g\tilde{\boldsymbol{p}}_{\text{b}}(g) - \tilde{\boldsymbol{p}}_{\text{b}}(g)\nabla_g^T\tilde{p}_0(g) = -\tilde{p}_0H_{22}(g)\boldsymbol{V} - \tilde{\boldsymbol{p}}\tilde{\boldsymbol{p}}^T\boldsymbol{V} \\ &= -\tilde{p}_0\boldsymbol{P}^{-1}\boldsymbol{V} \end{aligned} \tag{B.8}$$

with $\boldsymbol{P}^{-1} = \boldsymbol{H}_{22}(g) - \tilde{\boldsymbol{p}}_{\mathrm{b}}\tilde{p}_0^{-1}\tilde{\boldsymbol{p}}_{\mathrm{b}}^T$. Using the partitioning in (B.4), we can write it as

$$\boldsymbol{P}^{-1} = \boldsymbol{H}_{22} - \boldsymbol{H}_{21}\boldsymbol{H}_{11}^{-1}\boldsymbol{H}_{12} \Rightarrow \boldsymbol{P} = (\boldsymbol{H}_{22} - \boldsymbol{H}_{21}\boldsymbol{H}_{11}^{-1}\boldsymbol{H}_{12})^{-1}. \tag{B.9}$$

Note that for an inverse of a block matrix holds

$$\begin{bmatrix} \boldsymbol{A} & \boldsymbol{B} \\ \boldsymbol{C} & \boldsymbol{D} \end{bmatrix}^{-1} = \begin{bmatrix} \boldsymbol{A^{-1} + A^{-1}B(D - CA^{-1}B)^{-1}CA^{-1}} & \boldsymbol{-A^{-1}B(D - CA^{-1}B)^{-1}} \\ \boldsymbol{-(D - CA^{-1}B)^{-1}CA^{-1}} & \boldsymbol{(D - CA^{-1}B)^{-1}} \end{bmatrix}. \tag{B.10}$$

It also holds

$$\begin{bmatrix} H_{11} & \boldsymbol{H}_{12} \\ \boldsymbol{H}_{21} & \boldsymbol{H}_{22} \end{bmatrix}^{-1} = \begin{bmatrix} \tilde{\boldsymbol{G}}_{11} & \tilde{\boldsymbol{G}}_{12} \\ \tilde{\boldsymbol{G}}_{21} & \tilde{\boldsymbol{G}}_{22} \end{bmatrix}. \tag{B.11}$$

Hence, combining (B.10) with (B.11) it follows that $\boldsymbol{P}^{-1} = (\boldsymbol{H_{22}} - \boldsymbol{H_{21}H_{11}^{-1}H_{12}})^{-1} = \tilde{\boldsymbol{G}}_{22}$. Then

$$\begin{aligned} \boldsymbol{M} &= \tilde{p}_0(g)\nabla_g\tilde{\boldsymbol{p}}_{\mathrm{b}}(g) - \tilde{\boldsymbol{p}}_{\mathrm{b}}(g)\nabla_g^T\tilde{p}_0(g) \\ &= -\tilde{p}_0(g)\boldsymbol{P}^{-1}(g)\boldsymbol{V} = -\tilde{p}_0(g)\tilde{\boldsymbol{G}}_{22}^{-1}(g)\boldsymbol{V}. \end{aligned} \tag{B.12}$$

Finally, using (B.12), the Jacobian (B.1) can be expressed as

$$\boldsymbol{J} = p_{\mathrm{in}}\left[\boldsymbol{I} - \mathrm{diag}\,(\boldsymbol{g})\,\tilde{\boldsymbol{G}}_{22}^{-1}(g)\right]\mathrm{diag}\left(\frac{\tilde{\boldsymbol{p}}_{\mathrm{b}}(g)}{\tilde{p}_0(g)}\right). \tag{B.13}$$

$\square$

Proof of Theorem 4. The Jacobian (9.15) can be written as

$$\begin{aligned} \boldsymbol{J} &= p_{\mathrm{in}}\mathrm{diag}\,(\boldsymbol{g})\,[\mathrm{diag}\,(\boldsymbol{g})^{-1} - \tilde{\boldsymbol{G}}_{22}^{-1}(g)]\mathrm{diag}\left(\frac{\tilde{\boldsymbol{p}}_{\mathrm{b}}(g)}{\tilde{p}_0(g)}\right) \\ &= p_{\mathrm{in}}\mathrm{diag}\,(\boldsymbol{g})\,\boldsymbol{M}(g)\mathrm{diag}\left(\frac{\tilde{\boldsymbol{p}}_{\mathrm{b}}(g)}{\tilde{p}_0(g)}\right). \end{aligned} \tag{B.14}$$

The matrix $\boldsymbol{M}(g) = \mathrm{diag}\,(\boldsymbol{g})^{-1} - \tilde{\boldsymbol{G}}_{22}^{-1}(g)$ is a symmetric matrix, because it is a sum of a diagonal matrix $\mathrm{diag}\,(\boldsymbol{g})^{-1}$ and an inverse of a positive definite symmetric matrix $\tilde{\boldsymbol{G}}_{22}^{-1}(g)$. Therefore, the matrix $\boldsymbol{M}(g)$ has real eigenvalues. Denote $\boldsymbol{D}_1 = \mathrm{diag}\,(\boldsymbol{g})$ and $\boldsymbol{D}_2 = \mathrm{diag}\left(\frac{\tilde{\boldsymbol{p}}_{\mathrm{b}}(g)}{\tilde{p}_0(g)}\right)$. From (B.14) we have $\boldsymbol{J} = p_{\mathrm{in}}\boldsymbol{D}_1\boldsymbol{M}(g)\boldsymbol{D}_2$. We now show that $\boldsymbol{J}$ has real eigenvalues. Consider the transformation $\boldsymbol{T} = \boldsymbol{D}_1^{1/2}\boldsymbol{D}_2^{-1/2}$. Then by similarity $\boldsymbol{T^{-1}JT}$ has the same eigenvalues as $\boldsymbol{J}$. We have

$$\begin{aligned} \boldsymbol{T}^{-1}\boldsymbol{J}\boldsymbol{T} &= p_{\mathrm{in}}(\boldsymbol{D}^{1/2}\boldsymbol{D}_2^{-1/2})^{-1}\boldsymbol{D}_1\boldsymbol{M}\boldsymbol{D}_2\boldsymbol{D}_1^{1/2}\boldsymbol{D}_2^{-1/2} \\ &= p_{\mathrm{in}}\boldsymbol{D}_1^{1/2}\boldsymbol{D}_2^{1/2}\boldsymbol{M}\boldsymbol{D}_1^{1/2}\boldsymbol{D}_2^{1/2} = p_{\mathrm{in}}\boldsymbol{Q}^{\mathrm{T}}\boldsymbol{M}\boldsymbol{Q} \end{aligned} \tag{B.15}$$

with $\boldsymbol{Q} = \boldsymbol{D}_1^{1/2}\boldsymbol{D}_2^{1/2}$. The matrix $\boldsymbol{Q}^T\boldsymbol{M}\boldsymbol{Q}$ is a symmetric matrix, so its eigenvalues are real. This matrix is also similar to the original $\boldsymbol{J} = p_{\mathrm{in}}\boldsymbol{D}_1\boldsymbol{M}\boldsymbol{D}_2$, so $\boldsymbol{J}$ has real eigenvalues as well. Similarity to a symmetric matrix also means that $\boldsymbol{J}$ is diagonalizable.

Now we show the fact that the eigenvalues are all positive and less than one. Using the previous proof, the term $(\boldsymbol{I} - \mathrm{diag}\,(\boldsymbol{g})\,\tilde{\boldsymbol{G}}_{22}^{-1})$ in (9.15) has real eigenvalues. From Gershgorin's theorem [236, Fact 4.10.16] it is known that

$$\lambda_i\left(\boldsymbol{I} - \mathrm{diag}\,(\boldsymbol{g})\,\tilde{\boldsymbol{G}}_{22}^{-1}\right) = 1 - \lambda_i\left(\mathrm{diag}\,(\boldsymbol{g})\,\tilde{\boldsymbol{G}}_{22}^{-1}\right), \tag{B.16}$$

We now show that the eigenvalues of $\mathrm{diag}\,(\boldsymbol{g})\,\tilde{\boldsymbol{G}}_{22}^{-1}$ are positive and less than one. The following holds: $\lambda_i(\mathrm{diag}\,(\boldsymbol{g})\,\tilde{\boldsymbol{G}}_{22}^{-1}) < 1 \Leftrightarrow \lambda_i(\tilde{\boldsymbol{G}}_{22}\mathrm{diag}\,(\boldsymbol{g})^{-1}) > 1$. Note that by (9.6) $\tilde{\boldsymbol{G}}_{22} = \mathrm{diag}\,(\boldsymbol{g}) + \boldsymbol{L}_{22}$, where $\boldsymbol{L}_{22}$ was obtained from $\boldsymbol{L}$ by removing the first row and column. Then we can write

$$\begin{aligned}
&\lambda_i(\tilde{\boldsymbol{G}}_{22}\mathrm{diag}\,(\boldsymbol{g})^{-1}) && \text{(B.17)}\\
&= \lambda_i\Big((\mathrm{diag}\,(\boldsymbol{g}) + \boldsymbol{L}_{22})\mathrm{diag}\,(\boldsymbol{g})^{-1}\,\Big) \\
&= \lambda_i(\boldsymbol{I} + \boldsymbol{L}_{22}\,\mathrm{diag}\,(\boldsymbol{g})^{-1}) = 1 + \lambda_i(\boldsymbol{L}_{22}\,\mathrm{diag}\,(\boldsymbol{g})^{-1}). && \text{(B.18)}
\end{aligned}$$

Matrix $\boldsymbol{L}_{22}\,\mathrm{diag}\,(\boldsymbol{g})^{-1}$ is a scaled pinned Laplacian [107], post-multiplied by a positive diagonal matrix, so has positive eigenvalues. Then it follows that $\lambda_i(\boldsymbol{I} + \boldsymbol{L}_{22}\mathrm{diag}\,(\boldsymbol{g})^{-1}) = 1 + \lambda_i(\boldsymbol{L}_{22}\mathrm{diag}\,(\boldsymbol{g})^{-1})^{-1} > 1$. Hence, $0 < \lambda(\mathrm{diag}\,(\boldsymbol{g})\,\tilde{\boldsymbol{G}}_{22}^{-1} < 1$ and then $0 < \lambda(I - \mathrm{diag}\,(\boldsymbol{g})\,\tilde{\boldsymbol{G}}_{22}^{-1}) < 1$.

In (9.15), the post-multiplying factor $\mathrm{diag}\left(\frac{\tilde{\boldsymbol{p}}_{\mathrm{b}}(g)}{\tilde{p}_0(g)}\right)$ has all entries less than one (pressure at nodes divided by the total pressure). Such a multiplication only shrinks the Gershgorin disks, so $\lambda\left((\boldsymbol{I} - \mathrm{diag}\,(\boldsymbol{g})\,\tilde{\boldsymbol{G}}_{22}^{-1})\mathrm{diag}\left(\frac{\tilde{\boldsymbol{p}}_{\mathrm{b}}(g)}{\tilde{p}_0(g)}\right)\right) \leq \lambda\left(\boldsymbol{I} - \mathrm{diag}\,(\boldsymbol{g})\,\tilde{\boldsymbol{G}}_{22}^{-1}\right)$. Therefore, the eigenvalues of $\boldsymbol{J}$ are bounded as

$$0 < \lambda_i(\boldsymbol{J}) = p_{\mathrm{in}}\lambda_i\left(\Big(\boldsymbol{I} - \mathrm{diag}\,(\boldsymbol{g})\,\tilde{\boldsymbol{G}}_{22}^{-1}(g)\Big)\mathrm{diag}\left(\frac{\tilde{\boldsymbol{p}}_{\mathrm{b}}(g)}{\tilde{p}_0(g)}\right)\right) \leq p_{\mathrm{in}},\ \forall i. \tag{B.19}$$

□

C. Interconnection of LTI systems

Consider having a number of dynamic sub-systems in a state-space representation

$$\mathcal{S}_i : \begin{array}{rcl} \dot{\boldsymbol{x}}_i & = & \boldsymbol{A}_i\boldsymbol{x}_i + \boldsymbol{B}_i\boldsymbol{u}_i \\ \boldsymbol{y}_i & = & \boldsymbol{C}_i\boldsymbol{x}_i + \boldsymbol{D}_i\boldsymbol{u}_i \end{array}$$

where $i \in \{1,\dots,N\}$, N is the number of sub-systems, and $\boldsymbol{x}_i \in \mathbb{R}^{n^i_\mathrm{x}\times 1}$,$\boldsymbol{u}_i \in \mathbb{R}^{n^i_\mathrm{u}\times 1}$, and $\boldsymbol{y}_i \in \mathbb{R}^{n^i_\mathrm{y}\times 1}$ are state, input and output vectors, respectively. Define an aggregated state, input and output vector

$$\boldsymbol{x} = \left[\boldsymbol{x}_1^\mathsf{T},\dots,\boldsymbol{x}_N^\mathsf{T}\right]^\mathsf{T}, \boldsymbol{u} = \left[\boldsymbol{u}_1^\mathsf{T},\dots,\boldsymbol{u}_N^\mathsf{T}\right]^\mathsf{T}, \boldsymbol{y} = \left[\boldsymbol{y}_1^\mathsf{T},\dots,\boldsymbol{y}_N^\mathsf{T}\right]^\mathsf{T},$$

where $\boldsymbol{x} \in \mathbb{R}^{n_\mathrm{x}\times 1}$, $n_\mathrm{x} = \sum_{i=1}^{\mathrm{N}} n^i_\mathrm{x}$, $\boldsymbol{u} \in \mathbb{R}^{n_\mathrm{u}\times 1}$, $n_\mathrm{u} = \sum_{i=1}^{\mathrm{N}} n^i_\mathrm{u}$, $\boldsymbol{y} \in \mathbb{R}^{n_\mathrm{y}\times 1}$, and $n_\mathrm{y} = \sum_{i=1}^{\mathrm{N}} n^i_\mathrm{y}$.
What is the state-space representation of a system, where the connections between the sub-systems' inputs, outputs, external inputs $\boldsymbol{u}_\mathrm{x} \in \mathbb{R}^{1\times n^\mathrm{x}_\mathrm{u}}$ and external outputs $\boldsymbol{y}_\mathrm{x} \in \mathbb{R}^{1\times n^\mathrm{x}_\mathrm{y}}$ are specified by an interconnection matrix $\boldsymbol{M} \in \mathbb{R}^{\left(n^\mathrm{x}_\mathrm{y}+n_\mathrm{y}\right)\times\left(n^\mathrm{x}_\mathrm{u}+n_\mathrm{u}\right)}$? Or, in precise terms, what are the systems matrices $\boldsymbol{A}$,$\boldsymbol{B}$,$\boldsymbol{C}$,$\boldsymbol{D}$ of a system $\mathcal{S}$

$$\begin{aligned} \dot{\boldsymbol{x}} &= \boldsymbol{A}\boldsymbol{x} + \boldsymbol{B}\boldsymbol{u}_\mathrm{x} && \text{(C.1)} \\ \boldsymbol{y}_\mathrm{x} &= \boldsymbol{C}\boldsymbol{x} + \boldsymbol{D}\boldsymbol{u}_\mathrm{x}, && \text{(C.2)} \end{aligned}$$

where the interconnection of the systems is defined as

$$\begin{bmatrix} \boldsymbol{y}_\mathrm{x} \\ \boldsymbol{u} \end{bmatrix} = \boldsymbol{M} \begin{bmatrix} \boldsymbol{u}_\mathrm{x} \\ \boldsymbol{y} \end{bmatrix}?$$

First, partition $\boldsymbol{M}$ into

$$\boldsymbol{M} = \begin{bmatrix} \boldsymbol{M}_1 & \boldsymbol{M}_2 \\ \boldsymbol{M}_3 & \boldsymbol{M}_4 \end{bmatrix}$$

such that

$$\begin{aligned} \boldsymbol{y}_\mathrm{x} &= \boldsymbol{M}_1\boldsymbol{u}_\mathrm{x} + \boldsymbol{M}_2\boldsymbol{y} && \text{(C.3)} \\ \boldsymbol{u} &= \boldsymbol{M}_3\boldsymbol{u}_\mathrm{x} + \boldsymbol{M}_4\boldsymbol{y}. && \text{(C.4)} \end{aligned}$$

Then define an aggerated state-space system $\mathcal{S}_\mathrm{p}$ as a parallel stack of all the sub-systems

$$\begin{aligned} \dot{\boldsymbol{x}} &= \boldsymbol{A}_\mathrm{p}\boldsymbol{x} + \boldsymbol{B}_\mathrm{p}\boldsymbol{u} && \text{(C.5)} \\ \boldsymbol{y} &= \boldsymbol{C}_\mathrm{p}\boldsymbol{x} + \boldsymbol{D}_\mathrm{p}\boldsymbol{u}, && \text{(C.6)} \end{aligned}$$

where $\boldsymbol{A}_\mathrm{p} = \mathrm{blkdiag}\left(\{\boldsymbol{A}_i\}_{i\in\Omega}\right)$, $\boldsymbol{B}_\mathrm{p} = \mathrm{blkdiag}\left(\{\boldsymbol{B}_i\}_{i\in\Omega}\right)$, $\boldsymbol{C}_\mathrm{p} = \mathrm{blkdiag}\left(\{\boldsymbol{C}_i\}_{i\in\Omega}\right)$, $\boldsymbol{D}_\mathrm{p} = \mathrm{blkdiag}\left(\{\boldsymbol{D}_i\}_{i\in\Omega}\right)$, $\Omega = \{1,\dots,N\}$ and the 'blkdiag' operator is defined as

$$\boldsymbol{X} = \mathrm{blkdiag}\left(\{\boldsymbol{X}_i\}_{i\in\Omega}\right) = \begin{bmatrix} \boldsymbol{X}_1 & 0 & 0 \\ 0 & \ddots & 0 \\ 0 & 0 & \boldsymbol{X}_N \end{bmatrix}.$$

Now substituting (C.6) into (C.4) the vector $\boldsymbol{u}$ can be extracted

$$\begin{aligned}\boldsymbol{u} &= \boldsymbol{M}_3\boldsymbol{u}_\mathrm{x} + \boldsymbol{M}_4\left(\boldsymbol{C}_\mathrm{p}\boldsymbol{x} + \boldsymbol{D}_\mathrm{p}\boldsymbol{u}\right)\\ \left(\boldsymbol{I} - \boldsymbol{M}_4\boldsymbol{D}_\mathrm{p}\right)\boldsymbol{u} &= \boldsymbol{M}_3\boldsymbol{u}_\mathrm{x} + \boldsymbol{M}_4\boldsymbol{C}_\mathrm{p}\boldsymbol{x}\end{aligned}$$

where by defining

$$\boldsymbol{E} = \left(\boldsymbol{I} - \boldsymbol{M}_4\boldsymbol{D}_\mathrm{p}\right)^{-1} \tag{C.7}$$

we get

$$\boldsymbol{u} = \boldsymbol{E}\left(\boldsymbol{M}_4\boldsymbol{C}_\mathrm{p}\boldsymbol{x} + \boldsymbol{M}_3\boldsymbol{u}_\mathrm{x}\right). \tag{C.8}$$

Substituting (C.8) into (C.5)

$$\begin{aligned}\dot{\boldsymbol{x}} &= \boldsymbol{A}_\mathrm{p}\boldsymbol{x} + \boldsymbol{B}_\mathrm{p}\boldsymbol{E}\left(\boldsymbol{M}_4\boldsymbol{C}_\mathrm{p}\boldsymbol{x} + \boldsymbol{M}_3\boldsymbol{u}_\mathrm{x}\right)\\ &= \left(\boldsymbol{A}_\mathrm{p} + \boldsymbol{B}_\mathrm{p}\boldsymbol{E}\boldsymbol{M}_4\boldsymbol{C}_\mathrm{p}\right)\boldsymbol{x} + \boldsymbol{B}_\mathrm{p}\boldsymbol{E}\boldsymbol{M}_3\boldsymbol{u}_\mathrm{x}\end{aligned}$$

a comparing to (C.1), the $\boldsymbol{A}$ and $\boldsymbol{B}$ matrices are found

$$\boxed{\begin{aligned}\boldsymbol{A} &= \boldsymbol{A}_\mathrm{p} + \boldsymbol{B}_\mathrm{p}\boldsymbol{E}\boldsymbol{M}_4\boldsymbol{C}_\mathrm{p} && \text{(C.9)}\\ \boldsymbol{B} &= \boldsymbol{B}_\mathrm{p}\boldsymbol{E}\boldsymbol{M}_3. && \text{(C.10)}\end{aligned}}$$

Substituting (C.8) into (C.6)

$$\begin{aligned}\boldsymbol{y} &= \boldsymbol{C}_\mathrm{p}\boldsymbol{x} + \boldsymbol{D}_\mathrm{p}\boldsymbol{E}\left(\boldsymbol{M}_4\boldsymbol{C}_\mathrm{p}\boldsymbol{x} + \boldsymbol{M}_3\boldsymbol{u}_\mathrm{x}\right)\\ &= \left(\boldsymbol{C}_\mathrm{p} + \boldsymbol{D}_\mathrm{p}\boldsymbol{E}\boldsymbol{M}_4\boldsymbol{C}_\mathrm{p}\right)\boldsymbol{x} + \boldsymbol{D}_\mathrm{p}\boldsymbol{E}\boldsymbol{M}_3\boldsymbol{u}_\mathrm{x},\end{aligned}$$

substituting this result further into (C.3)

$$\begin{aligned}\boldsymbol{y}_\mathrm{x} &= \boldsymbol{M}_1\boldsymbol{u}_\mathrm{x} + \boldsymbol{M}_2\left(\boldsymbol{C}_\mathrm{p} + \boldsymbol{D}_\mathrm{p}\boldsymbol{E}\boldsymbol{M}_4\boldsymbol{C}_\mathrm{p}\right)\boldsymbol{x} + \boldsymbol{D}_\mathrm{p}\boldsymbol{E}\boldsymbol{M}_3\boldsymbol{u}_\mathrm{x}\\ &= \boldsymbol{M}_2\left(\boldsymbol{C}_\mathrm{p} + \boldsymbol{D}_\mathrm{p}\boldsymbol{E}\boldsymbol{M}_4\boldsymbol{C}_\mathrm{p}\right)\boldsymbol{x} + \left(\boldsymbol{M}_1 + \boldsymbol{D}_\mathrm{p}\boldsymbol{E}\boldsymbol{M}_3\right)\boldsymbol{u}_\mathrm{x}\end{aligned}$$

and comparing to (C.2), the $\boldsymbol{C}$ and $\boldsymbol{D}$ matrices are found

$$\boxed{\begin{aligned}\boldsymbol{C} &= \boldsymbol{M}_2\left(\boldsymbol{I} + \boldsymbol{D}_\mathrm{p}\boldsymbol{E}\boldsymbol{M}_4\right)\boldsymbol{C}_\mathrm{p} && \text{(C.11)}\\ \boldsymbol{D} &= \boldsymbol{M}_1 + \boldsymbol{D}_\mathrm{p}\boldsymbol{E}\boldsymbol{M}_3. && \text{(C.12)}\end{aligned}}$$

C.1. Minimal representation

Consider now having a subsystem with no dynamics

$$\mathcal{S}_i^\mathrm{s}: \begin{aligned}\dot{\boldsymbol{x}}_\mathrm{s} &= \boldsymbol{A}_\mathrm{s}\boldsymbol{x}_\mathrm{s} + \boldsymbol{B}_\mathrm{s}\boldsymbol{u}_\mathrm{s}\\ \boldsymbol{y}_\mathrm{s} &= \boldsymbol{C}_\mathrm{s}\boldsymbol{x}_\mathrm{s} + \boldsymbol{D}_\mathrm{s}\boldsymbol{u}_\mathrm{s},\end{aligned}$$

where $\boldsymbol{A}_\mathrm{s} = \boldsymbol{0}, \boldsymbol{B}_\mathrm{s} = \boldsymbol{0}, \boldsymbol{C}_\mathrm{s} = \boldsymbol{0}$. This is an averabundant representation of a simple

$$\mathcal{S}_\mathrm{s} \quad : \quad \boldsymbol{y}_\mathrm{s} = \boldsymbol{D}_\mathrm{s}\boldsymbol{u}_\mathrm{s} \tag{C.13}$$

relation, but it is represented in the full form for two reasons. First, it is the standard format in which a systems, dynamic or not, enter the merging process and second it illustrates beforehand, that there would be uncontrollable and unobservable states in the merged representation when using merging eqs. (C.9) to (C.12) over the standard form;

the resulting merged system would not be in a minimal representation form.

In order to prevent non-minimal representations, it can be observed that the static system (C.13) is an algebraic relation between input and output, as is the interconnection matrix $\boldsymbol{M}$. Therefore by incorporating the relation directly into the interconnection matrix and only then merging by eqs. (C.9) to (C.12) non-minimal representation is avoided. Recall the eqn. (C.4), we can split the interconnection matrix to separate the inputs $\boldsymbol{u}_\mathrm{s}$ and outputs $\boldsymbol{y}_\mathrm{s}$ as

$$\left[\begin{array}{c} \boldsymbol{u} \\ \hline \boldsymbol{u}_\mathrm{s} \end{array}\right] = \left[\begin{array}{c} \boldsymbol{M}_3 \\ \hline \boldsymbol{M}_3^\mathrm{s} \end{array}\right] \boldsymbol{u}_\mathrm{x} + \left[\begin{array}{c|c} \boldsymbol{M}_4 & \overline{\boldsymbol{M}}_4^\mathrm{s} \\ \hline \boldsymbol{M}_4^\mathrm{s} & \boldsymbol{L}_4^\mathrm{s} \end{array}\right] \left[\begin{array}{c} \boldsymbol{y} \\ \hline \boldsymbol{y}_\mathrm{s} \end{array}\right] \tag{C.14}$$

Now combining (C.13) and (C.14) we get

$$\begin{aligned} \boldsymbol{y}_\mathrm{s} &= \boldsymbol{D}_\mathrm{s}\left(\boldsymbol{M}_3^\mathrm{s}\boldsymbol{u}_\mathrm{x} + \boldsymbol{M}_4^\mathrm{s}\boldsymbol{y} + \boldsymbol{L}_4^\mathrm{s}\boldsymbol{y}_\mathrm{s}\right) \\ \left(\boldsymbol{I} - \boldsymbol{D}_\mathrm{s}\boldsymbol{L}_4^\mathrm{s}\right)\boldsymbol{y}_\mathrm{s} &= \boldsymbol{D}_\mathrm{s}\boldsymbol{M}_3^\mathrm{s}\boldsymbol{u}_\mathrm{x} + \boldsymbol{D}_\mathrm{s}\boldsymbol{M}_4^\mathrm{s}\boldsymbol{y} \end{aligned}$$

where by defining

$$\boldsymbol{F} = \left(\boldsymbol{I} - \boldsymbol{D}_\mathrm{s}\boldsymbol{L}_4^\mathrm{s}\right)^{-1}\boldsymbol{D}_\mathrm{s}$$

we get

$$\boldsymbol{y}_\mathrm{s} = \boldsymbol{F}\boldsymbol{M}_3^\mathrm{s}\boldsymbol{u}_\mathrm{x} + \boldsymbol{F}\boldsymbol{M}_4^\mathrm{s}\boldsymbol{y}. \tag{C.15}$$

Inserting now (C.15) back to (C.14) we get

$$\begin{aligned} \boldsymbol{u} &= \boldsymbol{M}_3\boldsymbol{u}_\mathrm{x} + \boldsymbol{M}_4\boldsymbol{y} + \overline{\boldsymbol{M}}_4^\mathrm{s}\boldsymbol{y}_\mathrm{s} \\ &= \left(\boldsymbol{M}_3 + \overline{\boldsymbol{M}}_4^\mathrm{s}\boldsymbol{F}\boldsymbol{M}_3^\mathrm{s}\right)\boldsymbol{u}_\mathrm{x} + \left(\boldsymbol{M}_4 + \overline{\boldsymbol{M}}_4^\mathrm{s}\boldsymbol{F}\boldsymbol{M}_4^\mathrm{s}\right)\boldsymbol{y} \\ &= \boldsymbol{M}_3^\mathrm{N}\boldsymbol{u}_\mathrm{x} + \boldsymbol{M}_4^\mathrm{N}\boldsymbol{y}, \end{aligned}$$

where the updated interconnection submatrices are

$$\boxed{\begin{aligned} \boldsymbol{M}_3^\mathrm{N} &= \boldsymbol{M}_3 + \overline{\boldsymbol{M}}_4^\mathrm{s}\boldsymbol{F}\boldsymbol{M}_3^\mathrm{s} && \text{(C.16)} \\ \boldsymbol{M}_4^\mathrm{N} &= \boldsymbol{M}_4 + \overline{\boldsymbol{M}}_4^\mathrm{s}\boldsymbol{F}\boldsymbol{M}_4^\mathrm{s}. && \text{(C.17)} \end{aligned}}$$

Now recall eqn. (C.3)

$$\boldsymbol{y}_\mathrm{x} = \boldsymbol{M}_1\boldsymbol{u}_\mathrm{x} + \left[\begin{array}{c|c} \boldsymbol{M}_2 & \boldsymbol{M}_2^\mathrm{s} \end{array}\right] \left[\begin{array}{c} \boldsymbol{y} \\ \hline \boldsymbol{y}_\mathrm{s} \end{array}\right]$$

inserting now (C.15) we get

$$\begin{aligned} \boldsymbol{y}_\mathrm{x} &= \boldsymbol{M}_1\boldsymbol{u}_\mathrm{x} + \boldsymbol{M}_2\boldsymbol{y} + \boldsymbol{M}_2^\mathrm{s}\boldsymbol{y}_\mathrm{s} \\ &= \left(\boldsymbol{M}_1 + \boldsymbol{M}_2^\mathrm{s}\boldsymbol{F}\boldsymbol{M}_3^\mathrm{s}\right)\boldsymbol{u}_\mathrm{x} + \left(\boldsymbol{M}_2 + \boldsymbol{M}_2^\mathrm{s}\boldsymbol{F}\boldsymbol{M}_4^\mathrm{s}\right)\boldsymbol{y} \\ &= \boldsymbol{M}_1^\mathrm{N}\boldsymbol{u}_\mathrm{x} + \boldsymbol{M}_2^\mathrm{N}\boldsymbol{y}, \end{aligned}$$

where the updated interconnection submatrices are

$$\boxed{\begin{aligned} \boldsymbol{M}_1^\mathrm{N} &= \boldsymbol{M}_1 + \boldsymbol{M}_2^\mathrm{s}\boldsymbol{F}\boldsymbol{M}_3^\mathrm{s} && \text{(C.18)} \\ \boldsymbol{M}_2^\mathrm{N} &= \boldsymbol{M}_2 + \boldsymbol{M}_2^\mathrm{s}\boldsymbol{F}\boldsymbol{M}_4^\mathrm{s}. && \text{(C.19)} \end{aligned}}$$

Algorithm C.1 Merge LTI subsystems

```
Input: $(\boldsymbol{A}_i, \boldsymbol{B}_i, \boldsymbol{C}_i, \boldsymbol{D}_i)_{i=1,\ldots,N}$, $\boldsymbol{M}_1, \boldsymbol{M}_2, \boldsymbol{M}_3, \boldsymbol{M}_4$
Output: $\boldsymbol{A}, \boldsymbol{B}, \boldsymbol{C}, \boldsymbol{D}$
Initialize $\boldsymbol{A}_\mathrm{p}, \boldsymbol{B}_\mathrm{p}, \boldsymbol{C}_\mathrm{p}, \boldsymbol{D}_\mathrm{p} = \boldsymbol{0}, r_\mathrm{u} = 0, c_\mathrm{y} = 0$
for $i = 1$ to $N$ do
    if $(\boldsymbol{A}_i, \boldsymbol{B}_i, \boldsymbol{C}_i = \boldsymbol{0} \wedge \boldsymbol{D}_i \neq \boldsymbol{0})$ then
        Update $\boldsymbol{M}_j$ using eqs. (C.16) to (C.19), $j = 1 \ldots 4$
        $\boldsymbol{M}_j = \boldsymbol{M}_j^N, j = 1 \ldots 4$
    else
        $r_\mathrm{u} = r_\mathrm{u} + n_\mathrm{u}, c_\mathrm{y} = c_\mathrm{y} + n_\mathrm{y}$
        $\boldsymbol{A}_\mathrm{p} = \mathrm{blkdiag}\left(\boldsymbol{A}_\mathrm{p}, \boldsymbol{A}_i\right), \boldsymbol{B}_\mathrm{p} = \mathrm{blkdiag}\left(\boldsymbol{B}_\mathrm{p}, \boldsymbol{B}_i\right)$
        $\boldsymbol{C}_\mathrm{p} = \mathrm{blkdiag}\left(\boldsymbol{C}_\mathrm{p}, \boldsymbol{C}_i\right), \boldsymbol{D}_\mathrm{p} = \mathrm{blkdiag}\left(\boldsymbol{D}_\mathrm{p}, \boldsymbol{D}_i\right)$
    end if
end for
Merge using eqs. (C.9) to (C.12)
return $\boldsymbol{A}, \boldsymbol{B}, \boldsymbol{C}, \boldsymbol{D}$
```

Nomenclature

Roman Symbols

C	Heat capacity rate [W/K]; Hazen-Williams roughness coefficient	
c_p	Specific heat capacity	[J/kg/K]
d	Diameter	
f	Multiplication factor (of flow)	
f_D	Darcy friction factor	
$\mathcal{H}$	Total heat transfer coefficient	[W/K]
H	Hydraulic head	
K	Hydraulic conductance	
L	Length	
$\dot{m}$	Mass flow rate	[kg/s]
m	Mass	
N	Number of elements	
n	Number of elements	
$\mathcal{P}$	Temperature effectiveness	[-]
P	Power	[W]
Q	Flow rate	
q	Heat flow	[W]
Re	Reynolds number	
t	Temporal coordinate; time	
T	Temperature	[°C]
$\dot{V}$	Volumetric flow rate	[m3/s]
v	Velocity	
x	System state variable; normalized spatial coordinate; valve stroke	
D	Diffusion coefficient (matrix)	

Greek Symbols

χ	Efficiency reduction exponent	[-]
ϵ	Pipe wall roughness	
η	Efficiency	
μ	Dynamic viscosity	
ν	Kinematic viscosity	
ρ	Density	
σ	Oversizing factor	[-]
∂_t	Partial derivative w.r.t. time	
∂_x	Partial derivative w.r.t. space	

Subscripts

0	Initial (condition)
a	Air (side)
ai	Air inlet
ao	Air outlet
ba	Body-to-air
b	Boiler
C	Centralized
c	Cross-section; capacity
d	Discrete; disturbance
D	Drop (e.g. of temperature); decentralized
e	Electric
g	of a graph
h	Hydraulic
i	Inlet
max	Maximal
min	Minimal
n	Nominal; normalized
nom	Nominal
o	Outlet; outside
op	Operative (temperature)
pi	Primary inlet
po	Primary outlet
p	Primary; parallel; pump
REF	Reference; setpoint
sg	Solar gain
si	Secondary inlet
so	Secondary outlet
SP	Setpoint; reference
s	Heat supply; serial; secondary
tot	Total
wi	Water inlet
wo	Water outlet
w	Water (side)
x	x^{th} in a row
z	Zone

Abbreviations

CNC	Automated machining tool
CV	Control valve
EEI	Energy efficiecy index
FCU	Fan coil unit
HQ	Head-flow pump characteristics
HVAC	Heating, ventilation, and air conditioning
HX	Heat exchanger
IAQ	Indoor air quality
ID	Indoor design (temperature)
I/O	Input and output
MCU	Microcontroller unit
MPC	Model predictive control
OD	Outdoor design (temperature)
PCP	Power control pump
PCV	Power control valve
PICV	Pressure-independent control valve
PLC	Programmable logic controller
PoE	Power-over-Ethernet
PQ	Power-flow pump characteristics
QCV	Q-valve; power control valve
QP	Q-pump; Power control pump
SF	Safety factor

Mathematical Symbols

Δ	Difference (temperature, pressure, etc.)
diag()	Diagonal of a matrix (formed or extracted)

Bibliography

[1] *Clean Energy For All Europeans*. Technical report. Brussel: European Commision, 2016.

[2] Luis Pérez-Lombard, José Ortiz, and Christine Pout. "A review on buildings energy consumption information". In: *Energy and Buildings* 40 (2008), pp. 394–398. ISSN: 0378-7788. DOI: `10.1016/j.enbuild.2007.03.007`.

[3] Inge Blom, Laure Itard, and Arjen Meijer. "Environmental impact of building-related and user-related energy consumption in dwellings". In: *Building and Environment* 46 (2011), pp. 1657–1669. ISSN: 0360-1323. DOI: `10.1016/j.buildenv.2011.02.002`.

[4] *Heat Roadmap Europe: Profile of heating and cooling demand in 2015*. Technical report. Frauhofer Institute for Systems and Innovation Research, 2017.

[5] Agis Papadopoulos. "Energy Cost and its Impact on Regulating Building Energy Behaviour". In: *Advances in Building Energy Research* 1 (Jan. 2007), pp. 105–121. DOI: `10.1080/17512549.2007.9687271`.

[6] Jiří Cigler. "Model predictive control for buildings". Ph.D. thesis. Czech Technical University in Prague, June 2013.

[7] Kim Trenbath et al. *Commercial Building Sensors and Controls Systems - Barriers, Drivers, and Costs*. Technical report. National Renewable Energy Laboratory, 2022.

[8] *Directive (EU) 2018/844 of the European Parliament and of the Council of 30 May 2018*. Technical report. European Commision, 2018.

[9] Wilo AG. "Circulators and Pumps: The future is high efficiency". In: *Ecodesign Dir. Mag. Wilo* 2010/2011 (2010).

[10] *High-performance commercial buildings - a technology roadmap*. Technical report. NREL, 2001.

[11] *Hydronics 4.0*. Grant n. TK01020024. Technology Agency of the Czech Republic. June 2018. URL: `https://starfos.tacr.cz/cs/project/TK01020024`.

[12] Munson, Young, Okiishi, and Huebsch. *Fundamentals of Fluid Mechanics*. 6th ed. Wiley, 2009. ISBN: 978-0470-26284-9.

[13] Frank M. White. *Fluid Mechanics*. 7th ed. New York: McGraw-Hill, 2011. ISBN: 978-0-07-352934-9.

[14] Frank P. Incropera, David P. DeWitt, and Theodore L. Bergman. *Principles of Heat and Mass Transfer*. John Wiley & Sons, 2012. ISBN: 978-0470646151.

[15] William Kent and Robert Thurston Kent. *The Mechanical Engineers' Pocket-book: A Reference-book of Rules, Tables, Data, and Formulæ*. John Wiley & Sons, 1916, p. 1526.

[16] Grundfos. *The Centrifugal Pump*. 2021.

[17] Francois Wahl and T. Espinasse. "Polynomial regression under shape constraints". working paper or preprint. Oct. 2014. URL: `https://inria.hal.science/hal-01073514`.

[18] Jiří Dostál. *Polynomial fitting under shape constraints tool: "polyfitsc"*. Oct. 2021.

[19] John Siegenthaler. *Modern Hydronic Heating: For Residential and Light Commercial Buildings*. 3rd ed. Delmar, Cengage Learning, 2012, p. 746. ISBN: 9781428335158.

[20] Jiří Dostál and Vladimír Havlena. "Mixed Mesh Finite Volume Method for 1D Hyperbolic Systems with Application to Plug-flow Heat Exchangers". In: *Mathematics* 9.20 (Oct. 2021), p. 2609. ISSN: 2227-7390. DOI: `10.3390/math9202609`.

[21] Gerhard H. Jirka Scott A. Socolofsky. *CVEN 489-501: Special Topics in Mixing and Transport Processes in the Environment*. Texas A&M University, 2005.

[22] Sergei Konstantinovich Godunov. "A difference method for numerical calculation of discontinuous solutions of the equations of hydrodynamics". In: *Matematicheskii Sbornik* 89.3 (1959), pp. 271–306.

[23] Bram Van Leer. "Towards the ultimate conservative difference scheme. V. A second-order sequel to Godunov's method". In: *Journal of Computational Physics* 32.1 (1979), pp. 101–136. DOI: `10.1016/0021-9991(79)90145-1`.

[24] Bram Van Leer. “Towards the ultimate conservative difference scheme. II. Monotonicity and conservation combined in a second-order scheme”. In: *Journal of Computational Physics* 14.4 (1974), pp. 361–370. DOI: `10.1016/0021-9991(74)90019-9`.

[25] Ami Harten. “High resolution schemes for hyperbolic conservation laws”. In: *Journal of Computational Physics* 49.3 (1983), pp. 357–393. DOI: `10.1016/0021-9991(83)90136-5`.

[26] A. Vande Wouwer, Philippe Saucez, and Carlos Vilas. *Simulation of ODE/PDE Models with MATLAB, OCTAVE and SCILAB*. Springer, 2014. DOI: `10.1007/978-3-319-06790-2`.

[27] H. K. Versteeg and W. Malalasekera. *An Introduction to Computational Fluid Dynamics: The Finite Volume Method*. Second. Pearson Education Limited, 2007. ISBN: 9780131274983.

[28] Richard Courant, Kurt Friedrichs, and Hans Lewy. “On the partial difference equations of mathematical physics”. In: *IBM journal of Research and Development* 11.2 (1967), pp. 215–234. DOI: `10.1147/rd.112.0215`.

[29] Hugo A. Jakobsen. *Chemical Reactor Modeling*. Springer International Publishing, 2014. DOI: `10.1007/978-3-319-05092-8`.

[30] C. P. Dullemond and A. Johansen. “Numerical methods and applications”. In: *Lecture Hydrodynamics*. Heidelberg University, May 2007, pp. 0–0.

[31] Jiří Dostál and Vladimír Havlena. “Convection oriented heat exchanger model”. In: *IEEE International Conference on Control and Automation, ICCA*. Vol. 2016-July. Kathmandu, Nepal, 2016, pp. 347–352. DOI: `10.1109/ICCA.2016.7505301`.

[32] Jiří Dostál, Václav Prajzner, and Vladimír Havlena. “Convection oriented heat exchanger model - Identification”. In: *CLIMA 2016 - proceedings of the 12th REHVA World Congress*. Ed. by Per Kvols Heiselberg. Vol. 9. Aalborg University. Aalborg, 2016, pp. 1–8.

[33] Huilan Shang, J. Fraser Forbes, and Martin Guay. “Characteristics-based model predictive control of distributed parameter systems”. In: *American Control Conference, 2002. Proceedings of the 2002*. Vol. 6. IEEE. 2002, pp. 4383–4388. DOI: `10.1109/ACC.2002.1025336`.

[34] Huilan Shang, J. Fraser Forbes, and Martin Guay. “Model predictive control for quasilinear hyperbolic distributed parameter systems”. In: *Industrial & Engineering Chemistry Research* 43.9 (2004), pp. 2140–2149. DOI: `10.1021/ie030653z`.

[35] P. L. Roe. “Characteristic-based schemes for the Euler equations”. In: *Annual Review of Fluid Mechanics* 18.1 (Jan. 1986), pp. 337–365. DOI: `10.1146/annurev.fl.18.010186.002005`.

[36] P. Bogacki and L. F. Shampine. “A 3(2) pair of Runge - Kutta formulas”. In: *Applied Mathematics Letters* 2.4 (1989), pp. 321–325. ISSN: 0893-9659. DOI: `10.1016/0893-9659(89)90079-7`.

[37] L. F. Shampine and S. Thompson. “Event location for ordinary differential equations”. In: *Computers & Mathematics with Applications* 39.5 (2000), pp. 43–54. ISSN: 0898-1221. DOI: `10.1016/S0898-1221(00)00045-6`.

[38] N. P. Waterson and H. Deconinck. “A unified approach to the design and application of bounded higher-order convection schemes”. In: *Numerical Methods in Laminar and Turbulent Flow* 9 (1995), pp. 203–214.

[39] Jiří Dostál. *MMFVM-HX-Model*. English. Czech Technical University in Prague, Oct. 2021. URL: `https://github.com/dostaji4/MMFVM-HX-Model`.

[40] María del Mar Castilla, José Domingo Álvarez, Francisco Rodríguez, and Manuel Berenguel. *Comfort Control in Buildings*. Springer London, Limited, 2014. ISBN: 9781447163473.

[41] Pavel Trnka, Jiří Dostál, Václav Prajzner, and Christoph Sturm. “Method for operating a hydronic heating and/or cooling system, control valve and hydronic heating and/or cooling system”. European pat. EP3073205. Sept. 2016. URL: `https://register.epo.org/application?number=EP15161449`.

[42] Ramesh K. Shah and Dušan P. Sekulić. *Fundamentals of Heat Exchanger Design*. Hoboken, NJ: Wiley-Interscience, 2003. ISBN: 9780470172605. DOI: `10.1002/9780470172605`.

[43] Jiří Dostál, Tomáš Bäumelt, and Jiří Cvrček. “Control device for pumping one-pipe hydronic systems”. In: *The REHVA European HVAC Journal* (June 2022), pp. 45–51. ISSN: 1307-3729. URL: `https://www.rehva.eu/rehva-journal/chapter/control-device-for-pumping-one-pipe-hydronic-systems`.

[44] *Wilo-Geniax: Der Komfort-Manager für die Heizung*. Technical report. Wilo SE, 2014.

[45] *Taco LoadMatch System*. Online. 2021. URL: `https://www.tacocomfort.com/commercial-solutions/loadmatch-system/`.

[46] Jiří Dostál and Vladimír Havlena. "Modeling, optimization and analysis of hydronic networks with decentralized pumping". In: *CACS 2014 - 2014 International Automatic Control Conference, Conference Digest*. 2014, pp. 269–274. doi: 10.1109/CACS.2014.7097200.

[47] Jiří Dostál. "Zapojení systému pro řízení výkonu a diagnostiku tepelného výměníku". Pat. CZ2015399A3. Feb. 2017. url: https://worldwide.espacenet.com/patent/search?q=pn=CZ2015399A3.

[48] Jiří Dostál. "Heat Exchanger Control and Diagnostic Apparatus". Pat. req. WO2016202316A1. Dec. 2016. url: https://worldwide.espacenet.com/patent/search?q=pn=WO2016202316A1.

[49] Jiří Dostál. "Heat Exchanger Control and Diagnostic Apparatus". U.S. pat. US10443861B2. Oct. 2019. url: https://worldwide.espacenet.com/patent/search?q=pn=US2018149371A1.

[50] Jiří Dostál. "Heat Exchanger Control and Diagnostic Apparatus". European pat. EP3308081B1. Mar. 2020. url: https://worldwide.espacenet.com/patent/search?q=pn=EP3308081A1.

[51] Jiří Dostál. "Heat Exchanger Control and Diagnostic Apparatus". Pat. CA2986606C. Mar. 2023. url: https://worldwide.espacenet.com/patent/search?q=pn=CA2986606C.

[52] Jiří Dostál et al. "Zařízení pro řízení tepelného výměníku v jednopotrubní otopné síti". Pat. CZ2018225A3. 2018. url: https://worldwide.espacenet.com/patent/search?q=pn=CZ2018225A3.

[53] Jiří Dostál et al. "One-pipe Hydronic Heating Control Device". Pat. req. WO2019220297A1. Nov. 2019. url: https://worldwide.espacenet.com/patent/search?q=pn=WO2019220297A1.

[54] Jiří Dostál et al. "One-pipe Hydronic Heating Control Device". U.S. pat. US2021088230A1. May 2021. url: https://worldwide.espacenet.com/patent/search?q=pn=US2021088230A1.

[55] Jiří Dostál et al. *IQ-pump Conceptual Functional Specification*. (CTU-TK01020024-1). Buštěhrad: CTU UCEEB, June 22, 2021. unpublished.

[56] *Directive (EU) 2018/844 of the European Parliament and of the Council of 30 May 2018*. Technical report. Official Journal of the European Union, 2018.

[57] René Kemma. *Average EU building heat load for HVAC equipment*. Technical report. European Commision, 2014.

[58] Europump - the European Association of Pump Manufacturers. *Energy Effiency of Circulators*. 2011.

[59] Jiří Dostál et al. *IQ-pump Body Design*. (CTU-TK01020024-4). Buštěhrad: CTU UCEEB, June 22, 2021. unpublished.

[60] Daniel Kubeš, Karim Al Reyahi, and Jan Předota. *IQP Compute module*. Research report. Czech Technical University in Prague, May 28, 2017.

[61] *Application Note:s 3-Phase Sensorless PMSM Motor Control Kit with S32K144*. Technical report AN12235. NXP Semiconductors, 2020. url: https://www.nxp.com/docs/en/application-note/AN12235.pdf.

[62] Mohinder S. Grewal. *Kalman filtering theory and practice using MATLAB. theory and practice using MATLAB*. John Wiley & Sons Inc., 2015, p. 617. isbn: 9781118851210.

[63] Pavel Trnka et al. *Non-linear continuous models (NLCM). Matlab toolbox*. Prague, May 2021.

[64] Ondřej Šrámek. "Heat transfer media detection on a centrifugal pump". Master's thesis. Czech Technical University in Prague, 2020.

[65] J. Paulo García-Sandoval, Víctor González-Álvarez, and Carlos Pelayo-Ortiz. "Robust continuous velocity control of convective spatially distributed systems". In: *Chemical Engineering Science* 63.17 (Sept. 2008), pp. 4373–4385. issn: 0009-2509. doi: https://doi.org/10.1016/j.ces.2008.06.004.

[66] Jingqing Han. "From PID to active disturbance rejection control". In: *IEEE Transactions on Industrial Electronics* 56.3 (2009). Cited by: 4615, pp. 900–906. doi: 10.1109/TIE.2008.2011621.

[67] David Zelenka. "Cyber-physical one-pipe hydronic heating testbed". Master's thesis. Czech Technical University in Prague, 2019.

[68] Jiří Cvrček. "Hydronic heating testbed automation". Master's thesis. Czech Technical University in Prague, 2019.

[69] National Renewable Energy Laboratory (NREL). *EnergyPlus*™. 2018. url: https://github.com/NREL/EnergyPlus.

[70] The MathWorks Inc. *MATLAB version: 9.13.0 (R2022b)*. Natick, Massachusetts, United States, 2022. url: https://www.mathworks.com.

[71] Jiří Dostál. *EnergyPlus Co-simulation Toolbox*. Comp. software. 2018. url: `http://github.com/dostaji4/EnergyPlus-co-simulation-toolbox`.

[72] Jiří Dostál. *Hydronic heating toolbox*. unpublished. 2018.

[73] Joel A. E. Andersson et al. "CasADi – A software framework for nonlinear optimization and optimal control". In: *Mathematical Programming Computation* (In Press, 2018).

[74] Andreas Wächter and Lorenz T. Biegler. "On the implementation of an interior-point filter line-search algorithm for large-scale nonlinear programming". In: *Mathematical Programming* 106.1 (Apr. 2005), pp. 25–57. doi: `10.1007/s10107-004-0559-y`.

[75] D. P. Muniak. *Radiators in Hydronic Heating Installations: Structure, Selection and Thermal Characteristics*. Studies in Systems, Decision and Control. Springer International Publishing, 2017. isbn: 9783319552422.

[76] "Modernization of Hydronic Systems". In: *RSES SAM* 630.82 (2009).

[77] *Renovation of one-pipe system in an easier way*. Technical report. Danfoss, 2017.

[78] Susanne Kreft. "Dezentrale Heizungspumpen". In: *BINE Informationdienst - projektinfo* 13 (2006).

[79] W. Richter, A. Abdel Fattah, A. Kremonke, and A. Persch. *Entwicklung und Einsatz energiesparender dezentraler Heizungspumpen - Systemanalyse der Heizungsanlage - Schlussbericht*. Technical report. Technische Universität Dresden, 2005.

[80] Annina Abdel Fattah. *Zum Einsatz Dezentraler Umwälzpumpen in Heizsystemen*. TUDpress Verlag der Wissenschaften GmbH, 2012. isbn: 3942710773.

[81] Thorsten Kettner. *Entwicklung und Einsatz energiesparender dezentraler Heizungs-pumpen - Entwiclung notwendiger Systemteilfunktionen un Verfahren zur Erhöhung der Zuverlässigkeit*. Technical report. Wilo SE, 2009.

[82] Michael Eberl, Almuth Schade, and Herbert Sinnesbichler. "Decentralized circulation pumps". In: *Fraunhofer IBP Report* 37.508 (2010).

[83] Somchai Paarporn. "Decentralized pumping system". US6607141B2. 2000.

[84] Edgar Grosse Westhoff, Günter Strelow, and Thorsten Kettner. "Method for operating a network of pipes". Pat. WO2008025453A1. 2006.

[85] Sam K. H. Lam et al. "Distributed Pumping Chilled Water Hydronic System for Air-conditioning Systems". In: *Energy Procedia* 143 (Dec. 2017), pp. 88–93. doi: `10.1016/j.egypro.2017.12.652`.

[86] Somchai Paarporn. "Local Pumping System". In: *ASHRAE J.* 42.9 (2000), pp. 26–28, 30–32.

[87] Caroline Markusson. "Efficiency of building related pump and fan operation". Ph.D. thesis. Chalmers University of Technology, Göteborg, Sweden, 2011.

[88] Peter Schonenberger. "eu.bac System". In: *Energy and Buildings* 100 (2015), pp. 16–19. issn: 0378-7788. doi: `https://doi.org/10.1016/j.enbuild.2014.11.051`.

[89] *ISO 52120-1:2021 Energy performance of buildings - Contribution of building automation, controls and building management - Part 1: General framework and procedures*. Standard. Geneva, CH: International Organization for Standardization, Dec. 2021.

[90] Michael Wetter, Wangda Zuo, Thierry S. Nouidui, and Xiufeng Pang. "Modelica Buildings library". en. In: *J. Build. Perform. Simul.* 7.4 (Mar. 2013), pp. 253–270. issn: 1940-1493. doi: `10.1080/19401493.2013.765506`.

[91] Amar Aganovic. "Analysis of dynamical behaviour of the boiler room at Mechanical Engineering Faculty in Sarajevo in standard exploitation conditions." Master thesis. Norwegian University of Science and Technology, 2013.

[92] Roel Vandenbulcke, Luc Mertens, and Eddy Janssen. "A simulation methodology for heat and cold distribution in thermo-hydronic networks". In: *Build. Simul.* 5.3 (Mar. 2012), pp. 203–217. issn: 1996-3599. doi: `10.1007/s12273-012-0066-7`.

[93] Vikas Chandan. "Modeling and Control of Hydronic Building HVAC Systems". Ph.D. thesis. University of Illinois at Urbana-Champaign, 2010, p. 255.

[94] Hardy Cross. "Analysis of flow in networks of conduits or conductors". In: *Eng. Exp. Stn.* 34 (1936), pp. 1–29.

[95] Mauro Gamberi, Riccardo Manzini, and Alberto Regattieri. "Simulink© simulator for building hydronic heating systems using the Newton-Raphson algorithm". In: *Energy Build.* 41.8 (Aug. 2009), pp. 848–855. issn: 0378-7788. doi: `10.1016/j.enbuild.2009.03.006`.

[96] P. Riederer. “Matlab/simulink for building and HVAC simulation - state of the art”. In: *IBPSA 2005 - Int. Build. Perform. Simul. Assoc. 2005* (2005), pp. 1019–1026.

[97] Jiří Dostál. *Hydro toolbox. Hydronic heating toolbox for MATLAB.* `https://git.uceeb.cvut.cz/team-control/hydronics-4.0/hydro-toolbox`. 2023.

[98] Ian H. Bell, Jorrit Wronski, Sylvain Quoilin, and Vincent Lemort. “Pure and Pseudo-pure Fluid Thermophysical Property Evaluation and the Open-Source Thermophysical Property Library CoolProp”. In: *Industrial & Engineering Chemistry Research* 53.6 (2014), pp. 2498–2508. DOI: `10.1021/ie4033999`.

[99] Ivo Herman, Štefan Knotek, Jiří Dostál, and Václav Prajzner. “Stability of hydronic networks with independent zone controllers”. In: *IEEE Transactions on Control Systems Technology* 26.6 (Nov. 2018), pp. 2214–2222. ISSN: 1063-6536. DOI: `10.1109/TCST.2017.2753179`.

[100] Kyu Nam Rhee, Myoung Souk Yeo, and Kwang Woo Kim. “Evaluation of the control performance of hydronic radiant heating systems based on the emulation using hardware-in-the-loop simulation”. In: *Building and Environment* 46.10 (2011), pp. 2012–2022. ISSN: 0360-1323.

[101] Samuel Prívara, Jan Široký, Lukáš Ferkl, and Jiří Cígler. “Model predictive control of a building heating system: The first experience”. In: *Energy and Buildings* 43.2-3 (2011), pp. 564–572. ISSN: 0378-7788.

[102] Vikas Chandan and Andrew Alleyne. “Optimal partitioning for the decentralized thermal control of buildings”. In: *IEEE Transactions on Control Systems Technology* 21.5 (2013), pp. 1756–1770. ISSN: 1063-6536.

[103] M. Killian, B. Mayer, and M. Kozek. “Cooperative fuzzy model predictive control for heating and cooling of buildings”. In: *Energy and Buildings* 112 (2016), pp. 130–140. ISSN: 0378-7788. DOI: `10.1016/j.enbuild.2015.12.017`.

[104] Yunan Hu, Olga I. Koroleva, and Miroslav Krstić. “Nonlinear control of mine ventilation networks”. In: *Systems & Control Letters* 49.4 (2003), pp. 239–254. ISSN: 0167-6911. DOI: `10.1016/S0167-6911(02)00336-5`.

[105] Olga I. Koroleva, Miroslav Krstić, and Geert W. Schmid-Schönbein. “Decentralized and adaptive control of nonlinear fluid flow networks”. In: *International Journal of Control* 79.12 (2006), pp. 1495–1504. ISSN: 0020-7179. DOI: `10.1080/00207170600849402`.

[106] J. A. Fax and R. M. Murray. “Information Flow and Cooperative Control of Vehicle Formations”. In: *IEEE Transactions on Automatic Control* 49.9 (Sept. 2004), pp. 1465–1476. ISSN: 0018-9286. DOI: `10.1109/TAC.2004.834433`.

[107] Reza Olfati-Saber, J. Alex Fax, and Richard M. Murray. “Consensus and Cooperation in Networked Multi-Agent Systems”. In: *Proceedings of the IEEE* 95.1 (Jan. 2007), pp. 215–233. ISSN: 0018-9219.

[108] Shinji Hara, Hideaki Tanaka, and Tetsuya Iwasaki. “Stability analysis of systems with generalized frequency variables”. In: *IEEE Transactions on Automatic Control* 59.2 (2014), pp. 313–326. ISSN: 0018-9286. DOI: `10.1109/TAC.2013.2281482`.

[109] Forbes T. Brown. *Engineering System Dynamics: A Unified graph-centered approach*. CRC Press, 2006, p. 1082. ISBN: 9780849396489.

[110] Fatemeh Tahersima, Jakob Stoustrup, and Henrik Rasmussen. “An analytical solution for stability-performance dilemma of hydronic radiators”. In: *Energy Build.* 64 (Sept. 2013), pp. 439–446. ISSN: 0378-7788. DOI: `10.1016/j.enbuild.2013.05.023`.

[111] Arpita Ghosh, Stephen Boyd, and Amin Saberi. “Minimizing Effective Resistance of a Graph”. In: *SIAM Review* 50.1 (2008), pp. 37–66. ISSN: 0036-1445.

[112] Mohammad Pirani and Shreyas Sundaram. “On the Smallest Eigenvalue of Grounded Laplacian Matrices”. In: *IEEE Transactions on Automatic Control* 61.2 (2015), pp. 509–514. ISSN: 0018-9286. arXiv: `1406.2271`.

[113] Ivo Herman, Dan Martinec, Zdenek Hurák, and Michael Sebek. “Nonzero Bound on Fiedler Eigenvalue Causes Exponential Growth of H-Infinity Norm of Vehicular Platoon”. In: *IEEE Transactions on Automatic Control* 60.8 (Aug. 2015), pp. 2248–2253. ISSN: 0018-9286. eprint: `1409.4605`.

[114] Kristian Hengster-Movric, Frank L. Lewis, Michael Šebek, and Tomáš Vyhlídal. “Cooperative synchronization control for agents with control delays: A synchronizing region approach”. In: *Journal of the Franklin Institute* 352.5 (2015), pp. 2002–2028. ISSN: 0016-0032.

[115] “Section Vb1: Valves”. In: *Eng. Data B. Valve Actuator Man.* Johnson Controls, Inc., 1994, p. 30.

[116] Fatemeh Tahersima, Jakob Stoustrup, and Henrik Rasmussen. “Stability performance dilemma in hydronic radiators with TRV”. In: *2011 IEEE Int. Conf. Control Appl.* (Sept. 2011), pp. 102–106. DOI: `10.1109/CCA.2011.6044404`.

[117] Wilo AG. *Fundamental principles of pump technology - Pump Basics*. 2005.

[118] Paul F. Boulos, Kevin E. Lansey, and Bryan W. Karney. *Comprehensive Water Distribution Systems Analysis Handbook for Engineers and Planers*. 2nd ed. MWH Soft, 2009, p. 490. ISBN: 0974568953.

[119] J. Pekar, P. Trnka, and V. Havlena. “Matlab as a Prototyping Tool for Hydronic Networks Balancing”. In: *Proc. Int. Conf. - Tech. Comput. Prague* (2008), p. 92.

[120] John Siegenthaler. *Modern Hydronic Heating, 3rd Edition*. Cengage Learning, Inc., Jan. 26, 2011. 640 pp. ISBN: 1428335153.

[121] Greg Cunniff and Brett Zebra. “Single-pipe systems for commercial applications”. In: *HPAC Engineering* Oct. (2006), pp. 42–46.

[122] Kirk Mescher. “One-pipe geothermal design: Simplified GCHP system”. In: *ASHRAE Journal* Oct. (2009), pp. 24–40.

[123] Greg Cunniff. “Less is More: Single-pipe hydronic system solves high-rise troubles”. In: *PM Engineer* (2011).

[124] Joe Britt. *A Low Cost Method for Adding Hydronic Heating to Building Uplift and Renovation Projects*. Hooked on Hydronics Blog. Feb. 2016.

[125] Mike Miller. “Hydronic Controls: Less is More”. In: *HPAC Magazine* (2014).

[126] John C. Fischer et al. “Chilled beam pump module, system, and method”. English. U.S. pat. US 2013 0199772A1. 2013.

[127] Laurent Gagné-Boisvert and Michel Bernier. “Integrated Model for Comparison of One- and Two-pipe GCHP Network Configurations”. In: *Science and Technology for the Built Environment* 24 (2018), pp. 726–742. DOI: `10.1080/23744731.2017.1366184`.

[128] John Siegenthaler. “Injection versus 4-way valves”. In: *PM Engineer* 10 (2002).

[129] Marina Economidou. *Europe’s buildings under the microscope*. Technical report. BPIE, 2011.

[130] Arthur A. Bell. *HVAC Equations, Data and Rules of Thumb*. McGraw-Hill Professional, 2000, p. 576. ISBN: 9780071361293.

[131] *How to Assure "Right Sizing" HVAC Systemsfor Efficient Operation*. Technical report. Goodway - Green Buildings & Green Technology, Feb. 2022.

[132] Robin K. Vieira et al. *How Contractors Really SIze Air Conditioning Systems*. Research report. Florida Solar Energy Center, 1996.

[133] Liam Buckley. *ASHRAE Heating & Cooling Load Calculations - technical insight*. Technical report. IES, 2020. URL: `https://www.iesve.com/discoveries/article/10017/ashrae-heating-and-cooling-load-calculations`.

[134] ASHRAE. *Climatic Conditions: ashrae-meteo.info*. ASHRAE, 2021. URL: `http://ashrae-meteo.info/`.

[135] *Heating and cooling degree days - statistics*. Technical report. Eurostat, 2022. URL: `https://ec.europa.eu/eurostat/statistics-explained/index.php?title=Heating_and_cooling_degree_days_-_statistics#Heating_and_cooling_degree_days_at_EU_level`.

[136] *European climate zones and bio-climatic design requirements*. Research report. PVSITES (H2020 project), 2016. URL: `https://www.pvsites.eu/downloads/download/d2-2-european-climate-zones-and-bioclimatic-design`.

[137] Phil Jones, Paul Woods, and Martin Crane. *Heat networks: Code of Practice for the UK*. Ed. by Eileen Bell and Alasdair Deas. 2nd ed. CIBSE, 2020. ISBN: 978-1-912034-80-2.

[138] Gregory Nellis and Sanford Klein. *Heat Transfer*. Cambridge University Press, Dec. 2008. DOI: `10.1017/cbo9780511841606`.

[139] Alain Triboix. “Exact and approximate formulas for cross flow heat exchangers with unmixed fluids”. In: *International Communications in Heat and Mass Transfer* 36.2 (Feb. 2009), pp. 121–124. DOI: `10.1016/j.icheatmasstransfer.2008.10.012`.

[140] Frank P. Incropera. *Fundamentals of Heat and Mass Transfer*. Wiley, 2006. ISBN: 9780471457282.

[141] T. L. Bergman, Adrienne S. Lavine, Frank P. Incropera, and David P. Dewitt. *Fundamentals of heat and mass transfer*. 7th ed. Hoboken: John Wiley & Sons, 2011, p. 1048. ISBN: 9780470501979.

[142] Ondřej Zlevor and Jiří Dostál. "Demand-oriented Hydronic Heating System and the Active One-pipe System Design Tool". In: ed. by S. I. Tanabe et al. Vol. 111. EDP Sciences, 2019, p. 01091. DOI: `10.1051/e3sconf/201911101091`.

[143] Ondřej Zlevor and Jiří Dostál. *One-pipe Hydronic System Design Tool*. CTU UCEEB, Feb. 2019. URL: `https://github.com/UCEEB/Onepipe-Hydronic-Design-Tool`.

[144] *Control Valve Handbook*. Third edit. Marshalltown: Fisher Controls International, Inc., 2001.

[145] *Balancing and Control Valve Sizing for Direct-Return, Variable-Flow Hydronic Systems*. Technical report 149-990. Siemens Industry Inc., 2006.

[146] Nathan F. Rothman and Ian Dempster. "Controlled Hydronic Distribution System". U.S. pat. US009810438B2. Belimo AG. Nov. 7, 2017.

[147] Jiří Dostál and Tomáš Bäumelt. "Model Predictive Control for Buildings with Active One-pipe Hydronic Heating". In: ed. by S. I. Tanabe et al. Vol. 111. EDP Sciences, 2019, p. 04050. DOI: `10.1051/e3sconf/201911104050`.

[148] E. Toffoli et al. "Thermodynamic identification of buildings using wireless sensor networks". In: *IFAC Proceedings Volumes* 41.2 (2008), pp. 8860–8865. DOI: `10.3182/20080706-5-KR-1001.01497`.

[149] Francesco Scotton, Lirong Huang, Seyed A. Ahmadi, and Bo Wahlberg. "Physics-based modeling and identification for HVAC systems?" In: *2013 European Control Conference (ECC)*. August. IEEE, July 2013, pp. 1404–1409. ISBN: 978-3-033-03962-9. DOI: `10.23919/ECC.2013.6669134`.

[150] *Energy performance of buildings directive 2018/844*. European directive. Brussels, May 30, 2018. URL: `https://eur-lex.europa.eu/legal-content/EN/TXT/PDF/?uri=CELEX:32018L0844`.

[151] Ye Yao and Divyanshu Kumar Shekhar. "State of the art review on model predictive control (MPC) in Heating Ventilation and Air-conditioning (HVAC) field". In: *Building and Environment* 200 (2021), p. 107952. ISSN: 0360-1323. DOI: `https://doi.org/10.1016/j.buildenv.2021.107952`.

[152] Jan Široký, Frauke Oldewurtel, Jiří Cígler, and Samuel Prívara. "Experimental analysis of model predictive control for an energy efficient building heating system". In: *Applied Energy* 88.9 (Sept. 2011), pp. 3079–3087. DOI: `10.1016/j.apenergy.2011.03.009`.

[153] R. Judkoff and Joel Neymark. *The BESTEST method for evaluating and diagnosing building energy software*. Technical report. National Renewable Energy Laboratory, Golden, CO (US), 1998.

[154] *ESP-r*. `http://www.esru.strath.ac.uk/Programs/ESP-r.htm`. Accessed: 2019-10-04.

[155] University of Wisconsin–Madison. *TRNSYS: a Transient Simulation Program*. Ed. by Solar Energy Laboratory. 1975.

[156] Brian Coffey, Fariborz Haghighat, Edward Morofsky, and Edward Kutrowski. "A software framework for model predictive control with GenOpt". In: *Energy & Buildings* 42 (2010), pp. 1084–1092. ISSN: 0378-7788. DOI: `10.1016/j.enbuild.2010.01.022`.

[157] Marie-Andree Leduc Kummert Michael and Alain Moreau. "Using MPC to reduce the peak demand associated with electric heating". In: *Model predictive control in buildings workshop*. IBPSA, 2011.

[158] Khee Poh Lam Zhao Jie and B. Erik Ydstie. "EnergyPlus model-based predictive control (EPMPC) by using MATLAB/SIMULINK and MLE+". In: *Proceedings of 13th Conference of International Building Performance Simulation Association*. 2013.

[159] Marija Trcka, Michael Wetter, and Jan Hensen. "Comparison of co-simulation approaches for building and HVAC/R simulation". In: *Proceedings of the 10+-th IBPSA Conference*. 2007.

[160] Michael Wetter. "Co-simulation of building energy and control systems with the Building Controls Virtual Test Bed". In: *Journal of Building Performance Simulation* 4.3 (Sept. 2011), pp. 185–203. DOI: `10.1080/19401493.2010.518631`.

[161] Truong Xuan Nghiem. *MLE+: a Matlab-EnergyPlus Co-simulation Interface*. Technical report. EPFL, 2015. DOI: `10.13140/rg.2.1.1127.0880`.

[162] Georg Engel, Ajay S. Chakkaravarthy, and Gerald Schweiger. "A methodology to compare different co-simulation interfaces: A thermal engineering case study". In: *Proceedings of the 7th International Conference on Simulation and Modeling Methodologies, Technologies and Applications*. SCITEPRESS - Science and Technology Publications, 2017. DOI: `10.5220/0006480204100415`.

[163] Samuel Prívara et al. “Modeling and identification of a large multi-zone office building”. In: *2011 IEEE International Conference on Control Applications (CCA)*. IEEE, Sept. 2011, pp. 55–60. DOI: `10.1109/CCA.2011.6044402`.

[164] Zheng O’Neill et al. “Model-based real-time whole building energy performance monitoring and diagnostics”. In: *Journal of Building Performance Simulation* 7.2 (Apr. 2013), pp. 83–99. DOI: `10.1080/19401493.2013.777118`.

[165] Mohamad Ibrahim, Etienne Wurtz, Pascal Henry Biwole, and Patrick Achard. “Transferring the south solar energy to the north facade through embedded water pipes”. In: *Energy* 78 (2014), pp. 834–845. ISSN: 0360-5442. DOI: `10.1016/j.energy.2014.10.078`.

[166] Jie Zhao, Khee Poh Lam, B. Erik Ydstie, and Omer T. Karaguzel. “EnergyPlus model-based predictive control within design–build–operate energy information modelling infrastructure”. In: *Journal of Building Performance Simulation* 8.3 (2015), pp. 121–134.

[167] Datong Zhou, Qie Hu, and Claire J. Tomlin. “Model comparison of a data-driven and a physical model for simulating HVAC systems”. In: *CoRR* (2016). arXiv: `abs/1603.05951`.

[168] Michael Wetter and Christoph van Treeck. *Annex 60: New generation computational tools for building and community energy systems*. Technical report. IEA EBC, Sept. 2017.

[169] Modelica Association. *Modelica*. 2020. URL: `www.modelica.org`.

[170] Tomáš. Bäumelt and Jiří Dostál. “Distributed agent-based building grey-box model identification”. In: *Control Engineering Practice* 101 (2020), p. 104427. ISSN: 0967-0661. DOI: `10.1016/j.conengprac.2020.104427`.

[171] Samuel Prívara et al. “Building modeling as a crucial part for building predictive control”. In: *Energy and Buildings* 56 (Jan. 2013), pp. 8–22. DOI: `10.1016/j.enbuild.2012.10.024`.

[172] Xiwang Li and Jin Wen. “Review of building energy modeling for control and operation”. In: *Renewable and Sustainable Energy Reviews* 37 (Sept. 2014), pp. 517–537. DOI: `10.1016/j.rser.2014.05.056`.

[173] Zakia Afroz, G. M. Shafiullah, Tania Urmee, and Gary Higgins. “Modeling techniques used in building HVAC control systems: A review”. In: *Renewable and Sustainable Energy Reviews* 83 (Mar. 2018), pp. 64–84. DOI: `10.1016/j.rser.2017.10.044`.

[174] Samuel Prívara, Zdeněk Váňa, Eva Žáčeková, and Jiří Cigler. “Building modeling: Selection of the most appropriate model for predictive control”. In: *Energy and Buildings* 55 (Dec. 2012), pp. 341–350. DOI: `10.1016/j.enbuild.2012.08.040`.

[175] Gianluca Serale et al. “Model predictive control (MPC) for enhancing building and HVAC system energy efficiency: problem formulation, applications and opportunities”. In: *Energies* 11.3 (Mar. 2018), p. 631. DOI: `10.3390/en11030631`.

[176] Venkatesh Chinde. “Modeling and control of complex building energy systems”. Ph.D. thesis. Iowa State Univeristy, 2018. DOI: `10.31274/etd-180810-5960`.

[177] Lennart Ljung, ed. *System identification: Theory for the user*. Second edition. Upper Saddle River, NJ, USA: Prentice Hall PTR, 1999. ISBN: 0-13-656695-2. DOI: `10.1002/047134608x.w1046`.

[178] Pavel Trnka and Vladimír Havlena. “Subspace like identification incorporating prior information”. In: *Automatica* 45.4 (2009), pp. 1086–1091. DOI: `10.1016/j.automatica.2008.12.005`.

[179] B. L. de Moor Peter van Overschee. *Subspace identification for linear systems: Theory-Implementation-Application*. Springer, 2012.

[180] M. J. Jiménez, H. Madsen, and K. K. Andersen. “Identification of the main thermal characteristics of building components using MATLAB”. In: *Building and Environment* 43.2 (Feb. 2008), pp. 170–180. DOI: `10.1016/j.buildenv.2006.10.030`.

[181] G. Reynders, J. Diriken, and D. Saelens. “Quality of grey-box models and identified parameters as function of the accuracy of input and observation signals”. In: *Energy and Buildings* 82 (Oct. 2014), pp. 263–274. DOI: `10.1016/j.enbuild.2014.07.025`.

[182] Kumar Saurav and Vikas Chandan. “Gray-box approach for thermal modelling of buildings for applications in district heating and cooling networks”. In: *Proceedings of the Eighth International Conference on Future Energy Systems*. New York, NY, USA: ACM, 2017, pp. 347–352. ISBN: 978-1-4503-5036-5. DOI: `10.1145/3077839.3084078`.

[183] S. F. Graebe and T. Bohlin. "Identification of nonlinear stochastic grey box models: Theory, implementation, and experiences". In: *IFAC Proceedings Volumes* 25.14 (July 1992), pp. 47–52. doi: `10.1016/s1474-6670(17)50711-9`.

[184] Torsten Bohlin and Stefan F. Graebe. "Issues in nonlinear stochastic grey box identification". In: *International Journal of Adaptive Control and Signal Processing* 9.6 (Nov. 1995), pp. 465–490. doi: `10.1002/acs.4480090603`.

[185] A. Aswani et al. "Identifying models of HVAC systems using semiparametric regression". In: *2012 American Control Conference (ACC)*. IEEE, June 2012. doi: `10.1109/acc.2012.6315566`.

[186] Elena Mocanu, Phuong H. Nguyen, Madeleine Gibescu, and Wil L. Kling. "Deep learning for estimating building energy consumption". In: *Sustainable Energy, Grids and Networks* 6 (June 2016), pp. 91–99. doi: `10.1016/j.segan.2016.02.005`.

[187] Achin Jain, Madhur Behl, and Rahul Mangharam. "Data Predictive Control for building energy management". In: *2017 American Control Conference (ACC)*. IEEE, May 2017. doi: `10.23919/acc.2017.7962928`.

[188] Daniel Goerges. "Relations between Model Predictive Control and Reinforcement Learning". In: *IFAC-PapersOnLine* 50.1 (July 2017), pp. 4920–4928. doi: `10.1016/j.ifacol.2017.08.747`.

[189] Ján Drgoňa, Damien Picard, Michal Kvasnica, and Lieve Helsen. "Approximate model predictive building control via machine learning". In: *Applied Energy* 218 (May 2018), pp. 199–216. doi: `10.1016/j.apenergy.2018.02.156`.

[190] Katarina Katić, Rongling Li, Jacob Verhaart, and Wim Zeiler. "Neural network based predictive control of personalized heating systems". In: *Energy and Buildings* 174 (Sept. 2018), pp. 199–213. doi: `10.1016/j.enbuild.2018.06.033`.

[191] D. H. Blum et al. "Practical factors of envelope model setup and their effects on the performance of model predictive control for building heating, ventilating, and air conditioning systems". In: *Applied Energy* 236 (Feb. 2019), pp. 410–425. doi: `10.1016/j.apenergy.2018.11.093`.

[192] Ercan Atam and Lieve Helsen. "Control-Oriented Thermal Modeling of Multizone Buildings: Methods and Issues: Intelligent Control of a Building System". In: *IEEE Control Systems* 36.3 (June 2016), pp. 86–111. doi: `10.1109/mcs.2016.2535913`.

[193] *MPC Laboratory at UC Berkeley*. `http://www.mpc.berkeley.edu/`. Accessed: 2019-10-04.

[194] *Automatic Control Laboratory, ETH Zurich*. `http://www.control.ee.ethz.ch`. Accessed: 2019-10-04.

[195] *Department of Civil Engineering, KU Leuven*. `http://www.bwk.kuleuven.be`. Accessed: 2019-10-04.

[196] David Sturzenegger. "Model predictive building climate control: Steps towards practice". Ph.D. thesis. ETH Zurich, 2014.

[197] Roel De Coninck, Fredrik Magnusson, Johan Åkesson, and Lieve Helsen. "Toolbox for development and validation of grey-box building models for forecasting and control". In: *Journal of Building Performance Simulation* 9.3 (June 2015), pp. 288–303. doi: `10.1080/19401493.2015.1046933`.

[198] Hassan Harb et al. "Development and validation of grey-box models for forecasting the thermal response of occupied buildings". In: *Energy and Buildings* 117 (Apr. 2016), pp. 199–207. doi: `10.1016/j.enbuild.2016.02.021`.

[199] T. Zakula, P. R. Armstrong, and L. Norford. "Modeling environment for model predictive control of buildings". In: *Energy and Buildings* 85 (Dec. 2014), pp. 549–559. doi: `10.1016/j.enbuild.2014.09.039`.

[200] David H. Blum, Tea Zakula, and Leslie K. Norford. "Opportunity Cost Quantification for Ancillary Services Provided by Heating, Ventilating, and Air-Conditioning Systems". In: *IEEE Transactions on Smart Grid* 8.3 (May 2017), pp. 1264–1273. doi: `10.1109/tsg.2016.2582207`.

[201] Maarten Sourbron, Clara Verhelst, and Lieve Helsen. "Building models for model predictive control of office buildings with concrete core activation". In: *Journal of Building Performance Simulation* 6.3 (May 2013), pp. 175–198. doi: `10.1080/19401493.2012.680497`.

[202] Kyoung-ho Lee and James E. Braun. "Model-based demand-limiting control of building thermal mass". In: *Building and Environment* 43.10 (Oct. 2008), pp. 1633–1646. doi: `10.1016/j.buildenv.2007.10.009`.

[203] Javier Bonilla, Jose Antonio Carballo, Lidia Roca, and Manuel Berenguel. "Development of an open source multi-platform software tool for parameter estimation studies in FMI models". In: *Proceedings of the 12th International Modelica Conference, Prague, Czech Republic, May 15-17, 2017*. Linköping University Electronic Press, 2017. doi: `10.3384/ecp17132683`.

[204] Eva Žáčeková, Zdeněk Váňa, and Jiří Cigler. “Towards the real-life implementation of MPC for an office building: Identification issues”. In: *Applied Energy* 135 (Dec. 2014), pp. 53–62. DOI: `10.1016/j.apenergy.2014.08.004`.

[205] Edward O’Dwyer et al. “Modelling and disturbance estimation for model predictive control in building heating systems”. In: *Energy and Buildings* 130 (Oct. 2016), pp. 532–545. DOI: `10.1016/j.enbuild.2016.08.077`.

[206] Jaewan Joe and Panagiota Karava. “Agent-based system identification for control-oriented building models”. In: *Journal of Building Performance Simulation* 10.2 (Aug. 2016), pp. 183–204. DOI: `10.1080/19401493.2016.1212272`.

[207] N. R. Jennings and S. Bussmann. “Agent-based control systems: Why are they suited to engineering complex systems?” In: *IEEE Control Systems* 23.3 (June 2003), pp. 61–73. DOI: `10.1109/mcs.2003.1200249`.

[208] Sikandar Samar, Stephen Boyd, and Dimitry Gorinevsky. “Distributed estimation via dual decomposition”. In: *2007 European Control Conference (ECC)*. IEEE, July 2007. DOI: `10.23919/ECC.2007.7069016`.

[209] Hakan Terelius, Ufuk Topcu, and Richard M. Murray. “Decentralized multi-agent optimization via dual decomposition”. In: *IFAC Proceedings Volumes* 44.1 (Jan. 2011), pp. 11245–11251. DOI: `10.3182/20110828-6-IT-1002.01959`.

[210] Ion Necoara, Valentin Nedelcu, and Ioan Dumitrache. “Parallel and distributed optimization methods for estimation and control in networks”. In: *Journal of Process Control* 21.5 (June 2011), pp. 756–766. DOI: `10.1016/j.jprocont.2010.12.010`.

[211] Tomáš Bäumelt. “Distributed building identification”. Master’s thesis. Prague: Czech Technical University in Prague, June 2016.

[212] Pavel Trnka, Vladimir Havlena, and Jaroslav Pekar. “Distributed MPC with parametric coordination”. In: *2016 American Control Conference (ACC)*. IEEE, July 2016. DOI: `10.1109/acc.2016.7526652`.

[213] Jonathan Eckstein and Dimitri P. Bertsekas. “On the Douglas-Rachford splitting method and the proximal point algorithm for maximal monotone operators”. In: *Mathematical Programming* 55 (1992), pp. 293–318. ISSN: 0025-5610. DOI: `10.1007/bf01581204`.

[214] Joseph J. Yame et al. “Optimality Condition Decomposition Approach to Distributed Model Predictive Control”. In: *2019 American Control Conference (ACC)*. IEEE, July 2019. DOI: `10.23919/acc.2019.8814374`.

[215] Yucai Zhu. *Multivariable system identification for process control*. Elsevier, 2001.

[216] Jiří Cigler et al. “Beyond theory: the challenge of implementing model predictive control in buildings”. In: *Proceedings of 11th Rehva world congress, Clima*. Vol. 250. 2013.

[217] E. L. Duke and Dryden Flight Research Facility. *Combining and connecting linear, multi-input, multi-output subsystem models*. National Aeronautics and Space Administration, Ames Research Center, Dryden Flight Research Center, 1986. Google Books: `Tm5GAQAAIAAJ`.

[218] Pavel Trnka et al. “Structured Model Order Reduction of Parallel Models in Feedback”. In: *IEEE Transactions on Control Systems Technology* 21.3 (May 2013), pp. 739–752. DOI: `10.1109/tcst.2012.2192735`.

[219] Jiří Řehoř and Vladimír Havlena. “Maximum likelihood estimation of LTI continuous-time grey-box models”. In: *IFAC Proceedings Volumes* 47.3 (2014), pp. 3739–3744. DOI: `10.3182/20140824-6-ZA-1003.02269`.

[220] Yurii Nesterov. *Introductory lectures on convex optimization: A basic course*. Kluwer Academic Publishers, 2004, p. 254. ISBN: 9781402075537. DOI: `10.1007/978-1-4419-8853-9`.

[221] Miroslav Urban, Michal Bejček, Petr Wolf, and Aleš Vodička. “Koncept administrativní budovy jako budovy s téměř nulovou spotřebou energie”. In: *Vytapeni, Vetrani, Instalace* 26.1 (2017), pp. 30–36. ISSN: 1210-1389.

[222] Tomáš Bäumelt. *Distributed-building-identification*. `https://github.com/UCEEB/Distributed-building-identification`. GitHub repository. 2020.

[223] Tomáš Bäumelt. *Distributed-building-identification*. Mendeley Data. 2020. DOI: `10.17632/c6ht8jgtp3.2`.

[224] Timothy O’Grady, Heap-Yih Chong, and Gregory M. Morrison. “A systematic review and meta-analysis of building automation systems”. In: *Building and Environment* 195 (2021), p. 107770. ISSN: 0360-1323. DOI: `https://doi.org/10.1016/j.buildenv.2021.107770`.

[225] *RoboPID - diagnostics and automatic tuning of controller parameters for industrial use in buildings*. Grant n. EG21_374/0026965. Ministry of Industry and Trade CZE. Sept. 2021. URL: `https://starfos.tacr.cz/cs/project/EG21_374/0026965`.

[226] Jan Široký, Jiří Cvrček, and Jiří Dostál. "The Most Common Heating System Control Errors and the Possibility of Solving Them with Self-Adjusting Controllers; [Nejčastější chyby regulace otopných systémů a možnost jejich řešení samonastavujícími se regulátory]". In: *Heating, Ventilation, Installations (VVI)* 4 (2023).

[227] Jan Hauser. "Distributed predictive control of buildings". Master's thesis. Prague: Czech Technical University in Prague, June 2017.

[228] Pavel Trnka and Jan Prášek. *Decentralized Model Predictive Control with Global Constraints*. Technical report. Honeywell, 2020.

[229] B. Lehmann et al. "Intermediate complexity model for Model Predictive Control of Integrated Room Automation". In: *Energy and Buildings* 58 (Mar. 2013), pp. 250–262. DOI: `10.1016/j.enbuild.2012.12.007`.

[230] L. T. Biegler. *Nonlinear programming: Concepts, algorithms, and applications to chemical processes*. MOS-SIAM Series on Optimization. Society for Industrial and Applied Mathematics (SIAM, 3600 Market Street, Floor 6, Philadelphia, PA 19104), 2010. ISBN: 9780898719383.

[231] J. Löfberg. "YALMIP : A Toolbox for Modeling and Optimization in MATLAB". In: *Proc. CACSD Conf.* IEEE. IEEE, 2004, pp. 284–289. ISBN: 0780386361. DOI: `10.1109/CACSD.2004.1393890`.

[232] *Gurobi optimizer*. Technical report. Gurobi Optimization, LLC., 2018.

[233] Andreas Wächter and Lorenz T. Biegler. "On the implementation of an interior-point filter line-search algorithm for large-scale nonlinear programming". In: *Mathematical Programming* 106.1 (Mar. 2006), pp. 25–57. ISSN: 1436-4646. DOI: `10.1007/s10107-004-0559-y`.

[234] Jan Předota. "Model predictive control for buildings with one-pipe hydronic heating". Master's thesis. Prague: Czech Technical University in Prague, June 2018.

[235] Ondřej Zlevor. *Onepipe Hydronic Design Tool*. Technical report. github.com/UCEEB/Onepipe-Hydronic-Design-Tool, 2018.

[236] Dennis S. Bernstein. *Matrix Mathematics*. 3rd ed. Vol. 1. 2009, p. 1059. ISBN: 9788578110796.

[237] Tomáš Bäumelt and Jiří Dostál. "Distributed building model identification for advanced control purposes; [Distribuovaná identifikace modelu budovy pro účely pokročilé regulace]". In: *Heating, Ventilation, Installations (VVI)* 27.5 (2018), pp. 266–270.

[238] Jiří Dostál et al. "One-pipe Hydronic Heating Control Device". European pat. EP3781892A4. June 2021. URL: `https://worldwide.espacenet.com/patent/search?q=pn=EP3781892A4`.

[239] Jiří Dostál, Tomáš Bäumelt, and Jiří Cvrček. "Control device for pumping one-pipe hydronic systems". In: *Proceedings CLIMA 2022: The 14th REHVA HVAC World Congress*. Rotterdam, Netherlands: TU Delft, 2022. ISBN: 978-94-6366-564-3. DOI: `10.34641/clima.2022.349`.

[240] *Concept Prague: Sub-project IQ-pump*. Grant n. CZ.07.1.02/0.0/0.0/16_023/0000113. EU ESIF - Operational Programme Prague - Growth Pole of the Czech Republic. Jan. 2017.

[241] *IQ-pump*. Grant n. ED2.1.00/03.0091. National Sustainability Programme - Ministry of Industry and Trade CZE. 2015. URL: `https://starfos.tacr.cz/projekty/ED2.1.00/03.0091`.

[242] Jiří Valtr. "Mass flow estimation and control in pump driven hydronic systems". Master's thesis. Prague: Czech Technical University in Prague, Jan. 2017.

[243] Ondřej Zlevor. "Heat flow control of water-to-air heat exchanger". Master's thesis. Prague: Czech Technical University in Prague, May 2017.

[244] Jiří Kubeš. "Návrh elektroniky čerpadla se sférickým motorem". Master's thesis. Praha: České Vysoké Učení Technické v Praze, June 2016.

[245] Pavel Trnka and Jiří Dostál. "Anti-windup reference shaping filter for control". European pat. EP3093718. Nov. 2016. URL: `https://register.epo.org/application?number=EP16168196`.

[246] Pavel Trnka and Jiří Dostál. "Anti-windup reference shaping filter for control". U.S. pat. US20160334761. Nov. 2016. URL: `https://patentscope.wipo.int/search/en/detail.jsf?docId=US179481457&_cid=P21-LJ45SQ-97679-1`.

[247] Jiří Dostál and Lukáš Ferkl. "Model predictive control of climatic chamber with on-off actuators". In: *IFAC Proceedings Volumes (IFAC-PapersOnline)*. Vol. 19. Cited By :1. 2014, pp. 4423–4428. DOI: `10.3182/20140824-6-ZA-1003.01571`.

[248] *Increasing the safety of traction batteries for transport*. Grant n. CK04000097. Technology Agency of the Czech Republic. Jan. 2023. URL: `https://starfos.tacr.cz/en/project/CK04000097`.

[249] *GLocalFlex*. Grant n. EU HORIZON-CL5-2022-D3-01-12. European Commission. 2022.

[250] *Inferential sensing of concentration/viscosity of abrasive slurries*. Grant n. EG20_321/0024688. Ministry of Industry and Trade CZE. June 2021. URL: `https://starfos.tacr.cz/cs/project/EG20_321/0024688`.

[251] *Open dispatching system with principles of business intelligence and semantic data description*. Grant n. EG20_321/0024003. Ministry of Industry and Trade CZE. Jan. 2021. URL: `https://starfos.tacr.cz/en/project/EG20_321/0024003`.

[252] Pavel Souček. “Heat transfer media detection on a centrifugal pumpAtmospheric water generator optimization”. Master’s thesis. Czech Technical University in Prague, 2022.

Author's publications and projects

Thesis related publications and projects

Impacted journal publications

[J1] Jiří Dostál and Vladimír Havlena. “Mixed Mesh Finite Volume Method for 1D Hyperbolic Systems with Application to Plug-flow Heat Exchangers”. In: *Mathematics* 9.20 (Oct. 2021), p. 2609. ISSN: 2227-7390. DOI: 10.3390/math9202609

Authorship: 95% , **WOS citations: 2** , **Scopus citations: 2** , **D1**

[J2] Tomáš. Bäumelt and Jiří Dostál. “Distributed agent-based building grey-box model identification”. In: *Control Engineering Practice* 101 (2020), p. 104427. ISSN: 0967-0661. DOI: 10.1016/j.conengprac.2020.104427

Authorship: 30% , **WOS citations: 7** , **Scopus citations: 7**

[J3] Ivo Herman, Štefan Knotek, Jiří Dostál, and Václav Prajzner. “Stability of hydronic networks with independent zone controllers”. In: *IEEE Transactions on Control Systems Technology* 26.6 (Nov. 2018), pp. 2214–2222. ISSN: 1063-6536. DOI: 10.1109/TCST.2017.2753179

Authorship: 20% , **WOS citations: 2**

Peer-reviewed journal publications

[S1] Jan Široký, Jiří Cvrček, and Jiří Dostál. “The Most Common Heating System Control Errors and the Possibility of Solving Them with Self-Adjusting Controllers; [Nejčastější chyby regulace otopných systémů a možnost jejich řešení samonastavujícími se regulátory]”. In: *Heating, Ventilation, Installations (VVI)* 4 (2023)

Authorship: 30%

[S2] Jiří Dostál, Tomáš Bäumelt, and Jiří Cvrček. “Control device for pumping one-pipe hydronic systems”. In: *The REHVA European HVAC Journal* (June 2022), pp. 45–51. ISSN: 1307-3729. URL: https://www.rehva.eu/rehva-journal/chapter/control-device-for-pumping-one-pipe-hydronic-systems

Authorship: 90%

[S3] Tomáš Bäumelt and Jiří Dostál. “Distributed building model identification for advanced control purposes; [Distribuovaná identifikace modelu budovy pro účely pokročilé regulace]”. In: *Heating, Ventilation, Installations (VVI)* 27.5 (2018), pp. 266–270

Authorship: 50%

Patents

[P1] Jiří Dostál. “Heat Exchanger Control and Diagnostic Apparatus”. Pat. CA2986606C. Mar. 2023. URL: https://worldwide.espacenet.com/patent/search?q=pn=CA2986606C

[P2] Jiří Dostál et al. “One-pipe Hydronic Heating Control Device”. U.S. pat. US2021088230A1. May 2021. URL: https://worldwide.espacenet.com/patent/search?q=pn=US2021088230A1

[P3] Jiří Dostál et al. “One-pipe Hydronic Heating Control Device”. European pat. EP3781892A4. June 2021. URL: https://worldwide.espacenet.com/patent/search?q=pn=EP3781892A4

[P4] Jiří Dostál. “Heat Exchanger Control and Diagnostic Apparatus”. European pat. EP3308081B1. Mar. 2020. URL: https://worldwide.espacenet.com/patent/search?q=pn=EP3308081A1

[P5] Jiří Dostál. “Heat Exchanger Control and Diagnostic Apparatus”. U.S. pat. US10443861B2. Oct. 2019. URL: https://worldwide.espacenet.com/patent/search?q=pn=US2018149371A1

[P6] Jiří Dostál et al. “Zařízení pro řízení tepelného výměníku v jednopotrubní otopné síti”. Pat. CZ2018225A3. 2018. URL: `https://worldwide.espacenet.com/patent/search?q=pn=CZ2018225A3`

[P7] Jiří Dostál. “Zapojení systému pro řízení výkonu a diagnostiku tepelného výměníku”. Pat. CZ2015399A3. Feb. 2017. URL: `https://worldwide.espacenet.com/patent/search?q=pn=CZ2015399A3`

[P8] Pavel Trnka, Jiří Dostál, Václav Prajzner, and Christoph Sturm. “Method for operating a hydronic heating and/or cooling system, control valve and hydronic heating and/or cooling system”. European pat. EP3073205. Sept. 2016. URL: `https://register.epo.org/application?number=EP15161449`

Conference papers

[C1] Jiří Dostál, Tomáš Bäumelt, and Jiří Cvrček. “Control device for pumping one-pipe hydronic systems”. In: *Proceedings CLIMA 2022: The 14th REHVA HVAC World Congress*. Rotterdam, Netherlands: TU Delft, 2022. ISBN: 978-94-6366-564-3. DOI: `10.34641/clima.2022.349`
Authorship: 90%

[C2] Ondřej Zlevor and Jiří Dostál. “Demand-oriented Hydronic Heating System and the Active One-pipe System Design Tool”. In: ed. by S. I. Tanabe et al. Vol. 111. EDP Sciences, 2019, p. 01091. DOI: `10.1051/e3sconf/201911101091`
Authorship: 50%

[C3] Jiří Dostál and Tomáš Bäumelt. “Model Predictive Control for Buildings with Active One-pipe Hydronic Heating”. In: ed. by S. I. Tanabe et al. Vol. 111. EDP Sciences, 2019, p. 04050. DOI: `10.1051/e3sconf/201911104050`
Authorship: 90% , **Scopus citations: 13**

[C4] Jiří Dostál and Vladimír Havlena. “Convection oriented heat exchanger model”. In: *IEEE International Conference on Control and Automation, ICCA*. Vol. 2016-July. Kathmandu, Nepal, 2016, pp. 347–352. DOI: `10.1109/ICCA.2016.7505301`
Authorship: 80% , **WOS citations: 2** , **Scopus citations: 2**

[C5] Jiří Dostál, Václav Prajzner, and Vladimír Havlena. “Convection oriented heat exchanger model - Identification”. In: *CLIMA 2016 - proceedings of the 12th REHVA World Congress*. Ed. by Per Kvols Heiselberg. Vol. 9. Aalborg University. Aalborg, 2016, pp. 1–8
Authorship: 80% , **WOS citation: 0** , **Scopus citation: 0**

[C6] Jiří Dostál and Vladimír Havlena. “Modeling, optimization and analysis of hydronic networks with decentralized pumping”. In: *CACS 2014 - 2014 International Automatic Control Conference, Conference Digest*. 2014, pp. 269–274. DOI: `10.1109/CACS.2014.7097200`
Authorship: 80% , **WOS citation: 1** , **Scopus citations: 4** , **Best student paper award**

Grant projects

[G1] *Hydronics 4.0*. Grant n. TK01020024. Technology Agency of the Czech Republic. June 2018. URL: `https://starfos.tacr.cz/cs/project/TK01020024`
Role: **Principle investigator by CTU**

[G2] *Concept Prague: Sub-project IQ-pump*. Grant n. CZ.07.1.02/0.0/0.0/16_023/0000113. EU ESIF - Operational Programme Prague - Growth Pole of the Czech Republic. Jan. 2017
Role: **Sub-project investigator**

[G3] *IQ-pump*. Grant n. ED2.1.00/03.0091. National Sustainability Programme - Ministry of Industry and Trade CZE. 2015. URL: `https://starfos.tacr.cz/projekty/ED2.1.00/03.0091`
Role: Technical lead of an internal project

Supervised Master’s Theses

[M1] Ondřej Šrámek. “Heat transfer media detection on a centrifugal pump”. Master’s thesis. Czech Technical University in Prague, 2020

[M2] David Zelenka. “Cyber-physical one-pipe hydronic heating testbed”. Master’s thesis. Czech Technical University in Prague, 2019

[M3] Jiří Cvrček. “Hydronic heating testbed automation”. Master’s thesis. Czech Technical University in Prague, 2019

[M4] Jan Předota. “Model predictive control for buildings with one-pipe hydronic heating”. Master’s thesis. Prague: Czech Technical University in Prague, June 2018

[M5] Jiří Valtr. “Mass flow estimation and control in pump driven hydronic systems”. Master’s thesis. Prague: Czech Technical University in Prague, Jan. 2017

[M6] Ondřej Zlevor. “Heat flow control of water-to-air heat exchanger”. Master’s thesis. Prague: Czech Technical University in Prague, May 2017

[M7] Jan Hauser. “Distributed predictive control of buildings”. Master’s thesis. Prague: Czech Technical University in Prague, June 2017

[M8] Tomáš Bäumelt. “Distributed building identification”. Master’s thesis. Prague: Czech Technical University in Prague, June 2016

[M9] Jiří Kubeš. “Návrh elektroniky čerpadla se sférickým motorem”. Master’s thesis. Praha: České Vysoké Učení Technické v Praze, June 2016

Unrelated publications and projects

Peer-reviewed journal publications

[S4] Jan Široký, Jiří Cvrček, and Jiří Dostál. “The Most Common Heating System Control Errors and the Possibility of Solving Them with Self-Adjusting Controllers; [Nejčastější chyby regulace otopných systémů a možnost jejich řešení samonastavujícími se regulátory]”. In: *Heating, Ventilation, Installations (VVI)* 4 (2023)
Authorship: 30%

Patents

[P9] Pavel Trnka and Jiří Dostál. “Anti-windup reference shaping filter for control”. European pat. EP3093718. Nov. 2016. URL: `https://register.epo.org/application?number=EP16168196`

[P10] Pavel Trnka and Jiří Dostál. “Anti-windup reference shaping filter for control”. U.S. pat. US20160334761. Nov. 2016. URL: `https://patentscope.wipo.int/search/en/detail.jsf?docId=US179481457&_cid=P21-LJ45SQ-97679-1`

Conference papers

[C7] Jiří Dostál and Lukáš Ferkl. “Model predictive control of climatic chamber with on-off actuators”. In: *IFAC Proceedings Volumes (IFAC-PapersOnline)*. Vol. 19. Cited By :1. 2014, pp. 4423–4428. DOI: `10.3182/20140824-6-ZA-1003.01571`
Authorship: 95% , **Scopus citations: 11**

Grant projects

[G4] *Increasing the safety of traction batteries for transport*. Grant n. CK04000097. Technology Agency of the Czech Republic. Jan. 2023. URL: `https://starfos.tacr.cz/en/project/CK04000097`
Role: **Principle investigator**

[G5] *GLocalFlex*. Grant n. EU HORIZON-CL5-2022-D3-01-12. European Commission. 2022
Role: **Researcher**

[G6] *Inferential sensing of concentration/viscosity of abrasive slurries*. Grant n. EG20_321/0024688. Ministry of Industry and Trade CZE. June 2021. URL: `https://starfos.tacr.cz/cs/project/EG20_321/`

`0024688`
Role: **Principle investigator by CTU**

[G7] *Open dispatching system with principles of business intelligence and semantic data description*. Grant n. EG20_321/0024003. Ministry of Industry and Trade CZE. Jan. 2021. URL: `https://starfos.tacr.cz/en/project/EG20_321/0024003`
Role: **Principle investigator by CTU**

[G8] *RoboPID - diagnostics and automatic tuning of controller parameters for industrial use in buildings*. Grant n. EG21_374/0026965. Ministry of Industry and Trade CZE. Sept. 2021. URL: `https://starfos.tacr.cz/cs/project/EG21_374/0026965`
Role: **Principle investigator by CTU**

Supervised Master's Theses

[M10] Pavel Souček. “Heat transfer media detection on a centrifugal pumpAtmospheric water generator optimization”. Master's thesis. Czech Technical University in Prague, 2022

Awards

- Excelent result: ‘Zapojení systému pro řízení výkonu a diagnostiku tepelného výměníku’, CTU UCEEB, Buštěhrad, 2022
- Best student paper award, International Automatic Control Conference CACS, Taiwan, 2014
- Dean of the Faculty Award for Outstanding Academic Achievement (masters's program), CTU FEE, Prague, 2013
- Dean's Award for Outstanding Master's Thesis, CTU FEE, Prague, 2013